D.4.1.2 Report on case studies: physical investigation

Document Control Sheet

Project number:	10048765
Project acronym	ASTERIS
Project Title	Adaptation to Saltwater inTrusion in sEa level RIse Scenarios
Start of the project	January 2019
Duration	24 months

Related activity:	Activity 4.1 Case studies: physical investigation
Deliverable name:	Report on case studies: physical investigation
Type of deliverable	Report
Language	English
Work Package Title	Identifying needs and barriers in coastal aquifer management
Work Package number	4
Work Package Leader	INSTITUT ZA JADRANSKE KULTURE I MELIORACIJU KRŠA

Status	Final
Author (s)	Branimir Urlic (IACKR) Monika Zovko, Davor Romić, Marina Bubalo Kovačić, Marija Romić, Marko Reljić, Helena Bakić Begić, Stjepan Husnjak. (University of Zagreb)
Version	1
Due date of deliverable	30 June 2021
Delivery date	30 June 2021

INDEX

1. INTRODUCTION

The objective of WP 4 is to identify and map needs and barriers in coastal aquifer management in the assessed risk scenarios through three activities. This report is a delivery (D 4.1.2) related to the implementation of Activity 4.1 "Case studies: physical investigation". The delivery (D 4.1.2) reports in the form of a study on the spatial, temporal and methodological characterization of water monitoring and the spatial, temporal and methodological characterization of water quality for the three PILOT AREAS:

- Fano coastal groundwater system (Italy)
- Ravenna coastal system (Italy)
- Neretva Delta (Croatia)

2. PILOT AREA: THE FANO COASTAL GROUNDWATER SYSTEM

2.1 Study area

The study area is located in the lower part of the coastal plain of the Metauro river, close to Fano, Northern Adriatic Sea (Italy). It is included within a sedimentary valley and comprises a 10 km wide strip of land parallel to the coast with an extension of about 60 km^2 (Fig. 2.1a). The riverine hydrographic system includes the course of the Metauro River and a secondary network of drainage channels. The Metauro drainage basin has a total extension of about 1400 km^2 and is the largest one in the Marche region. The coastal plain is situated at the foothills of the northern Marche Apennine and is part of the eastern side of the northern Apennine orogenic belt, which developed as a result of convergence processes, active since the Late Oligocene-Early Miocene, between the continental Corsica-Sardinia European margins to the West, and the Adria block of African origin to the East (Savelli et al., 2002; Doglioni et al., 1999; Barchi et al., 1998). The Umbria–Marche–Romagna sector

of the Northern Apennine chain is characterized by thrust anticlines involving a Mesozoic-Tertiary (mainly carbonate) marine succession. By geological point of view, the study area is characterized by Miocene, Pliocene and Quaternary sedimentary deposits (Deiana, and Pialli, 1994; Capuano et al., 2009). The fluvial Metauro valley is orthogonal to the Adriatic coastline and the Quaternary deposits filling the valley are consisting of gravels, gravelly–sands, and gravelly-clays, locally intercalated with lenticular bodies, composed by fine clayey, clayey-sandy and clayey-silty deposits (Fig. 2.2 – Di Girolamo, 2004). The alluvial deposits host a mainly phreatic aquifer system with a thickness variable between 5 and 15 m in the western sector and up to 40 m close to the coast. The reliefs surrounding the studied plain mainly consist of low permeability rocks (Fig. 2.1), apparently excluding any significant contribution of groundwater flow from fractured aquifers toward the phreatic aquifer hosted in the alluvial deposits.

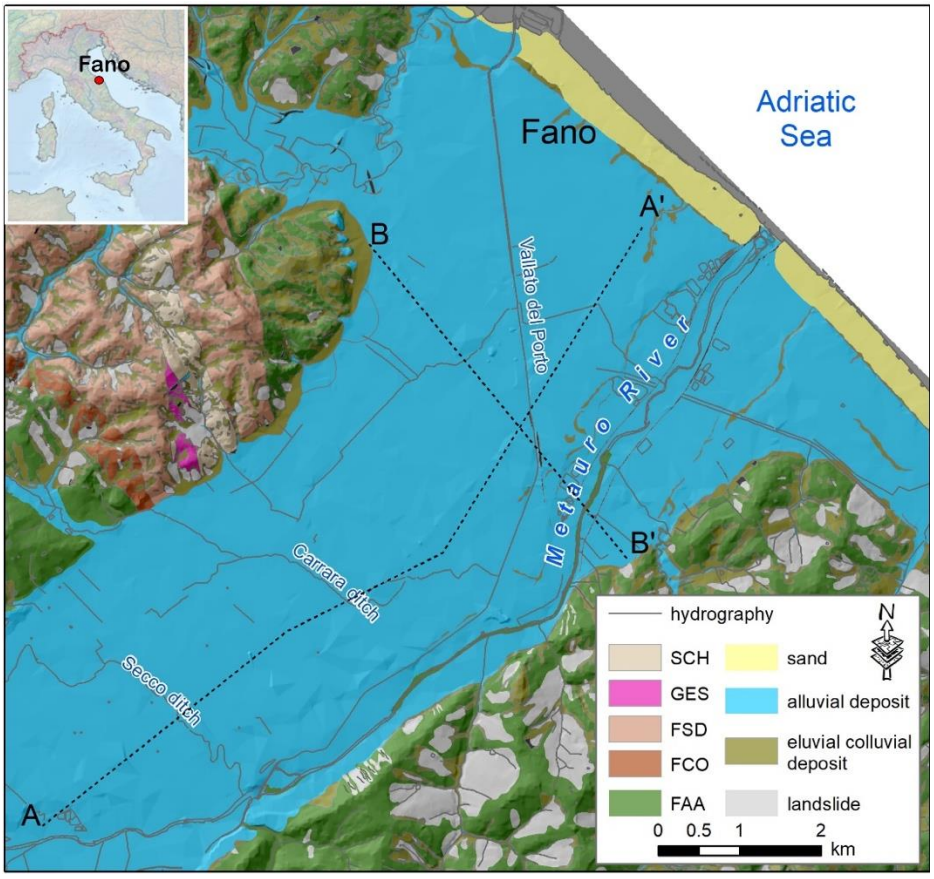

Fig. 2.1 Location of the study area and simplified geological map (SCH: Schlier-marls and clayey marls; GES: flinty gypsum formation; FSD: San Donato formation- marls and clayey marls; FCO: Colombacci formation – pelites; FAA: blue clays formation, modified from Capuano et al., 2009). The dotted lines show the indicative traces of the cross-sections in Fig 2.2.

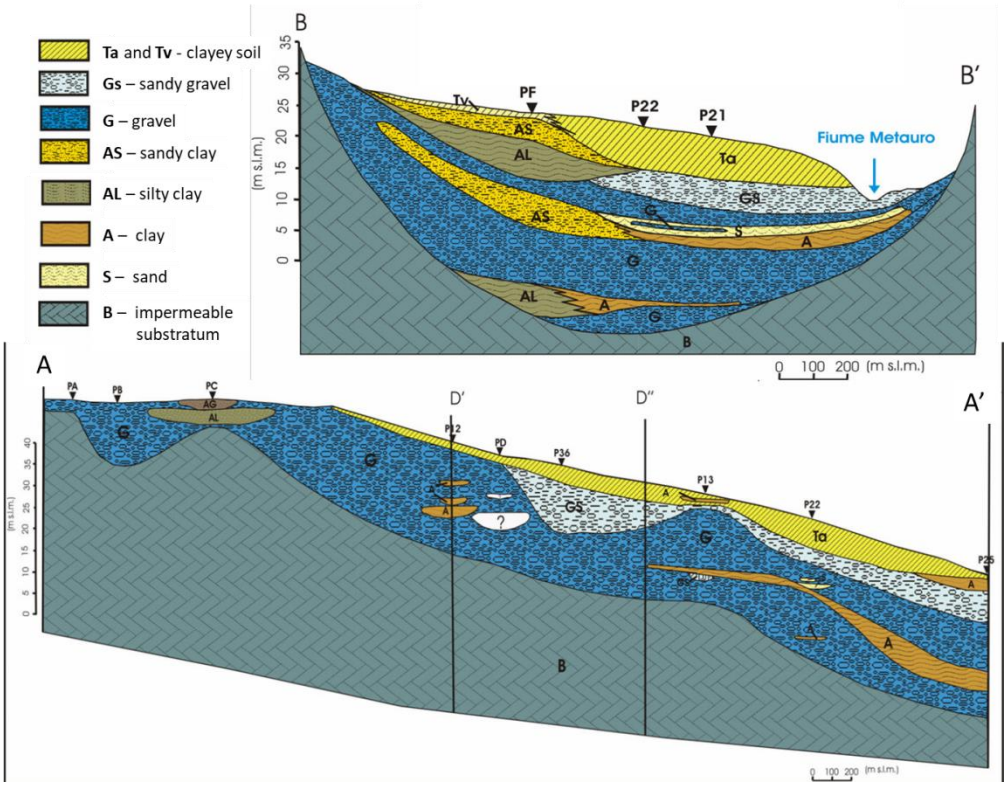

Fig. 2.2 Schematic stratigraphic section of the coastal system (modified from Di Girolamo, 2004). The indicative traces of the cross-sections are shown in Fig. 2.1.

2.2 Materials and methods

The sampling points were selected on the basis of a monitoring network used in a previous work (ASET, 2010) and in order to obtain a distribution as homogeneous as possible over the investigated territory. The sampling sites are mainly consisting of domestic and industrial wells and wells operated by the local water management company (ASET S.p.A.) that supplies drinkable water to Fano inhabitants. Moreover, well depth and well conditions were other two parameters that were taken into account to define the sampling strategy (Fig. 2.3). The study was also extended to selected surface waters (e.g. Metauro River, artificial lakes). The monitoring network established in the framework of the Asteris project was consisting of 46 sites (Fig. 2.3): waters collected from domestic and industrial wells (#0, #2, #3, #4, #7, #9, #10, #12, #13, #14,

#16, #17, #36, #44, #45, #46, #47, #48, #49, #50, #51, #52, #53, #54, and #55), from ASET wells (#18, #19, #21, #22, #23, #24, #27, #28, #29, #30, #34, #35, #37, #38, #39, #41) and surface drainage (Metauro River: #40, #42; artificial channel: #43 and artificial lakes: #20

and #25). It is worthwhile to point out that the Metauro river waters in the area called “Torno” are used to artificially recharge the aquifer via the ASET wells #34, #37 and #38. This action is performed by the water service in order to reduce the general high concentration of nitrates in groundwater (Di Girolamo et al., 2004). At present, a special remote-control system is also used to control the nitrate concentration of the local groundwater.

For each monitoring point, X-Y coordinates and elevation were registered by a high precision Leica GPS (with an error <0.05 m) (Fig. 2.3 and appendix A.1 and A.2). In order to highlight the possible geochemical differences due to the influence of different climatic conditions, three surveys (June 2019, September 2020 and November 2020) were carried out on the selected sites (#0, #4, #7, #10, #12, #14, #16, #17, #18, #19, #21, #22, #23, #24, #27, #28, #29, #30, #34, #35, #37, #38, #39, #40, #42, #43, #44, #49 and #50) during which water sampling (for water chemistry and isotopes) and physicochemical parameters and water level and vertical physicochemical log were measured. It is to mention that in November 2020, a top and bottom water sampling was carried out at the ASET well #39 after registering a significant stratification during the log profile. Since June 2019, six hydrogeological monitoring campaigns (June 2019, September 2019, December 2019, June 2020, September 2020 and November 2020) for water level, temperature, electrical conductivity and, occasionally, vertical physicochemical logs were carried out on all sites, with the exception of some wells since they were not accessible (i.e. in June 2020, due to the COVID-19 sanitary emergency and the consequent restricted measurements).

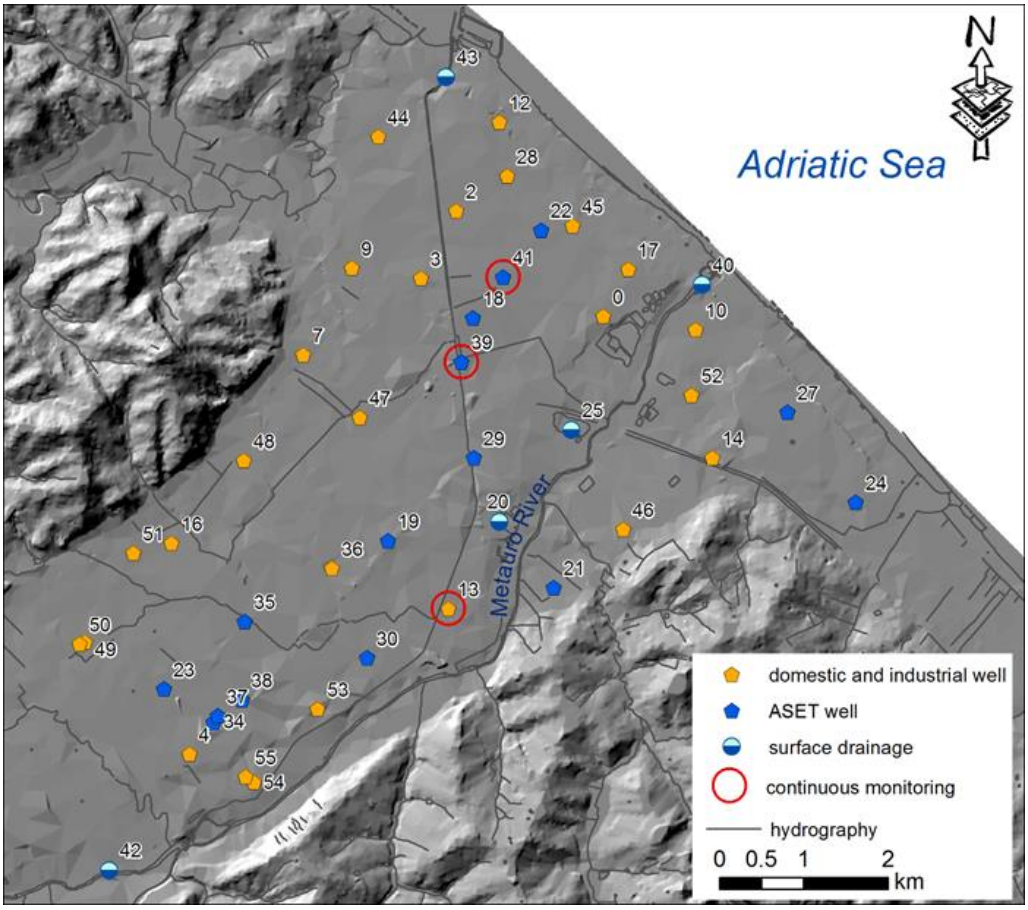

Fig. 2.3 – Monitoring network for Fano coastal system

Since September 2019, three multi-parametric probes (CTD-Diver Schlumberger) were installed in selected wells (#13, #39 and #41) for continuous monitoring of the piezometric level and physical-chemical parameters (electrical conductivity and temperature) (Fig. 2.4). In addition, pressure measurements by means of a baro-thermometric sensor in one of the three wells (#13) for barometric compensation were acquired. Once the project will be over, two multi-parametric probes will be left into two wells to keep acquiring data under the responsibility of the Municipality of Fano and ASET and transmitted on a monthly basis to the IGG-CNR team, in order to verify whether the evolution of the considered parameters is fitting with the predicted scenario(s).

Here below, the measuring and sampling activity can be summarized, as follows:

- 18-20 June 2019 – water sampling piezometric and physicochemical measurements;
- 16-18-25 September 2019 – piezometric and physicochemical measurements and vertical physicochemical logs;
- 2-3-4-10 December 2019 – piezometric and physicochemical measurements;

- 9-11-12 June 2020 – piezometric and physicochemical measurements;
- 3-4 September 2020 – water sampling, piezometric and physicochemical measurements and vertical physicochemical logs;
- 23-24-25 November 2020 – water sampling, piezometric and physicochemical measurements and vertical physicochemical logs.

Based on the rainfall regime reported in Fig. 2.4, the monitoring campaigns of June 2020 and September 2020 can be considered representative of a dry period, June 2019, September 2019 and December 2019 of a wet period while that of November 2020 is to be referred to intermediate hydrological conditions.

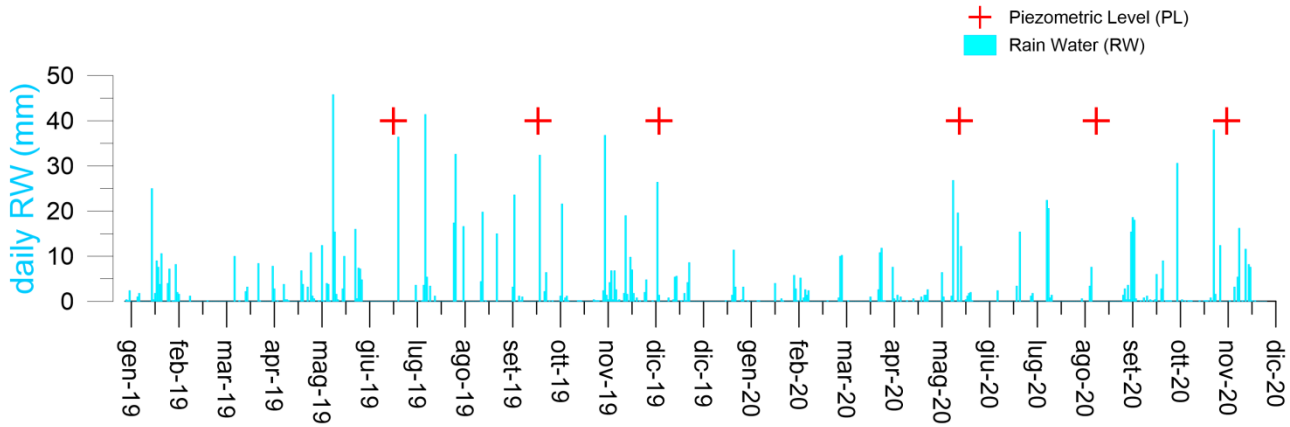

Fig. 2.4. Rainfall regime and sampling/field activity period (daily rainfall from http://app.protezionecivile.marche.it/)

2.2.1 Water level surveys: water table level and vertical logs

Periodical measurements of water level, T, pH and EC (Electrical Conductivity), were performed for all campaigns in order to verify the variation over time of the salt water wedge, if present, in the aquifer and the relationship with the hydrodynamic conditions (Fig. 2.5).

Fig. 2.5 Photos taken during the measurements of coordinates, elevation, water table level and vertical logs.

Once the elevation of the site was measured with the Leica GPS device, the water table level was measured with a phreatimeter in order to obtain the piezometric head above sea level (in m). During the first campaign, vertical logs (electrical conductivity and temperature) were carried out on selected sites to identify possible vertical stratifications of the water column to decide the installation depth of the probe for continuous monitoring. During the subsequent campaigns, some vertical logs were repeatedly measured to verify whether any stratification was occurring.

2.2.2 Water sampling surveys: physicochemical parameters, chemical and isotopic analyses

The physicochemical parameters (temperature, pH, electrical conductivity and oxidation-reduction potential) were determined in situ with a multi-probe Hanna HI98194 (Fig. 2.6). For the chemical and isotopic analyses, four aliquots were collected, as follows:

1. 125 mL of filtered (at 0.45 µm) water for determining the main anions (HCO_3^-, Cl^-, SO_4^{2-}, F^-, Br^-, NO_3^-) and NH_4^+;

2. 50 mL of filtered (at 0.45 µm) water acidified with 0.5 mL of HCl suprapur for the analysis of the main cations (Na^+, K^+, Mg^{2+}, Ca^{2+});
3. 50 mL of filtered (at 0.45 µm) water acidified with HNO_3 suprapur for the analysis of trace elements (Al, Sb, As, Ba, B, Co, Cr, Fe, Li, Mn, Ni, Pb, Cu, Rb, Zn, V, Sr and SiO_2);
4. 125 mL of unfiltered water for the analysis of the water isotopes.

Fig. 2.6 Sampling site and water sampling images

The main cations and anions (with the exception HCO_3^-), analyzed at the CNR-IGG (Unit of Florence), were determined by ionic chromatography using 861 Advanced Compact IC-Metrohm and 761 Compact IC-Metrohm, respectively, while HCO_3^- was analyzed within 24h from sampling by acidimetric titration using a Multi Dosimat 645-Metrohm; the titrating solution was 0.01 N HCl and methyl-orange was used as indicator. Ammonium was analyzed by colorimetry according to the Nessler method by using a HACH DR2000 molecular spectrophotometer. Trace elements (Al, Sb, As, Ba, B, Co, Cr, Fe, Li, Mn, Ni, Pb, Cu, Rb, Zn, V, Sr and SiO_2) were analyzed by ICP-MS (Method: EPA 6020B 2014) at the CSA Research Group of Rimini (Italy). The analytical errors were <5% and 10% for the main ions and trace elements, respectively. The oxygen and hydrogen isotopes (expressed as $\delta^{18}O$ ‰ vs. V-SMOW and δD ‰ vs. V-SMOW, respectively) were determined by IRMS

(Isotope Mass Ratio Spectrometry) at the CNR-IGG of Pisa and University of Parma (Italy) with an automatic preparation line coupled with a Finnigan MAT Delta Plus dual collector mass spectrometer. The oxygen isotopic composition was determined by equilibration with CO_2 while that of hydrogen was analyzed by using platinum as a catalyst. International (V-SMOW, GISP and SLAP) and internal standards were periodically analyzed. The standard deviation was ±0.08 to ±0.12‰ (2σ) for oxygen and ±1.0 to ±2.0‰ (2σ) for hydrogen isotopes as "□" notation (Longinelli and Selmo, 2003).

2.2.3 Geostatistical data processing

Concerning the data processing for visualizing the piezometric maps, iso-level lines were drawn hypothesizing a spatial continuity of the selected variables, to interpolate the experimental points. For this purpose, it is fundamental not to "create" information, but to make the best use of the existing information (Chilés & Chauvet, 1973), evaluating the reliability of each map with the estimation of the interpolation error. Common interpolation methods (splines, influence polynomials, the inverse of the distance square) lack of objective criterions to evaluate the "quality" of the map. The method that overcomes this problem is kriging (Krige, 1951; Matheron, 1962; 1965; 1969; 1970), widely developed in the 80's (Chauvet, 1982; Chauvet, 1991; Chauvet, 1993; Chauvet and Galli, 1982, Armstrong, 1984a; Armstrong 1984; Wackernagel, 1995), and applied to different case studies by many authors (e.g. Clark, 1979; David, 1973; Davis, 1986). The iso-lines maps comprise, as mandatory preliminary steps: (a) realization of experimental variograms, and (b) selection of best fitting mathematical models. A "cross-validation" test was performed to evaluate the goodness of the mathematical models (Devijver and Kittler, 1982). The geostatistical data processing was carried out by using the ISATIS® software package that allows the realization of experimental variograms, variogram models and "cross-validation" tests. The estimation error maps, evaluated as standard deviation, were also displayed. The variography study was performed with the analysis of anisotropy, in order to define the mathematical models representing the structure of the regionalized variables.

2.3 Results

2.3.1 Hydrodynamic data

All water level data (both hydrometric, in case of stream waters or rivers, and piezometric, in case of groundwater) produced in the six campaigns are reported in Table 2.1.
In Table 1, the minimum and the maximum values of the water level measured at each point are also reported, as well as the relative maximum variation in the monitoring period. For an overall evaluation, the maximum variations were very limited, being close to or less than 1 m. Only a few points showed greater variations, some of which being located in the artificial recharge area (e.g. #34, #37, #38) and others in the sectors facing the hills (#9, #46, #48).

In order to better understand the variations of the water level of the whole system for the different survey, the box plot with the median value (in bold), 25° e 75° quartiles, maximum and minimum value are reported in Fig. 2.7.

Table 2.1 Water level data in the different survey periods, minimum and maximum value, and maximum variation recorded

	water level (m a.s.l.)								
CODE	jun-19	sept-19	dec-19	jun-20	sept-20	nov-20	Min	Max	Delta
0	1.01	1.01	0.81	1.17	0.39	0.54	0.39	1.17	0.78
2	2.89	2.94	3.03	2.69	2.27	2.49	2.27	3.03	0.76
3	5.47	5.36	5.33	4.97	4.58	4.59	4.58	5.47	0.89
4	23.80	23.16	23.13	23.80	22.99	22.91	22.91	23.80	0.89
7	16.21	16.17	16.31	16.32	16.05	16.27	16.05	16.32	0.27
9	9.09	9.15	9.16	7.75	-	8.81	7.75	9.16	1.41
10	0.52	-	-0.17	0.44	0.24	0.51	-0.17	0.52	0.69
12	1.47	1.50	1.56	1.46	1.35	1.45	1.35	1.56	0.21
13	13.02	12.59	13.04	12.98	12.21	12.51	12.21	13.04	0.83
14	3.81	3.67	3.79	3.75	3.61	3.71	3.61	3.81	0.19
17	1.43	1.30	1.46	1.27	1.10	1.28	1.10	1.46	0.36
18	5.09	4.88	4.89	-	4.38	4.31	4.31	5.09	0.77
19	12.01	11.96	11.89	11.86	11.20	11.11	11.11	12.01	0.90
20	-	9.39	-	-	9.11	-	9.11	9.39	0.28
21	9.26	9.06	8.92	8.90	8.64	8.45	8.45	9.26	0.81
23	22.72	23.58	23.25	23.68	22.78	22.74	22.72	23.68	0.96
24	0.30	0.16	0.58	0.21	0.00	0.26	0.00	0.58	0.58
25	-	4.83	-	-	4.52	4.58	4.52	4.83	0.31
27	0.21	0.39	0.64	0.32	0.14	0.35	0.14	0.64	0.50
29	7.26	7.45	7.65	7.41	5.76	7.02	5.76	7.65	1.89
30	16.18	16.07	15.99	16.23	16.31	16.46	15.99	16.46	0.47
34	24.35	21.93	22.68	23.40	24.54	26.31	21.93	26.31	4.38
35	19.24	19.57	19.19	19.70	19.07	19.05	19.05	19.70	0.65
36	13.92	13.76	13.51	13.71	13.08	12.96	12.96	13.92	0.96
37	-	21.55	22.40	23.10	22.68	22.66	21.55	23.10	1.55
38	-	20.69	20.96	21.81	21.07	21.08	20.69	21.81	1.12
39	6.08	5.83	5.80	5.43	5.28	5.14	5.14	6.08	0.94
40	-	0.32	1.00	0.39	0.27	0.44	0.27	1.00	0.73
41	-	3.68	3.72	3.45	3.16	3.24	3.16	3.72	0.56
42	-	27.09	28.77	27.52	26.88	26.92	26.88	28.77	1.89
43	-	-0.29	0.20	0.08	-0.02	0.07	-0.29	0.20	0.49
44	-	3.19	3.19	2.94	2.59	2.79	2.59	3.19	0.60
45	-	1.77	1.91	1.71	1.51	1.64	1.51	1.91	0.40
46	-	5.76	5.58	4.02	3.86	5.36	3.86	5.76	1.90
47	-	9.83	9.57	9.50	8.99	8.85	8.85	9.83	0.98
48	-	22.92	23.15	22.97	21.65	22.97	21.65	23.15	1.50
50	-	32.90	32.95	-	32.73	32.67	32.67	32.95	0.28
51	-	30.19	30.18	-	30.07	30.11	30.07	30.19	0.12
52	-	1.23	1.37	-	0.96	1.17	0.96	1.37	0.41
53	-	18.90	19.18	19.57	-	18.56	18.56	19.57	1.01
54	-	21.65	21.56	22.22	21.21	21.22	21.21	22.22	1.01
55	-	21.69	-	-	-	-	-	-	-

Considering the median values, it is possible to observe relatively important variations between the different campaigns. In particular, the maximum values recorded were related to September 2019 with a median value of 9.2 m a.s.l., while the minimum values were observed in September 2020. This is still congruent with the abovementioned hydrological regime (Fig. 2.4), and it points out that the system in general is dynamic and roughly homogeneously affected by rainfall conditions.

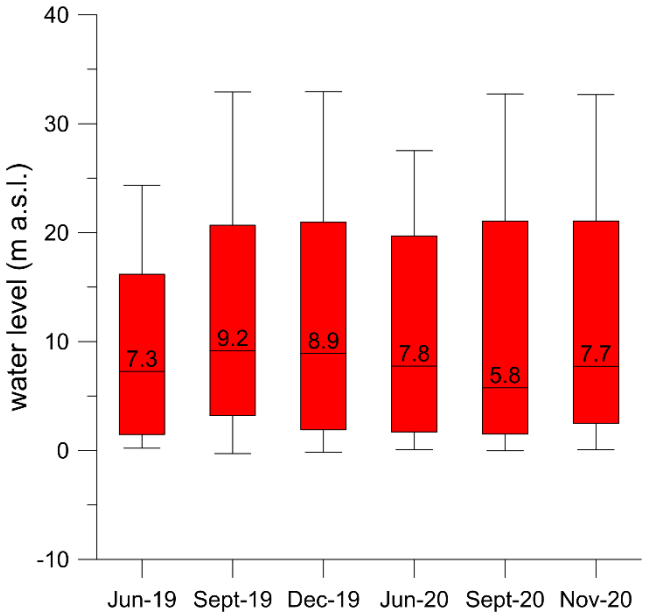

Fig. 2.7 Box plots of the water level for June 2019 to November 2020 monitoring campaigns (in bold the median value).

Changes in piezometric levels as a function of the hydrological regime were further observed in the chronograms of the continuous monitoring probes (Figs 2.8 a, b, c) where piezometric level (PL), T and EC are reported with the daily rainfall (DR) and, only for #13 well, hydrometric level (HL) (available at http://app.protezionecivile.marche.it/). In the chronograms of #39 and #41 wells the vertical log of EC and T carried out in the last two campaigns (September and November 2020) are also listed.

The #13 well with a depth of about 13 m is located near the Metauro river; the CTD diver was installed at 12 m below ground level (about 10 m a.s.l.). The PL ranged from 13.5 m to 12 m a.s.l. with the maximum value recorded in December 2019 and May 2020. The PL had a seasonal behavior, but it also appeared to be partly influenced by the levels of the Metauro River. From September 2019, the EC increased until February-March 2020, when it reached its maximum value (about 820 µS/cm), then it decreased, with some occasionally abrupt increase, until it reached the minimum values in September-October 2020 (about 750 µS/cm). The T remained more or less constant with values a little lower than 16 °C. The #39 and #41 well depth is of 45 and 32 m, respectively, and they are located in the central area of the plain. At #39 and #41, the divers were both installed at about 19 m below ground level (about -1 m and -3 m a.s.l., respectively). The PL variations in these wells were much less pronounced, but there was still a slight downward trend over the long period. The EC of #39 showed values of about 800 µS/cm in the first monitoring period (until February 2020), and then, decreased in spring and summer (about 660 µS/cm), reaching once again values

clustering around 800 µS/cm from the end of August 2020 until the end of the monitoring period. The T had a similar trend but with values varying between 16/17 °C and slightly less than 15 °C. The EC of #41 well was continually decreasing, with values of >1000 µS/cm in the first period, until it reached values of around 850 µS/cm at the end of the monitoring period whilst the T always remained constant (ca. 15 °C).

The vertical logs performed at #39 well showed a constant value of about 800 µS/cm until -16 m (a.s.l.), then a gradual increase in the EC was observed when about 3000 µS/cm were measured at the well bottom. The vertical logs at # 41 only showed a less evidenced EC increase with depth, with values ranging from about 650 to 1150 µS/cm.

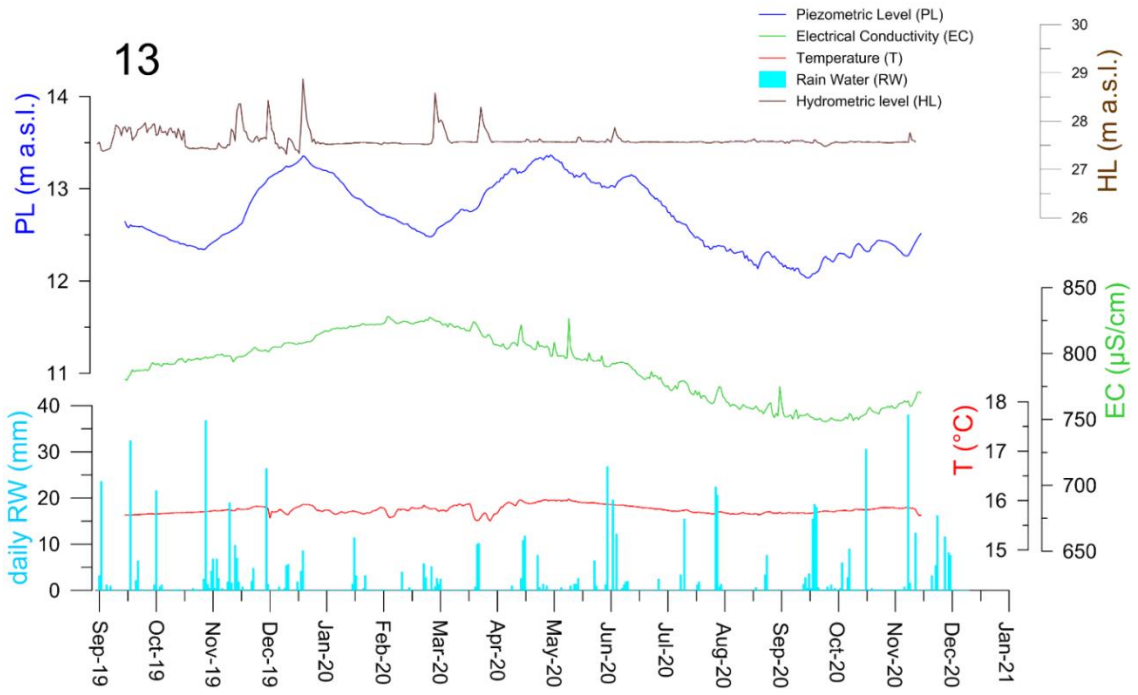

Fig. 2.8a Chronogram of continuous monitoring of PL, T, EC of 13 well; daily rainfall and hydrometric level at Lucrezia station (data available from http://app.protezionecivile.marche.it/)

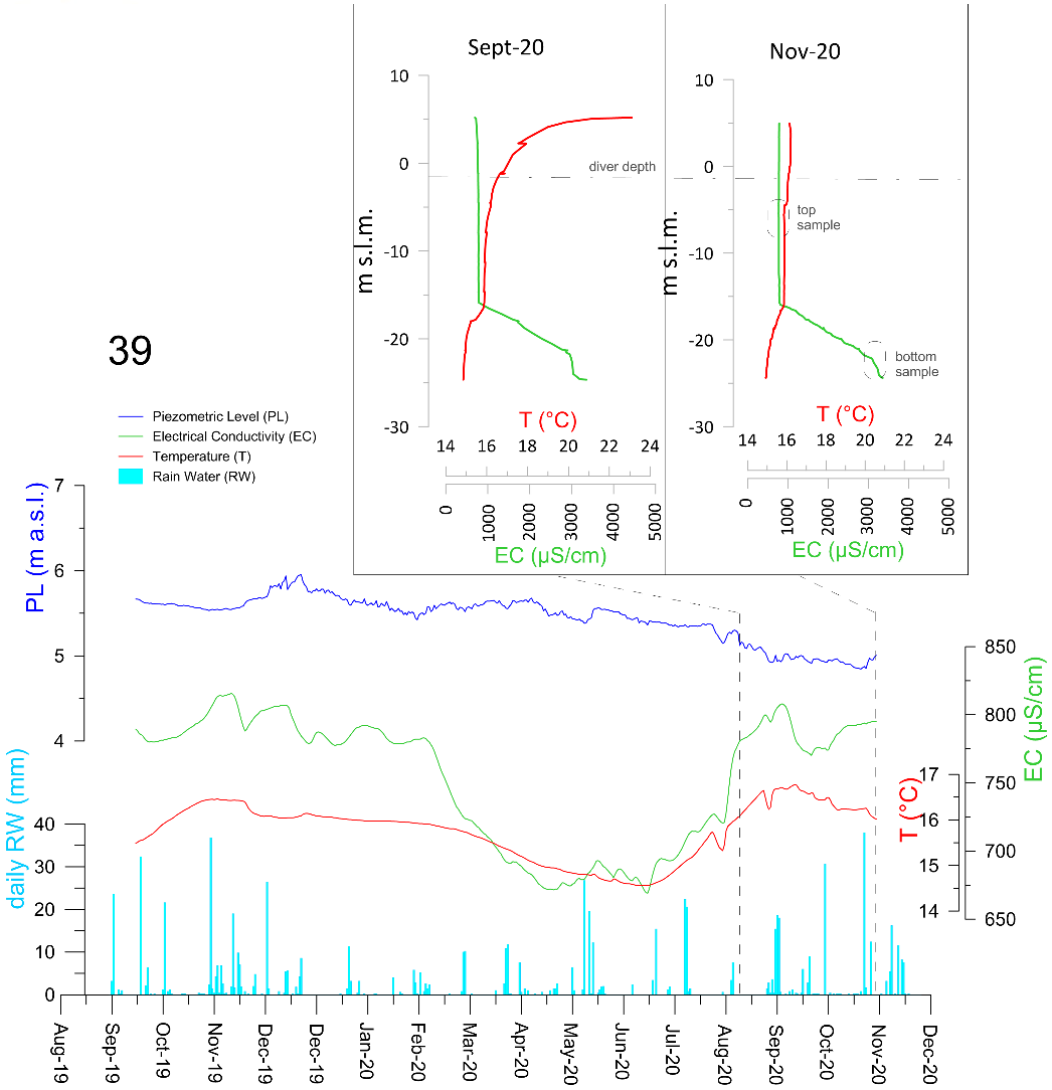

Fig. 2.8b Chronogram of continuous monitoring of PL, T, EC of 39 well; vertical logs, and daily rainfall (data available from http://app.protezionecivile.marche.it/)

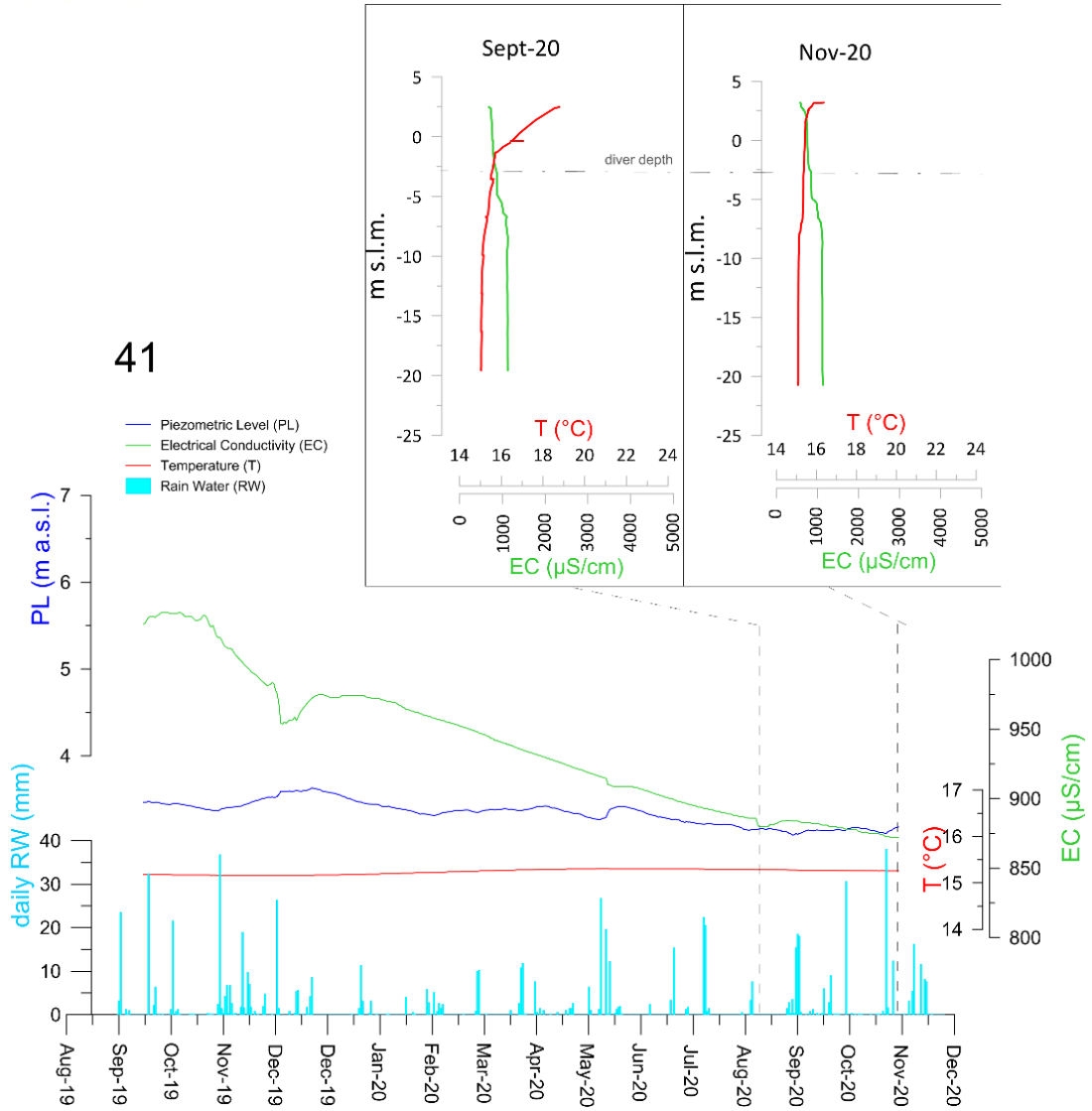

Fig. 2.8c Chronogram of continuous monitoring of PL, T, EC of 41 well; vertical logs, and daily rainfall (data available from http://app.protezionecivile.marche.it/)

2.3.2 Electrical conductivity data

The electrical conductivity thematic maps were selected for those campaigns that had a statistically significant number of measurements. The results obtained for the two selected surveys (December 2019 and September 2020) are reported in Table 2.2, while the two omni-directional experimental variograms are shown in Fig. 2.9

Table 2.2 Summary of variographic analysis results

period	Variable	Model
December 2019	Electrical conductivity	Exponential (range 1316 m; sill 4.7E04)
September 2020	Electrical conductivity	Spherical (range 2652 m; sill 1.2E05) + nugget (sill 4.1E04)

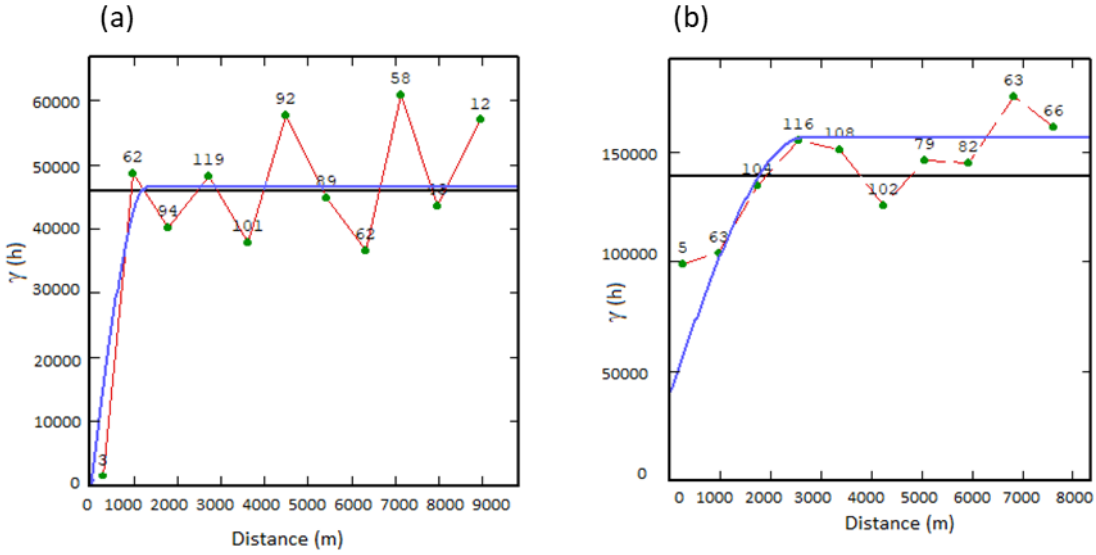

Fig. 2.9 Omni-directional experimental variogram (red line with green dots) and fitted variogram model (blue line) for the electrical conductivity measured in December 2019 (a) and September 2020 (b). Labels close to the experimental variogram green dots indicate the number of couples driving each point.

The reliability of the mathematical models was tested by cross validation, a procedure that uses the variogram model to re-calculate each measurement. The results of this procedure, related to December 2019, are shown in Fig. 2.9 (a), while those referred to September 2020 are reported in Fig. 2.9 (b). Cross-validation diagrams related to December 2019 (Fig. 2.10) show significant differences between true and re-computed values only for two points. The difference between measured and estimated values for the remaining points does not exceed 2.5 σ, which is the threshold usually adopted as acceptance limit for a reliable model. The September 2020 data do not show any excess of the 2.5 σ threshold (Fig. 2.11). Upon validation of the variogram model, the iso-Electrical conductivity maps were generated by means of the Ordinary Kriging estimator, for a grid with cell size of 100 x 100 m.

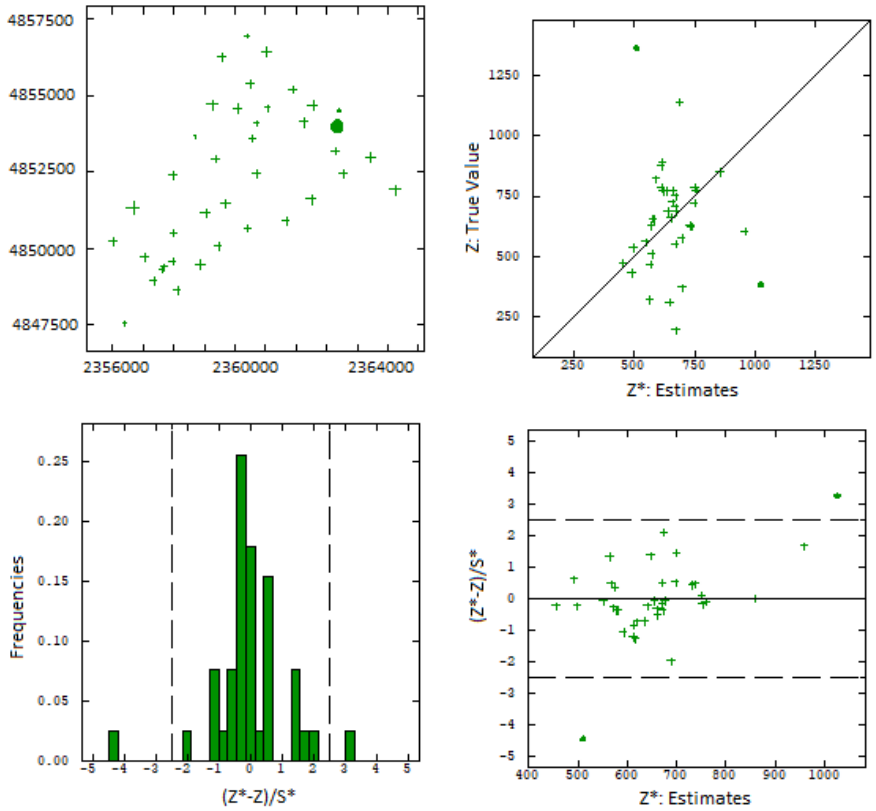

Fig. 2.10 Cross validation diagrams for the variogram model of electrical conductivity measured in December 2019. The full green circles represent the two wells, where the difference between measured and computed values exceeds 2.5σ.

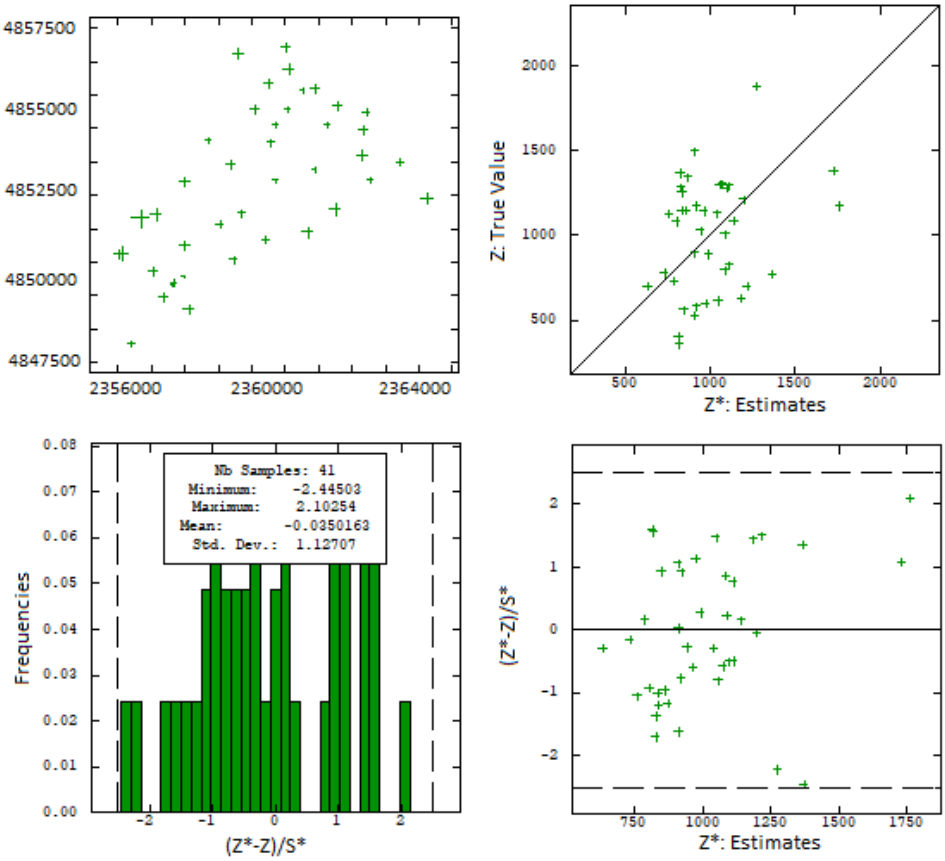

Fig. 2.11 Cross validation diagrams for the variogram model of Electrical conductivity measured in September 2020.

2.3.4 Water chemistry data

In this section, the results of the monitoring surveys for the Fano shallow coastal aquifer are presented to provide a general framework of the studied area. The analytical results are listed in Appendix A.3. The tables are numbered in chronological order, as follows:

- **Table I, Table V and Table VI:** chemical-physical parameters, major and minor species (including the N-bearing species), error % (always <5%) for evaluating the analytical precision, Total Dissolved Solids (TDS) and stable isotopes oxygen and hydrogen in H_2O, for monitoring campaigns of June 2019, September 2020 and November 2020, respectively**;**
- **Table I-a, Table V-a and Table VI-a:** trace elements for the monitoring campaigns of June 2019, September 2020 and November 2020, respectively;
- **Table II, Table III and Table IV:** chemical-physical parameters for the monitoring campaigns of September 2019, December 2020 and June 2020, respectively.

In Tables 2.3 and 2.3a, Table 2.4, Table 2.5, Table 2.6, Tables 2.7 and 2.7a and Tables 2.8 and 2.8a a summary of univariate statistical parameters (valid case, minimum, maximum, geometric mean, median and std. dev. values) is listed. The results clearly illustrate that most distributions of the studied components are typically right-skewed. In this case, the shape of the data frequency distribution is better describable by using the geometric mean parameter instead of the mean.

Table 2.3 Statistic parameters (chemical-physical parameters, major and minor species, including the N-bearing, species, TDS and stable isotopes) for June 2019.

Variable	Valid case	Mean	Geometric mean	Median	Minimum	Maximum	Std.Dev.
T (°C)	21	17	17	16	14	27	2.9
pH	21	7.3	7.3	7.3	6.9	7.7	0.25
E.C. (µS cm-1)	21	1126	1099	1200	670	1400	230
Eh (mV)	21	229	210	164	110	420	97
HCO_3 (mg/L)	21	384	377	406	244	501	71
F (mg/L)	15	0.46	0.40	0.40	0.17	1.52	0.32
Cl (mg/L)	21	65	60	65	28	139	28
Br (mg/L)	17	0.39	0.35	0.42	0.10	0.59	0.15
NO_3 (mg/L)	21	49	37	55	4.7	91	27
NO_2 (mg/L)	21	0.13	0.08	0.07	0.03	1.31	0.27
SO_4 (mg/L)	21	97	95	97	70	126	17
Na (mg/L)	21	51	48	49	26	104	22
NH_4 (mg/L)	21	0.06	0.06	0.05	0.04	0.15	0.02
K (mg/L)	21	5.5	4.2	3.6	1.8	33.9	6.8
Mg (mg/L)	21	26	25	25	14	42	8
Ca (mg/L)	21	135	131	140	76	178	28
TDS (mg/L)	21	814	794	883	482	986	167
$\delta^{18}O$-H_2O (V-SMOW)	21	-7.5		-7.5	-8.1	-6.5	0.4
$\delta^{2}H$-H_2O (V-SMOW)	21	-48.6		-48.9	-51.5	-43.4	2.1

Table 2.3a Statistic parameters (trace elements) for June 2019.

Variable	Valid case	Mean	Geometric mean	Median	Minimum	Maximum	Std.Dev.
Al (µg/L)	9	9.00	7.54	6.00	5.00	29.00	7.62
Sb (µg/L)	21	0.13	0.12	0.10	0.10	0.20	0.05
As (µg/L)	21	0.28	0.25	0.20	0.20	0.70	0.16
Ba (µg/L)	21	81.68	78.24	81.10	44.20	137.00	24.43
B (µg/L)	21	176.8	165.0	137.0	104.0	393.0	75.58
Co (µg/L)	15	0.17	0.14	0.10	0.10	0.60	0.13
Cr (µg/L)	21	1.34	0.93	0.90	0.20	5.30	1.40
Fe (µg/L)	19	38.16	19.47	15.00	5.00	220.0	53.85
Li (µg/L)	21	16.07	15.46	14.40	10.90	30.90	5.04
Mn (µg/L)	8	15.85	8.34	8.70	1.40	74.90	24.16
Ni (µg/L)	21	2.25	2.08	2.00	1.30	4.90	1.01
Pb (µg/L)	21	0.21	0.19	0.20	0.10	0.40	0.10
Cu (µg/L)	21	2.75	2.36	2.00	1.30	9.60	1.91
Rb (µg/L)	4	2.42	1.77	1.29	1.01	6.08	2.45
Zn (µg/L)	17	18.76	13.35	9.00	5.00	50.00	16.16
V (µg/L)	21	0.49	0.46	0.40	0.30	1.00	0.17
SiO_2 (mg/L)	21	19.00	18.25	22.00	9.00	25.00	5.04
Sr (µg/L)	21	787.9	775.6	731.0	642.0	1148.0	150.0

Table 2.4 Statistic parameters (chemical-physical parameters) for September 2019.

Variable	Valid case	Mean	Geometric mean	Median	Minimum	Maximum	Std.Dev.
T (°C)	8	17.5	17.5	17.3	17.0	18.5	0.598
pH	9	7.4	7.4	7.4	7.3	7.7	0.117
E.C. (µS cm-1)	28	2050	1083	1074	235	<30000	5487
Eh (mV)	9	140		142	-106	335	140

Table 2.5 Statistic parameters (chemical-physical parameters) for December 2019.

Variable	Valid case	Mean	Geometric mean	Median	Minimum	Maximum	Std.Dev.
T (°C)	39	15.5	15.4	15.5	10.0	19.0	1.71
pH	39	7.5	7.5	7.5	6.9	8.4	0.4
E.C. (µS cm-1)	39	661	624	663	198	1363	217

Table 2.6 Statistic parameters (chemical-physical parameters) for June 2020.

Variable	Valid case	Mean	Geometric mean	Median	Minimum	Maximum	Std.Dev.
T (°C)	35	16.4	16.3	16.1	14.2	20.2	1.26
pH	35	7.2	7.2	7.1	6.9	8.1	0.3
E.C. (µS cm-1)	35	1031	985	1068	528	1883	305

Table 2.7 Statistic parameters (chemical-physical parameters, major and minor species, including the N-bearing species, TDS and stable isotopes) for September 2020.

Variable	Valid case	Mean	Geometric mean	Median	Minimum	Maximum	Std.Dev.
T (°C)	39	18	18	17	16	26	2.5
pH	39	7.4	7.4	7.2	7.0	9.1	0.42
E.C. (µS cm-1)	39	1169	987	1086	359	7400	1090
Eh (mV)	25	121		134	-170	213	81
HCO_3 (mg/L)	27	380	368	411	204	486	87
F (mg/L)	27	0.63	0.56	0.61	0.11	1.40	0.29
Cl (mg/L)	27	88	78	72	43	340	58
Br (mg/L)	27	0.38	0.36	0.33	0.21	1.00	0.16
NO_3 (mg/L)	27	45	26	52	1.4	84	29
NO_2 (mg/L)	27	0.04	0.02	0.02	0.01	0.52	0.10
SO_4 (mg/L)	27	108	101	110	15	167	32
Na (mg/L)	27	62	57	53	30	186	31
NH_4 (mg/L)	27	0.05	0.04	0.04	0.01	0.23	0.04
K (mg/L)	27	6.3	5.1	4.4	2.6	36.8	6.4
Mg (mg/L)	27	31	29	30	18	55	10
Ca (mg/L)	27	132	125	141	23	166	33
TDS (mg/L)	27	852	820	921	373	1401	224
$\delta^{18}O$-H_2O (V-SMOW)	27	-7.2		-7.3	-7.6	-5.9	0.4
$\delta^{2}H$-H_2O (V-SMOW)	27	-47.9		-47.8	-53.5	-42.6	2.3

Table 2.7a Statistic parameters (trace elements) for September 2020.

Variable	Valid case	Mean	Geometric mean	Median	Minimum	Maximum	Std.Dev.
Al (µg/L)	12	7.83	7.03	6.00	5.00	24.00	5.18
Sb (µg/L)	26	0.15	0.13	0.10	0.10	0.60	0.11
As (µg/L)	26	0.35	0.25	0.20	0.10	1.20	0.35
Ba (µg/L)	27	92.41	85.02	88.60	15.10	177.00	34.70
B (µg/L)	27	130.3	122.6	116.0	73.0	282.0	51.72
Co (µg/L)	21	0.21	0.16	0.10	0.10	1.00	0.22
Cr (µg/L)	27	0.81	0.58	0.70	0.10	2.30	0.63
Fe (µg/L)	23	83.52	14.21	9.00	6.00	1562.0	322.97
Li (µg/L)	27	14.04	13.22	11.80	8.20	28.70	5.56
Mn (µg/L)	27	13.74	2.09	0.90	0.20	123.00	32.97
Ni (µg/L)	27	2.31	2.03	1.80	0.90	6.50	1.29
Pb (µg/L)	27	0.23	0.19	0.20	0.10	1.40	0.24
Cu (µg/L)	27	3.52	2.24	1.70	0.70	23.50	4.80
Rb (µg/L)	27	1.24	0.85	0.66	0.38	7.60	1.52
Zn (µg/L)	26	27.88	17.59	14.50	6.00	179.00	39.87
V (µg/L)	26	0.41	0.37	0.30	0.20	0.90	0.21
SiO_2 (mg/L)	27	19.92	18.27	20.70	1.45	28.00	5.73
Sr (µg/L)	27	733.9	694.0	715.0	122.0	1081.0	201.5

Table 2.8 Statistic parameters (chemical-physical parameters, major and minor species, including the N-bearing species, TDS and stable isotopes) for November 2020.

Variable	Valid case	Mean	Geometric mean	Median	Minimum	Maximum	Std.Dev.
T (°C)	45	14	14	15	8	18	2.4
pH	45	7.4	7.3	7.3	6.7	8.6	0.39
E.C. (µS cm-1)	45	1141	1069	1125	567	2965	450
Eh (mV)	23	-10		-9	-58	25	18
HCO_3 (mg/L)	30	370	343	402	31	565	101
F (mg/L)	30	0.31	0.28	0.28	0.16	0.80	0.14
Cl (mg/L)	30	118	75	67	19	915	173
Br (mg/L)	30	0.58	0.36	0.36	0.03	3.90	0.81
NO_3 (mg/L)	30	44	16	46	0.1	104	38
NO_2 (mg/L)	30	0.02	0.02	0.02	0.01	0.08	0.01
SO_4 (mg/L)	30	83	73	83	6	155	32
Na (mg/L)	30	71	57	52	21	265	61
NH_4 (mg/L)	30	0.37	0.11	0.08	0.03	7.10	1.28
K (mg/L)	30	6.4	5.2	4.5	2.5	34.0	6.0
Mg (mg/L)	30	31	29	29	17	64	12
Ca (mg/L)	30	131	118	140	7	272	44
TDS (mg/L)	30	856	810	875	353	1585	288
$\delta^{18}O$-H_2O (V-SMOW)	30	-7.4		-7.4	-7.7	-6.6	0.21
$\delta^{2}H$-H_2O (V-SMOW)	30	-47.3		-47.2	-49.9	-44.0	1.3

Table 2.8a Statistic parameters (trace elements) for November 2020.

Variable	Valid case	Mean	Geometric mean	Median	Minimum	Maximum	Std.Dev.
Al (µg/L)	2	7.50	7.48	7.50	7.00	8.00	0.71
Sb (µg/L)	11	0.18	0.14	0.10	0.10	0.60	0.17
As (µg/L)	29	0.36	0.29	0.30	0.10	1.30	0.28
Ba (µg/L)	30	126	84.73	80.30	10.20	1289	223.24
B (µg/L)	30	123.0	105.3	93.0	58.0	590.0	100.79
Co (µg/L)	29	0.41	0.33	0.30	0.10	1.20	0.29
Cr (µg/L)	24	0.66	0.49	0.50	0.10	2.10	0.52
Fe (µg/L)	30	1979	29.32	19.00	8.00	58100	10600
Li (µg/L)	30	14.14	12.43	11.65	6.50	52.60	9.18
Mn (µg/L)	16	32.75	8.31	4.20	1.20	250.00	64.35
Ni (µg/L)	30	3.84	3.31	3.00	1.40	9.40	2.26
Pb (µg/L)	19	0.33	0.26	0.30	0.10	1.00	0.25
Cu (µg/L)	30	4.79	1.85	1.50	0.40	71.90	13.17
Rb (µg/L)	8	3.08	2.53	1.85	1.50	7.40	2.33
Zn (µg/L)	24	47.1	18.71	17.00	5.00	612.00	122.64
V (µg/L)	10	0.37	0.29	0.30	0.10	0.90	0.27
SiO_2 (mg/L)	30	17.3	14.82	17.15	1.00	27.00	7.05
Sr (µg/L)	30	485.0	440.6	453.5	53.0	1430.0	222.3

The temperatures, observed during the six campaigns, were between 8 °C (November 2020) and 27 °C (June 2019) as a function of the sampling period with a median value of about 16 °C (Fig. 2.12). The pH had a median of 7.1, when all the monitoring surveys are considered, the higher (September 2020 at site #25) and the lowest pH values being of 9.1 of 6.7 (November 2020 at site # 54), respectively (Fig. 2.13).

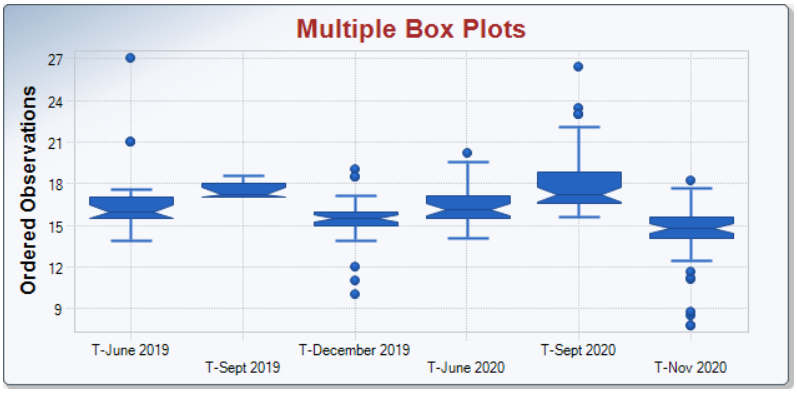

Fig. 2.12 Box plots of the temperature values in °C for the June 2019 to November 2020 monitoring campaigns

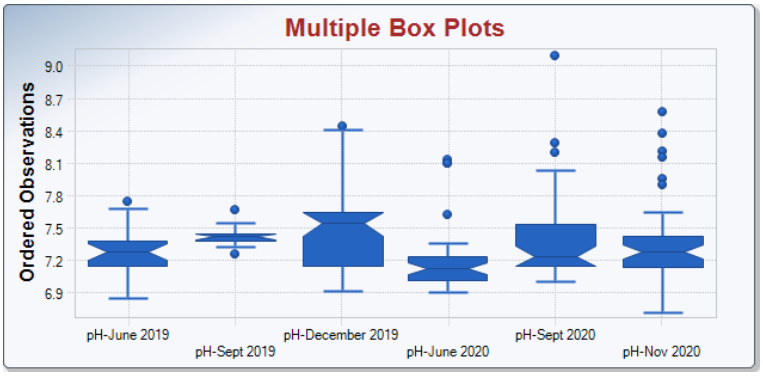

Fig. 2.13 Box plots of the pH values for the June 2019 to November 2020 monitoring campaigns

The EC values during the monitoring samplings showed a median value of about 1,048 µS/cm (Fig. 2.14). Setting aside sample #43, whose EC values were relatively highly variable and comprised between 373 (December 2019) and <30,000 (September 2019) µS/cm, the EC ranged between 670 (#34) and 1,400 (#24) µS/cm; from 235 (#7) to 2,930 (#51) µS/cm; from 198 (#7) to 1,363 (#10) µS/cm; from 528 (#40) to 1,883 (#24) µS/cm; from 359 (#38) to 2,170 (#51) µS/cm and from 567 (#25) to 2,965 (#39 bottom) µS/cm for June 2019, September 2019, December 2019, June 2020, September 2020 and November 2020, respectively (Fig. 2.13).

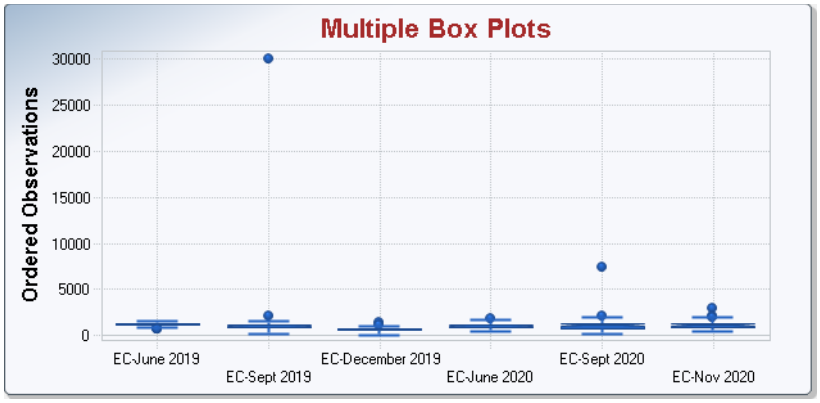

Fig. 2.14 Box plots of the electrical conductivity (EC) values in µS/cm for the June 2019 to November 2020 monitoring campaigns

The median Eh values for each monitoring campaigns was observed to be decreasing from 164 mV to -9 mV, as shown in Fig. 2.15

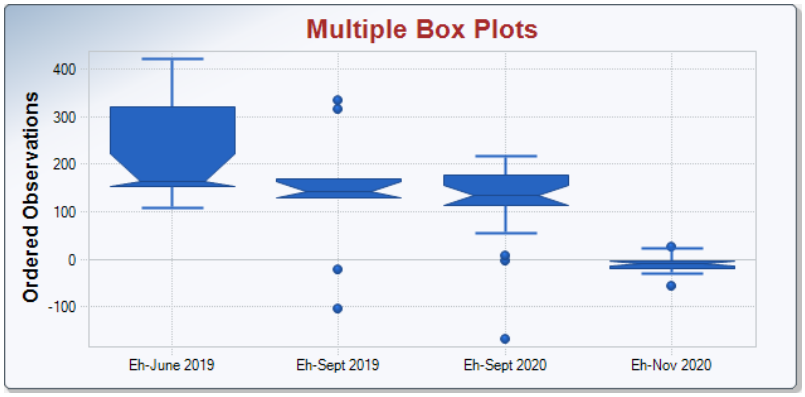

Fig. 2.15 Box plots of the Eh values (in mV) for the June 2019 to November 2020 monitoring campaigns

The box plots of the dissolved major species for June 2019, September 2020 and November 2020 campaigns are displayed in Fig. 2.16. Among the concentration of HCO_3, SO_4, Ca, Mg and K species, no significant variations were recorded during the sampling seasons, as evidenced by the median values (ca. HCO_3 = 400 mg/L, SO_4 = 97 mg/L, Ca= 140 mg/L, Mg= 28 mg/L and K= 3.6 mg/L). Differently, Cl and Na showed a variability from June 2019 (Cl between 28 and 139 mg/L; Na between 26 and 104 mg/L) to November 2020 (Cl between 19 and 915 mg/L; Na between 21 and 265 mg/L), although they were clustering around a median value of 68 mg/L and 52 mg/L, respectively. The HCO_3 concentrations presented a relatively wide variability, being comprised between 31 mg/L (#31 bottom) and 565 (#24) mg/L in November 2020. The sulfate content was between a minimum of 6 mg/L (#18, November 2020) and a maximum of 167 mg/L (#49, September 2020). Ca reached the lowest (# 18 = 7 mg/L) and the highest (#39 bottom = 272 mg/L) contents in November 2020 while those of Mg were from 14 mg/L (#30 in September 2020) to 64 mg/L (#49 in November 2020). The concentration of potassium ranged between 1.8 (#30 in July 2019) and 37 (#12 in September 2020) mg/L.

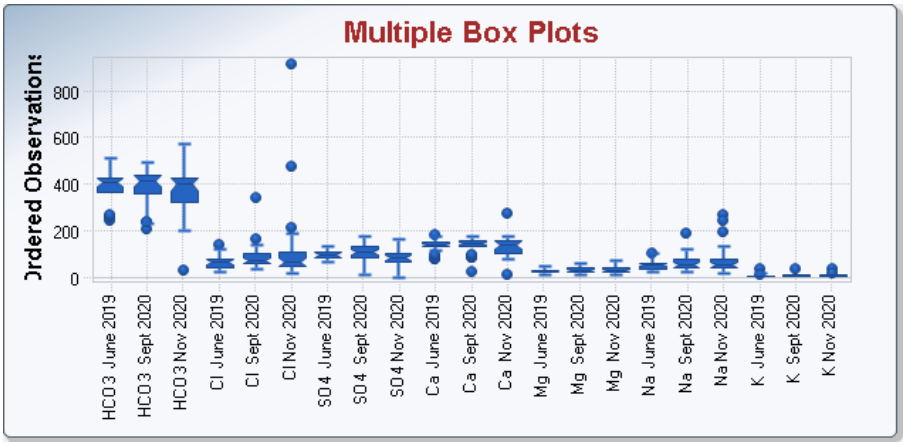

Fig. 2.16 Box plots of the dissolved major species in mg/L for the June 2019, September 2020 and November 2020 monitoring campaigns.

Among the N-bearing species, setting aside the sample #39 bottom (NH_4 = 7.1 mg/L) and #40 (NO_2 = 1.31 mg/L), the sampling sessions for NH_4 and NO_2 were characterized by low concentrations (<0.1 and <0.5 mg/L, respectively) with a median value of 0.05 and 0.03 mg/L, respectively (Fig. 2.17). Conversely, those of NO_3 were characterized by a large variability, being comprised between 4.7 (#34) and 91 (#0) mg/L (median value: 55 mg/L), from 1.4 (#34) to 84 (#12) mg/L (median value: 52 mg/L) and from 0.1 (#38 top) to 104 (#35) mg/L (median value: 46 mg/L), for June 2019, September 2020 and November 2020, respectively (Fig. 2.17). General speaking, the NO_3 contents were characterized by concentrations above the maximum limit according to European Union established for groundwater (Directive 2006/118/EC).

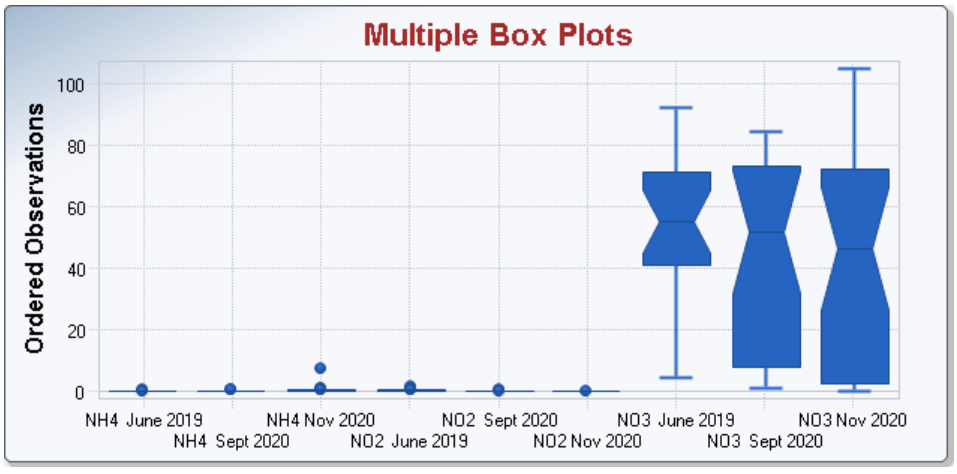

Fig. 2.17 Box plots of the dissolved NH4, NO2 and NO3 species in mg/L for the June 2019, September 2020 and November 2020 monitoring campaigns.

Data variability for dissolved minor species (Br, F and SiO_2) in June 2019, September 2020 and November 2020 campaigns are displayed in Fig. 2.18. Bromide contents during the sampling sessions varied between 0.1 (#22 and #29: June 2019) and 3.9 (#39 bottom: November 2020) mg/L with a median value of about 0.43 mg/L. Fluoride contents were ranging from 0.2 (#14, #22 and #28) to 1.5 (#24) mg/L (June 2019) with a median value of about 3.7 mg/L. Finally, SiO_2 concentrations were characterized by a wide variability and comprised between 1 (#18: September and November 2020) and 28 mg/L (#21: September 2020) with a median value of 22, 20.7 and 17 mg/L for June 2019, September 2020 and November 2020, respectively.

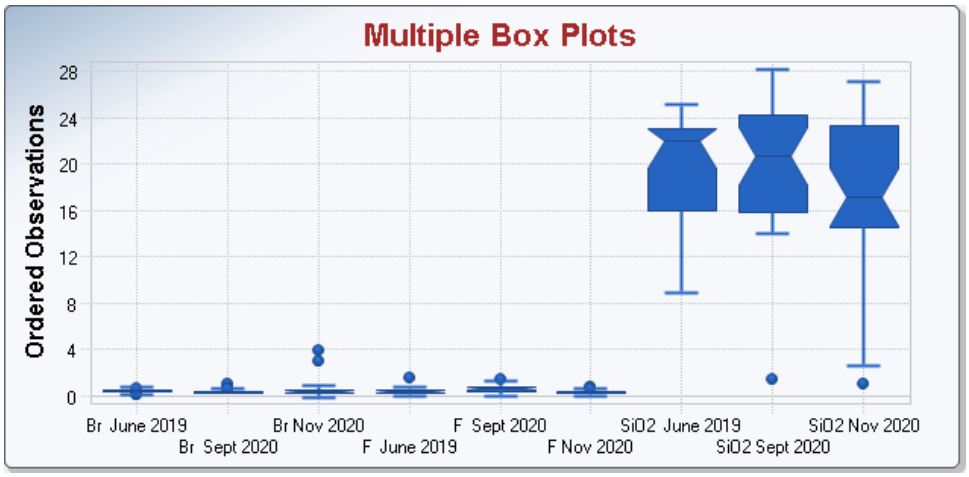

Fig. 2.18 Box plots of the dissolved minor species in mg/L for the June 2019, September 2020 and November 2020 monitoring campaigns.

The valid case, mean, geometric mean, median, the minimum and the maximum values for the concentrations of trace elements are shown in Tables 3.1a; 3.5a and 3.6a. The distribution of the trace elements is summarized in the box-plots of Fig. 2.19 For Sb, As, Co, Cr, Pb, Ni, Rb and V, the concentrations were varying within 2 orders of magnitude while for those of Ba, B, Fe, Li, Mn, Cu, Zn and Sr the contents ranged up to 3–4 orders of magnitude, while only those of Fe (u to 58,100 µg/L for #39 bottom) spanned within 6 orders of magnitude.

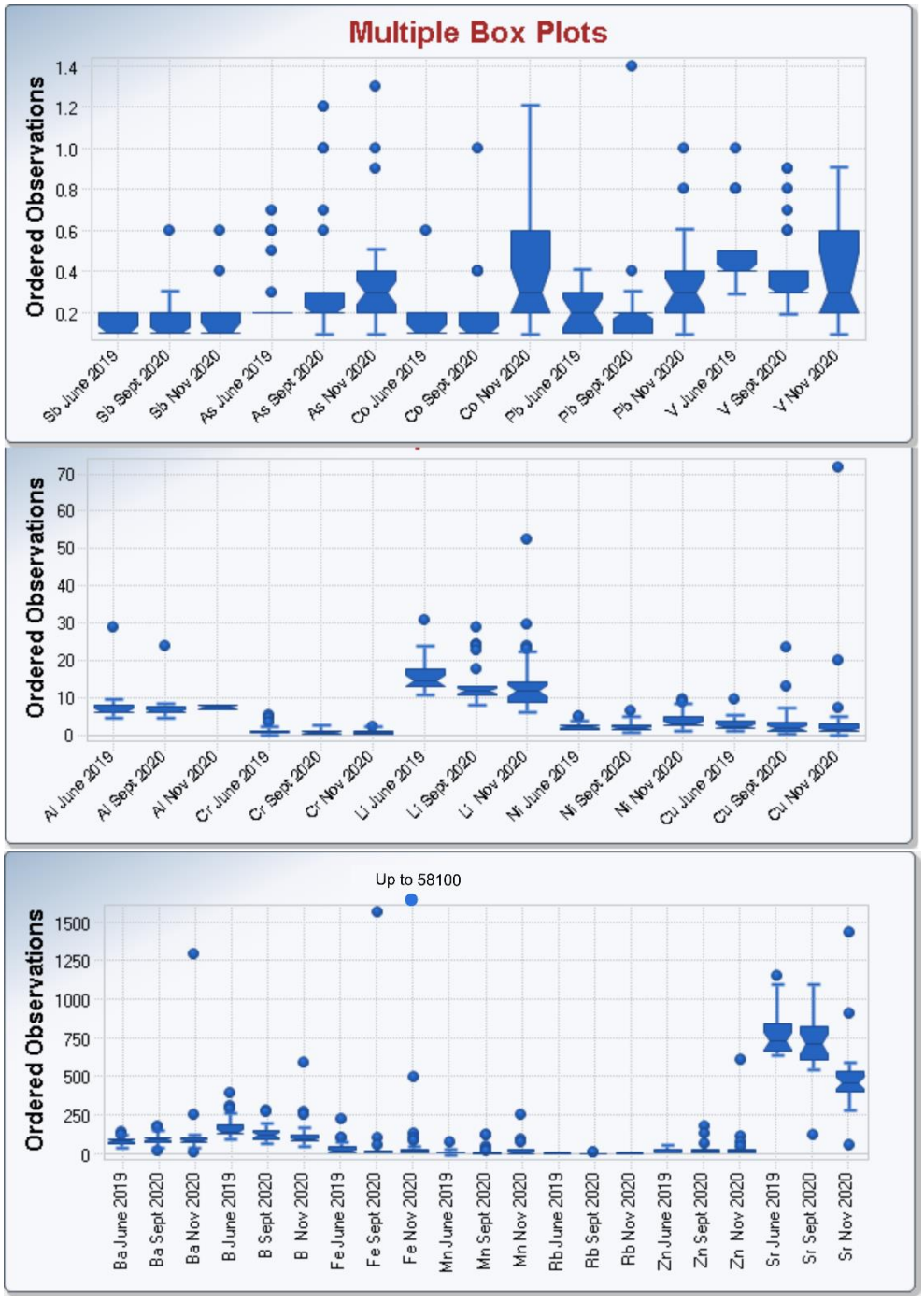

Fig. 2.19 Box plots of the trace elements in µg/L for the June 2019, September 2020 and November 2020 monitoring campaigns

Among the analyzed trace elements, the international groundwater legislation (Directive 2006/118/CE) has classified Sb, As, B, Cr, Ni, Pb and V as pollutant elements. As a consequence, the European Union established a precautionary concentration limit for groundwaters, which was also adopted by the Italian Legislation (D.Lgs. 30/2009). Among

these trace elements all analyzed samples for monitoring seasonal were data below the maximum concentration limits.

The isotopic ratios of oxygen (expressed as $\delta^{18}O\text{-}H_2O$ vs. V-SMOW ‰) are shown in Fig. 2.20. Their variability was from -8.1 (# 34) and -6.5 ‰ (# 10) V-SMOW in June 2019, from -7.6 (# 12) to -5.9 ‰ (# 40) V-SMOW in September 2020 and from -7.7 (# 7) to -6.6 ‰ (# 10) V-SMOW in November 2020. The median values for each sampling gradually increased from June 2019 (-7.5‰ V-SMOW) to September (-7.3 ‰ V-SMOW) and then, decreased in November 2020, down to -7.4 ‰ V-SMOW. An almost similar behavior was shown by the hydrogen isotopes (expressed as $\delta^{2}H\text{-}H_2O$ vs. V-SMOW ‰), the median values increasing from June 2019 (-48.9 ‰ V-SMOW) to November 2020 (up to -47.2 ‰ V-SMOW) as shown in Fig. 2.21. General speaking, the $\delta^{2}H\text{-}H_2O$ intervals were between -51.5 (# 34) and -43.4 ‰ (# 10) V-SMOW in June 2019, from -50.5 (# 23) to -42.6 ‰ (# 40) V-SMOW in September 2020 and from -49.9 (# 12) to -44 ‰ (# 10) V-SMOW in November 2020.

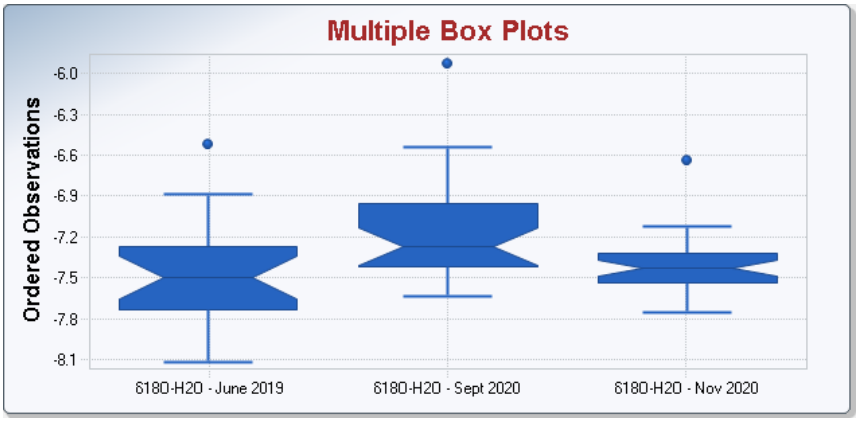

Fig. 2.20 - Box plots of the isotopic ratio of oxygen ($\delta^{18}O\text{-}H_2O$), expressed in ‰ using the δ-notation referring to the standard value in seawater (V-SMOW, Vienna Standard Mean Ocean Water) for the June 2019, September 2020 and November 2020 monitoring campaigns.

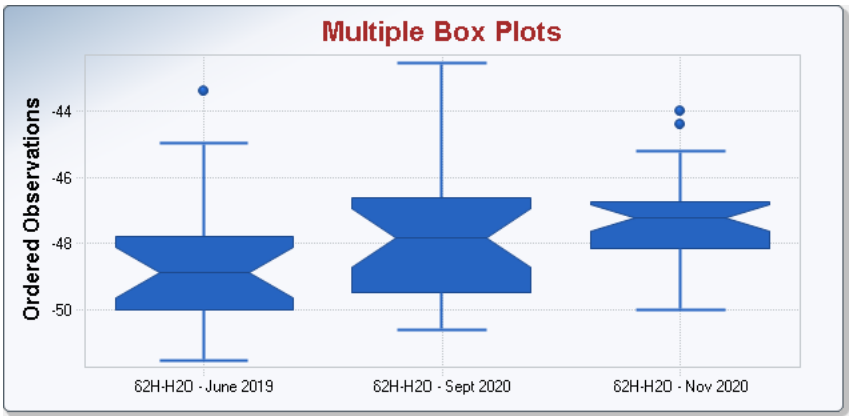

Fig. 2.21 Box plots of the isotopic ratio of hydrogen (δ^2H-H_2O), expressed in ‰ using the δ-notation referring to the standard value in seawater (V-SMOW, Vienna Standard Mean Ocean Water), for the June 2019, September 2020 and November 2020 monitoring campaigns.

A first assessment of the chemical composition for the waters from the Fano coastal area, related to the monitoring campaigns from June 2019, September 2020 and November 2020, is obtained by considering the Cl-SO_4-HCO_3 (Figs. 2.22-2.23-2.24) and (Na+K)-Ca-Mg (Figs. 2.25-2.26-2.27) triangular plots, and the Langelier-Ludwig diagrams (Figs. 2.28-2.29-2.30). The (Na+K)-Mg-Ca and Cl-SO_4-HCO_3 ternary diagrams for cationic and for anionic species are shown in Figs. 2.25-2.27, starting with concentrations expressed in meq/L and calculated to 100%. The main anion triangular diagram shows that the water samples are included in the HCO_3 sector in June 2019 (Fig. 2.22). Chloride is always present in relatively subordinate amounts, with the exception of #49 and #39 bottom, which were collected in September and November 2020, respectively (Fig. 2.23 and Fig. 2.24). The diagrams of Figs. 2.25-2.27 show a clear dominance of Ca among cations for the Fano coastal aquifer in June 2019 (Fig. 2.25), except for a few samples collected in September and November 2020. In these cases, three water samples (#49, #24 and #18) are dominated by Na+K (Fig. 2.26 and Fig. 2.27).

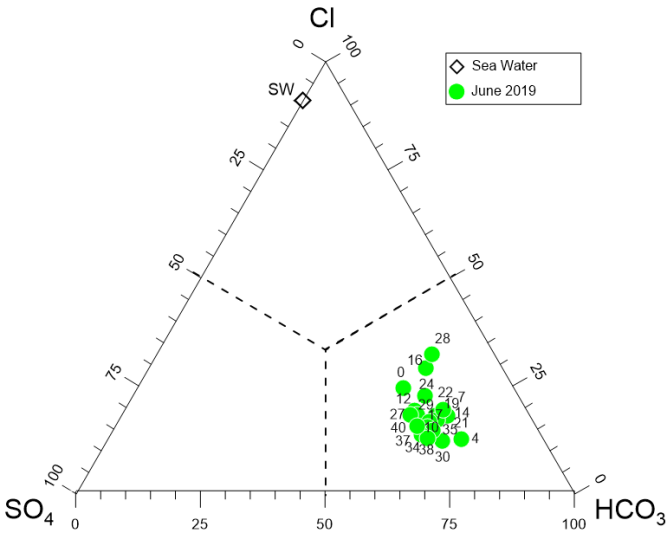

Fig. 2.22 Cl-HCO_3-SO_4 ternary diagram for the investigated samples in June 2019.

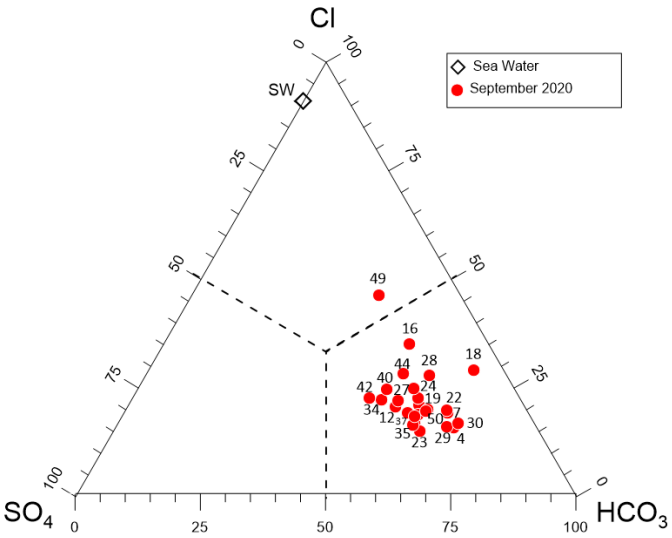

Fig. 2.23 Cl-HCO_3-SO_4 ternary diagram for the investigated samples in September 2020.

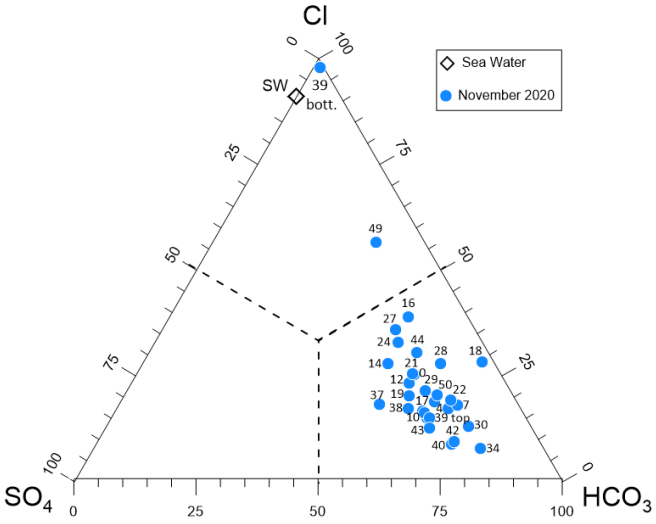

Fig. 2.24 Cl-HCO_3-SO_4 ternary diagram for the investigated samples in September 2020.

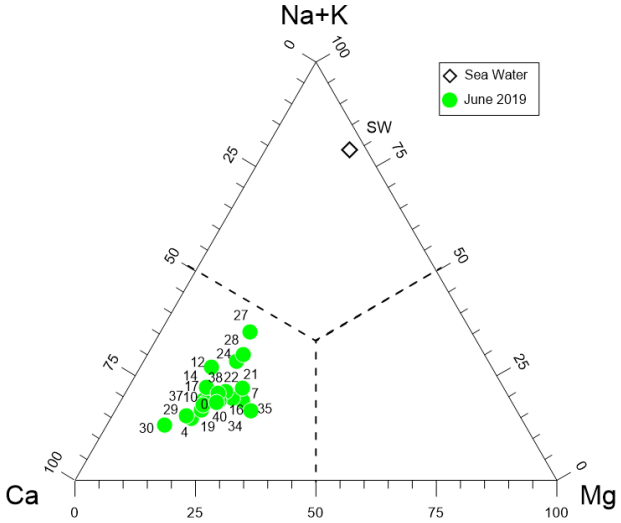

Fig. 2.25 (Na + K)-Ca-Mg ternary diagram for the investigated samples in June 2019.

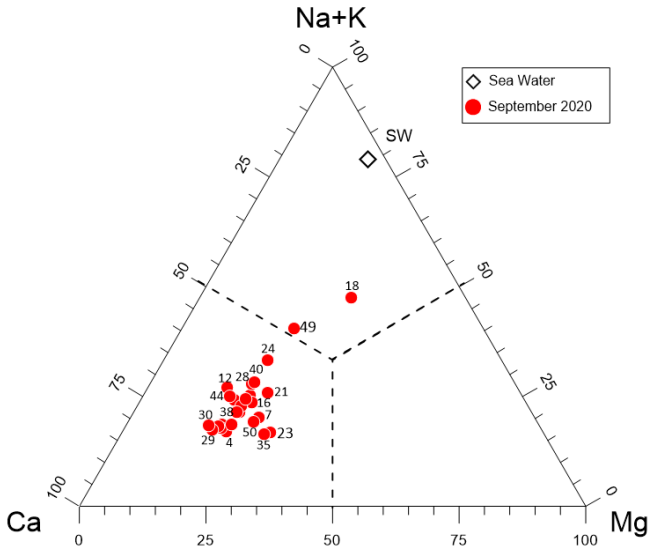

Fig. 2.26 (Na + K)-Ca-Mg ternary diagram for the investigated samples in September 2020.

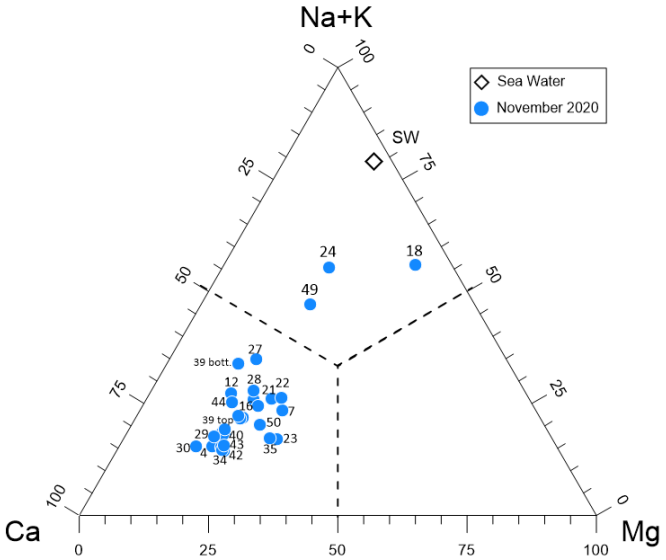

Fig. 2.27 (Na + K)-Ca-Mg ternary diagram for the investigated samples in November 2020.

Similar considerations can be depicted by the square diagrams, which show a mainly Ca-HCO_3 composition in June 2019 and secondarily, a (Na+K)-HCO_3-Cl geochemical facies that tends to be more evident in September and November 2020 (Figs. 2.28-2.30). Another useful parameter for the water classification is the Total Ionic Salinity (TIS) that represents the sum of the concentrations of major anions and cations in meq/L. The Iso-TIS lines are drawn in the correlation graph of HCO_3 vs. SO_4+Cl (Fig. 2.31), in which most waters are found to be distributed between the iso-TIS lines of 10 and 30 meq/L, whereas #24, #49 and #39bottom are characterized by higher TIS, being comprised between 35 and 55 meq/L. According to these plots, it is possible to distinguish three groups of waters with different compositions, reflecting the lithological type and the main geochemical processes characterizing the shallow aquifer of the Fano coastal area, as follows:

(I) Ca-HCO_3 composition. It includes the great majority of the analyzed water samples, whose salinity is from 10 to 30 meq/L.

(II) Ca-Cl facies. It is only represented by the #39bottom water for which the highest recorded salinity (about 55 meq/L) among the studied samples was recorded.

(III) (Na+K)-HCO_3-Cl facies. It is characterized by three waters: # 49 and # 24 that are characterized by an intermediate salinity between 35 and 48 meq/L and #18 with salinity of 12 meq/L.

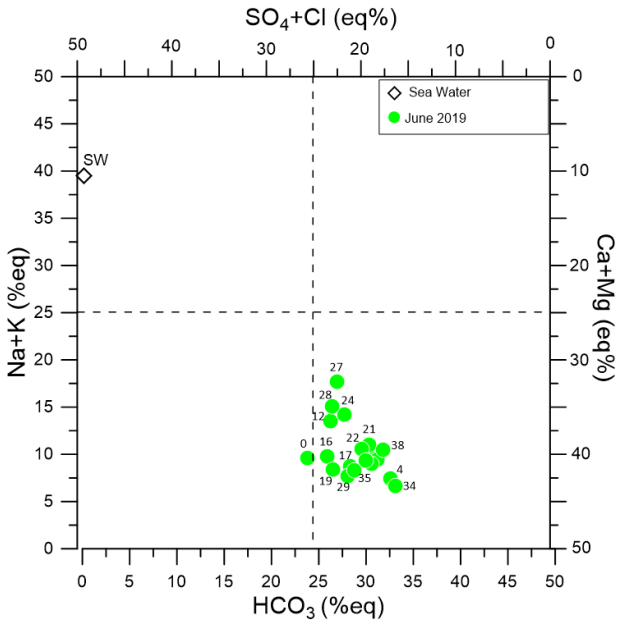

Fig. 2.28 Square diagram for the investigated samples in June 2019.

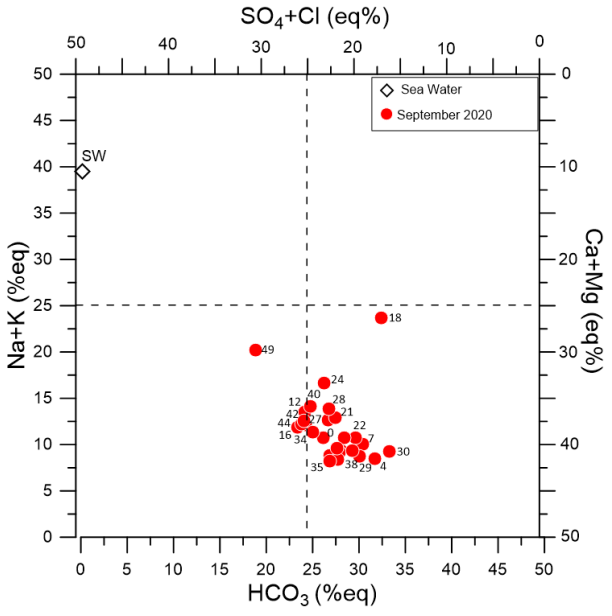

Fig. 2.29 Square diagram for the investigated samples in September 2020.

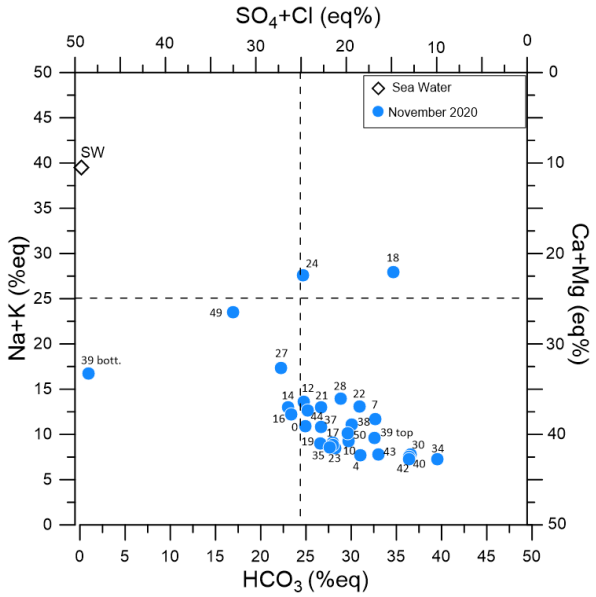

Fig. 2.30 Square diagram for the investigated samples in November 2020

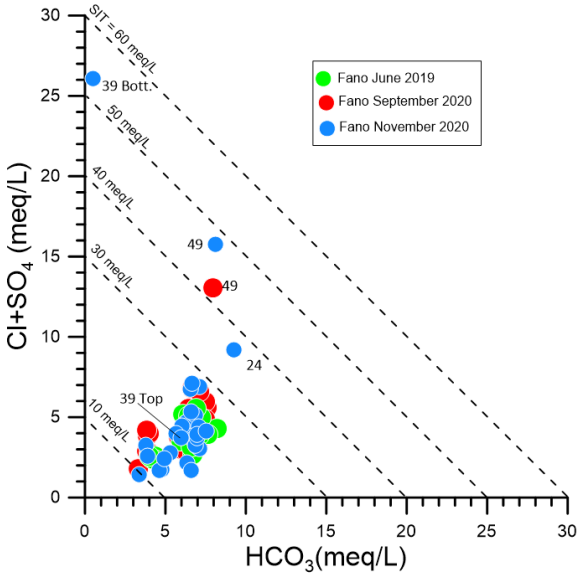

Fig. 2.31 HCO_3 vs. SO_4+Cl binary plot for the investigated samples from 2019 to 2020

2.4 Discussion

2.4.1 Piezometric and electrical conductivity maps

Based on the collected piezometric levels and riverbed lidar data (available on http://www.pcn.minambiente.it/viewer/index.php?services=LiDAR_Marche), the maps of Fig. 2.32 were elaborated. In general, a SW to NE groundwater circulation is observed with

absolute values always above sea level, except in a very tiny and narrow coastal band. A feeding component from the hillsides facing the studied area does not seem to be present, in agreement with the outcropping lithotypes, while the aquifer artificial recharge in the inner southern sector is well evidenced. The Metauro river seems to drain the aquifer system in all the survey periods up to the central part of the investigated area, whereas from the central area down to the coast the river/aquifer water level relationship are variable according to the hydrological regime. Specifically, in the wet seasons (e.g. September 2019 and December 2019), characterized by higher piezometric levels, the river drains the aquifer almost down to the coastline. In the dry periods the river is in either equilibrium with the aquifer or it is even feeding it (e.g. September 2020). Finally, the piezometric maps also clearly show the effects of the artificial recharge of the aquifer by the Metauro river waters in the SW sector.

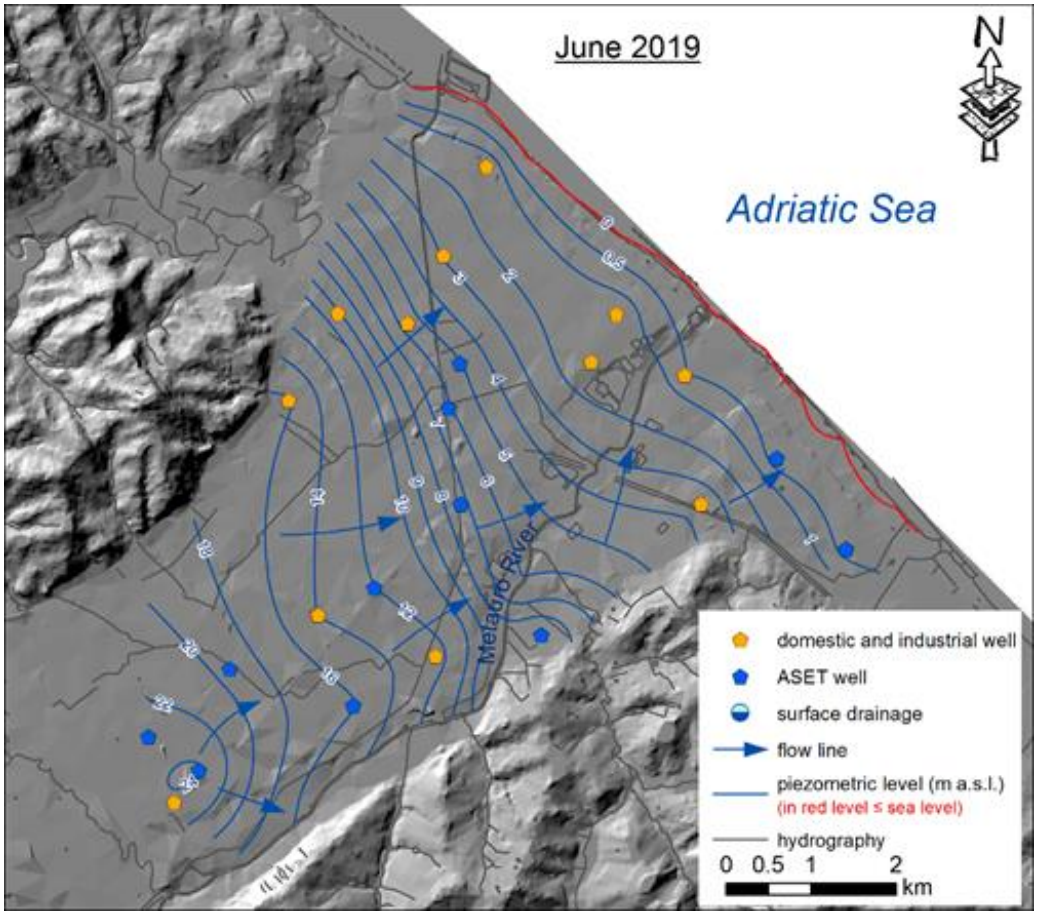

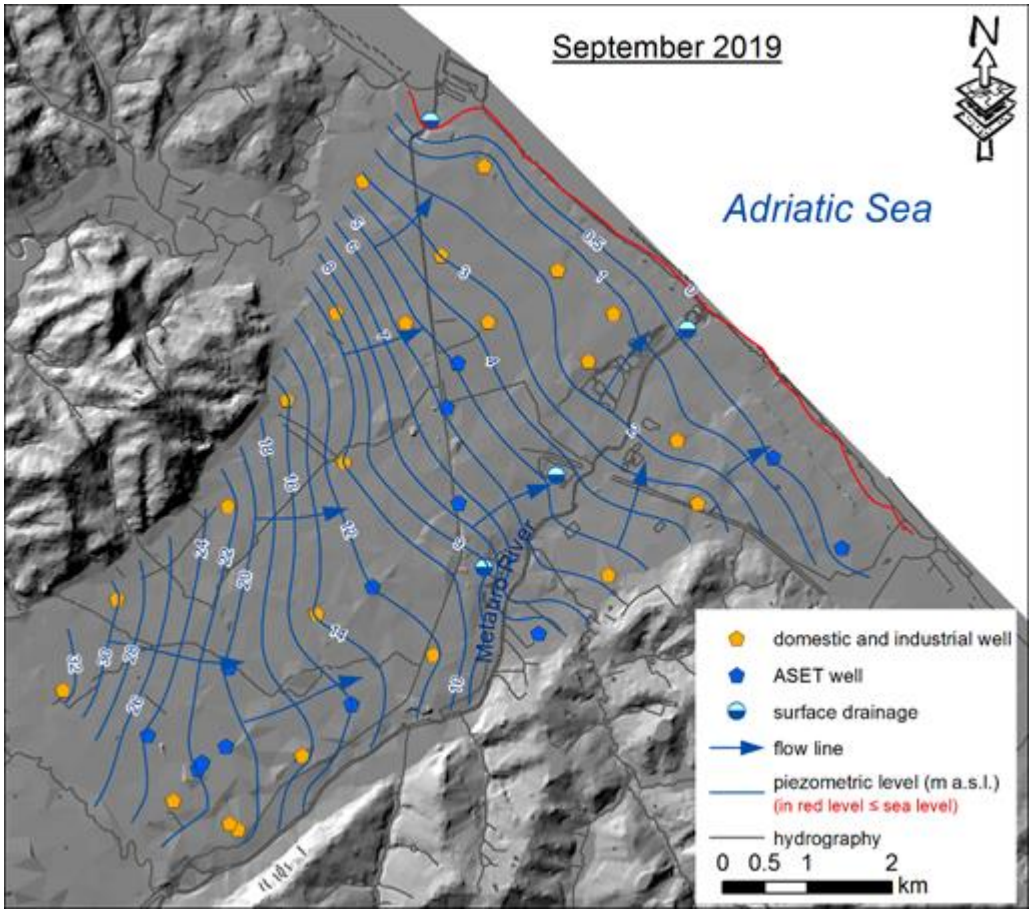
September 2019
N
Adriatic Sea
Metauro River
domestic and industrial well
ASET well
surface drainage
flow line
piezometric level (m a.s.l.)
(in red level ≤ sea level)
hydrography
0 0.5 1 2
km

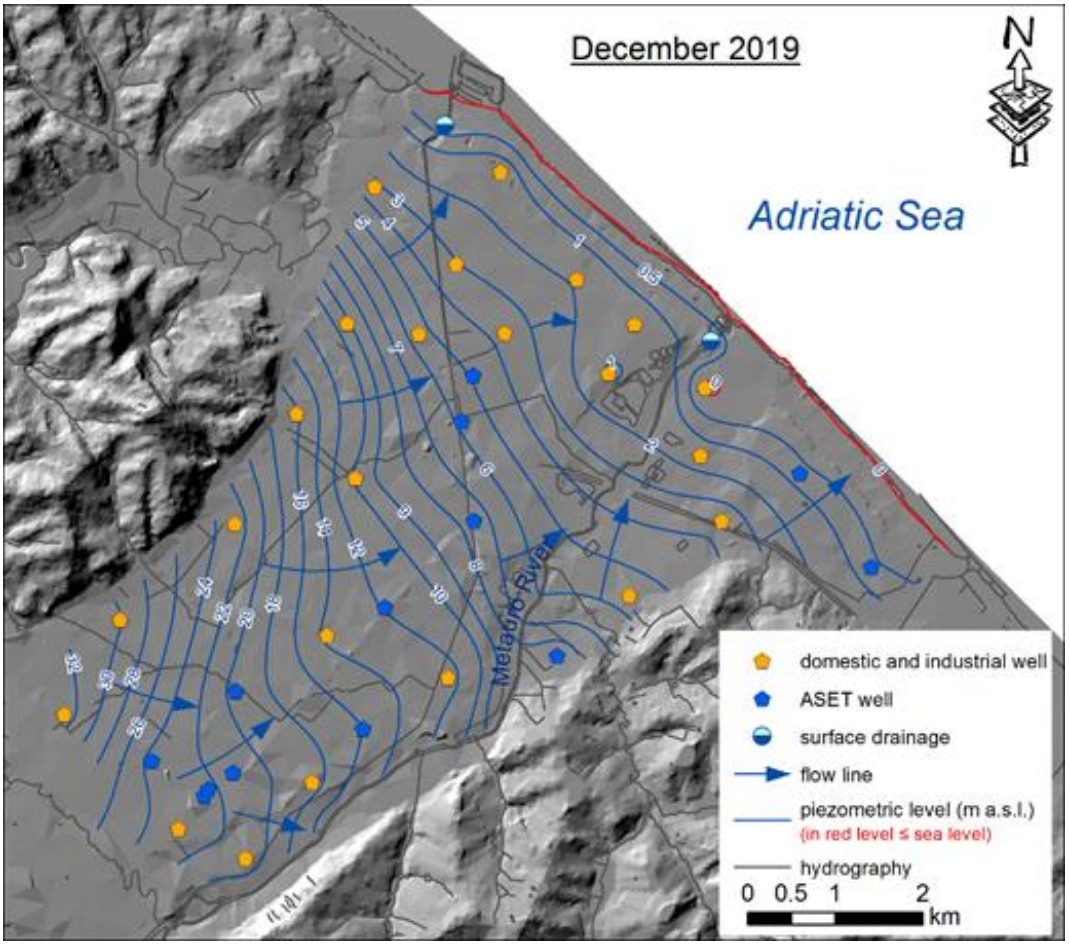
December 2019
N
Adriatic Sea
Metauro River
domestic and industrial well
ASET well
surface drainage
flow line
piezometric level (m a.s.l.)
(in red level ≤ sea level)
hydrography
0 0.5 1 2
km

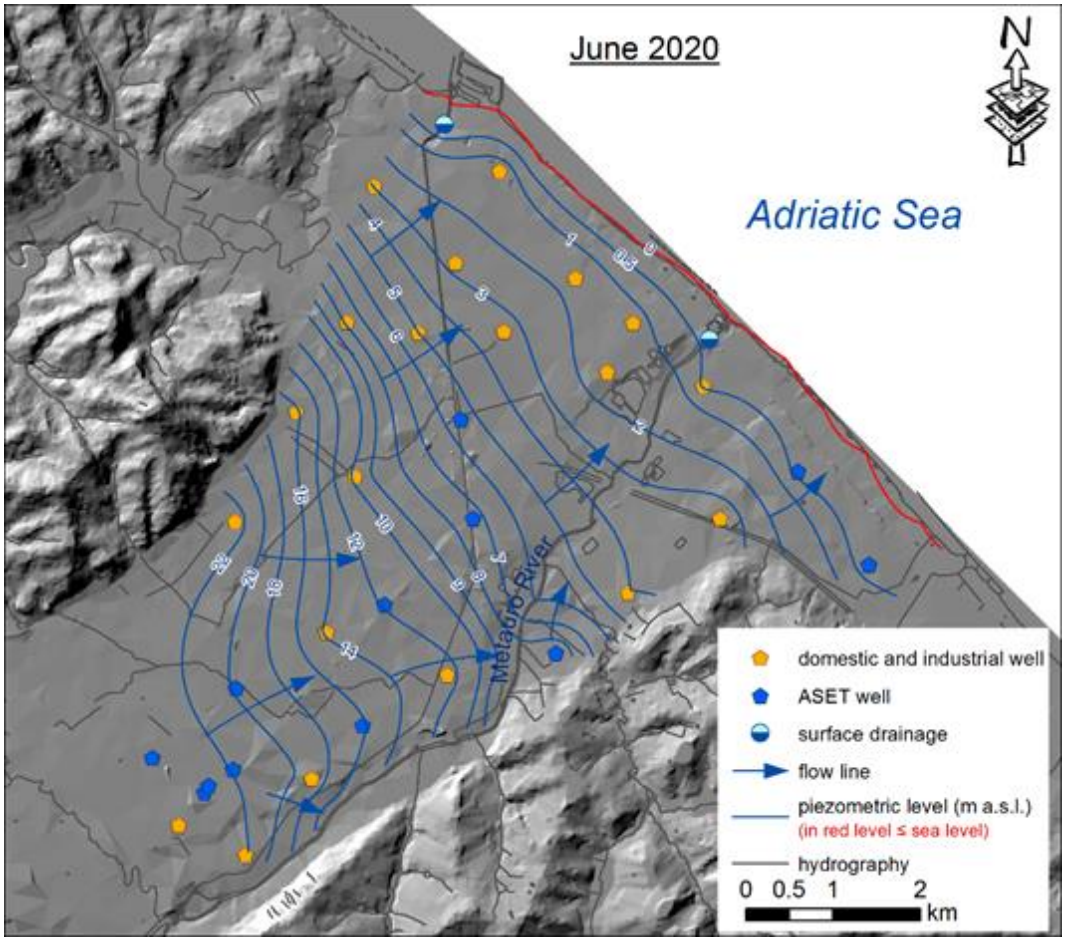
June 2020
N
Adriatic Sea
Metauro River
domestic and industrial well
ASET well
surface drainage
flow line
piezometric level (m a.s.l.)
(in red level ≤ sea level)
hydrography
0 0.5 1 2
km

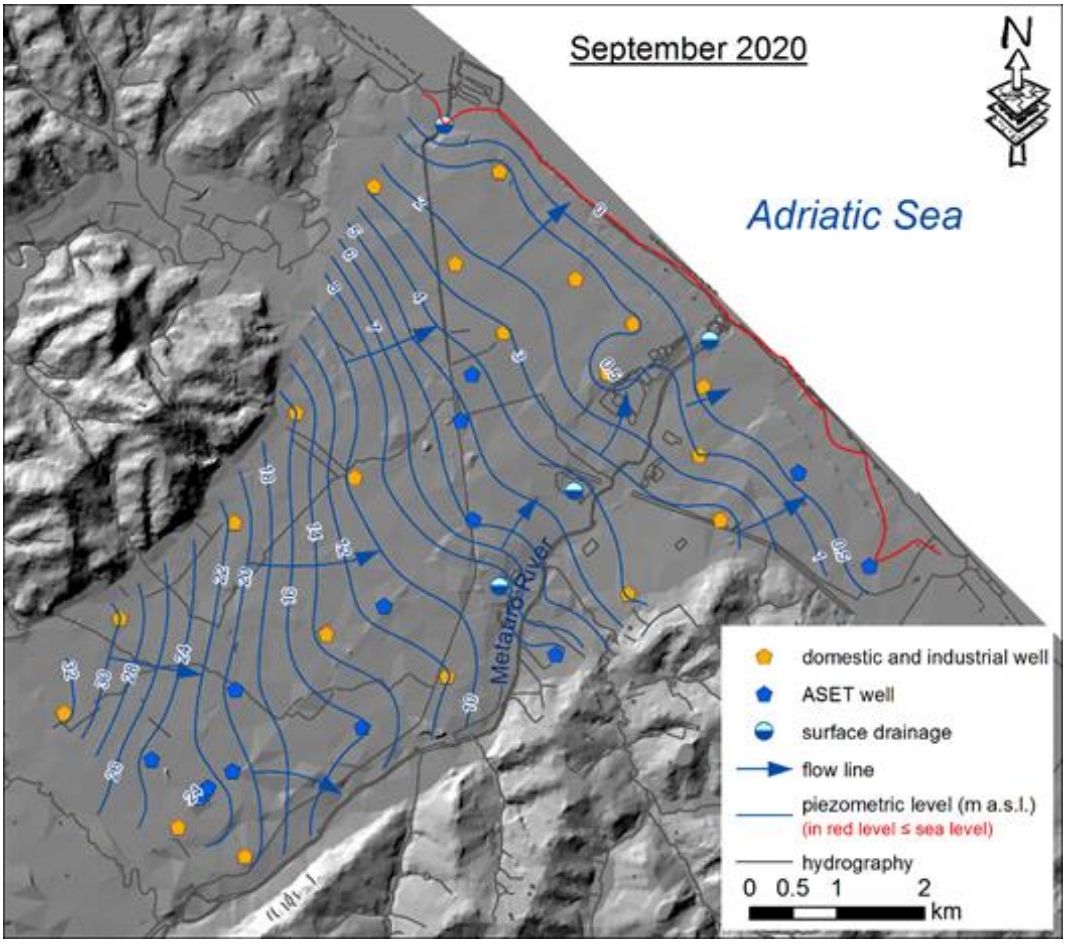
September 2020
N
Adriatic Sea
Metauro River
domestic and industrial well
ASET well
surface drainage
flow line
piezometric level (m a.s.l.)
(in red level ≤ sea level)
hydrography
0 0.5 1 2
km

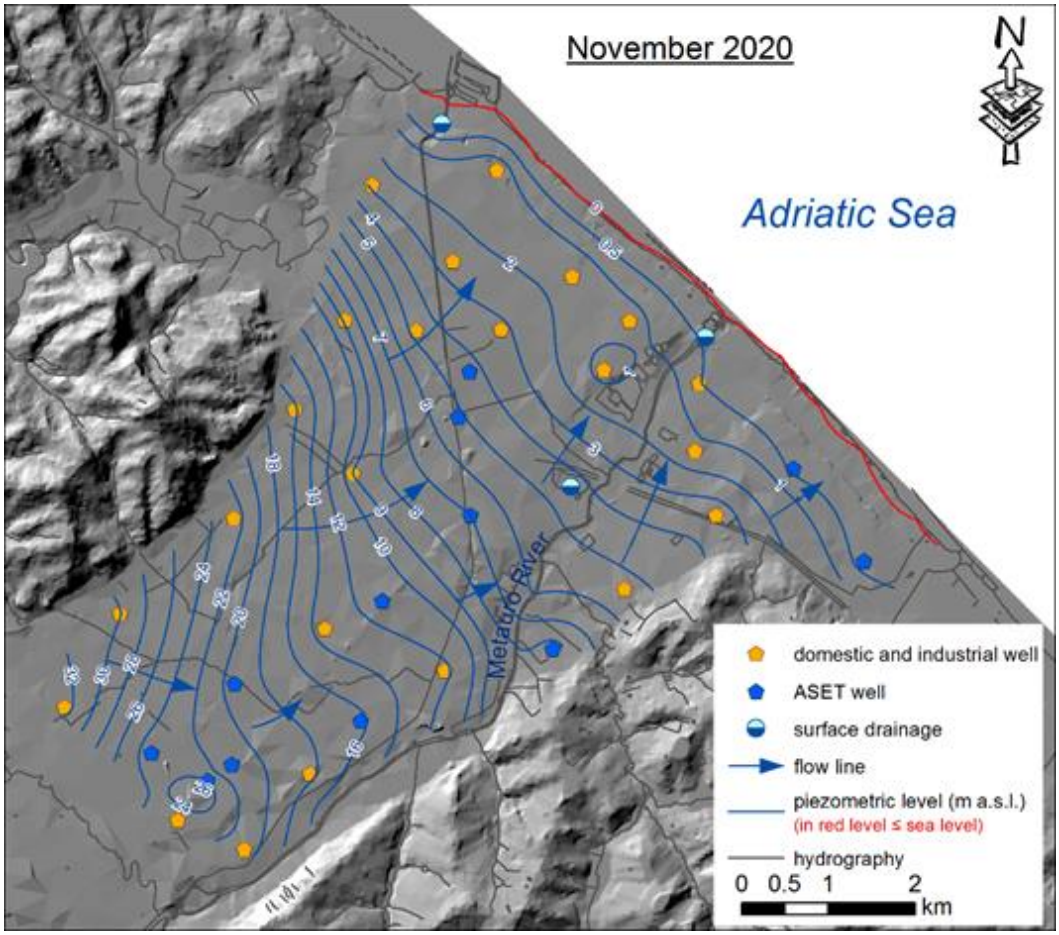

Fig. 2.32 Piezometric level maps for June 2019, September 2019, December 2019, June 2020, September 2020 and November 2020

The iso- EC maps are shown in Fig. 2.33 for December 2019 and September 2020, while the corresponding standard deviation maps are displayed in Fig. 2.34. The maps were elaborated for these two periods because they can be considered as representative of opposite hydrological regime conditions, i.e. wet and dry seasons. In December 2019, the EC values were relatively low (< 800 µS/cm over most the studied area), thus indicating the local rainfall recharge effects during the wet season. On the contrary, in September 2020 the low EC values extended to form a sort of plume, which starts from the group of wells used for the aquifer artificial recharge (#34-37-38) following a SW-NE direction down to the shoreline. Close to this plume, the EC rises up to values over 1500 µS/cm, indicating the presence of natural or anthropic processes, likely responsible of the registerd salinity increase. As a whole, the EC arrangement suggests a groundwater dilution generated by the injection of the Metauro River (#42) waters by the artificial recharge wells into the shallow aquifer.

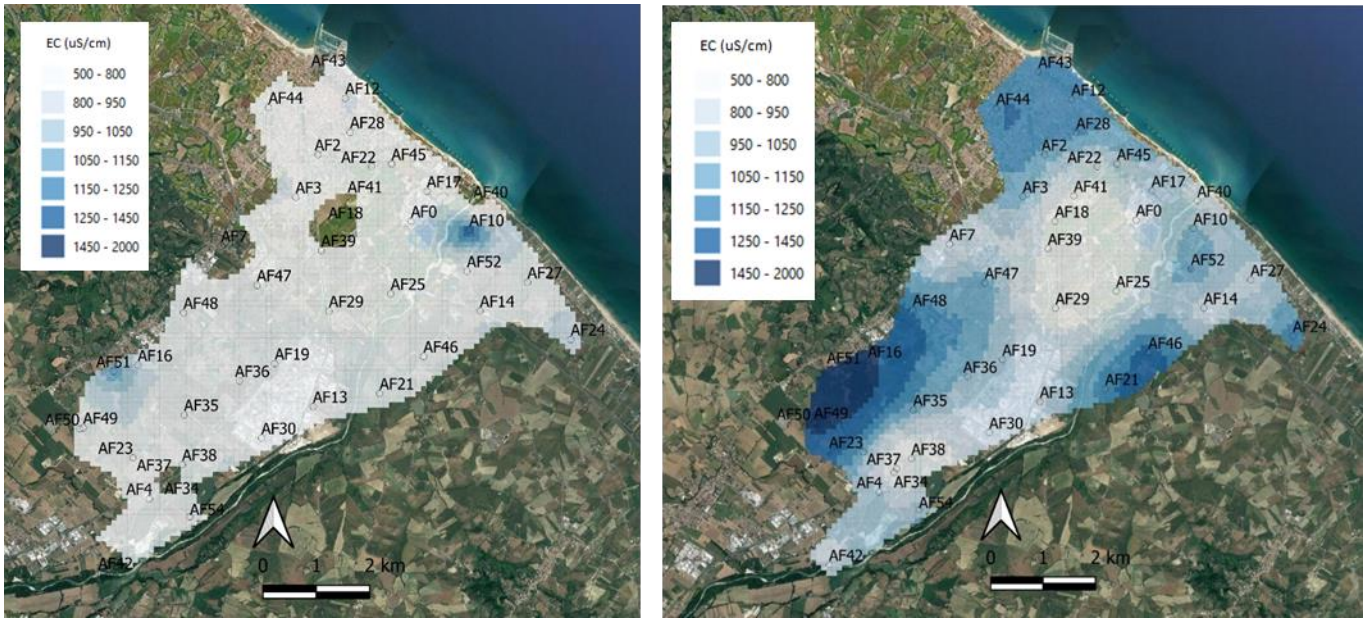

Fig. 2.33 Iso-conductivity map generated by Ordinary Kriging for December 2019 (left panel) and September 2020 (right panel). Values in µS/cm.

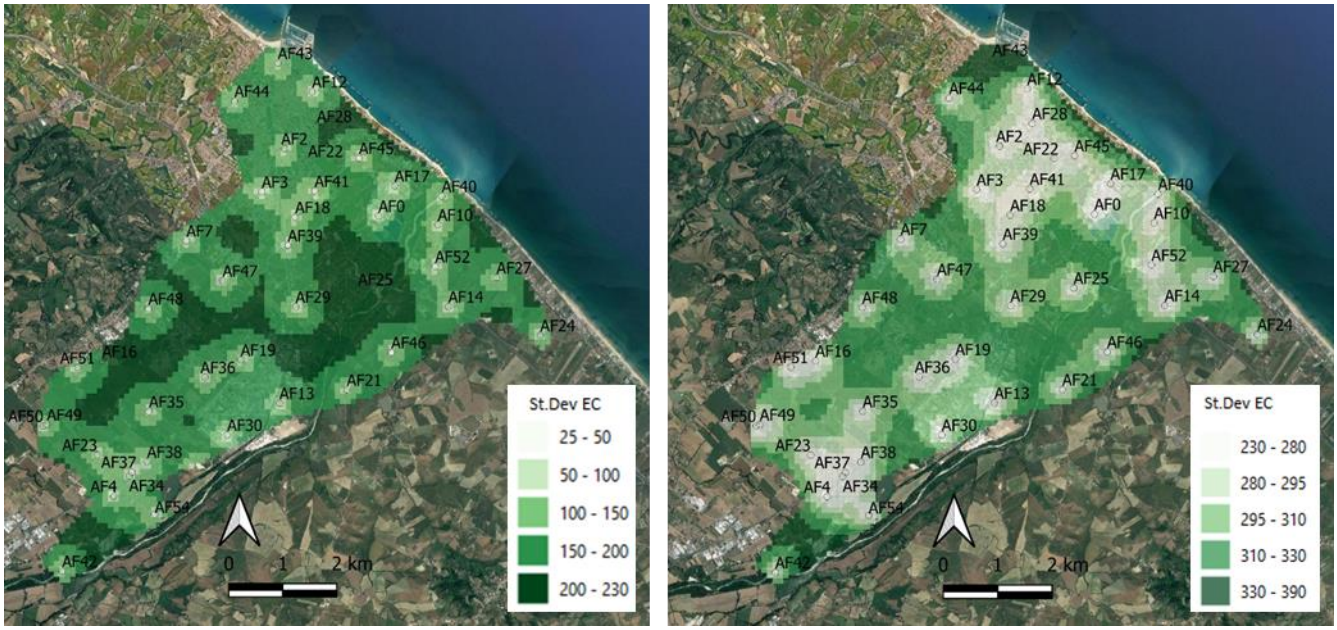

Fig. 2.34 Standard deviation maps related to December 2019 (left panel) and September 2020 (right panel). Values in µS/cm.

2.4.2 Origin the main solutes

Most surface and shallow ground waters from the Fano coastal area were mostly characterized by a Ca-HCO_3 composition with a few exceptions, i.e. #18, #24, #49 and

#39Bottom (#39bott, afterwards), whose geochemical facies were (Na+K)-HCO_3-Cl and Ca-Cl. For the sake of clarity, in the following diagrams the chemical composition of the June 2019 and September and November 2020 campaigns are presented in the same plots.

The binary diagrams of Na, Cl, Ca+Mg and SO_4 vs. Total Dissolved Solid (TDS) (in mg/L) for the three geochemical surveys are reported in Fig. 2.35. The #18, #14, #24, #27, #39bott and #49 samples were labeled in order to better show the chemical differences in terms of seasonality for the Na, Cl, Ca+Mg vs. TDS diagrams since most waters showed a relatively linear increasing trend of the considered parameters. It is to remind that #39 was only sampled at the surface and the bottom in November 2020 since a significant stratification was recorded while measuring the log profile. More scattered is resulting the SO_4 vs. TDS diagram and consequently, more waters were labeled.

As expected, all the considered parameters are increasing with the TDS values although different behaviors can be observed. First of all, most samples are grouped in a relatively narrow TDS range (ca. 500 to 1100 mg/L) and few of them tend to either trend away from the main pattern (Fig. 2.35 A, B and D) or result to be more dispersed (D). Additionally, within the 500 to 1100 mg/L TDS interval, the contents Ca+Mg and Cl seem to be representing about ¼ of the TDS, while those of Na and SO_4 are slightly lower, HCO_3 (not shown) being up to ½ of TDS. While in the Na vs TDS diagram water samples are distributed along a well-defined trend, those of Cl and Ca+Mg vs. SO_4 show that #39bott and #49 (September and November 2020) and #24 (November 2020) are not aligned along the main pattern. Slightly complicated is instead the SO_4 vs. TDS diagram, where a general increase of the two parameters can be observed but the distribution is more chaotic when compared to the other considered parameters. In particular, #39bott is characterized by the lowest SO_4 content, similar to those of #18 but with a much higher TDS. In September and November 2020, #49 showed a dramatic SO_4 drop and, eventually, #34, #37, #38, #40, #42 (September and November 2020) had a lower SO_4 content with respect the expected TDS. On the whole, it can be said that the main water chemistry of the June 2019 campaign is apparently more homogeneous whereas those of September and November 2020 result to be chemically more variable.

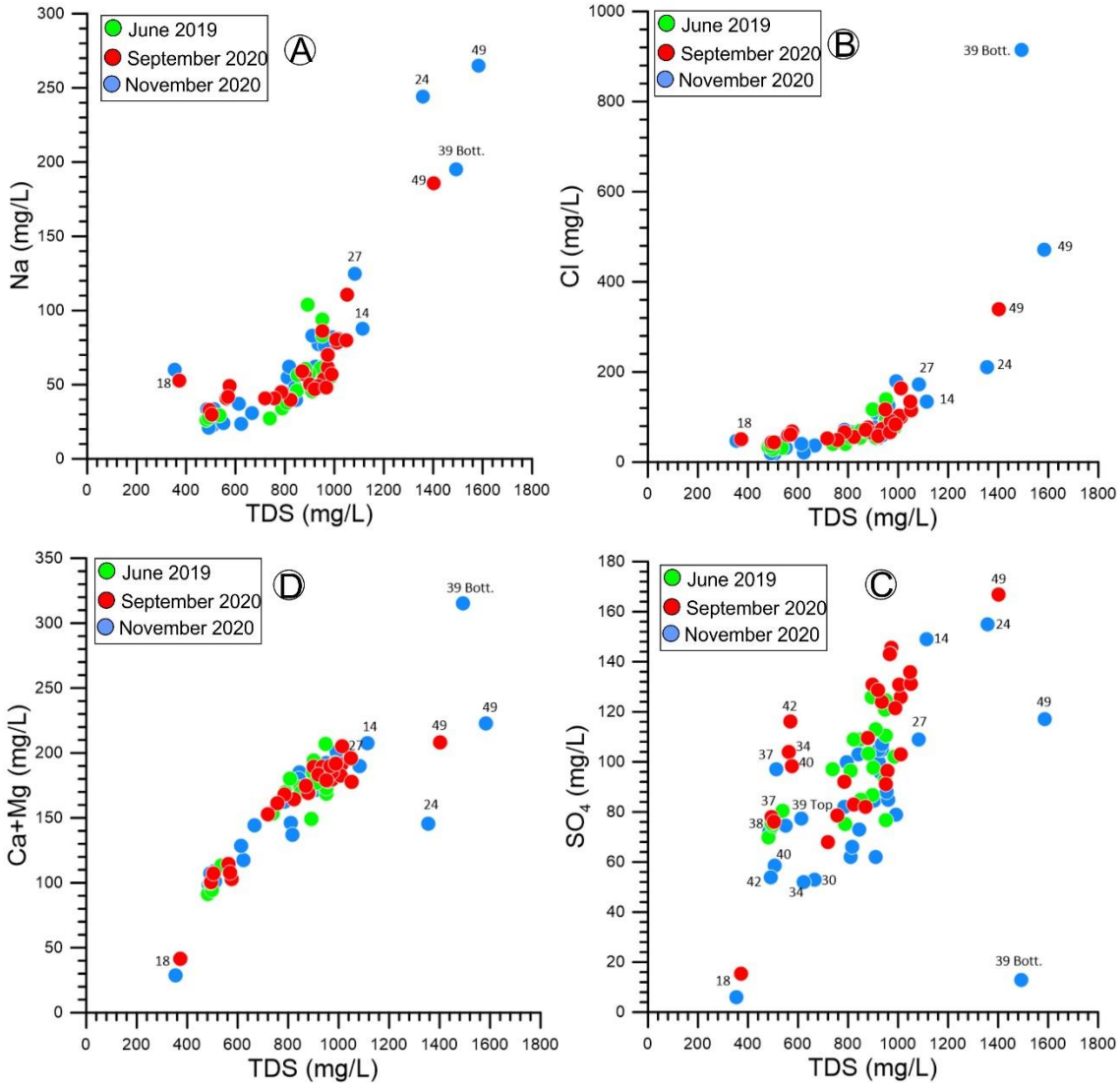

Fig. 2.35 Total Dissolved Solid (TDS) vs. Na, Cl, SO4 and (Ca+Mg) binary plot for the investigated samples from 2019 to 2020.

The sources of the main solutes can be derived by considering the 4 diagrams reported in Fig. 2.36 where the stoichiometric ratios between Ca+Mg and Na vs. HCO_3 and Na and Ca vs. Cl (in meq/L) are reported.

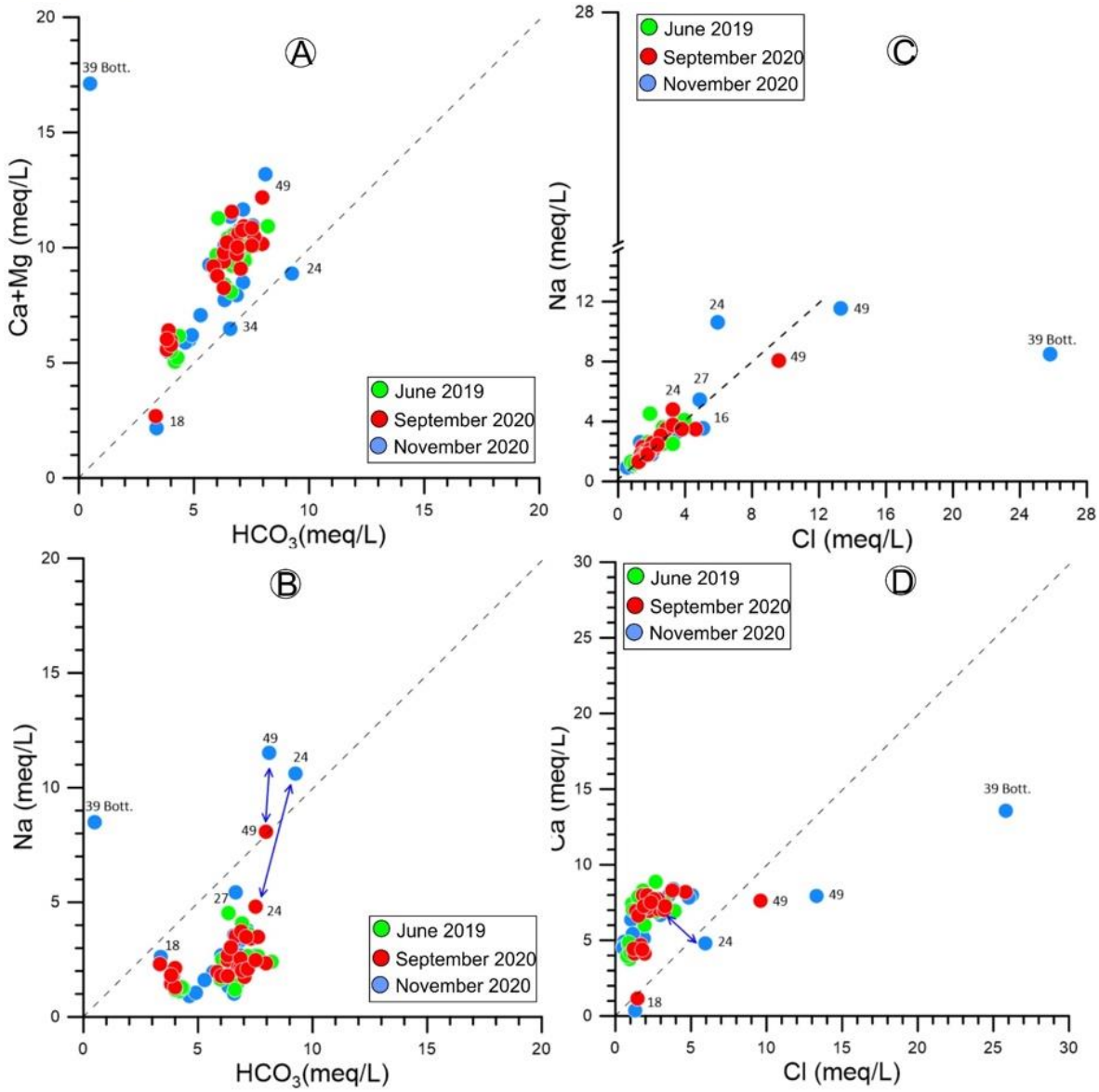

Fig. 2.36 Stoichiometric diagrams of Ca+Mg (A) and Na (B) vs. HCO_3 and Na (C) and Ca (D) vs. Cl. All values are in meq/L.

Congruent dissolution of carbonate phases (mainly, calcite) is evidenced by the Ca+Mg vs. HCO_3 diagram (A) although an excess in the earth alkaline ions is observed, indicating the occurrence of alteration processes that involve other mineralogical phases. It is interesting to highlight how the Na vs. HCO_3 diagram (B) is characterized by a clear enrichment in HCO_3 since only #49 (September 2020) is lying along the stoichiometric line whereas #24, #39bott and #49 (November 2020) are above it. No previous data are available for #39bott although it is clearly representing a "heavier" water underlying the typical Ca-HCO_3 composition recorded in the Fano waters whose origin is possibly related to different processes as it will be shown when the isotopic data are discussed. As far as the #24 and #49 waters collected in November 2020 are concerned, it is possible to hypothesize reverse ion exchange

processes between Na-Cl and Ca-HCO_3 waters as better shown in the Ca vs. Cl diagram (Fig. 2.36 D). This plot is showing how #24 and #49 are here approaching the stoichiometric line. The #39bott water is strongly diverting from the stoichiometric line. Finally, the Na vs. Cl (Fig. 2.36 C) binary diagram, whose contents are mostly < 6 meq/L, is apparently suggesting the same origin for these two parameters and related to both dissolution processes of NaCl and contribution by the rainwaters that, close to coastal areas, tend to be dominating by the rain chemistry. However, the slight enrichment in Na is possibly due to incongruent dissolution processes suffered by silicatic minerals whereas those of reverse ion exchange are here further confirmed for #39bott, #49 and, partly, #24. The latter sample is likely more affected by the presence of a silicatic phase that is exceeding that due to the carbonate minerals. To characterize whether other mineralogical components are contributing to the water geochemistry of the Fano waters, in Fig. 2.37 the (Ca+Mg)-HCO_3 vs. SO_4 (in meq/L) binary plot is reported. Basically, to the earth alkaline ions the carbonate component is subtracted to verify the possible presence of congruent dissolution of Ca-sulfate minerals. Actually, most water samples tend to approach the stoichiometric line although an enrichment in Ca+Mg is still evident, likely confirming the contribution of silicate minerals to the studied waters. It is to be pinpointed the relatively high Ca+Mg concentration at #39bott that, as previously described, has a rather low content of HCO_3. This observation is suggesting that #39 is not affected by CO_2-deep-seated gases, although the contribution by saline CH_4-rich waters, typically characterizing the peri-Adriatic sector of Italy, cannot be excluded (e.g. Minissale et al 2000; Tassi et al 2012). A few samples are slightly enriched in SO_4. Since no sulfur isotopes in sulfate are available, we may speculate that these water samples may be affected by oxidation processes of sulfide phases, dissolution of other sulfate minerals or anthropogenic-related components, e.g. fertilizers. The low concentrations of SO_4 and stoichiometric ratios between typical seawater ions allow to suggest that no intrusion of saline waters is recognizable or, if present, it can be considered negligible. Further discussion about this aspect will be treated while modeling the chemical and isotopic data.

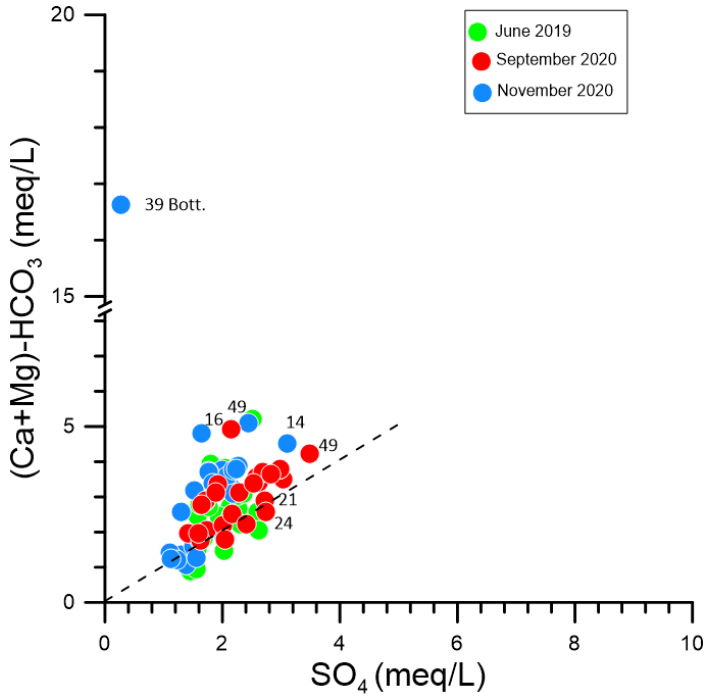

Fig. 2.37 (Ca+Mg)-HCO3 vs. SO4 binary plot.

The chemical composition of surface and shallow waters from the Fano coastal area does not necessarily reflect unambiguously natural geochemical processes. For example, TDS variations are possibly representing the results of combined effects, e.g. lithology and pollution (e.g. Gaillardet et al., 1999; Roy et al., 1999; Han and Liu, 2004). In this respect, dissolved nitrate in surface and shallow ground waters represents an important geochemical tracer of pollution and the origin of nitrate deserves a particular attention, this solute showing contents that are commonly related to polluted areas. The Fano waters are characterized by a large variability in terms of NO_3 concentrations as they spanned from 0.1 to 104 mg/L. Therefore, in Fig. 2.38 the TDS (in mg/L) values are plotted against the $HCO_3/(HCO_3+ NO_3)$ (in mg/L) ratio, the latter parameter considering NO_3 as mainly related to anthropogenic sources, while HCO_3 is regarded as representative of weathering processes. The binary plot of Fig. 2.38 shows the presence of three groups. The first two groups are characterized by relatively low TDS and $HCO_3/(HCO_3+ NO_3)$ ratios >0.96, suggesting that these samples are the less affected by anthropogenic factors. They can only be distinguished on the basis of their TDS values since the $HCO_3/(HCO_3+ NO_3)$ ratios are similar. The first group has a lower TDS while the second one shows a significantly higher TDS and represented by #24, 39bott and #49, these waters diverting from the main trends reported in Figs. 2.35 and 2.36. Finally, the third group has relatively constant TDS with a decreasing $HCO_3/(HCO_3+NO_3)$ ratio that reaches values down to 0.77. This group is referred to the most polluted waters, which are

strongly affected by the agricultural practices operating in the area, as already observed by Di **Girolamo (2004)**. Nevertheless, since no isotopic analyses of nitrogen and oxygen are available, input by domestic and/or industrial sewage cannot be ruled out. Such high contents of NO_3 also explain the necessity to pump the waters from the Meaturo river into the shallow aquifer with the aim to minimize the pollution and supply drinkable water to the population by the local company.

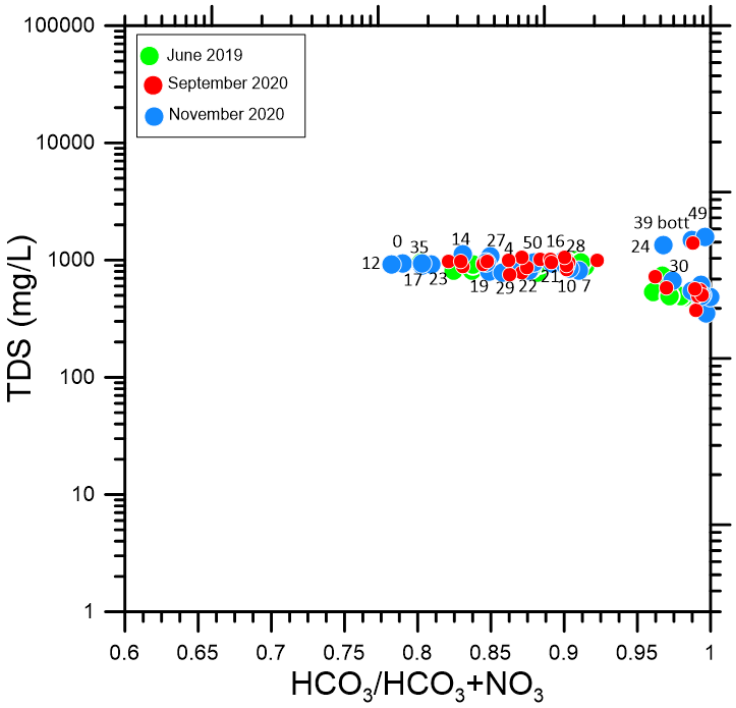

Fig. 2.38 TDS (in mg/L) vs. $HCO_3/(HCO_3+NO_3)$ binary plot.

According to the concentrations of the main solutes determined in the Fano waters, it can be summarized that they are mostly derived by congruent and incongruent dissolution of carbonate/sulfate and silicate minerals. In addition, an important anthropogenic component, likely due to fertilizers and/or sewage, was also recognized. The Fano coastal waters can then be reflecting three main lithologies undergoing chemical weathering: silicates, carbonates and evaporites. In a global approach, the waters draining each of these rock types are characterized by their own chemical signature that depends on both the chemical composition of the bedrock and the rate at which it is eroded. According to the estimations by Meybeck (1987), carbonate rocks and evaporites tend to be weathered 12 times and 40 to 80 times, respectively, more rapidly than silicate-bearing rocks. The Ca/Na, HCO_3/Na and Mg/Na molar ratios are thus particularly well suited to understand which are the lithologies that mostly affect the water geochemistry. Moreover, the use of these ratios has the very

important property of being independent on water fluxes and dilution and evaporation processes. The molar ratios of HCO_3/Na (a) and Mg/Na (b) vs. Ca/Na (log–log scaled) are reported in the binary diagrams of Fig. 2.39 where sea water and rock weathering end-members, as defined by Gaillardet et al. (1997) are also included. The Fano costal area waters can mainly be regarded as the result of mixing processes dominated by waters interacting with carbonate and silicate lithologies, while the contribution of the sea water is once again to be regarded as negligible. Water samples from #18 and #39bott (November 2020), as already previously recorded, trend away from the main pattern, being characterized by relatively low Ca/Na (Fig. 2.39 A and B) and HCO_3/Na (Fig. 2.39 A) ratios, respectively, suggesting a contribution by Na inputs which seems to be more dependent on secondary processes rather than due to weathering processes.

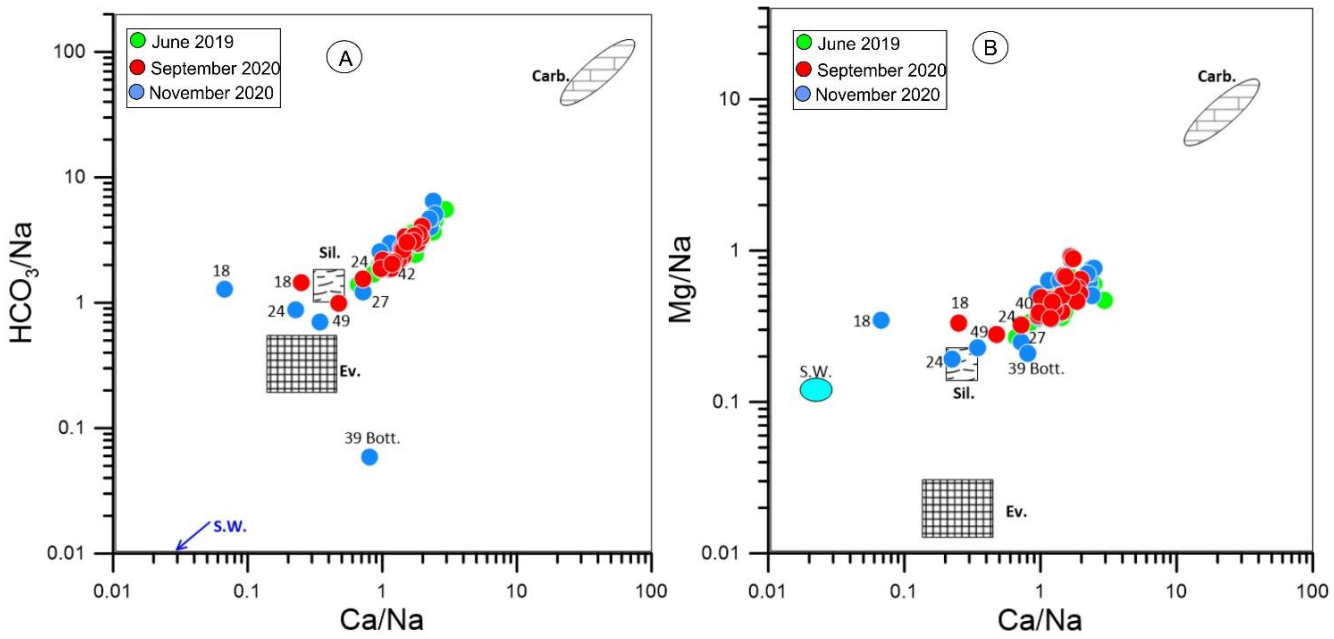

Fig. 2.39 HCO_3/Na vs. Ca/Na (A) and Mg/Na vs. Ca/Na (B) molar ratios binary plot for the investigated samples from 2019 to 2020. The evaporite, carbonate and silicate rock fields are by Gaillardet et al. (1997). S.W.: sea water.

Groundwater samples from coastal areas can show a surplus of cations which might be indicative of seawater intrusion. The chemical reactions during fresh/salt water displacements can be deduced more specifically by calculating a composition based on a conservative mixing of salt water and fresh water and comparing the conservative concentrations (based on Cl concentration) with those actually found in the water analysis as by the following reaction (1):

$$(1)\ m_{i,mix} = f_{SW} \times m_{i,SW} + (1 - f) \times m_{i,GW}$$

where m_i is the concentration of i, f_{sw} is fraction of seawater in the mixed water and $m_{i,mix}$ is the conservative mixture between the two end-members: seawater (SW) and groundwater (GW).

In Fig. 2.40, the binary diagrams of Ca, Na, K and Mg vs. Cl (eq/L) (log–log scaled) are reported with the computed theoretical lines representing the groundwater (GW) affected by seawater (SW) and computed by using low salinity water samples (#27 and #34, June 2019). To these samples an increasing amount of sea water was added. A clear positive correlation between Na, Mg, K and Ca vs. Cl is observed with the Fano waters grouped at the lowest concentrations indicating that the seawater contribution, once again, can be considered negligible. The Ca–Cl and Na-HCO_3 chemical composition of #39bott and, partly, #24 (November 2020), respectively, and the disappearance of the groundwater–seawater mixing line in Fig. 2.40 is likely suggesting the occurrence of reverse ion exchange processes. This favors the release of Ca^{2+} into the aqueous solution while Na^+ is adsorbed by phyllosilicates, i.e. clay minerals, as schematically indicated by the following reaction (2):

$$(2)\ Na^+ + Ca_{0.5} - X \rightarrow Na^+ - X + 1/2Ca^{2+}$$

where X indicates an unspecified cation exchanger present in the alluvial deposits (e.g., Appelo and Postma 1993 and references therein). Samples #24, #18 and #49, collected in November 2020, are slightly shifted towards or lower Ca/Na ratios or closer to the evaporitic field, respectively. Samples #18 and #49 are located at about 2 and 7 km, respectively, from the coastal line and thus, the presence of seawater can be excluded (as also showed by the previously discussed geochemical modeling) and ion exchange processes, similar to those affecting #39bott, can be invoked. Samples #24 is close to the sea and, according to the diagram of Fig. 2.39A, a very mild contribution by seawater cannot be ruled out, though only recorded in November 2020. However, the #24 waters can be considered a sort of sentinel of seawater ingression and it should be monitored after the end of the project by the local municipality. Finally, it is worth of noting that sample #12 tend to divert in Fig. 2.40C for a concentration of K^+ close to 36 mg/L likely related to an anthropogenic source being characterized by a NO_3−rich component (Fig. 2.38).

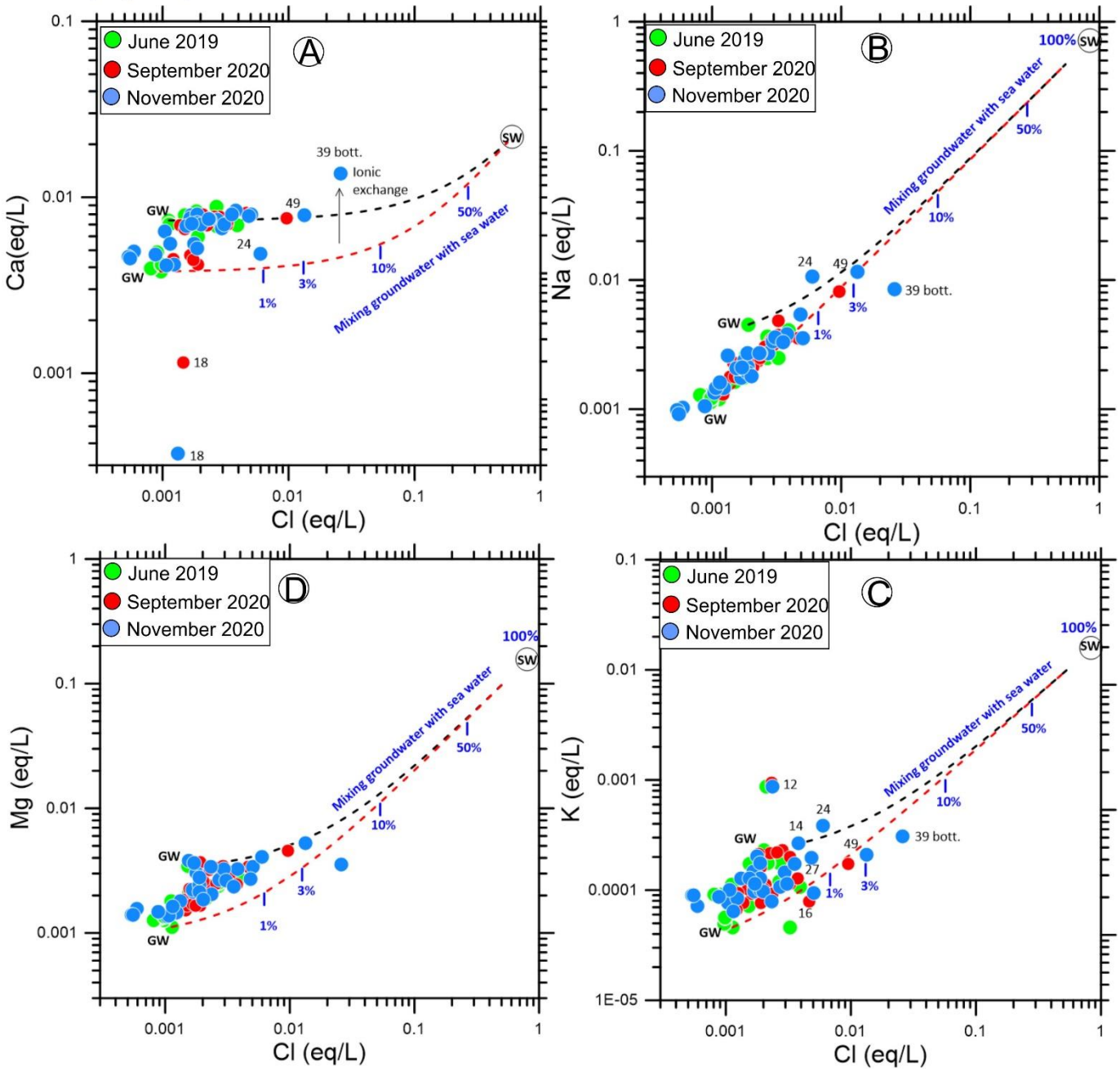

Fig. 2.40 Ca, Na, K and Mg vs. Cl (eq/L) (log–log scaled) binary plot. The black and red lines represent the theoretical mixing between sea (SW) and groundwater (GW) computed by using the low salinity water samples at which an increasing amount of sea water was added.

2.4.3 Trace elements

As previously described, the selected trace elements analyzed from the shallow aquifer of Fano were referred to June 2019 and September and November 2020. Unless the minor species, where relatively high concentrations of nitrate were recorded for a relatively large number of waters, trace elements did not seem to show specific criticalities with a few

exceptions. In fact, toxic elements, such as As, were below the required threshold for drinking water (10 µg/L) in all the samples since the highest content was 1.3 µg/L. Similarly, siderophile elements, e.g. Cr, Ni, Co and V, were below the Italian maximum permissible concentration. However, it is to mention that the concentration of Fe was in the great majority of the studied waters <200 µg/L, with the exception of a few samples: #19 in September and November 2020 and #39bott, the latter being characterized by a content of 58,100 µg/L. It is difficult to evaluate whether the presence of iron tubing of the wells was able to affect the water chemistry since no specific information was available by the wells' owners. Differently, it is the situation of #39bott. As evidenced when discussing the main and minor dissolved species, this sample was characterized by a significantly different composition with respect to both the overlying water and the other samples collected in the Fano area. It worth to mention that #39bott also showed the highest concentrations of Ba, Mn and Sr and the lowest content of SiO_2. No other enrichments or depletions were recorded for other trace elements. These evidences may likely support the hypothesis that #39bott is likely due to the presence of a distinct water whose origin is to be clarified, although the chemical features do not seem to be reflecting a seawater intrusion. In fact, both seawater-related main species and trace elements, e.g. boron, and the distance from the coast do not suggest any implication of seawater. Consequently, #39bott can be regarded as a deep-seated (?) water partly diluted with those belonging to the Ca-HCO_3 composition and likely affected by secondary process. Specific investigations are required to better constrain its source. It can be speculated that the #39bott water does not represent a pristine deep water but the result of a dilution process.

Setting aside As, in the studied waters, other chalcofile elements, i.e. Sb, Pb, Cu, did not show any critical enrichments when their concentrations are compared to those of the Italian law for the drinking waters. The same is true when Al, Ba, B and Rb concentrations are taken into account since they are in the concentration range of similar to those of shallow and surface waters. The relatively high abundance of Sr (up to 1,000 mg/L) is in agreement with the main composition of the Fano waters. In fact, Sr tends to replace Ca in the mineral phases and consequently, it tends to follow the fate of Ca when congruent and incongruent dissolution of carbonate/sulfate and silicate minerals are involved, respectively.

2.4.4 Stable isotopes of H and O

Water isotopic data are initially interpreted by means of the classical δ^2H vs. $\delta^{18}O$ plot (Fig. 2.41), where the Mediterranean Meteoric Water Line (MMWL, $\delta^2H = 8\ \delta^{18}O + 20$, Gat and Carmi), the Central Italy Meteoric Water Line (CIMWL, $\delta^2H = 7.05\ \delta^{18}O + 5.6$, Longinelli and Selmo, 2003), Global Meteoric Water Line (GMWL, $\delta^2H = 8\delta^{18}O + 10$, Craig 1961) and sea water (SW) end-members are reported as reference, for June 2019 and September and November 2020 campaigns, respectively. The recorded isotopic compositions of hydrogen and oxygen sampled in distinct hydrological periods of the year (2019-2020) from the Fano costal area waters mainly reflects the isotopic compositions of the meteoric precipitations in the drainage area which at their turn are related to seasonal variability, altitude, continental and evaporation effects. A more comprehensive examination is given by diagram of Fig. 2.42 A- B-C.

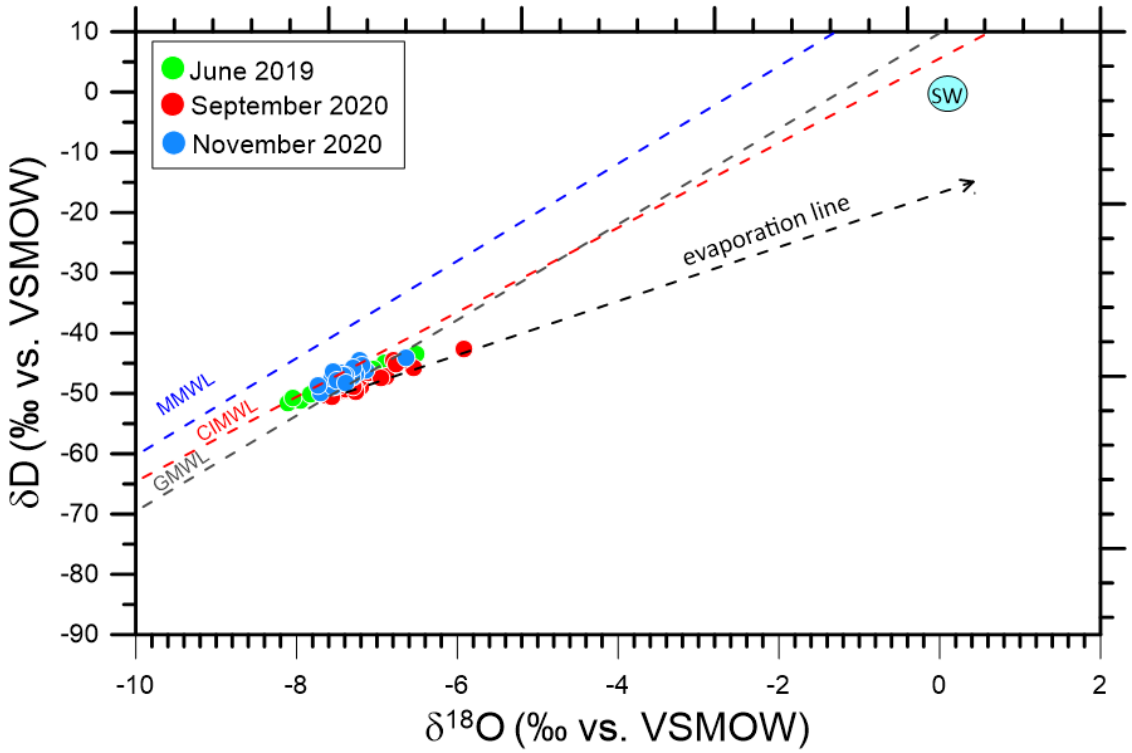

Fig. 2.41 Correlation plot of $\delta^{18}O$ values versus δ^2H of the Fano costal area waters for June 2019, September and November 2020, respectively.

Setting aside #10 in all campaigns and #40 in September 2020, the water samples are distributed close to the MWLs (in Fig. 2.42), confirming unequivocally their meteoric origin. The peculiar positions of the above mentioned #10 and #40 are mainly linkable to evaporation processes. The range of values is different within the three diagrams (4.11A-B-

C), thus indicating a significant seasonal isotopic variability. Such as behavior is in agreement with the unconfined character of the aquifer and it highlights a general high vulnerability of the system. In fact, this isotopic variability reflects that typical of rainfalls over the year, demonstrating the short infiltration time that characterizes the studied system. The isotopic ranges recorded for the different campaigns can also be referred to the different average altitudes at which the feeding waters generate. The lowest isotope signatures are observed in June 2019 at the artificial recharge wells (#34, #37, #38) where the waters of the Metauro River are injected. Such low values are therefore indicative of the average signature of rainfall occurred in the hill-mountain areas of the Metauro catchment during the rainy season (see Fig. 2.4 for the rainfall distribution over time). The highest isotopic values were registered in September 2020 and also in this case they concern the artificial recharge wells, given the particular positive values that regard the Metauro River (#40, #42) in this season. The water of the river denotes a significant rate of evaporation responsible of this isotopic positivization. Also, the #10, #24 and #27 wells, especially in September 2020, seem to be affected by evaporation phenomena. Given the proximity to the shoreline, the relatively high isotopic signatures of these wells could also be compatible with a very weak influence of seawater on groundwater. The isotopic intermediate values (-7.2÷ -7.5‰ and -47÷ -50‰ for $\delta^{18}O$ and $\delta^{2}H$, respectively) that are observed for all the sampling periods in most wells can be considered as indicative of rainfall occurring and infiltrating at the plain level. These values are in agreement with the rainfall isotopes signature registered by Longinelli and Selmo (2003) in the Fano zone.

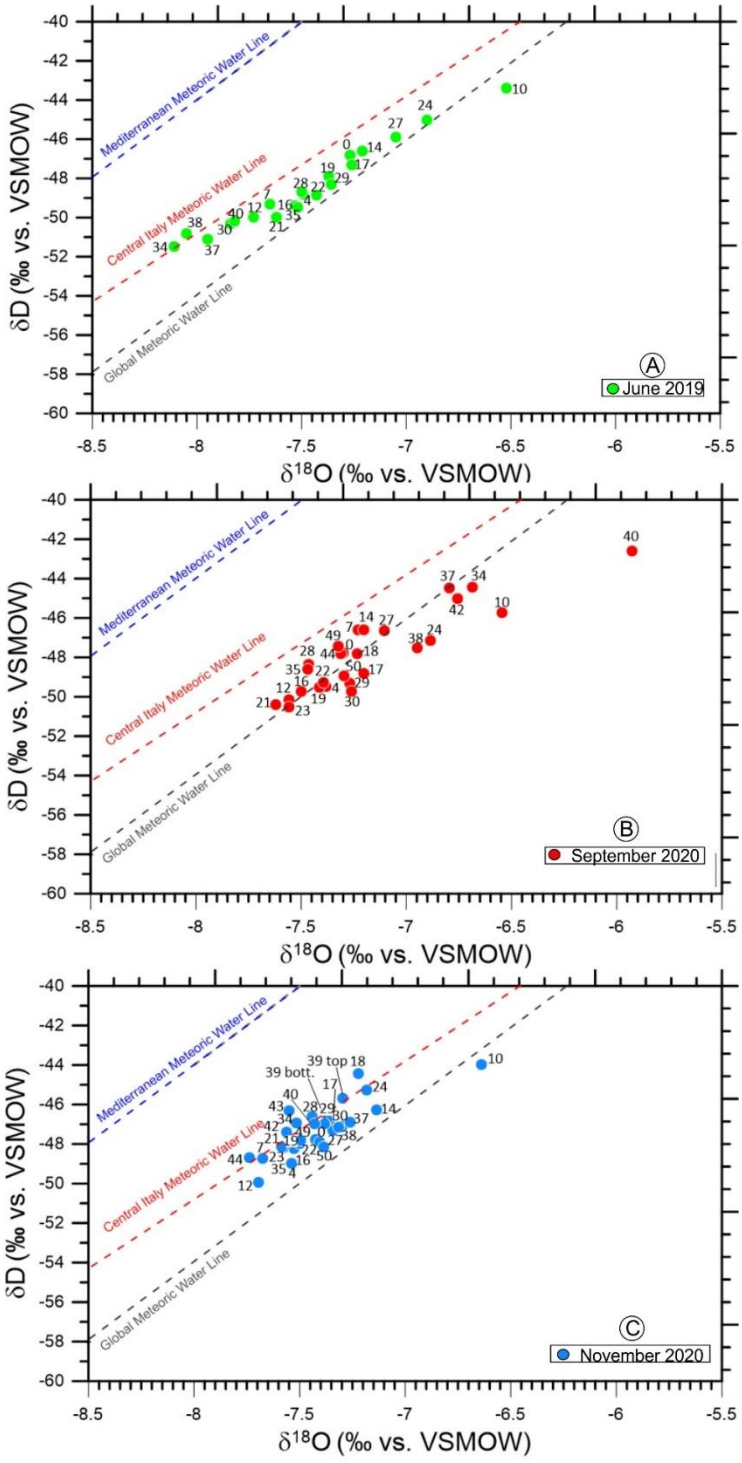

Fig. 2.42 Correlation plot of $\delta^{18}O$ values versus $\delta^{2}H$ of the Fano costal area waters for June 2019 (A), September (B) and November (C) 2020, respectively.

The meaning of the isotopic variability observed in the $\delta^{2}H$ versus $\delta^{18}O$ plot (Figs. 2.42 A-B-C) can be better explained when the $\delta^{18}O$ and $\delta^{2}H$ versus Cl correlation plots (Fig. 2.43 A-B-C) are taken into account. These diagrams being conservative (both parameters are indeed regarded as tracer) enable pointing out the main components in the aquifer and their relations. In the diagrams of Fig. 2.43 a significant positive correlation between Cl

concentrations and the water isotopic signature is not observed. Only the two wells #24 and #27 tend to highlight a relative increase in terms of both Cl and isotopic values in all periods with respect to the other samples. Taking into account the locations close to the shorelines for these two wells a very weak seawater intrusion affecting groundwater cannot be excluded. In September 2020, such a chemical-isotopic feature is apparently in agreement with the local negative piezometric level observed at NW where #24 and #27 (Fig. 2.32) are located. All the others samples in Fig. 2.43 tend to distribute vertically and horizontally. In the first case, the isotopic values are increasing whereas Cl concentrations are more or less constant. In the second case, the isotopic variability is minimal while the Cl contents increase. Therefore, we can exclude a seawater intrusion to explain the salinity increase while a passive increment of the Cl concentration is likely due to a progressive influence of water-rock interaction processes. This evolutive character involves the wells #49, #16, #39bott, #28 and #44. By crossing the location and the depth (when known) of these wells, we can suppose that the Cl increase is tied to either the substratum of the alluvial aquifer or to the presence of low-permeable interlayers (Fig. 2.46). Given the outcropping geological formations over the nearby hills (see FAA formation in Fig. 2.1), in both cases clayey to clayey-evaporitic materials could be present and therefore, be responsible of the increasing trend of Cl for these groundwaters whose flow-path interact with them. On the other hand, the vertical distribution of samples reported in Fig. 2.43 seems to confirm the possibility of a different water supply to the system (mainly local rainfall infiltration and injected river water), which flows and mixes at different degree with main water body. In this case, the groundwater system is therefore not showing a general and significant variation in terms of Cl and salinity in general, although secondary physical-chemical processes (as the ion exchange) or contamination by nitrogen compounds may intervene.

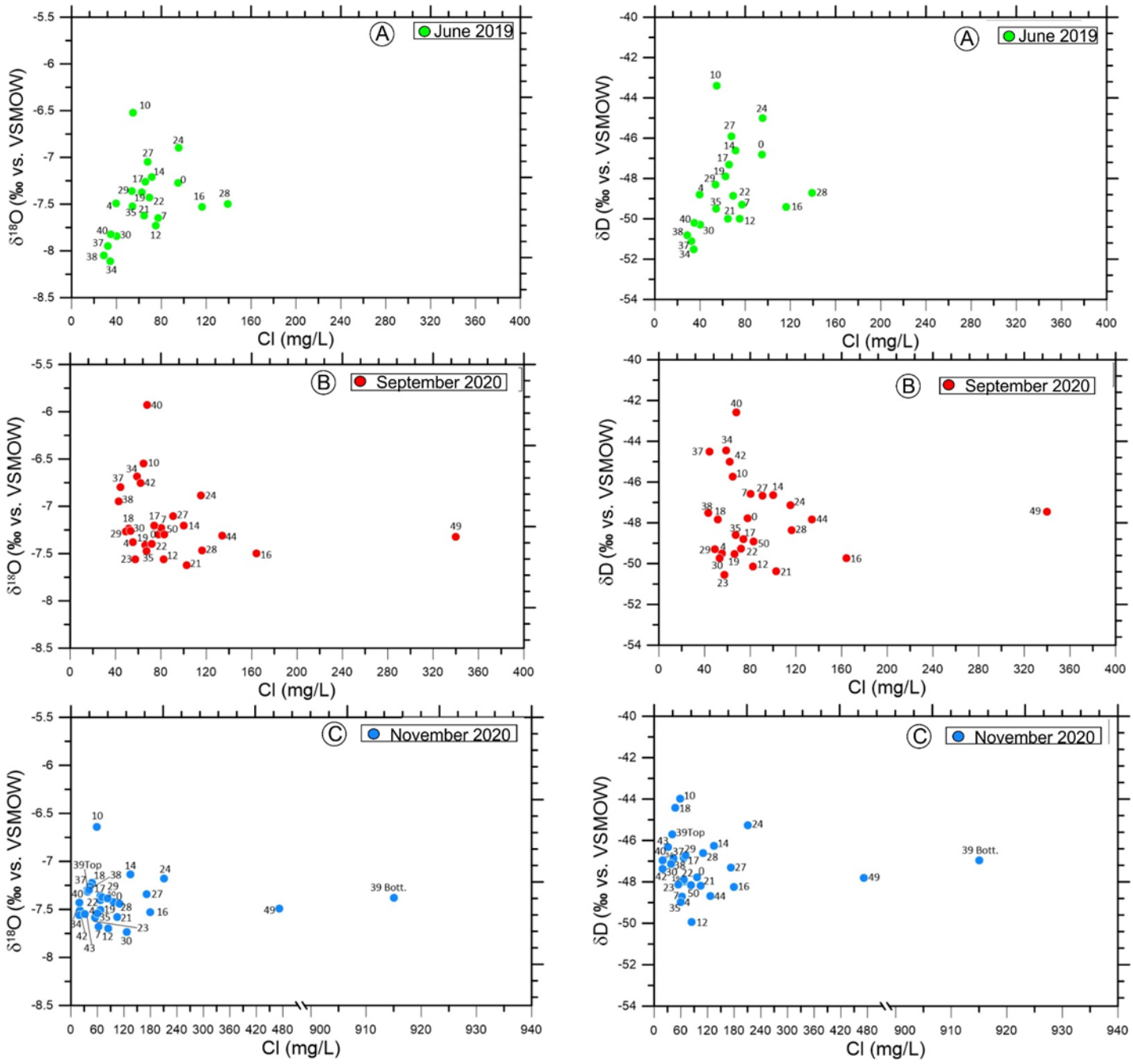

Fig. 2.43 (left) and Fig. 2.45 (right) – Correlation plot of δ18O and δD values vs. Cl of the Fano costal area waters for June 2019 (A), September (B) and November (C) 2020, respectively.

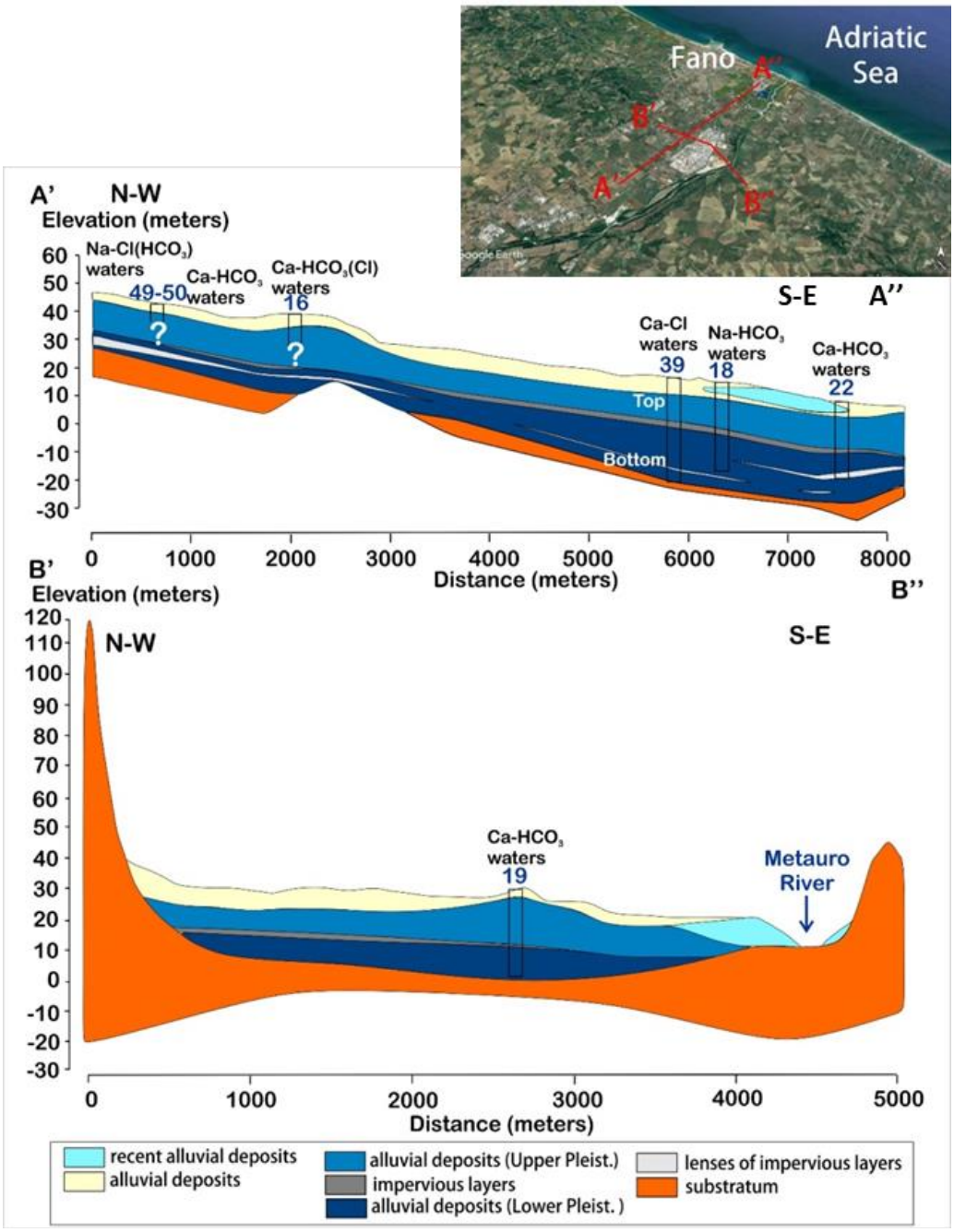

Fig. 2.46 Geological sections of the coastal aquifer system of Fano plain.

In order to further point out and interpret the observed seasonal variations of the water isotopes, the graphs of Fig. 2.47 were constructed for those samples collected in all three sampling campaigns. The most variable samples are those from the Metauro River near the coast (#40) with $\delta^{18}O$ values of -7.8‰ and -5.9‰ in June2019 and September 2020, respectively (Fig. 2.47), predominantly reflecting the seasonal variability of rainfall, instead of isotopic fractionation by evaporation processes (in September). The upstream river sample (#42), although sampled only twice, also shows a significant variation of the $\delta^{18}O$ (and $\delta^{2}H$) values: from -6.8‰ (September 2020) to -7.6‰ (November 2020). This behavior

is in agreement with that observed for the downstream sample (#40). The wells used to recharge the aquifer (#34; #37; #38) with the Metauro river waters show the same pattern (Fig. 2.47A). Other wells located close to the river and/or the artificial recharge area show similar, although more smoothed, trend (Fig. 2.47A), which allows to highlight the area that is likely directly (by seepage of surface water flowing along the riverbed and its effluent; e.g. Vallato del Porto, Fig.2.1) or indirectly (by artificial recharge of Torno well) affected by the Metauro feeding waters. When moving further away from the river and/or the artificial recharge area, the Metauro water isotopic footprint is increasingly masked by both homogenization processes and by mixing with other feeding inputs characterized by similar isotopic ratios, e.g. that of the local infiltration water. If we consider a rainfall isotopic value of -7.3‰, available for the area of interest from Longinelli and Selmo (2003), and the median value of the surface water (samples of Metauro and injection wells) of about -7.5‰, it is evident that the isotopic fingerprint of the river water is not so easily identifiable because of a very small difference. In this context, the only isotopic aspect that can provide an important hint of the Metauro feeding input is therefore only the seasonal and congruent variability of the groundwater system. However, in order to better understand this aspect, the EC map of September 2020 (Fig. 2.33) can help us to locate the low EC plume, being positioned from the artificial injection area, and continuing along the course of the river and its effluent (Vallato del Porto, Fig.2.1). The propagation of the low EC plume could be due to either seepage of surface water of the channel or underground circulation along more recent alluvial deposit of the Metauro river and characterized by high permeability, as shown in the schematic AA' cross-section (Fig. 2.46). The areas adjacent to the low EC plume therefore testify a diminishing influence of the Metauro water waters.

The other samples show relatively $\delta^{18}O$ values stable over time or at least varying within the analytical error. However, most of them shows a slight decrease in $\delta^{18}O$ between September and November 2020 (Fig. 2.47B), which is likely due to the infiltration of rainfall relatively negative. This appears to be congruent with the negativization of #42 (upstream point of Metauro river), which can be considered as representative of rainfall occurring in the upstream zone. The decrease of isotopic values in the second group (e.g. #0, #17) could therefore be attributable to a more important influence of local rainfall infiltration. The importance of a local meteoric infiltration throughout the study area was also previously highlighted by the December 2019 EC map (Fig. 2.33) where it can be observed that after

a relatively intense rainy period the whole area showed an homogeneous decrease of the EC values.

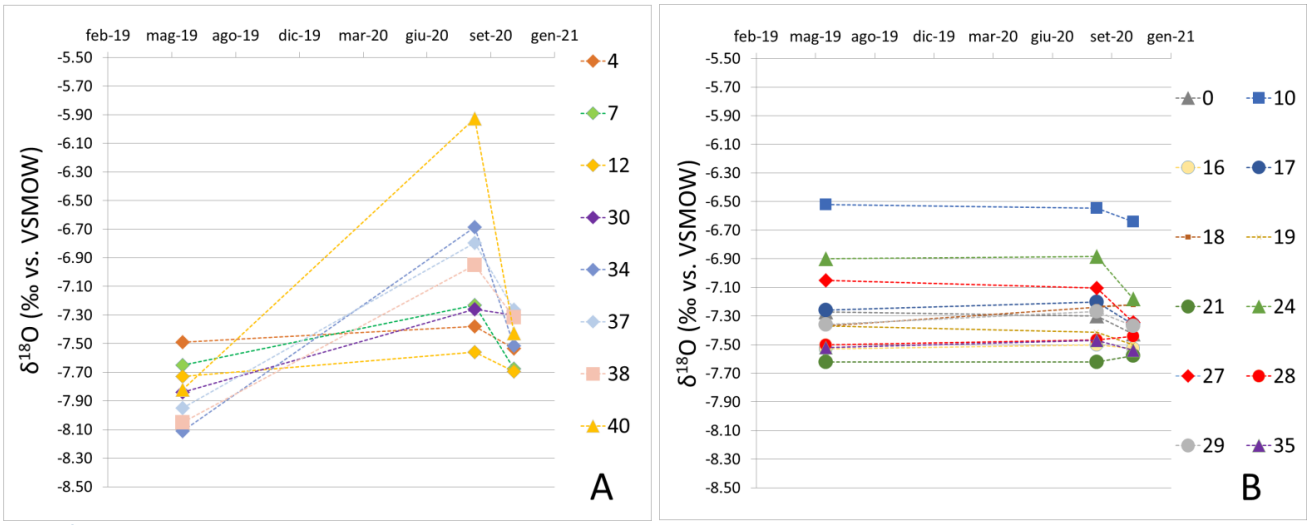

Fig. 2.47 $\delta^{18}O$ values of the Fano costal area waters for June 2019, September and November 2020.

2.5 Groundwater modeling of Fano aquifer system

Physically-based mathematical flow and transport models of the multilayer aquifer system from the Fano coastal plain were developed. The models allow a mathematical representation of the distribution of the hydraulic heads and concentrations (TDS - Total Dissolved Solids) of the aquifer system over the entire domain of interest. However, the development of such models requires a large amount of information and input data. It is indeed necessary to i) know the geometry of the system under study, the hydraulic parameters of the various lithotypes that make it up, and ii) identify and quantify the main input and output components (recharge, wells withdrawal, river seepage etc.). Moreover, the representativeness of the model itself is inextricably linked to the availability and reliability of the data required for calibration. For the aquifer system under study, previous information and the hydrogeochemical data acquired during this project can be considered suitable for a numerical modeling. However, the data distribution is not homogeneous over the territory and does not allow to provide a modeling with the same degree of reliability to be obtained over the entire domain of interest.

The purpose of this modelling phase is to create representative flow and transport models of the aquifer system that can simulate possible future sea level rise scenarios. Even if the results obtained from WP 4.1.2 highlighted the absence of significant seawater intrusion in the system, within either scenarios of sea level rise or a possible increasing of groundwater exploitation it should be taken into account that the system can be vulnerable to seawater intrusion.

2.5.1 Conceptual model

In order to avoid meaningless representations, a good numerical model requires an exhaustive knowledge of the conceptual model of the natural system. In this section, a summary of the main information obtained by comparing geological, hydrogeological, physical-chemical and geochemical-isotopic data (WP 4.1.2) is provided and supplemented by further elaborations preparatory to the development of the numerical model.

The coastal aquifer of Fano is hosted in Pleistocene and Holocene alluvial deposits. Gravels and sands mainly constitute the permeable alluvial deposits, which are locally interlayered by narrow layers of low permeability. The latter are characterized by low thicknesses and a

lack of any spatial continuity. Generally speaking, the aquifer system can be regarded as a monolayer aquifer. The substratum of the aquifer consists of low permeability formations outcropping in the surrounding hills.

In order to obtain a hydrostructural conceptual model of the aquifer system, all the available hydro-stratigraphic data from 85 boreholes were interpreted and correlated into hydrogeological cross sections (Fig. 2.48).

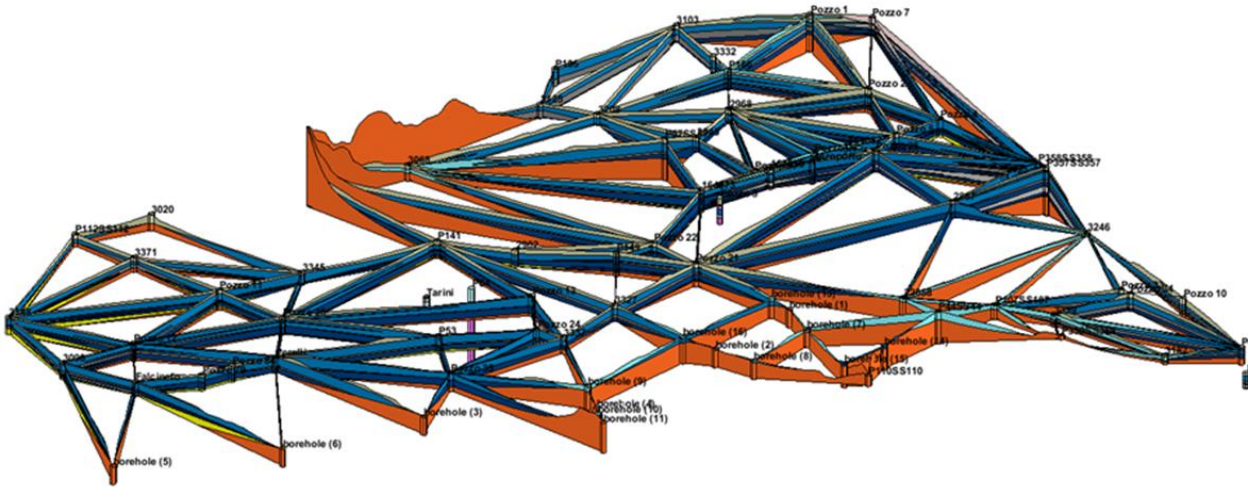

Fig. 2.48 Cross correlation of 85 boreholes (orange and yellow: substratum; blue and light blue: aquifer; grey: aquitard; light brown: cover).

In particular, many hydrostratigraphic units (HU), characterized by different permeability, were defined, as follows:

1. recent sand deposits with high permeability (about 10^{-3} m/s);
2. a relatively impervious cover consisting of sandy silts with medium-low permeability (about 10^{-5} m/s);
3. a shallow aquifer hosted in sands and gravels with high permeability (about $5*10^{-4}$ m/s);
4. an aquitard interposed between deep and shallow aquifers, consisting of silts and clays, with low permeability (about $5*10^{-7}$ m/s);
5. a deep aquifer consisting of sands and gravels with high permeability (about 10^{-3} m/s);
6. an aquitard within the deep aquifer, consisting of sandy silts, with medium-low permeability (about 10^{-5} m/s).

The hydraulic permeability of the different units was assigned on the basis of the average grain size composition of each HU.

Analyzing the piezometric maps processed within the WP 4.1.2, as a whole, a SW-NE groundwater circulation is observed with absolute piezometric values always above sea level, except in a very tiny and narrow coastal band. In the inland, the artificial recharge by wells results in a local piezometric maximum that appears to steer the groundwater flow-path downstream. The Metauro river seems to mainly act as a drainage axis up to the central part of the investigated area, whereas in the coastal sector it played as either drainage or a feeding input in the different seasons campaigns.

Groundwater can mainly be regarded as the result of mixing processes, mainly between two feeding components: i) diffuse local rainfall infiltration and; ii) waters from the Metauro river, artificially injected in the inland zone by some apposite wells. Other local and minor input can be represented by the infiltration of runoff from the hills nearby the plain.

On the basis of precipitation and temperature data from 4 weather stations located in or near the study area (data from 2000 to 2020), an average annual precipitation value of 778 mm and average evapotranspiration of 530 (using Turc's formula) was calculated, resulting in an effective precipitation of 248 mm. With regard to the injection area, surface waters from the Metauro River are released into the aquifer with an average flow rate of 45 l/s for a total of approximately 1.35 Mm^3 per year (data only for 2020, provided by water service ASET Ltd.).

The main outputs of the system are the wells' withdrawal, the drainage action of the Metauro river, as well as the natural groundwater flow towards the sea. On the basis of the available information and land use, all the wells located in the area (over 2000 wells) were categorized according their use (over 1200 domestic wells, 596 agricultural wells, 172 industrial wells, and 18 drinking water wells). For the drinking water wells, the quantities supplied were provided by ASET Ltd. (only 2020 data are available), while for the wells used for agricultural and industrial purposes they were estimated on the basis of the land use map. In table 2.9 the estimated pumped waters for each type of use are reported. The total amount of water exploited for domestic use is negligible compared to other uses and therefore, it was not taken into account.

Tab. 2.9 Annual total amount of water pumped for different use

	Mm^3/year
industrial use	1.5
drinking water	0.3

agricultural use	8
Total	**9.8**

By comparing the geological, hydrogeological, physical-chemical and geochemical-isotopic data a conceptual model of the coastal aquifer of Fano can be proposed. In particular, the geometry of the main hydrogeological layers was built, the main water components involved in the studied coastal system were individuated and the principal physical and chemical processes presently occurring in the system recognized.

The following points summarize the conceptual model of the aquifer under study (see also the scheme in Fig. 2.49):

- The coastal aquifer of Fano is hosted in Pleistocene and Holocene alluvial deposits. Gravels and sands mainly constitute such deposits, which are locally interlayered by narrow low permeability layers. The latter are characterized by a lack of spatial continuity, thus making the aquifer system a monolayer aquifer. However, the presence of separate flow-paths can locally be promoted by permeability variations. The substratum of the aquifer consists of low permeability formations outcropping in the surrounding hills, in which clay-rich sediments prevail, although the presence of silty-sandy layers and evaporitic minerals cannot be excluded. Additionally, relatively saline waters of deep origin, though diluted by the overlying freshwaters, may also be able to explain the high TDS values recorded at #39bot and #49. Consequently, geostructural investigations and specific geochemical studies should be addressed to better clarify the origin of these waters.
- As a whole, a SW to NE groundwater circulation was reconstructed on the basis of absolute piezometric values, which were always above the sea level, except in a very tiny and narrow coastal band. In the inland, the artificial recharge by wells results in a local piezometric maximum that appears to steer the groundwater flow-path downstream. This seems also responsible of an apparent chronological anomaly between the rainfall regime and the piezometric levels and the EC evolution in the groundwater system that was monitored in a continuative way by selected wells. The Metauro river seems to act as a drainage axis in all survey periods up to the central part of the investigated area. In the coastal sector, it acts as a drainage axis or, weakly, as a feeding input as evidenced by seasonal surveys according to the differences in the hydraulic head between the groundwater table and the river itself. Specifically, in the wet season (e.g. September 2019 and December 2019), characterized by higher

piezometric levels, the river drains the aquifer almost down to the coastline. In the dry periods the river is either in equilibrium with the aquifer or even feeding it (e.g. September 2020);

- Groundwater can mainly be regarded as the result of mixing processes between two components: ì) diffuse local rainfall infiltration, and ii) the artificially injected waters from the Metauro river in the inland zone by some apposite wells. Other local input can be represented by the infiltration of runoff from the hills nearby the plain;
- At the present the seawater intrusion process is negligible in the aquifer. Only locally, in the NE sector, close to the shoreline a weak groundwater-seawater mixing was evidenced;
- The chemical quality of the groundwater system is mainly governed by interaction of the water with carbonate and silicate minerals. On the resulting and dominating Ca-HCO_3 groundwater composition some secondary processes are overlapping. The first one is the input of N-rich contaminants that are affecting a large sector of the study area. Such pollution is relatively contrasted and diluted in those zones where the plume originated by the injection of the Metauro river waters via artificial recharge wells was recognized. Other secondary processes are likely due to the interaction of groundwater and clay-rich evaporitic minerals of the substratum that favored the increase of Cl concentrations in some wells. Additionally, ion exchange processes were invoked when Na-HCO_3 and Ca-Cl waters, though very locally, were found.

As a general and significant result in the framework of the ASTERIS project, this study highlighted the absence of significant seawater intrusion in the shallow aquifer system of Fano. Nevertheless, within scenarios of sea-level rise and/or possible increasing water exploitation, it should be taken into account that the shallow aquifer can be vulnerable to the seawater intrusion.

The schematic sections in figure 2.49 summarize the conceptual model outlined above with the main input and output components affecting the aquifer system.

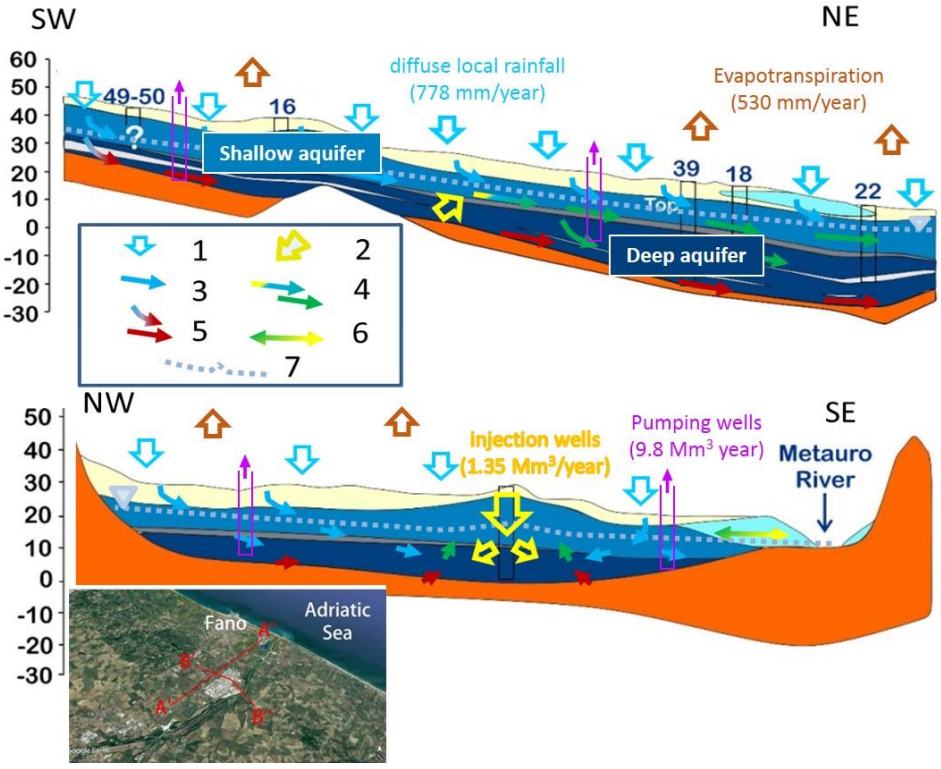

Fig. 2.49 Schematic quantitative conceptual model of the Fano coastal aquifer system: 1: local rainfall infiltration; 2: Ca-HCO_3 water of the Metauro River artificially injected in the aquifer; 3: Ca-HCO3 groundwater mainly fed by the infiltration of local and hills-surrounding rainfall ; 4: result of mixing between the component locally generated by rainfall and the component from artificial recharge; 5: chemical evolution resulting in Cl contents increasing due to groundwater interaction with the substratum; 6: exchanges between Metauro river waters and groundwater; 7: piezometric profile.

2.5.2. Numerical Model

Based on the conceptual model of the aquifer system, groundwater flow models were implemented using the MODFLOW-2005 (Harbaugh, 2005) and MT3DMS, SEAWAT and PEST related codes; Groundwater Vistas (v7) was used as graphical user interface. Initially, a steady-state flow model was created and calibrated. Based on this model, a transient flow model was then created for 2019 and 2020 with monthly stress periods. Finally, a TDS transport model was realized in order to simulate scenarios of sea level rise and/or changes in climate conditions and/or increased water demand.

Implementation of the groundwater flow models

The active domain covers the coastal plain sector of Fano from the area of the injection wells to the coast and it is bounded to the NW and SE by the hills overlooking the plain (Fig. 2.50)

for a total of about 44 km^2. The domain was discretized horizontally with 115 row, 112 columns and 6 layers for a total of 77,280 cells, 41,352 of which are active cells (Fig. 2.51). In each layer, the different HU, reconstructed in the geological model elaborated, were distinguished using different value of hydraulic conductivities (Fig. 2.52). In particular:

- layer 1 represents the cover, the actual sandy deposits and the shallow aquifer;
- layer 2 refers to the shallow aquifer;
- layer 3 is the aquitard interposed between the deep and shallow aquifers, where present, otherwise a transition term between shallow and deep aquifers was considered;
- layers 4 and 6 are the upper part and the deepest part of the deep aquifer, respectively;
- layer 5 consists of the deep aquifer and aquitard within the deep aquifer, where present.

The values of hydraulic conductivity of each HU are reported in table of Fig. 2.52.

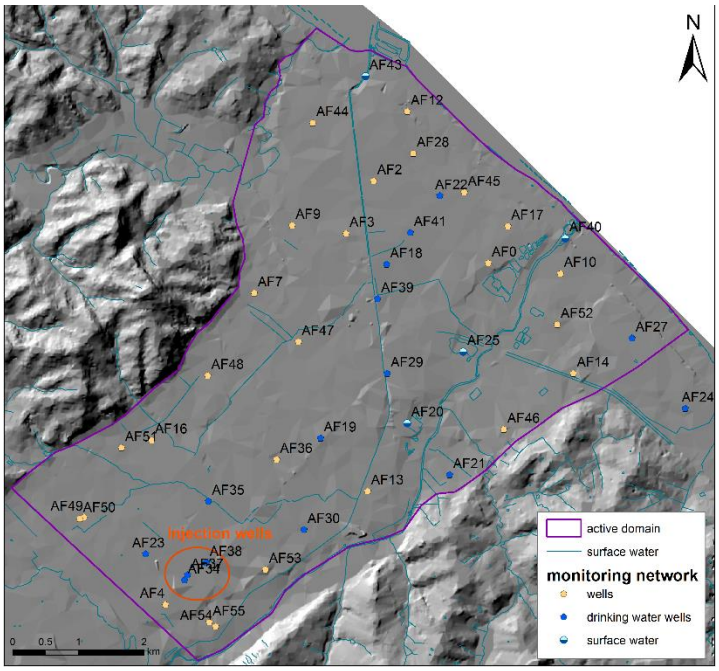

Fig. 2.50 Active domain and monitoring network.

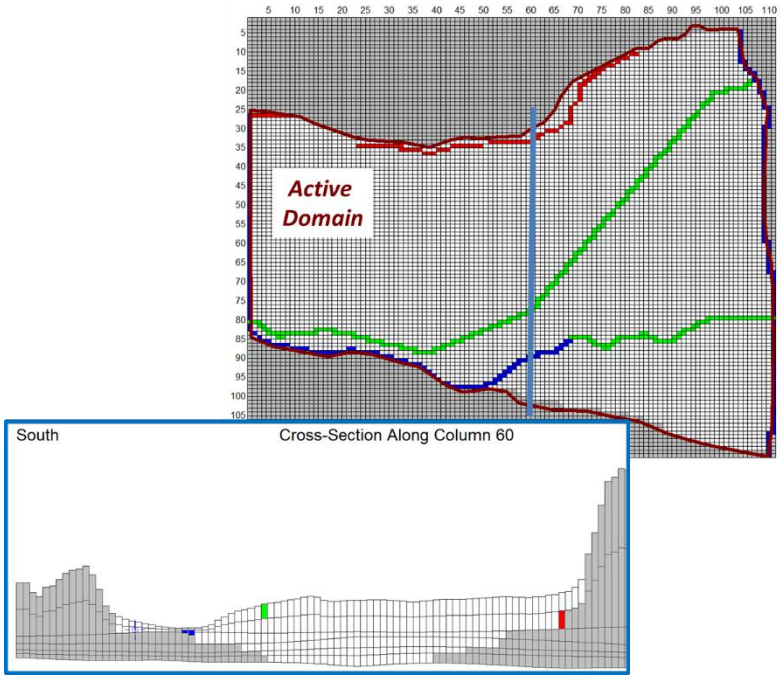

Fig. 2.51 Spatial discretization and some boundary condition (line in dark red: active domain; red cells: boundary condition with constant flux; blue cells: boundary condition with constant head; green cells: boundary condition head dependent flux).

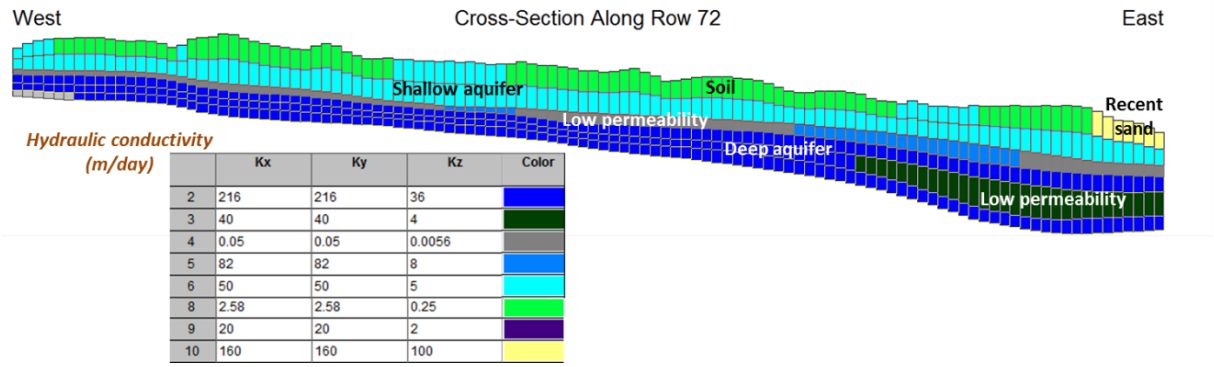

	Kx	Ky	Kz	Color
2	216	216	36	
3	40	40	4	
4	0.05	0.05	0.0056	
5	82	82	8	
6	50	50	5	
8	2.58	2.58	0.25	
9	20	20	2	
10	160	160	100	

Fig. 2.52 Zone and value of Hydraulic conductivity (m/day) assigned to the cell of the model, based on stratigraphy grain size and hydrostructural model.

Initially, the hydraulic parameters (hydraulic conductivity, specific yield, specific storage) assigned to each cell were evaluated considering the lithology of the reconstructed HUs and according to the literature data. Subsequently, the values were modified during the calibration phase. In the deep aquifer, the value of Specific Storage (Ss) was set at 0.0001 1/m, whereas in the shallow aquifer the value of Specific Yield (Sy) was set at 0.28.

Fig. 2.53 shows the boundary conditions of the model. In particular, the sea level to the east was implemented by using a Constant Head boundary condition (blue cells), whereas a Constant Flow was applied at the northern borders where the conceptual model indicates a feeding inflow component (red cells). In order to simulate a regional flow from SW to NE a Constant Head at the SW border was applied (blue cells). The others cells of the boundary are set as no-flow (grey cells).

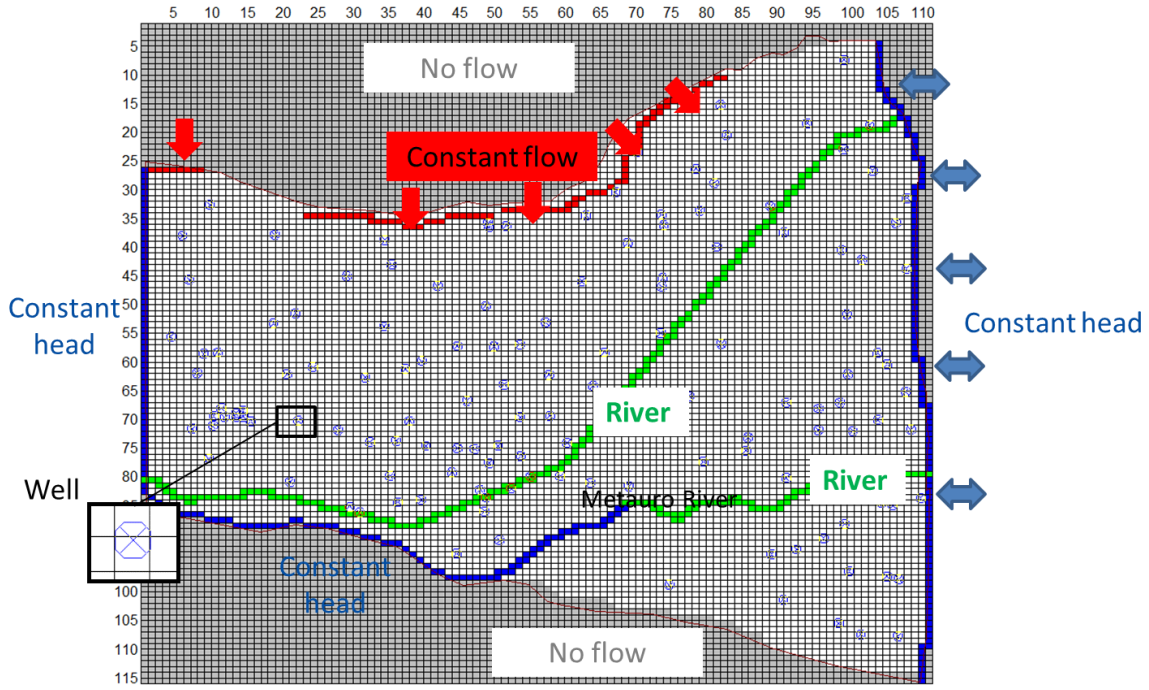

Fig. 2.53 Boundary conditions.

The main rivers (Metauro river and Albani channel) were implemented in the numerical model using the RIVER package (green cells); only in the innermost part of the plain, the Metauro river, where it flows directly on the model substrate, was implemented with Constant Head (blue cells).

As previously discussed, there are almost 800 wells for agricultural use, industrial use, and drinking water. Given the large number of wells, they were grouped in “cumulated wells” according to their specific use, location and depth. In particular, 76 “cumulated wells” for agricultural use, 45 “cumulated wells” for industrial use, 18 wells for drinking water and 7 wells for injection activity were implemented using the package WELL.

The recharge to the aquifer using the RECHARGE package was applied at the first active layer as effective infiltration rate. To obtain an effective rainfall for each stress period of simulation, the estimated evapotranspiration value was subtracted to the rainfall measured in order to calculate the effective rainfall. At this value, a potential infiltration coefficient was applied to discriminate the percentage that flows like either runoff or groundwater supply, basing on land use (urban or rural area). In particular, an Infiltration Coefficient of 0.4% and 0.7% was applied in the urban and rural area, respectively, to obtain the value of effective infiltration.

The initial condition of head for the steady-state is above the topographic elevation, whereas the initial condition of the transient state head is the output of the calibrated steady-state.

Model calibration and results

The objective of calibration is to identify a set of parameters that produces a satisfactory match between field observations and simulated values. The trial-and-error method and automatic calibration with PEST code were used to calibrate the model. Input parameters (hydrodynamic parameters and hydrologic parameter) were adjusted within reasonable ranges in sequential run of the model until the model produced an acceptable match. The input parameters that were mainly modified are those found to be more susceptible during the sensitivity analysis (e.g. Fig. 2.54). In particular, the more sensitivity parameters were found to be the i) horizontal hydraulic conductivity of zone 2 and 6 (shallow and deep aquifer), ii) vertical hydraulic conductivity of zone 2 (shallow aquifer), at which iii) conductance of the riverbed and iv) flow incoming from the NE sector are to be added.

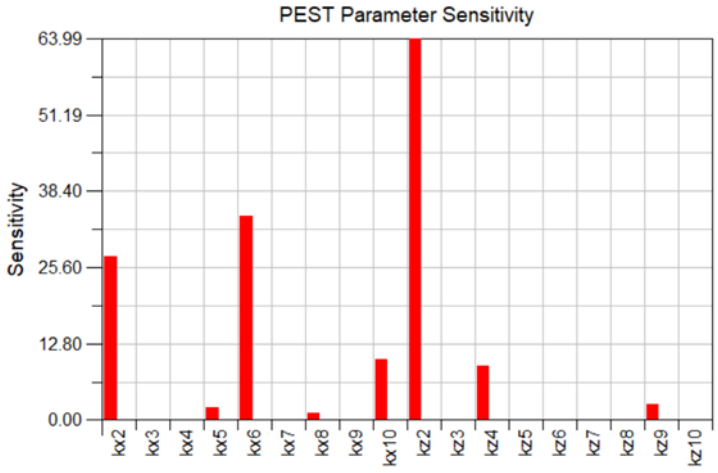

Fig. 2.54 An example of graph of sensitivity analysis.

The calibration target used for the calibration was the monitoring network of the activities of WP.1.2 (Fig. 3.1). In particular, for the steady state model, the mean value of the 6 surveys performed between June 2019 and November 2020 was applied, whereas for the 3 point of continuous monitoring the recorded mean value was used. For the transient model, the value acquired was attributed to the monthly stress period during which the campaign was carried out.

In Fig. 2.55 a binary scatterplot of observed and calculated value and some summary statistics of residual value are reported for the calibration target used for steady state simulation, testifying to a very good calibration of this model.

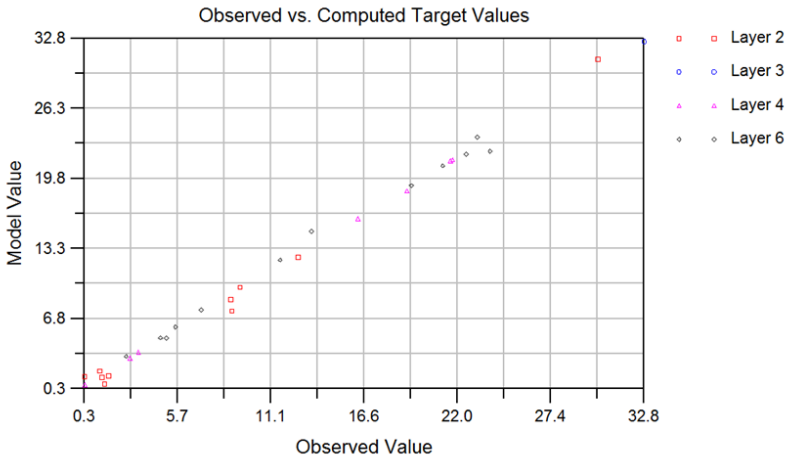

Target Statistics

Target	Residual	Name
19.05	0.38	AF53
19.30	0.16	AF35
2.72	-0.58	AF2
2.94	-0.19	AF44
21.12	0.12	AF38
21.57	0.11	AF54
21.69	0.15	AF55
22.48	0.39	AF37

Residual Mean	= -0.07
Residual Standard Dev.	= 0.61
Absolute Residual Mean	= 0.47
Residual Sum of Squares	=1.14e+001
RMS Error	=0.62
Minimum Residual	= -1.40
Maximum Residual	= 1.53
Range of Observations	= 32.51
Scaled Res. Std. Dev.	= 0.019
Scaled Abs. Mean	= 0.015
Scaled RMS	= 0.019
Number of Observations	= 30

Fig. 2.55 Observed vs simulated values graph for the steady state model.

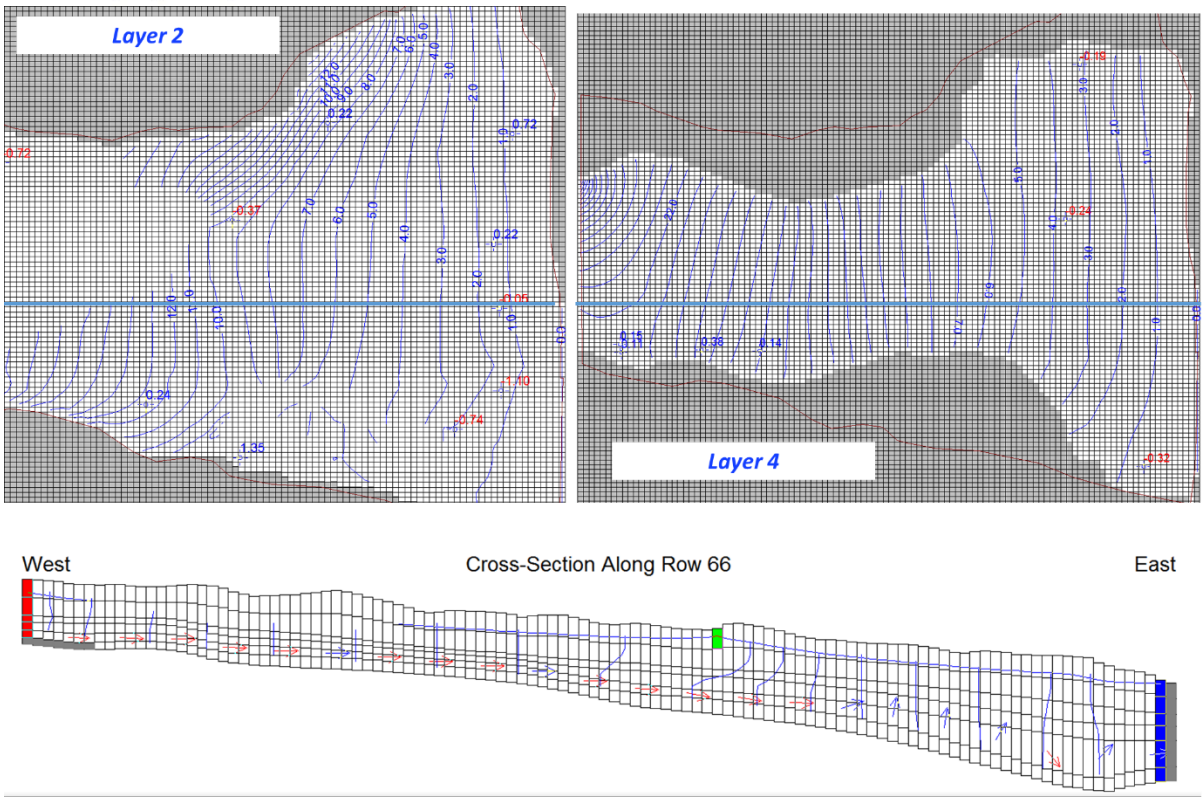

Fig. 2.56 Piezometric maps calculated by the model in layers 2 (shallow aquifer) and layer 4 (deep aquifer) and a cross section of row 66. In the maps the residual values (difference between measured and calculated value) are reported whereas in the section the velocity vectors are also shown.

In Fig. 2.56 the piezometric maps, calculated by the model in layers 2 (shallow aquifer) and 4 (deep aquifer) confirmed the conceptual model outlined above. In these maps, it is also possible to observe the spatial distribution of the error (residual value) in the different layers. The section in Fig. 2.56 also supports the outlined conceptual model and shows the absence of incoming marine flow from the coast. In other words, an absence of marine intrusion under steady-state conditions.

In Fig. 2.57, some graphs related to calibration phase of transient model are shown. It is possible to note a good calibration of this model. In particular, in the continuous chronograms it can be observed that the model, even if with a slight difference in the absolute value (maximum of 0.5), simulates the seasonal trend of the piezometric levels in the shallow and deep aquifers.

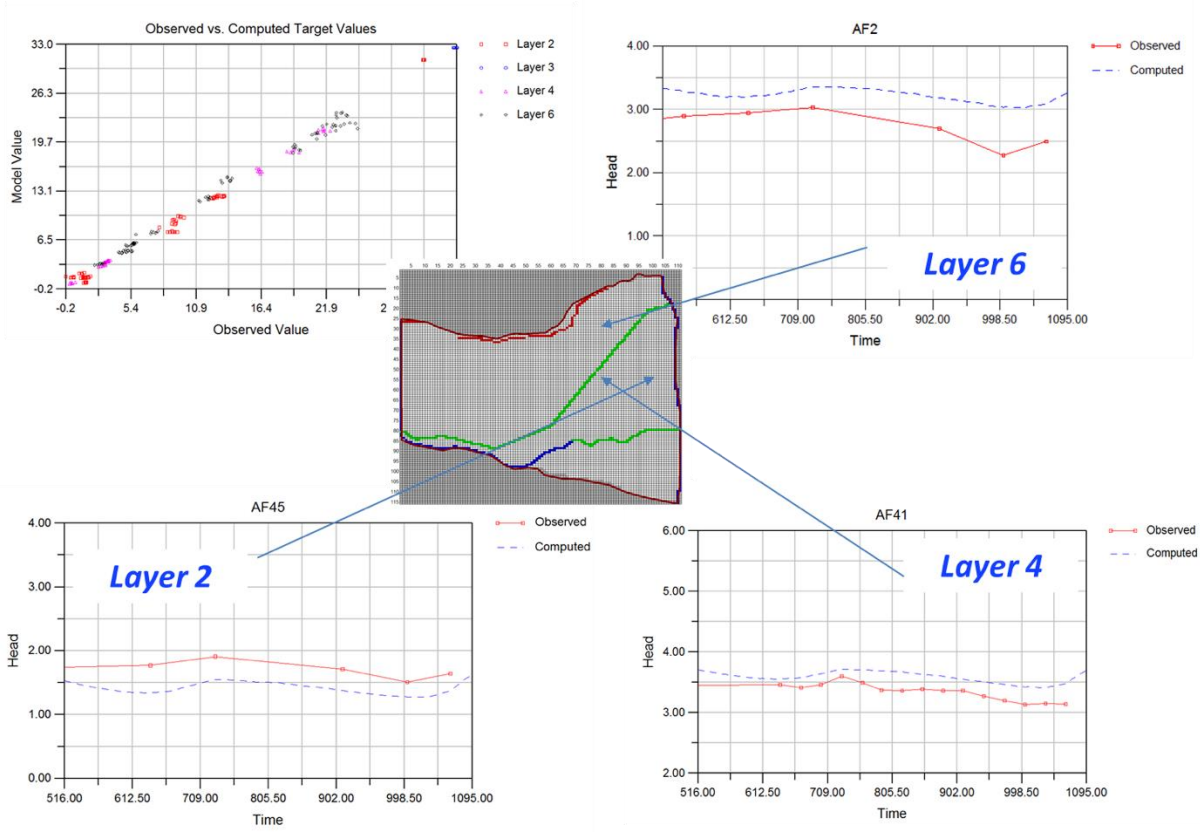

Fig. 2.57 Observed vs simulated values graph for transient model.

Transport model

Starting from the flow models outlined above, a TDS transport model was then implemented. A TDS value was then assigned to each boundary conditions applied to the model, based on the data collected in the three geochemical surveys (June 2019, September 2020, November 2020). In particular, the average value measured in the wells during each campaign (0.8 kg/m^3) was set as the initial concentration and also attributed to incoming boundary from the western sector. A slightly higher TDS (ranging between 0.85-1.1 kg/m^3) was implemented to the constant-flow boundary condition, as the wells receiving feed from that sector were found to be have a slightly higher TDS. TDS ranging from 0.3 to 0.5 kg/m^3 was attributed to the waters from the Metauro River and the injection wells. Finally, the boundary condition representing seawater was assigned a value of 35 kg/m^3.

With regard to the transport parameters, considering the lithologies of the aquifer system, a value of 10 was implemented for the longitudinal dispersivity, 1 for the transverse dispersivity and 0.1 for the vertical dispersivity, as well as an average effective porosity of 0.15.

Fig. 2.58 shows a TDS map calculated by the model in the deep aquifer (layer 4) that is representative of present conditions based on all the average input data acquired during the monitoring activities (WP 4.1.2) and implemented in the transport model. To understand the goodness of this simulation, the TDS map was compared with the measured EC map, as EC values are proportional to TDS. It is possible to observe that overall the distribution of TDS values seems to be in good agreement with those measured during the September 2020 campaign. The model also highlights the action of low salinity water injection activities and their effect up to the most distal part of the plain. Eventually, the transport model further supports the absence of marine intrusion process.

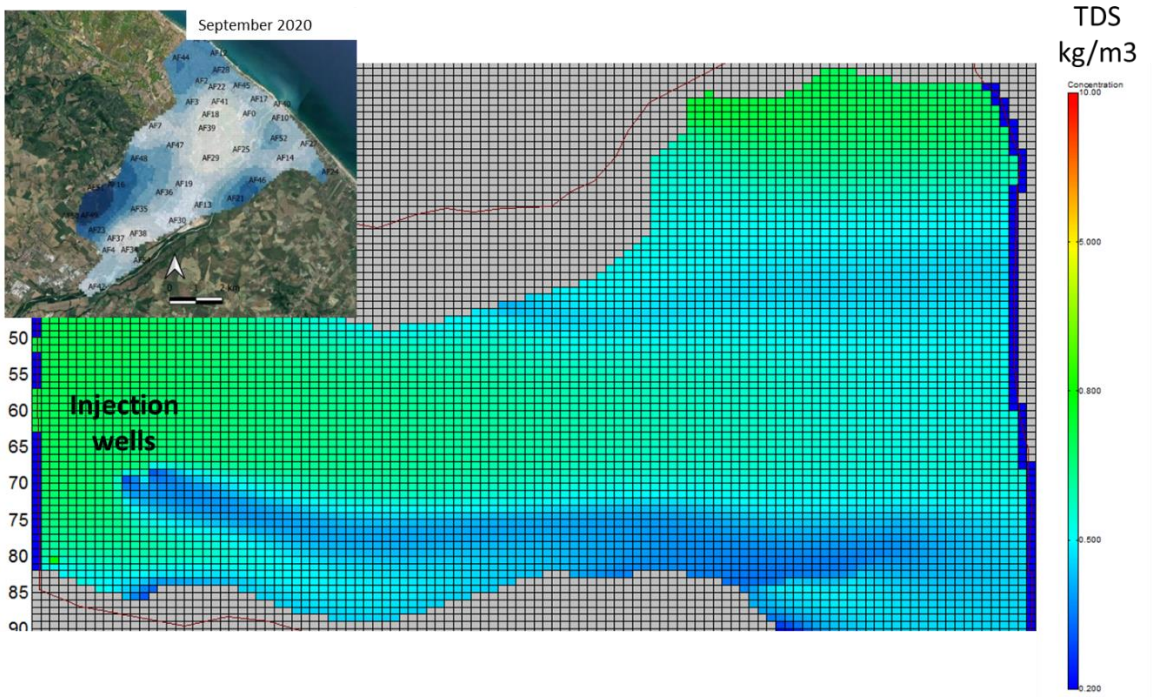

Fig. 2.58 TDS map calculated by the transport model in layer 4 – deep aquifer (at top left the Electrical Conductivity map of September 2020)

Fig. 2.59 shows the TDS map and a section in the southern sector of the model near the Metauro river calculated by the model for the shallow aquifer (layer 2). In this case, it is possible to observe the dilution effect of the Metauro river waters in proximity of the coastal sector, where it feeds the aquifer. Additionally, a slight feeding component by the waters flowing in the Albani channel is evidenced. The absence of marine intrusion in this sector of the coastal plain is once again confirmed.

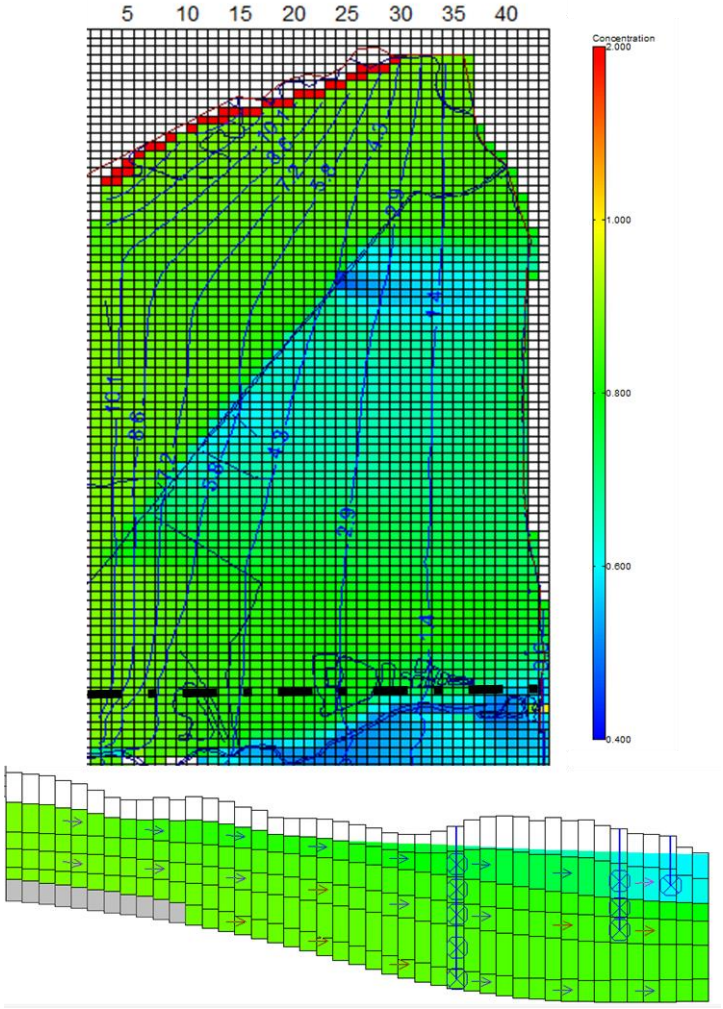

Fig. 2.59 TDS map calculated by the transport model in the layer 2 – shallow aquifer and section on the column 39 (in black dotted line the section trace)

2.6 Concluding remarks and forecasting simulation

The modelling activity has produced flow and transport models that are calibrated and are to be regarded as sufficiently representative of the natural aquifer system. The availability of such tools can allow the local authorities connected with water resources to use them in a more conscious and sustainable way in order to safeguard a precious resource such as groundwater. In fact, even if in the modelled area of Fano coastal plain does not seem to be currently affected by marine intrusion, possible scenarios of sea level rise, as well as global changes could modify the fragile balance between fresh and salt waters.

Aware of the inherent error in model definition and all the uncertainties involved in their construction, these models can be used to simulate numerous future scenarios by modifying the associated boundary conditions. In this project, a 100-year simulation with a sea level rise of 1 m was elaborated as an example.

Fig. 2.60 shows some results of this simulation for the shallow aquifer (layer 2). Considering that piezometric levels are currently well above sea level with values over 1 m, even in the most coastal sector, a sea level rise of 1 m does not seem to cause a direct effect to the aquifer, although a slight overall increase in TDS content is expected. This precariousness could however be broken by a decrease in precipitation and/or increasing water demand. However, the area that seems to be heavily affected by this sea level rise is the final part of the Metauro River, where it feeds the aquifer with sea water, substantially increasing the TDS of both the surface and deep aquifers.

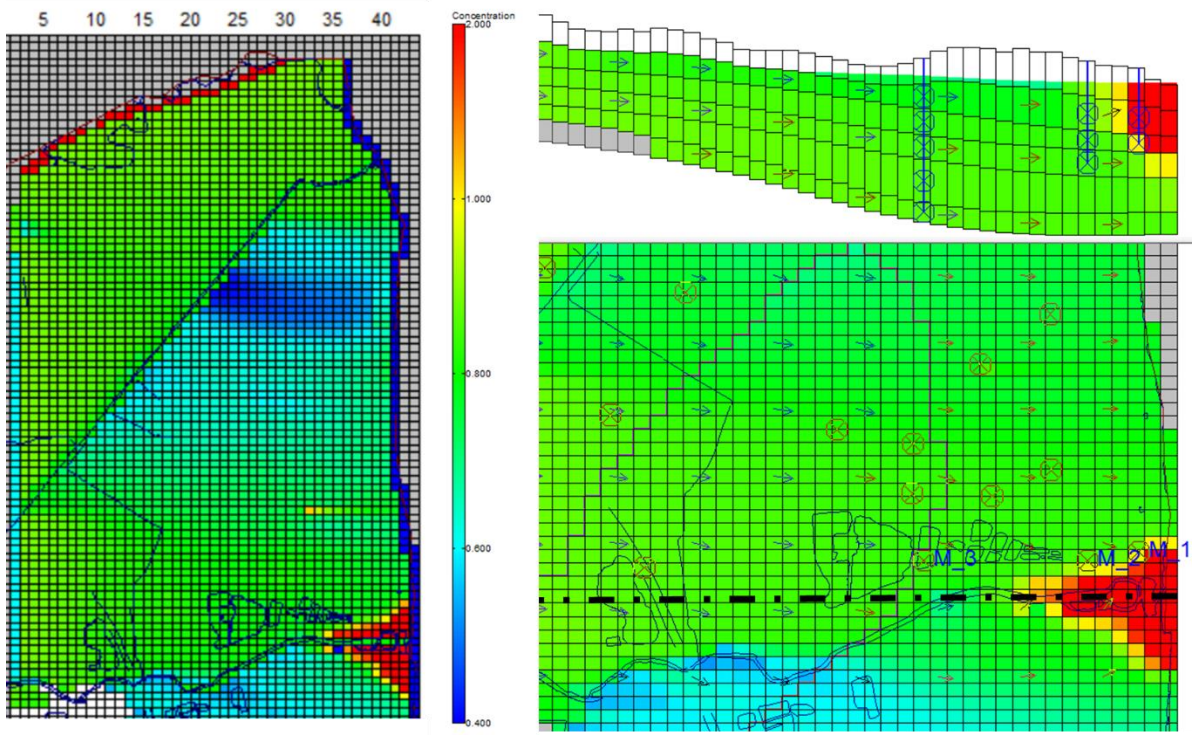

Fig. 2.60 A 100-year simulation with a sea level rise of 1 m (in black dotted line the section trace)

2.7 References

Appelo C.A.J., Postma D., 1993. Geochemistry, groundwater and pollution. Balkema A.A., Rotterdam, p. 536.

Armstrong, M., 1984a. Problems with universal Kriging. Math. Geol., 16(1): 101-108.

Armstrong, M., 1984b. Problems with universal Kriging. Math. Geol., 16(3): 305-316.

ASET Azienda Servizi sul territorio. 2010. Studio idrogeologico sul fondovalle del Fiume Metauro per l'utilizzo e/o il recupero per usi potabili della falda 570 dell'acquifero alluvionale. Fano Italy.

Barchi, M.R., Minelli, G., Pialli, G. (1998). The CROP 03 profile: a synthesis of results on deep structures of the northern Apennines. Mem. Soc. Geol. It. 52, 383-400.

Capuano, N. Savelli, D. Santini, S. Tonelli, G. (2009) Note illustrative della Carta Geologica D'Italia alla scala 1:50.000. Foglio 279 – Urbino. Servizio Geologico d'Italia, 109 p.

Chauvet P. (1991) Aide mémoire de géostatique linéeaire, Chaiers de Géostatistique, Fascicule 2. Ecole des Mines de Paris, Fontainebleau, 210 p.

Chauvet P. (1993) Processing data with a spatial support: geostatistics and its method, Chaiers de Géostatique, Facicule n. 4, Ecole des Mines de Paris, Fontainebleau, 57 p.

Chauvet P., (1982) The variogram cloud, Johnson TB & Barnes RJ (Ed.) 17th APCOM, Society of Mining Engineers, New York, 757 – 764.

Chauvet P., Galli A. (1982) Universal Kriging, Pubblication n. C – 96, Centre de Géostatique, Ecole des Mines de Paris, Fontainebleau.

Chiles J.P, Chauvet P. (1973) Application du krigeage a la cartographie des fonds marins, Cahiers de Geostatistiques, Ecole de Mines de Peris, Fontainebleu.

Clark I. (1979). Practical Geostatistics. Department of Mineral Resources Engineering, Royal School of Mines, Imperial College of Science and Technology, London, 129 p.

Craig H (1961) Isotopic variations in meteoric waters. Science 133:1702–1703

David M. (1977). Geostatistical ore Reserve Estimation (Amsterdam:Elsevier)

Davis J. (1986). Statistics and Data Analysis in Geology 2nd edition (New York: Wiley), 646 p.

Deiana G., Pialli G. (1994). The structural provinces of the Umbro-Marchean Apennines. Mem. Soc. Geol. It. 48, 473-484.

Devijver P.A., Kittler J. (1982) Pattern Recognition: A Statistical Approach. Prentice-Hall, London, 1982.

Di Girolamo M. (2004). Analisi delle risorse idriche e valutazione della vulnerabilità, con l'ausilio di metodologie GIS, dell'acquifero 550 alluvionale del fiume Metauro tra Montemaggiore e Fano (PU). Master's degree thesis, University of Chieti-Pescara G. 551 D'Annunzio, Chieti (Italy), 180 p.

Doglioni C., Gueguen E., Harabaglia P., Mongelli F. (1999). On the origin of west-directed subduction zones and applications to the western Mediterranean. In "The Mediterranean Basins: Tertiary Extension Within the Alpine Orogen", Durand B., Jolivet L., Horvath, F., Seranne, M., Eds.; Geol. Soc. London, Sp. Publ., London England, 156, 541-561.

Gaillardet J., Dupré B., Allègre C. J., Négrel P. (1997). Chemical and physical denudation in the Amozon River Basin. Chem. Geol. 142, 141 - 173.

Gat J.R., Carmi I. (1970). Evolution of the isotopic composition of atmospheric waters in the Mediterranean Sea area. J. Geophys. Res. 75, 3039–3048.

Han G., Liu C.-Q., 2004. Water geochemistry controlled by carbonate dissolution: a study of the river waters draining karst-dominated terrain, Guizhou Province, China. Chem. Geol., 204, 1-21.

Krige D.G. (1951). A statistical approach to some basic mine valuation problems on the Witwatersrand. J. Chem. Metall. Min. Soc. S. Afr. 52, 119-139.

Longinelli A., Selmo E. (2003). Isotopic composition of precipitation in Italy: a first overall map. J. Hydrol. 270, 75–88.

Marchina C., Bianchini G., Natali C., Pennisi M., Colombani N., Tassinari R., Knoeller K. (2015). The Po river water from the Alps to the Adriatic Sea (Italy): new insights from geochemical and isotopic ($\delta^{18}O$-δD) data. Environ Sci Pollut Res (2015) 22:5184–5203 DOI 10.1007/s11356-014-3750-6

Matheron G. (1962) Traité de géostatistique appliquée. Mémoire du BRGM 14, Ecole des Mines de Paris, Fontainebleau.

Matheron G. (1965) Les variables régionalisées et leur estimation: une application de la théorie des fonctions aléatoires aux sciences de la nature. Paris, Masson. 306 p.

Matheron G. (1969) Le krigeage universel. Les cahiers du CMM de Fontainebleau, Fasc. 1, Ecole des Mines de Paris.

Matheron G. (1970) The theory of regionalized variables and its applications, Fascicule n. 5, Les Cahiers du Centre De Morphologie Mathématique, Ecole des Mines de Paris, Fontainebleau, 211 p.

Meybeck M., 1987. Global chemical weathering of surficial rocks estimated from river dissolved loads. Am. J. Sci. 287, 401- 428.

Minissale A., Magro G., Martinelli G, Vaselli O., Tassi F. (2000). Fluid geochemical transect in the Northern Apennines (central-northern Italy): fluid genesis and migration and tectonic implications. Tectonophysics 319, 199–222.

Nanni T. (1985). Le faide di subalveo delle Marche: inquadramento idrogeologico, qualità delle acque (ed) elementi di neotettonica. In “Materiali per la programmazione 2”, Regione Marche Ed., Ancona (Italy), 112. 549.

Roy S., Gaillardet J., Allègre C. J., 1999. Geochemistry of dissolved and suspended loads of the Seine river, France: Anthropogenic impact, carbonate and silicate weathering. Geochim. Cosmochim. Acta. 63, 1277 - 1292.

Savelli D., De Donatis M., Mazzoli S., Nesci O., Tramontana M., Veneri F. (2002). Evidence of Quaternary faulting in the Metauro River Basin (Northern Marche Apennines). Boll. Soc. Geol. It., 1, 931-937.

Tassi F., Fiebig J., Vaselli O., Nocentini M. (2012). Origins of methane discharging from volcanic-hydrothermal, geothermal and cold emissions in Italy. Chemical Geology, 310-311 , 36-48.

Wackernagel H. (1995) Multivariate Geostatistics (Berlin: Springer) ISBN 978-3-662-03098-1.

2.8 Appendix

A.1. Characteristics and coordinates for each site

Code	Type	Est (GB Roma40)	Nord (GB Roma40)	Reference Altitude by GPS (m a.s.l.)	Depth (m)
0	well	2362265.35	4854135.21	13.81	29
2	well	2360523.38	4855382.60	14.57	15
3	well	2360102.71	4854583.93	19.95	-
4	well	2357356.18	4848946.44	38.08	28
7	well	2358706.09	4853677.92	27.71	21
9	well	2359282.84	4854707.21	21.59	19
10	well	2363362.49	4853974.14	4.80	7
12	well	2361033.65	4856435.79	2.51	-
13	well	2360429.51	4850669.48	22.52	13
14	well	2363558.70	4852457.84	11.37	-
16	well	2357144.48	4851442.58	-	-
17	well	2362562.57	4854692.98	10.23	12
18	ASET well	2360719.78	4854114.23	17.29	35
19	ASET well	2359713.09	4851472.20	27.17	35
20	surface water	2361033.14	4851693.62	-	-
21	ASET well	2361677.84	4850915.78	13.67	6.5
22	ASET well	2361526.69	4855154.69	-	35
23	ASET well	2357053.90	4849714.26	38.93	30
24	ASET well	2365261.51	4851925.51	10.13	-
25	surface water	2361885.83	4852779.53	5.06	-
27	ASET well	2364451.17	4852993.66	10.65	32.5
28	well	2361123.61	4855799.45	-	41
29	ASET well	2360728.18	4852454.98	22.20	40
30	ASET well	2359462.55	4850081.96	28.75	31
34	ASET well	2357644.84	4849318.67	36.98	28
35	ASET well	2358011.29	4850515.38	37.52	30
36	well	2359047.76	4851149.12	31.46	29
37	ASET well	2357693.86	4849396.15	36.60	-
38	ASET well	2357976.32	4849584.49	35.41	-
39	ASET well	2360583.14	4853590.23	18.02	45
40	surface water	2363436.30	4854502.58	7.42	-
41	ASET well	2361079.50	4854597.59	15.67	32
42	surface water	2356404.12	4847559.11	36.37	-
43	surface water	2360398.97	4856964.58	4.52	-
44	well	2359596.18	4856263.50	14.79	-
45	well	2361900.79	4855207.81	9.33	10
46	well	2362500.89	4851607.19	19.33	-
47	well	2359377.36	4852937.54	25.74	-
48	well	2358001.90	4852423.76	33.28	-
49	well	2356119.62	4850272.49	46.16	-
50	well	2356053.36	4850250.17	46.75	-
51	well	2356688.75	4851327.09	44.18	17
52	well	2363313.45	4853200.67	6.37	-
53	well	2358878.02	4849478.53	33.05	20
54	well	2358119.99	4848611.64	33.70	15.5
55	well	2358022.13	4848677.39	33.37	20

A.2. Sampling form for each site

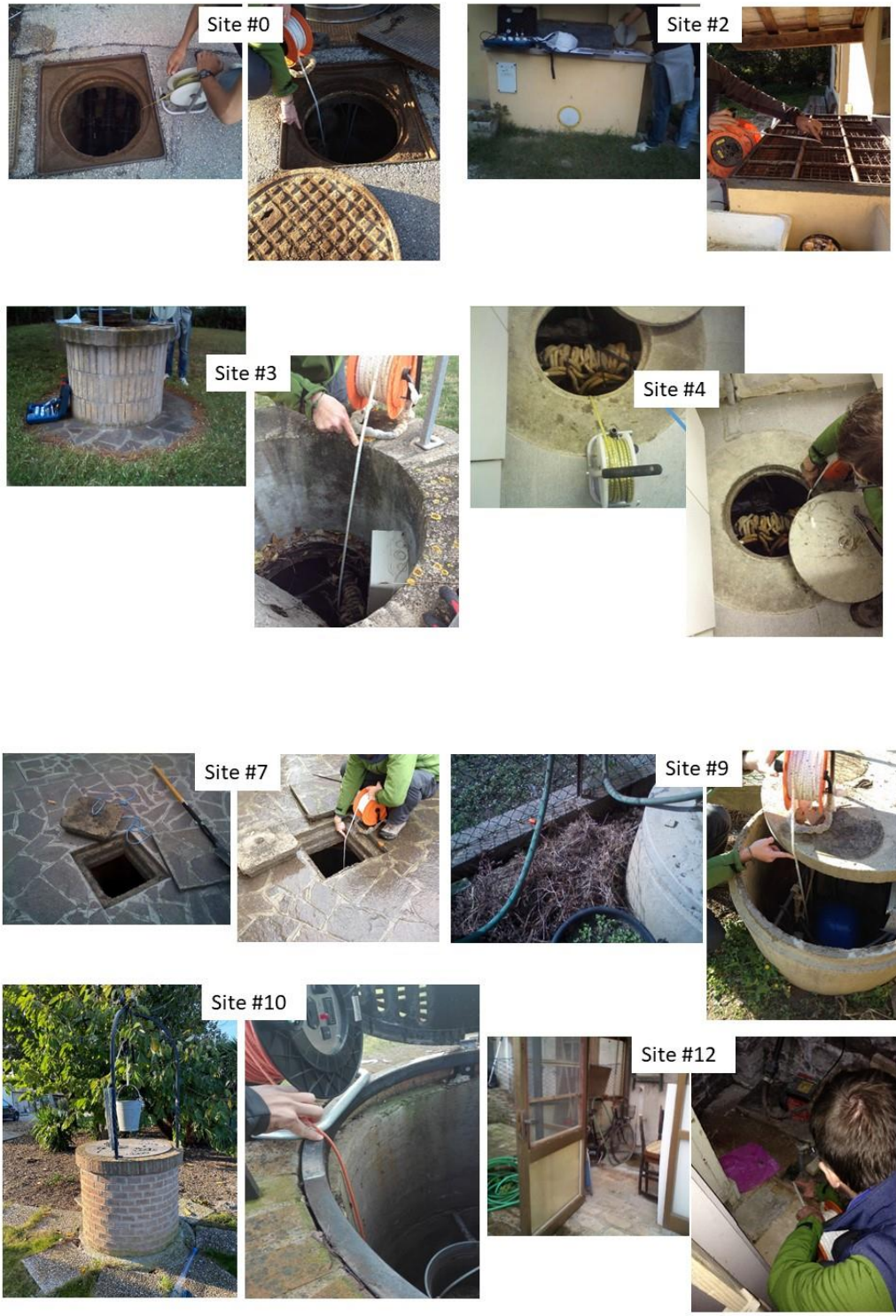

Site #13

Site #14

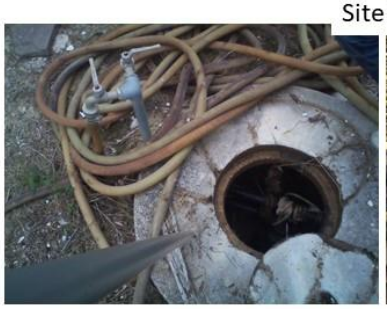

Site #16

Site #17

Site #18

Site #19

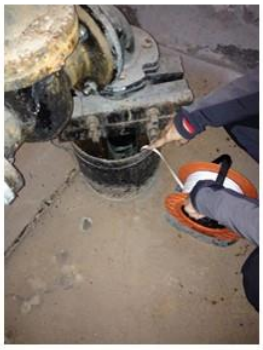

Site #20

Site #21

Site #22

Site #23

Site #24

Site #25

Site #27

Site #28

Site #29

Site #30

Site #34

Site #35

Site #36

Site #37

Site #38

Site #39

DIVER

Site #40

Site #41

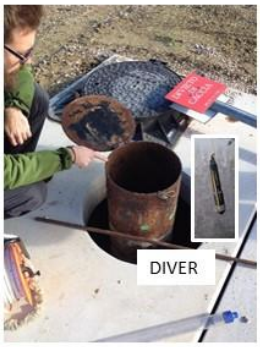

Site #42

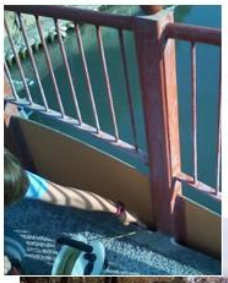

Site #43

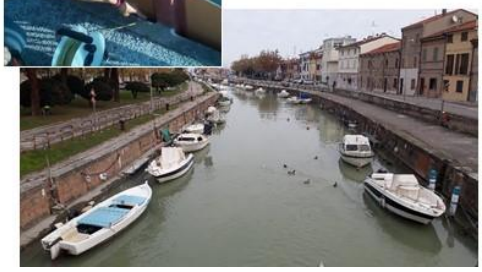

Site #44

Site #45

Site #46

Site #47

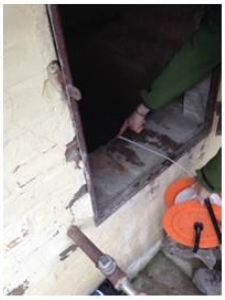

Site #48

Site #49

Site #50

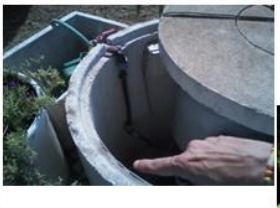

Site #51

Site #52

Site #53

Site #54

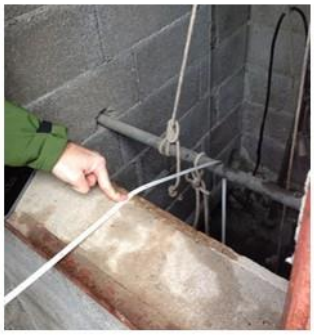

Site #55

A.3. Database 2019-2020: waters data

ID	T	pH	E.C.	Eh	HCO_3	F	Cl	Br	NO_3	NO_2	SO_4	Na	NH_4	K	Mg	Ca	Err.	TDS	$\delta^{18}O\text{-}H_2O$	$\delta^{2}H\text{-}H_2O$
#	°C		µS cm^{-1}	mV	mg/L	mg/L	mg/L	mg/L	mg/L	mg/L	mg/L	mg/L	mg/L	mg/L	mg/L	mg/L	%	mg/L	(V-SMOW)	(V-SMOW)
0	16	7.2	1260	135	370	0.6	95	0.2	91	0.07	121	57	0.04	6.8	29	178	4.57	949	-7.3	-47.8
4	16	7.3	1140	158	410	0.4	40	0.3	55	0.07	75	34	0.05	4.4	22	148	2.31	789	-7.5	-48.8
7	17	7.1	1320	147	501	0.4	77	0.4	51	0.07	102	55	0.04	6.8	41	151	0.59	986	-7.7	-49.3
10	16	7.3	1200	155	416	0.4	55	0.4	42	0.07	109	46	0.06	6.7	25	149	1.50	849	-6.5	-43.4
12	17.5	7.4	1350	110	406	0.4	75	0.4	82	0.07	125	59	0.05	33.9	23	148	-0.05	952	-7.7	-50.0
14	21	7.2	1300	146	465	0.2	71	0.6	61	0.03	93	61	0.05	9.1	25	160	1.63	947	-7.2	-46.6
16	15.5	7.4	1400	152	394	0.5	116	0.4	58	0.07	87	57	0.04	1.8	36	149	1.83	900	-7.5	-49.4
17	17	7.3	1200	164	412	0.3	65	0.6	79	0.03	98	49	0.05	3.6	28	167	3.65	902	-7.3	-47.3
19	16	7.4	1180	324	364	0.5	63	0.5	77	0.10	109	40	0.06	3.3	23	142	-1.83	822	-7.4	-47.9
21	14.8	7.4	1260	169	438	0.5	65	0.4	41	0.07	103	61	0.05	3.6	36	134	2.30	883	-7.6	-50.0
22	15.5	7.3	1100	163	410	0.2	69	0.1	57	0.07	85	56	0.06	3.4	30	140	2.67	851	-7.4	-48.9
24	15.5	6.9	1400	297	439	1.5	95	0.6	48	0.10	111	83	0.06	4.7	31	138	0.78	952	-6.9	-45.0
27	16.8	6.9	1270	321	387	0.6	68	0.5	55	0.16	126	104	0.09	3.5	29	120	4.99	894	-7.1	-45.9
28	16	7.1	1133	340	422	0.2	139	0.4	41	0.07	77	94	0.06	4.2	33	139	2.91	951	-7.5	-48.7
29	16	7.3	1120	310	365	0.4	54	0.1	71	0.07	97	38	0.05	4.9	21	158	3.62	809	-7.4	-48.3
30	16	7.4	960	330	404	<dl	40	<dl	14	0.03	97	27	0.06	1.8	14	140	-3.39	737	-7.8	-50.3
34	21	7.7	670	139	254	<dl	34	<dl	4.7	0.16	70	26	0.15	2.0	16	76	-3.16	482	-8.1	-51.5
35	15	6.9	1200	314	433	<dl	54	0.4	84	0.03	113	45	0.05	2.8	42	136	-0.30	910	-7.5	-49.5
37	15	7.6	740	420	266	<dl	32	0.4	11	0.10	81	29	0.08	3.6	16	97	2.91	536	-8.0	-51.1
38	14	7.7	730	352	261	<dl	28	<dl	5.4	0.07	74	30	0.05	3.6	15	79	-0.81	497	-8.1	-50.8
40	27	7.7	710	158	244	<dl	35	<dl	7.1	1.31	76	28	0.06	2.2	16	83	0.84	493	-7.8	-50.2

Table - 1- June 2019

ID	Al	Sb	As	Ba	B	Co	Cr	Fe	Li	Mn	Ni	Pb	Cu	Rb	Zn	V	SiO_2	Sr
#	µg/L	µg/L	µg/L	µg/L	µg/L	µg/L	µg/L	µg/L	µg/L	µg/L	µg/L	µg/L	µg/L	µg/L	µg/L	µg/L	µg/L	µg/L
0	< 5	0.10	0.20	85.80	185	0.10	4.60	25.0	14.4	< 1	3.30	0.10	1.30	< 1	< 5	0.50	24.0	721.0
4	6.0	0.20	0.30	79.40	137	0.10	1.00	15.0	12.9	< 1	2.20	0.30	4.20	< 1	11.00	0.40	23.0	680.0
7	7.0	0.10	0.20	81.10	133	0.20	3.40	15.0	17.8	< 1	3.00	0.20	3.60	1.51	5.00	0.50	17.0	652.0
10	< 5	0.10	0.20	44.20	165	< 0.1	0.40	5.0	22.9	1.40	2.40	0.10	1.80	< 1	5.00	0.40	22.0	1148.0
12	< 5	0.20	0.70	48.60	254	0.60	1.80	68.0	13.9	4.10	4.90	0.10	1.30	6.08	36.00	1.00	22.0	643.0
14	< 5	0.10	0.20	77.50	188	0.20	0.60	7.0	19.2	< 1	2.00	0.20	9.60	< 1	48.00	0.40	20.0	840.0
16	9.0	0.10	0.20	87.50	131	< 0.1	1.90	9.0	13.0	< 1	1.60	0.40	4.40	< 1	9.00	0.40	15.0	738.0
17	5.0	0.10	0.20	88.00	133	0.20	1.20	7.0	14.5	< 1	2.30	0.10	3.60	< 1	< 5	0.50	22.0	781.0
19	< 5	0.10	0.20	81.90	135	0.10	0.90	106.0	12.8	10.60	1.50	0.10	1.30	< 1	40.00	0.40	23.0	654.0
21	6.0	0.10	0.20	47.90	206	< 0.1	0.50	8.0	30.9	< 1	1.40	0.30	4.90	< 1	7.00	0.40	25.0	969.0
22	< 5	0.10	0.20	88.50	152	0.10	1.00	5.0	13.3	< 1	1.90	0.30	2.40	< 1	9.00	0.40	22.0	731.0
24	< 5	0.10	0.50	66.40	311	< 0.1	0.90	19.0	22.6	13.10	1.30	0.30	1.60	< 1	6.00	0.50	16.0	660.0
27	< 5	0.10	0.20	57.10	393	0.20	0.20	220.0	23.5	74.90	1.80	0.20	1.60	< 1	50.00	0.40	16.0	679.0
28	< 5	0.10	0.20	115.00	292	0.10	0.70	17.0	15.4	< 1	2.60	0.20	2.60	< 1	28.00	0.50	24.0	922.0
29	< 5	0.10	0.20	99.10	130	0.10	0.80	< 5	11.7	< 1	1.40	0.20	1.90	< 1	7.00	0.40	22.0	642.0
30	< 5	0.20	0.20	103.00	104	0.10	0.60	101.0	10.9	10.00	1.70	0.10	2.00	< 1	9.00	0.30	17.0	668.0
34	29.0	0.20	0.60	137.00	125	0.10	0.40	42.0	14.7	7.40	2.40	0.30	2.30	1.01	11.00	0.80	9.0	1084.0
35	< 5	0.10	0.20	68.80	172	0.10	1.10	7.0	14.4	< 1	2.10	0.20	1.80	< 1	31.00	0.40	25.0	712.0
37	6.0	0.20	0.20	67.80	120	< 0.1	0.50	< 5	12.2	< 1	1.30	0.40	1.70	< 1	< 5	0.40	12.0	838.0
38	5.0	0.10	0.20	66.70	123	< 0.1	0.40	11.0	12.7	< 1	1.40	0.10	1.40	< 1	< 5	0.40	13.0	837.0
40	8.0	0.20	0.60	124.00	123	0.20	5.30	38.0	13.8	5.30	4.70	0.30	2.50	1.06	7.00	0.80	10.0	947.0

Table - 1a - June 2019

ID #	T °C	pH	E.C. µS cm^{-1}	Eh mV
0	18	7.3	821	154
2	17	7.5	765	169
3	17.5	7.4	789	315
4	nd	nd	1090	nd
7	18	7.5	235	130
9	17	7.7	852	-106
12	18.5	7.4	853	335
13	nd	nd	1090	nd
14	17	7.3	778	139
17	17	7.4	850	142
18	nd	nd	1170	nd
36	nd	7.4	719	-22
39	nd	nd	770	nd
40	nd	nd	808	nd
41	nd	nd	1079	nd
43	nd	nd	<30000	nd
44	nd	nd	1082	nd
45	nd	nd	1120	nd
46	nd	nd	1340	nd
47	nd	nd	1188	nd
48	nd	nd	1270	nd
49	nd	nd	1328	nd
50	nd	nd	1350	nd
51	nd	nd	2093	nd
52	nd	nd	1068	nd
53	nd	nd	747	nd
54	nd	nd	1106	nd
55	nd	nd	1030	nd

Table - 2- September 2019

ID #	T °C	pH	E.C. µS cm^{-1}
0	15	7.5	787
2	16.5	7.6	752
3	16	7.8	786
4	16	7.5	563
7	16	6.9	198
9	14	7.7	877
10	15.4	7.0	1363
12	17	7.6	824
13	15.8	7.6	554
14	16.5	7.6	774
17	16	7.6	773
18	15	8.3	324
19	15.8	7.5	707
21	17	7.4	663
23	16	7.5	772
24	15.5	7.5	852
27	15	7.3	776
29	16	7.5	690
30	16	7.7	577
34	12	8.1	435
35	15.5	7.4	629
36	15.5	7.6	726
37	19	7.7	474
38	18.5	7.57	513
39	16.5	7.85	540
40	15	8.44	382
41	15	7.63	470
42	11	8.4	312
43	10	8.06	373
44	17	7.12	629
45	15.5	6.92	627
46	16	7.23	724
47	15.5	7.15	656
48	14.5	6.92	686
50	15	6.92	688
51	15	6.99	1141
52	18.5	7.18	607
53	14.3	7.14	891
54	15	7.03	659

Table - 3- December 2019

ID #	T °C	pH	E.C. µS cm^{-1}
0	18.2	7.0	1045
2	16.5	7.0	1017
3	16.1	7.1	1072
4	15.5	7.2	1015
7	16.8	7.2	1062
9	16.1	7.2	1244
10	15.4	6.9	1068
12	17.1	7.0	1271
13	16.5	7.1	887
14	15.8	7.0	1129
17	16.2	7.0	1145
19	15.9	7.0	1028
21	15.6	7.0	1397
23	15.3	7.0	1106
24	15.2	7.2	1883
27	15.5	7.0	1601
29	15.3	7.0	1068
30	16.5	6.95	793
34	20.2	7.35	694
35	15	7.01	1272
36	16.1	7.13	992
37	15.9	7.31	574
38	14.2	7.25	613
39	15.2	7.2	795
40	19.5	8.1	528
41	16.1	7.62	878
42	17.3	8.1	528
43	18.5	8.13	530
44	17.1	7.03	1125
45	16.4	7.08	1119
46	17.1	7.18	1350
47	15.9	7.23	1167
48	16.1	7.1	1316
53	15.5	7.28	652
54	17.8	6.91	1136

Table - 4 - June 2020

ID	T	pH	E.C.	Eh	HCO_3	F	Cl	Br	NO_3	NO_2	SO4	Na	NH_4	K	Mg	Ca	Err.	TDS	$\delta^{18}O\text{-}H_2O$	$\delta^{2}H\text{-}H_2O$
#	°C		µS cm^{-1}	mV	mg/L	mg/L	mg/L	mg/L	mg/L	mg/L	mg/L	mg/L	mg/L	mg/L	mg/L	mg/L	%	mg/L	(V-SMOW)	(V-SMOW)
0	17.5	7.2	602	91	383	0.6	78	0.3	78	0.030	110	57	0.03	3.7	30	140	-0.30	879	-7.3	-47.8
2	17.1	7.3	1088	nd																
3	17.1	7.0	1283	nd																
4	17.4	7.4	1086	187	429	0.5	55	0.3	47	0.013	83	40	0.04	4.4	27	137	-0.83	824	-7.4	-49.5
7	17.0	7.0	633	213	486	0.8	81	0.2	52	0.522	96	54	0.10	8.5	39	139	-1.54	957	-7.2	-46.6
10	17.0	7.2	1146	177	411	0.6	65	0.3	45	0.016	131	50	0.04	8.3	29	160	2.98	900	-6.5	-45.7
12	18.2	7.2	1213	nd	383	1.2	83	0.4	84	0.030	146	62	0.05	36.8	26	154	1.31	974	-7.6	-50.1
13	17.3	7.3	891	nd																
14	23.0	7.2	702	147	447	0.4	100	0.4	59	0.013	126	78	0.05	9.1	37	155	2.31	1011	-7.2	-46.6
16	16.5	7.4	1382	130	405	1.4	164	0.6	50	0.020	103	81	0.06	3.1	41	164	2.93	1013	-7.5	-49.7
17	17.4	7.1	1149	119	417	0.8	74	0.5	77	0.016	124	49	0.03	4.4	29	160	-0.58	936	-7.2	-48.8
18	17.0	8.3	565	-4	204	0.1	51	0.2	2	0.013	15	53	0.23	5.0	19	23	-0.34	373	-7.2	-47.8
19	16.6	7.2	1031	7.6	356	0.7	66	0.4	53	0.033	92	45	0.03	4.0	25	143	3.43	785	-7.4	-49.5
21	17.3	7.2	1280	203	464	1.1	103	0.5	39	0.033	131	80	0.03	5.7	42	141	0.73	1006	-7.6	-50.4
22	20.0	7.6	619	132	417	0.3	72	0.3	60	0.016	82	59	0.05	4.0	32	143	3.48	869	-7.4	-49.3
23	15.8	7.2	1132	136	422	0.6	58	0.3	78	0.033	129	47	0.04	3.6	46	138	1.03	921	-7.6	-53.5
24	15.7	7.3	1345	184	458	0.7	115	0.5	50.8	0.046	131	111	0.05	7.8	38	140	2.54	1052	-6.9	-47.1
25	26.4	9.1	585	nd																
27	16.0	7.4	829	115	393	0.6	91	0.4	81	0.013	143	70	0.03	8.6	30	155	0.66	972	-7.1	-46.7
28	16.8	7.2	1301	132	421	0.92	116	0.58	52	0.020	91	86	0.04	4.5	34	145	3.49	950	-7.5	-48.3
29	15.9	7.2	530	195	366	0.34	49	0.32	58.4	0.010	79	41	0.01	3.0	23	139	3.19	758	-7.3	-49.3
30	16.5	7.2	898	113	384	0.57	53	0.3	15	0.013	68	41	0.03	4.0	20	133	3.33	719	-7.3	-49.7
34	22.0	7.6	404	137	237	0.56	59	0.4	2	0.026	104	41	0.04	4.1	21	94	3.24	562	-6.7	-44.4
35	16.3	7.2	1177	137	437	0.56	67	0.26	78.8	0.020	143	48	0.05	3.0	45	145	-0.89	968	-7.5	-48.6
36	16.2	7.47	1010	105																
37	18.2	7.5	704	134	233	0.35	44	0.27	2.1	0.013	78	33	0.01	3.7	18	83	2.59	495	-6.8	-44.5
38	16.5	7.5	359	148	244	0.38	43	0.31	1.35	0.013	76	30	0.04	2.6	19	89	3.49	505	-6.9	-47.5
39	17.2	7.42	780	56																
40	21.8	7.7	796	nd	244	0.44	68	0.28	7.6	0.010	98	49	0.05	6.3	20	83	-0.20	577	-5.9	-42.6
41	19.3	7.79	734	-170																
42	23.4	8.0	774	nd	233	0.5	62	0.25	2.5	0.020	116	42	0.06	5.4	20	88	-0.47	569	-6.8	-45.0
43	23	8.2	7400	nd																
44	17.7	7.1	1304	nd	433	0.78	134	0.37	64.2	0.030	136	80	0.04	5.0	30	166	-1.48	1050	-7.3	-47.8
45	18.8	7.18	1149	190																
49	17.6	7.2	1882	nd	486	0.33	340	1	6.1	0.069	167	186	0.06	6.8	55	153	-1.71	1401	-7.3	-47.5
50	17.0	7.1	1176	nd	458	0.89	83	0.4	73.1	0.020	122	57	0.08	3.6	41	151	-0.56	989	-7.3	-48.9
51	16.6	7.01	2170	nd																
52	19	7.1	1370	nd																
54	16.6	7.01	1129	nd																

Table - 5 - September 2020

ID	Al	Sb	As	Ba	B	Co	Cr	Fe	Li	Mn	Ni	Pb	Cu	Rb	Zn	V	SiO_2	Sr
#	µg/L	µg/L	µg/L	µg/L	µg/L	µg/L	µg/L	µg/L	µg/L	µg/L	µg/L	µg/L	µg/L	µg/L	µg/L	µg/L	µg/L	µg/L
0	< 5	0.10	nd	93.0	116.0	0.10	0.80	8.00	11.70	0.60	4.00	0.20	1.10	0.48	10.00	0.40	24.60	718.0
4	< 5	0.10	0.20	92.6	98.0	0.10	0.50	6.00	11.60	0.80	2.10	0.20	6.80	0.59	20.00	0.30	24.00	727.0
7	< 5	0.10	0.20	85.9	87.0	0.20	2.30	7.00	13.10	1.20	3.40	0.30	23.50	2.07	6.00	0.60	15.70	553.0
10	< 5	0.10	0.20	49.7	145.0	< 0.1	0.30	< 5	22.60	0.90	2.70	0.20	2.20	0.49	16.00	0.30	24.00	1081.0
12	7	0.20	0.70	53.1	184.0	0.40	2.00	58.00	10.50	2.00	3.50	0.30	13.10	7.60	20.00	0.90	23.10	599.0
14	< 5	0.10	0.30	82.8	282.0	0.40	0.40	< 5	24.40	1.10	3.90	0.20	6.40	1.96	179.00	0.40	16.40	763.0
16	5.0	0.10	0.10	98.4	89.0	0.10	1.80	20.00	11.00	0.70	1.80	0.20	2.70	0.89	10.00	0.40	15.60	751.0
17	< 5	0.20	0.20	92.1	93.0	0.10	0.90	6.00	9.70	0.70	1.50	0.10	1.10	0.66	6.00	0.30	23.50	646.0
18	< 5	< 0.1	0.10	15.1	73.0	< 0.1	0.10	8.00	8.20	123.00	1.00	0.10	0.70	2.01	< 5	< 0.1	1.45	122.0
19	< 5	0.10	0.10	88.6	90.0	0.20	0.50	1562.00	10.30	47.80	2.30	0.10	1.70	0.43	64.00	0.30	24.20	607.0
21	< 5	0.10	0.20	59.1	169.0	< 0.1	0.50	< 5	28.70	0.20	1.10	0.20	2.30	0.79	12.00	0.20	28.00	947.0
22	7	0.10	0.10	102.0	104.0	0.10	1.20	7.00	13.00	0.60	2.30	0.20	1.10	4.12	15.00	0.30	23.30	715.0
23	24	0.10	0.20	63.3	119.0	0.10	1.30	12.00	12.90	0.70	1.20	0.20	2.10	0.40	8.00	0.30	26.70	691.0
24	5	0.10	0.60	75.7	270.0	< 0.1	0.90	8.00	24.30	5.40	1.70	0.10	1.30	0.71	14.00	0.30	17.20	659.0
27	< 5	0.10	0.20	71.6	161.0	0.10	1.00	8.00	17.60	5.50	1.70	0.30	1.00	0.45	132.00	0.30	19.90	621.0
28	< 5	0.10	0.20	115.0	173.0	0.10	0.70	7.00	12.40	1.20	1.70	0.10	1.10	0.61	27.00	0.30	25.00	825.0
29	< 5	0.10	0.20	108.0	86.0	0.10	0.80	< 5	9.70	0.20	1.50	1.40	1.70	0.45	23.00	0.30	24.80	607.0
30	< 5	0.10	0.10	103.0	88.0	0.10	0.40	98.00	10.80	14.00	1.40	0.10	1.20	0.45	10.00	0.20	21.60	704.0
34	6.0	0.30	1.00	170.0	112.0	0.10	0.30	8.00	11.80	3.70	2.50	0.20	2.80	1.41	11.00	0.80	14.20	1041.0
35	< 5	0.10	0.20	74.8	125.0	0.10	1.20	13.00	12.70	0.60	1.60	0.10	1.20	0.40	20.00	0.40	27.00	687.0
37	< 5	0.20	0.20	81.4	105.0	0.10	0.20	9.00	11.90	0.90	0.90	0.10	1.70	0.53	10.00	0.30	15.80	775.0
38	6.0	0.10	0.20	79.9	96.0	< 0.1	0.20	18.00	10.80	0.80	0.90	0.20	1.80	0.38	10.00	0.20	14.40	781.0
40	8	0.30	1.20	137.0	139.0	0.4	0.2	10.00	13.00	26.6	4.4	0.2	1.5	1.65	12.00	0.90	16.10	861
42	6	0.30	1.20	177.0	117.0	0.1	0.1	9.00	11.80	8.4	2.5	0.2	1.1	1.39	13.00	0.70	14.20	1077
44	6	0.10	0.20	101.0	146.0	0.4	1.4	9.00	9.80	0.4	2.6	0.2	4.7	0.72	27.00	0.40	17.40	601
49	6	0.60	1.00	140.0	151.0	1	0.2	13.00	24.00	122	6.5	0.2	3.5	1.33	31.00	0.60	20.70	1077
50	8	0.10	0.10	85.1	101.0	< 0.1	1.8	17.00	10.80	0.9	1.6	0.4	5.7	0.501	19.00	0.30	18.90	579

Table 5a - September 2020

ID	T	pH	E.C.	Eh	HCO_3	F	Cl	Br	NO_3	NO_2	SO4	Na	NH_4	K	Mg	Ca	Err.	TDS	$\delta^{18}O\text{-}H_2O$	$\delta^{2}H\text{-}H_2O$
#	°C		µS cm^{-1}	mV	mg/L	mg/L	mg/L	mg/L	mg/L	mg/L	mg/L	mg/L	mg/L	mg/L	mg/L	mg/L	%	mg/L	(V-SMOW)	(V-SMOW)
0	16.1	7.1	1284	nd	387	0.2	96	0.4	103	0.016	96	62	0.03	4.2	32	149	0.77	930	-7.4	-47.8
2	16.1	7.0	1005	nd																
3	14.9	7.1	1019	nd																
4	14.6	7.3	1022	nd	421	0.2	60	0.3	62	0.023	73	40	0.15	3.8	26	159	3.46	845	-7.5	-49.0
7	15.8	7.3	1055	nd	434	0.2	63	0.2	43	0.020	62	55	0.06	8.0	37	109	0.88	812	-7.7	-48.7
9	15.2	7.3	1323	-11																
10	15.4	7.2	1105	-5	403	0.3	59	0.3	43	0.020	103	48	0.22	5.8	27	153	4.24	842	-6.6	-44.0
12	16.5	7.1	1235	nd	366	0.3	84	0.3	102	0.026	100	62	0.06	34.0	25	150	3.95	924	-7.7	-49.9
13	16.0	6.8	854	nd																
14	11.2	7.5	1393	-20	434	0.3	135	0.6	89	0.020	149	88	0.12	10.5	40	168	0.78	1114	-7.1	-46.3
16	14.7	7.4	1378	-14	400	0.3	180	0.7	45	0.036	79	82	0.08	3.7	41	160	3.42	992	-7.5	-48.2
17	15.5	7.2	1223	nd	407	0.4	67	0.3	100	0.026	85	49	0.06	6.9	30	160	3.15	905	-7.4	-46.9
18	15.0	8.6	578	-8	205	0.5	47	0.2	1	0.020	6	60	0.08	5.0	22	7.0	0.54	353	-7.2	-44.4
19	14.1	7.5	1034	-22	346	0.4	67	0.4	62	0.026	100	45	0.14	3.9	26	143	2.90	794	-7.5	-48.0
21	16.5	7.2	1207	-4	417	0.5	105	0.7	51	0.016	105	77	0.17	5.7	40	134	2.31	935	-7.6	-48.2
22	15.6	7.4	1157	-17	418	0.3	67	0.3	59	0.020	66	62	0.28	5.0	34	103	-1.47	816	-7.4	-47.9
23	14.8	7.3	1125	-8	425	0.3	55	0.4	100	0.013	105	48	0.09	5.0	47	138	2.39	922	-7.6	-48.1
24	14.9	7.5	1840	-23	565	0.3	211	0.8	19	0.079	155	244	0.94	15.0	50	96	2.99	1357	-7.2	-45.3
25	11.1	7.9	567	nd																
27	14.7	7.3	1535	-11	406	0.2	172	0.8	72	0.020	109	125	0.39	7.7	33	157	3.99	1083	-7.3	-47.3
28	16.6	7.2	1267	-4	430	0.17	110	0.54	47	0.016	62	83	0.06	4.5	32	140	4.40	910	-7.4	-46.6
29	15.4	7.3	980	-7	364	0.2	71	0.37	60.3	0.013	82	41	0.04	3.8	22	140	0.28	785	-7.4	-46.7
30	15.3	7.0	811	4.8	387	0.16	37	0.3	10	0.016	53	31	0.09	3.0	17	128	2.83	666	-7.3	-47.1
34	8.8	8.2	639	-58	402	0.28	21	0.2	3	0.030	52	24	0.09	2.8	19	98	-4.73	622	-7.5	-46.9
35	14.9	7.2	1155	-6	425	0.26	60	0.43	104.0	0.020	107	49	0.05	4.5	45	142	1.55	936	-7.5	-49.0
36	13.1	7.4	934	nd																
37	17.6	7.6	673	-29	231	0.3	44	0.32	2.2	0.013	97	34	0.04	3.3	18	84	0.52	512	-7.3	-46.9
38	18.2	7.6	681	-27	238	0.29	38	0.34	0.1	0.013	72	34	0.05	3.9	17	82	4.00	485	-7.3	-47.1
39 Top	13.7	7.3	856	-10	323	0.27	41	0.22	2.2	0.016	78	37	0.06	2.5	20	109	3.64	613	-7.3	-45.7
39 Bottom	12.5	6.9	2965	nd	31	0.8	915	3.9	0.4	0.036	13	195	7.10	12.0	43	272	-0.69	1493	-7.4	-47.0
40	7.8	8.2	617	19	292	0.16	19	0.03	1.77	0.016	59	23	0.08	3.5	17	92	3.54	507	-7.4	-47.0
41	14.9	7.3	761	-9																
42	8.5	8.4	624	20	283	0.5	20	0.06	1.9	0.020	54	21	0.09	3.5	17	90	3.96	491	-7.6	-47.4
43	7.8	8.0	627	25	300	0.6	31	0.09	3.8	0.030	75	24	0.08	3.4	18	94	-0.76	551	-7.6	-46.3
44	16.6	7.1	1215	nd	404	0.22	126	0.5	73	0.013	85	76	0.04	6.8	29	160	2.54	960	-7.7	-48.7
45	14.1	7.17	1263	nd																
46	14.6	7.22	1334	nd																
47	14.4	7.1	1184	nd																
48	14.8	7	1401	nd																
49	11.6	7.2	2110	nd	494	0.24	472	3	1.8	0.016	117	265	0.40	8.2	64	159	2.10	1585	-7.5	-47.8
50	14.5	7.2	1231	nd	461	0.28	82	0.45	63.4	0.013	88	62	0.03	3.1	42	151	3.66	953	-7.4	-48.1
51	14.4	7	2020	nd																
52	17.1	7.33	1044	nd																
53	14	7.38	740	nd																
54	14.3	6.73	1263	nd																

Table - 6 - November 2020

ID	Al	Sb	As	Ba	B	Co	Cr	Fe	Li	Mn	Ni	Pb	Cu	Rb	Zn	V	SiO_2	Sr
#	µg/L	µg/L	µg/L	µg/L	µg/L	µg/L	µg/L	µg/L	µg/L	µg/L	µg/L	µg/L	µg/L	µg/L	µg/L	µg/L	mg/L	µg/L
0	7	<0.1	0.40	94.7	104.0	0.50	0.90	35.00	7.80	2.90	9.40	0.20	3.00	<1	17.00	0.10	25.00	399.0
4	<5	<0.1	0.40	82.4	87.0	0.70	0.40	27.00	7.40	<1	6.60	0.40	4.60	<1	17.00	<0.1	24.20	402.0
7	<5	<0.1	0.40	71.0	78.0	0.70	2.10	27.00	8.30	1.90	8.70	0.80	19.90	1.80	74.00	0.30	14.60	288.0
10	<5	<0.1	0.40	41.6	107.0	0.60	0.30	24.00	12.20	<1	5.70	<0.1	1.50	<1	5.00	<0.1	24.40	576.0
12	<5	0.20	0.90	43.7	123.0	0.90	1.80	37.00	6.50	<1	7.90	0.30	1.80	7.40	6.00	0.70	23.10	337.0
14	<5	0.10	0.50	74.1	256.0	0.90	0.40	19.00	20.10	<1	7.50	1.00	71.90	2.30	612.00	0.20	16.50	450.0
16	8.0	<0.1	0.40	89.4	93.0	0.40	1.20	134.00	8.70	1.30	4.80	0.20	3.70	<1	17.00	0.30	15.60	429.0
17	<5	0.60	0.40	81.0	90.0	0.60	0.90	27.00	6.50	<1	6.40	0.10	1.60	<1	7.00	0.20	22.90	363.0
18	<5	<0.1	<0.1	10.2	79.0	<0.1	0.10	10.00	7.70	77.30	1.40	<0.1	0.80	1.90	<5	<0.1	1.00	53.0
19	<5	<0.1	0.20	77.4	84.0	0.40	0.40	498.00	8.10	19.10	3.80	0.10	1.50	<1	43.00	<0.1	23.30	355.0
21	<5	<0.1	0.30	54.2	140.0	0.20	0.30	19.00	23.90	<1	2.80	0.20	1.90	<1	6.00	<0.1	27.00	545.0
22	<5	<0.1	0.20	99.1	93.0	0.30	0.70	13.00	14.90	<1	3.00	0.20	1.30	6.20	16.00	<0.1	22.20	457.0
23	<5	<0.1	0.20	60.9	104.0	0.20	1.00	14.00	13.20	<1	2.40	<0.1	0.90	<1	<5	<0.1	24.80	444.0
24	<5	<0.1	1.30	67.2	590.0	0.20	0.30	15.00	52.60	23.30	2.40	0.10	2.80	1.70	11.00	0.30	14.90	490.0
27	<5	<0.1	0.30	74.2	272.0	0.30	0.60	101.00	23.10	25.20	3.00	0.30	0.70	<1	110.00	0.10	19.00	463.0
28	<5	<0.1	0.30	106.0	154.0	0.30	0.40	12.00	13.30	<1	3.30	<0.1	0.70	<1	31.00	<0.1	24.00	514.0
29	<5	<0.1	0.20	105.0	87.0	0.20	0.60	12.00	11.30	<1	3.10	0.50	1.10	<1	14.00	<0.1	22.90	400.0
30	<5	<0.1	0.10	93.3	69.0	0.20	0.20	80.00	10.50	9.40	2.50	0.60	2.70	<1	9.00	<0.1	16.50	422.0
34	<5	0.10	0.30	115.0	58.0	0.20	<0.1	21.00	10.00	4.40	2.40	<0.1	1.20	<1	<5	<0.1	8.30	539.0
35	<5	<0.1	0.20	76.6	114.0	0.20	0.80	12.00	14.10	<1	3.00	0.10	1.20	<1	18.00	<0.1	25.50	462.0
37	<5	0.10	0.10	78.6	88.0	0.10	<0.1	9.00	12.40	1.20	1.40	<0.1	1.00	<1	7.00	<0.1	14.90	478.0
38	<5	0.10	0.10	79.6	92.0	0.10	<0.1	8.00	13.20	<1	1.40	<0.1	0.90	<1	<5	<0.1	14.60	518.0
39 top	<5	0.10	0.10	60.9	102.0	0.2	0.1	11.00	12.00	1.3	2	<0.1	1.5	<1	19.00	<0.1	13.70	441
39 bott	<5	<0.1	0.50	1289.0	82.0	1.2	<0.1	58100.00	21.90	250	2.6	<0.1	0.4	1.5	<5	0.90	2.80	1430
40	<5	0.10	0.30	114.0	63.0	0.2	0.3	32.00	10.70	4	2.3	0.3	1.1	<1	9.00	<0.1	8.20	539
42	<5	0.10	0.30	110.0	60.0	0.2	0.1	11.00	10.70	3.5	2.2	<0.1	0.8	<1	<5	<0.1	8.00	540
43	<5	0.10	0.30	111.0	64.0	0.2	<0.1	13.00	10.20	3.9	2.5	<0.1	0.9	<1	24.00	<0.1	8.20	531
44	<5	<0.1	0.20	72.6	116.0	0.7	0.8	11.00	10.20	<1	3.2	0.3	2	<1	17.00	<0.1	15.40	363
49	<5	0.40	1.00	255.0	140.0	0.8	<0.1	27.00	29.60	95.3	4.9	0.2	3.2	1.8	20.00	0.60	19.50	910
50	<5	<0.1	0.10	86.0	101.0	0.2	1.2	14.00	13.00	<1	2.5	0.4	7.1	<1	21.00	<0.1	17.80	411

Table 6a - November 2020

3. PILOT AREA: RAVENNA COASTAL SYSTEM

3.1 Study area

The study area is located along the Ravenna coastal system in the Northern Adriatic Sea (Italy). It comprises a 7 km wide strip of land parallel to the coast and extends for about 56 km^2 (Fig. 3.1a).

This coastal plain is connected to the north with the Po alluvial plain and is bordered to the south and to the west by the Apennines, a mountain chain of Late Alpine age (e.g. Rizzini, 1974). From east to west, the studied area is characterized by a narrow beach with coastal dunes that have been formed since 1690s and currently covered by a pine forest planted at the beginning of last century, and a beach town (Marina Romea, Fig. 3.1a; Mollema et al., 2013). Further to the west, there is Pialassa Baiona, a saltwater lagoon that is connected to the Adriatic Sea. An older dune belt, covered by the San Vitale Pine Forest, is located on the western edge of the Pialassa Baiona Lagoon (Amorosi et al., 1999) (Fig. 3.1a). The San Vitale pine forest represents a historical landmark of the Po river plain. It is surrounded by the urban area of Ravenna, industrial infrastructures and waterworks of the agricultural drainage system. From the western edge of the San Vitale Pine Forest up to the Apennine belt, about 40 km away, most land is used for agricultural practices. The surface hydrographic system includes the course of the Lamone river and a complex system of drainage channels that are regulated by drainage-pumping machines.

To the NW of the San Vitale Pine Forest, there is a hydrophilic forest, a sort of freshwater swamp forest or flooded forest (Punte Alberete) that is artificially maintained with fresh water supplied by the Lamone river. Inside the Punte Alberete, a lagoon consisting of two ponds separated by a tiny strip of land occurs. The ponds are also constantly filled with fresh waters from the Lamone river (Antonellini et al., 2010).

In order to characterize the phreatic aquifer, a schematic stratigraphic section of the shallow coastal aquifer is reported in Fig. 3.1b. From east to west, the main sedimentary packages consist of a wedge of fine-grained (fine sand to silty clays) sediments, deposited in shallow marine water, littoral sands formed in the foreshore, deep-shore, and in the adjacent beach

sand dune environments; clay backshore lagoon deposits are also present in the westernmost area (Bondesan et al. 1995, Amorosi et al. 2002). Some continental alluvial deposits (mostly clay and silt) are underlying the littoral sands (to the west) and the lagoon deposits. The coastal phreatic aquifer is primarily located within the littoral sands and, locally, in the shallow marine wedge deposits. The coastal aquifer is unconfined to the east, although at 3–4 km from the coast it is overlain and confined by the most recent alluvial fine-grained continental deposits. The thickness of the aquifer (Fig. 3.1b) varies from 8 to 30 m (Amorosi et al. 2002).

In the Ravenna coastal area, the study area was selected on the basis of previous works and related to a small portion of the local shallow aquifer (up to 5-25 m depth), already strongly affected by sea intrusion (Fig. 3.1b).

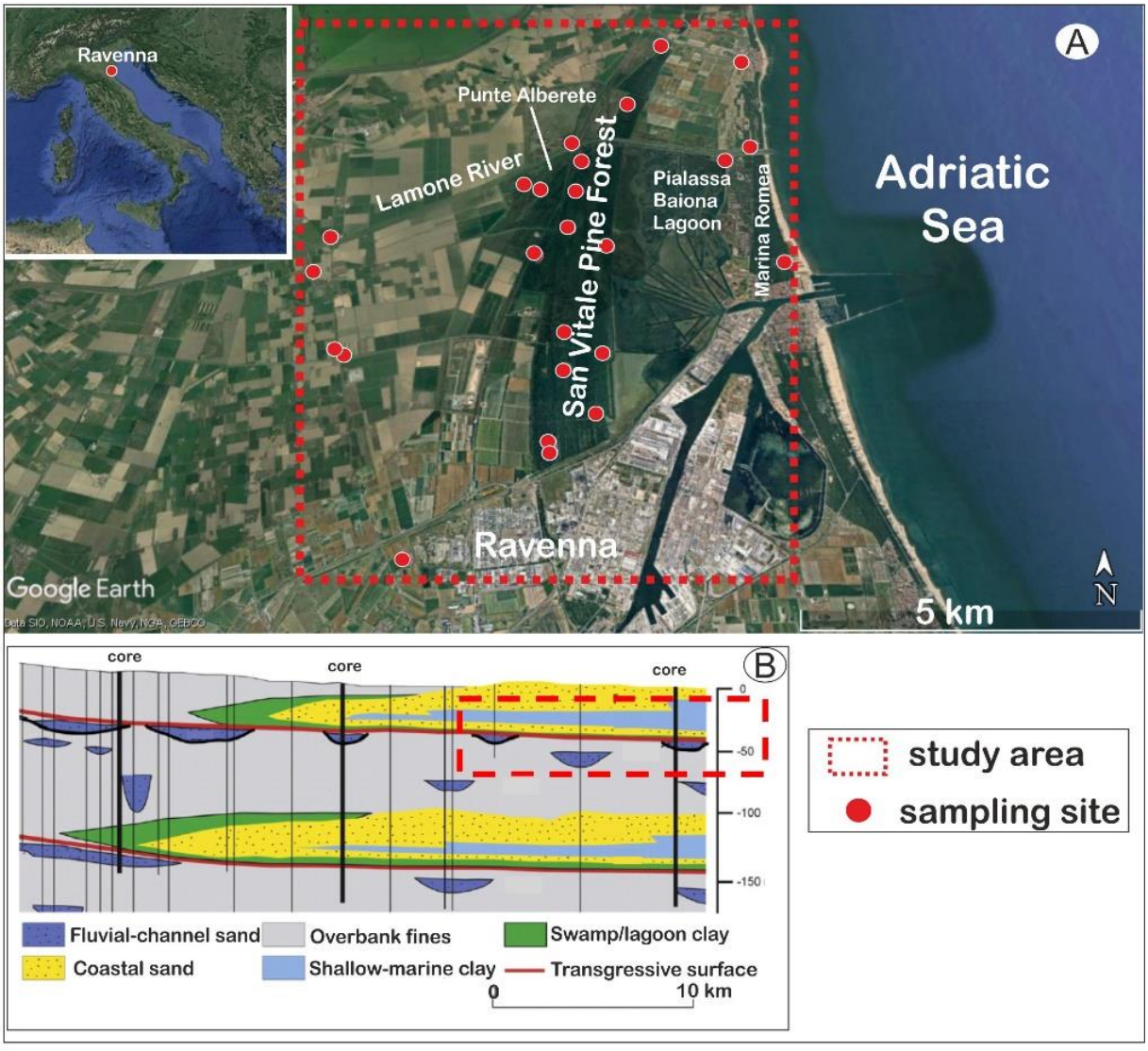

Fig. 3.1 a) Location of the study area and sampling sites; b) Schematic stratigraphic section of the phreatic coastal aquifer (modified after Campo et al., 2017)

3.2 Materials and methods

3.2.1 Sampling strategy

The sampling sites were selected according to previous monitoring networks (C.S.I.-Ra Project 2009; Giambastiani, 2007; Giambastiani et al., 2007; Antonellini and Mollema, 2010; Laghi et al., 2010; Laghi, 2010; Capo, 2011; Mollema et al., 2013; Vandenbohede et al., 2014). In particular, most sites were homogeneously distributed in the area of Pineta San Vitale (north of Ravenna), although a limited number of sampling points were selected more inland and near the coast (Fig. 3.2). The monitoring network established in the present project was consisting of 24 sites. Waters were thus collected from piezometers (#1, #2, #3, #4, #5, #6, #7, #8, #9, #10, #11, #12, #14, #16, #17, #19, #20, #21) and surface water bodies (Baiona lagoon: #13; channels: #15, #18 and Lamone river: #23, #24 and #25).

For each site, X-Y coordinates and elevation were recorded with a high precision Leica GPS. Nevertheless, because of the scarcity or lack of internet connection, altitude resulted to be affected by a significant error for some sites (see Table 1 in the Appendix). In order to highlight possible hydrological and geochemical differences due to the influence of different climatic conditions, three surveys (July 2019, September 2020 and November 2020) were carried out during which water sampling (for water chemistry and water isotope analyses), physicochemical parameters and water level measurements and vertical physicochemical logs were performed. In those sites where the vertical profiles evidenced significant water electrical conductivity (EC) stratification, two water samples were collected at different depths (Fig. 3.2). Since July 2019, periodical surveys (July 2019, December 2019, July 2020, September 2020 and November 2020) for water level, temperature, pH, EC and vertical physicochemical logs were focused on specific sites (#20, #11, #23, #10, #14, #19 and #21, #5, #4, #17, #18), arranged along two main transects and orthogonal to the coastline (Fig. 3.2).

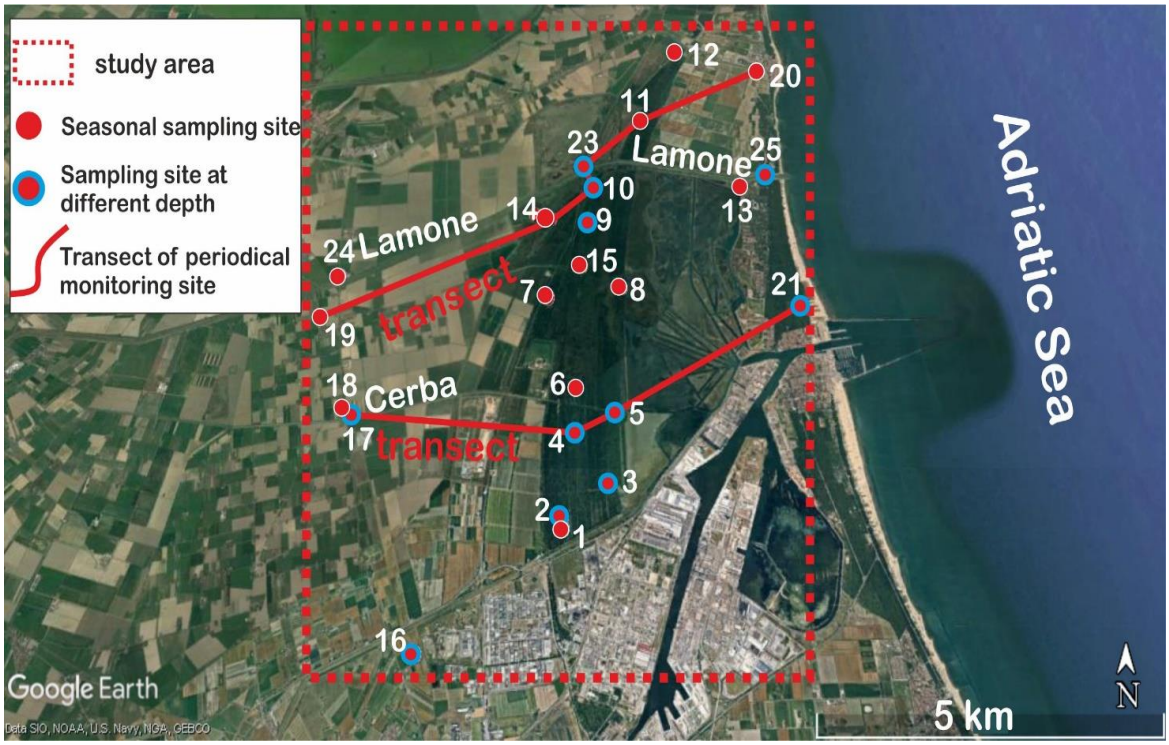

Fig. 3.2 Location of the study area. The sampling sites and monitoring transects are also reported.

The measuring and sampling activity can be summarized, as follows:

- 23-24-25 July 2019 – water sampling, piezometric and physicochemical measurements and vertical physicochemical log;
- 3-4 December 2019 – piezometric and physicochemical measurements and vertical physicochemical log;
- 23-24 July 2020 – piezometric and physicochemical measurements and vertical physicochemical log;
- 15-16-17 and 25 September 2020 – water sampling, piezometric and physicochemical measurements and vertical physicochemical log;
- From 23 to 27 November 2020 – water sampling, piezometric and physicochemical measurements and vertical physicochemical log;

With respect to the rainfall regime (Fig. 3.3), the sampling sessions were representative of dry (July and September 2020), wet (December 2019) and intermediate (July 2019 and November 2020) hydrological conditions.

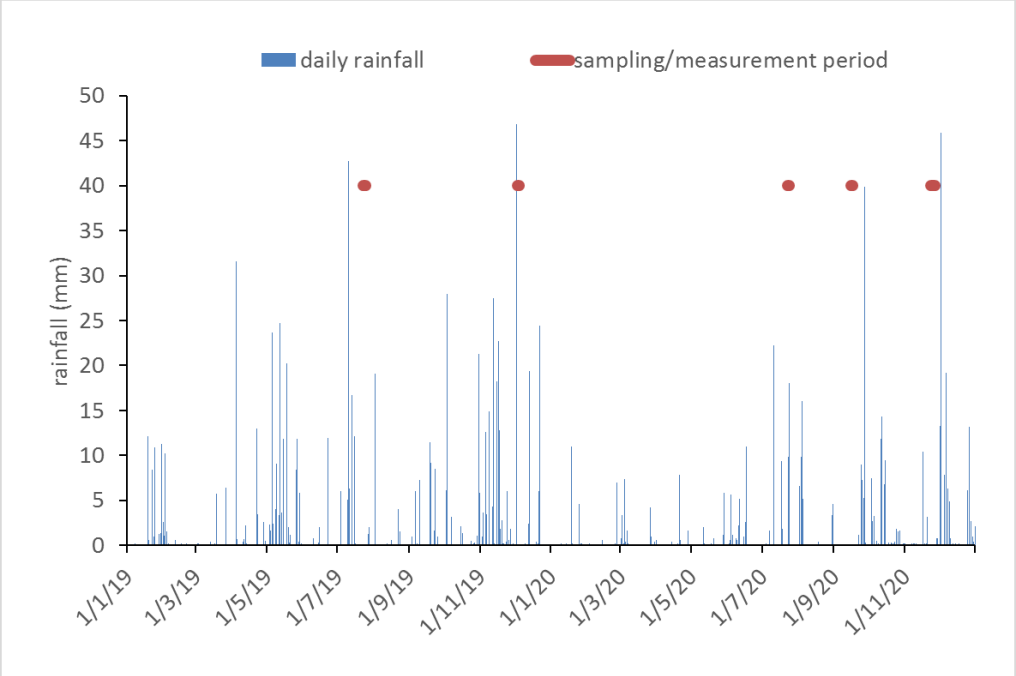

Fig. 3.3 Daily rainfall and periods of field activities (rainfall data refer to Marina di Ravenna and Ravenna Urbana monitoring stations; Arpae-SIMC, https://www.arpae.it)

3.2.2 Water sampling surveys: physicochemical parameters, chemical and isotopic analyses

The physicochemical parameters (temperature, pH, EC and oxidation-reduction potential) were determined in situ with a Hanna HI98194 multi-probe (Fig. 3.4). Waters from piezometers and streams were collected by using a low-flow pump connected to a 12V battery. Before the groundwater sampling, each piezometer was purged. Physical-chemical vertical logs were performed by a CTD-Diver (conductivity-temperature-depth[pressure] probe by Schlumberger Water Services) in order to verify possible water stratification in terms of salinity and choose whether water samples at different depths for the same site were to be collected.

Fig. 3.4 Different stages of water sampling

For most campaigns, piezometer purging was carried out by low or medium flow pumps (10 to 50 L/min) for at least 10-15 minutes to ensure that a total water volume equal or higher than twice the volume from the piezometric tubing was purged. With the aim to verify the correct hydraulic performance of piezometers, especially for those located in zones of the aquifer apparently interested by abundant silty-clayey materials, in the last campaign purging was performed by a professional company entrusted by the Ravenna Municipality. In this case, airlift techniques and more performant pumps were used (Fig. 2.4).

For the chemical and isotopic analyses, four aliquots were collected at each site, as follows:

1. 125 mL of filtered (at 0.45 µm) water where the main anions (HCO_3^-, Cl^-, SO_4^{2-}, F^-, Br^-, NO_3^-) and NH_4^+ were measured;
2. 50 mL of filtered (at 0.45 µm) water acidified with 0.5 mL of HCl suprapur for the analysis of the main cations (Na^+, K^+, Mg^{2+}, Ca^{2+});
3. 50 mL of filtered (at 0.45 µm) water acidified with HNO_3 suprapur for the analysis of trace elements (Al, Sb, As, Ba, B, Li, Rb, V, SiO_2, Sr);
4. 125 mL of unfiltered water for the analysis of the water isotopes.

Fig. 3.5 Piezometer purging during the November 2020 field work.

The main cations and anions (with the exception of HCO_3^-) were analyzed at the CNR-IGG (Unit of Florence) by ion chromatography (861 Advanced Compact IC-Metrohm and 761 Compact IC-Metrohm). HCO_3^- was analyzed within 24h from sampling by acidimetric titration using a Multi Dosimat 645-Metrohm; the titrating solution was 0.01 N HCl and methyl-orange was used as an indicator. Ammonium was determined by colorimetry according to the Nessler method by using a HACH DR2000 molecular spectrophotometer. Trace elements (Al, Sb, As, Ba, B, Li, Rb, V, SiO_2, Sr) were analyzed by ICP-MS (Method: EPA 6020B 2014) at the CSA Research Group of Rimini (Italy). The analytical errors were <5% and 10% for the main ions and trace elements, respectively. The oxygen and hydrogen stable isotopes (expressed as $\delta^{18}O$ ‰ vs. V-SMOW and δD ‰ vs. V-SMOW, respectively) were determined by IRMS (Isotope Mass Ratio Spectrometry) at the CNR-IGG of Pisa and University of Parma (Italy) with an automatic preparation line coupled with a Finnigan MAT Delta Plus dual collector mass spectrometer. The oxygen isotopic composition was determined by equilibration with CO_2 while that of hydrogen (deuterium) was analyzed by using platinum as a catalyst. International (V-SMOW, GISP and SLAP) and internal standards were periodically analyzed. The standard deviation was ±0.08 to ±0.12‰ (2σ) for oxygen and ±1.0 to ±2.0‰ (2σ) for hydrogen (Longinelli and Selmo, 2003).

3.2.3 Water level and physicochemical surveys along selected transects

At sites selected along the two transects orthogonal to the coastline, periodical measurements of water level, T, pH and EC were performed in order to verify the variation over time of the salt water wedge in the aquifer and the relationship with the hydrodynamic conditions. As a whole, five campaigns were carried out and for each transect four piezometers and sites along the two main streams (Lamone river and Cerba canal) were considered. Water levels were measured by a phreatimeter with respect to a reference point, whereas the physical-chemical parameters were measured by a portable instrument equipped with a multi-probe device was used. Moreover, a CTD-Diver was used to perform vertical EC-T logs. During each survey, the same chronological procedure to acquire the data was adopted, as follows:

- Water level measurement;
- EC, pH, T and vertical log;
- Purging, in case of piezometer;
- Water level measurement EC, pH, T and vertical log post purging;
- Water pumping from depths chosen on the basis of the log results and physical-chemical measurements in water.

3.3 Results

3.3.1 Hydrodynamic data

All water level data (both hydrometric, in case of stream waters, and piezometric, for groundwater) achieved in the different campaigns are reported in Table 3.1.

Table 3.1 Water level data for the different surveys (18, 23, 24 and 25 are points along canals and represent hydrometric levels; the other points are piezometers in which the piezometric levels were measured).

Code	Data	water level (m a.s.l.)	Data	water level (m a.s.l.)	Data	water level (m a.s.l.)	Data	water level (m a.s.l.)	Data	water level (m a.s.l.)
1RA	23/07/2019	0.50					16/09/2020	0.33	25/11/2020	0.54
2RA	23/07/2019	0.12					16/09/2020	-0.20	25/11/2020	0.23
3RA	23/07/2019	-1.28					16/09/2020	-1.70	25/11/2020	-1.34
4RA	23/07/2019	-0.99	03/12/2019	-0.29	23/07/2020	-1.37	16/09/2020	-1.04	25/11/2020	-0.74
5RA	23/07/2019	-0.18	03/12/2019	0.10	23/07/2020	-0.60	16/09/2020	-0.44	25/11/2020	-0.19
6RA	23/07/2019	-0.55					16/09/2020	-0.73	25/11/2020	-0.53
7RA	23/07/2019	-0.43					16/09/2020	-0.83	25/11/2020	-0.65
9RA	24/07/2019	-0.50					17/09/2020	-0.83	26/11/2020	-0.38
10RA	24/07/2019	0.41	03/12/2019	1.18	23/07/2020	0.32	17/09/2020	0.26	26/11/2020	0.65
11RA	24/07/2019	-1.53	03/12/2019	-1.41	23/07/2020	-1.58	17/09/2020	-1.58	26/11/2020	-1.56
12RA	24/07/2019	0.78					17/09/2020	0.62	26/11/2020	0.86
14RA	24/07/2019	0.18	03/12/2019	0.62	23/07/2020	0.44	17/09/2020	0.02	26/11/2020	0.60
16RA	25/07/2019	-1.86					15/09/2020	-2.43	26/11/2020	-2.13
17RA	25/07/2019	-0.97	03/12/2019	-0.68	24/07/2020	-1.15	15/09/2020	-1.32	26/11/2020	-1.30
18RA	25/07/2019	-1.16	03/12/2019	-1.38	24/07/2020	-1.21	15/09/2020	-1.17	24/11/2020	-1.46
19RA	25/07/2019	-0.28	04/12/2019	0.35	24/07/2020	-0.73	15/09/2020	-0.89	26/11/2020	-0.89
20RA	25/07/2019	-0.01	04/12/2019	0.77	24/07/2020	-0.17	17/09/2020	-0.04	26/11/2020	0.27
21RA	25/07/2019	-0.02	04/12/2019	0.24			17/09/2020	-0.15	27/11/2020	0.00
23RA			04/12/2019	0.194	24/07/2020	0.034	16/09/2020	-0.126	26/11/2020	-0.376
24RA							25/09/2020	2.076	26/11/2020	1.996
25RA							25/09/2020	0.33	26/11/2020	-0.25

For an overall evaluation of the hydrodynamic behavior of the aquifer system under study, all data concerning the whole network of piezometers measured during the three extended campaigns (July 2019, September 2020, and November 2020) are plotted in Fig. 3.6. Most piezometers were characterized by a similar behavior in terms of change in groundwater level over time, with a minimum in September 2020 while the highest values were recorded in July 2019 and November 2020. This is still congruent with the abovementioned hydrological regime (Fig. 3.6), and it indicates that, generally speaking, the groundwater system is dynamic and more or less homogeneously affected by rainfall conditions. Some differences in terms of evolution among the different field periods are attributable to local conditions, with particular references to the piezometers #19, #17 and #16 that are sited in the inland part of the studied area, where agricultural and industrial activities may affect groundwater dynamics by water pumping.

Concerning the absolute piezometric levels, in most cases they are close to or minor than sea level, thus favoring seawater intrusion. Nevertheless, only for a few more than a half of piezometers the reference elevation is of optimal quality (error <0.05 m), thus enabling detailed considerations. For the remaining piezometers (see Appendix 3.7.1) a significant error (of the order of 1 m) of the GPS system (scarce internet communication) made the absolute elevations not confident. Data acquired by logs along the two selected transects (Fig. 3.2) were elaborated in terms of EC vertical gradient and reported in Fig. 3.7. The

logs refer to measurements carried out into purged piezometers for all the campaigns. All five periods are showed, thus remarking the high seasonal variability. In agreement with the behavior of the water levels, major EC values were observed in summer 2020 (low-level conditions).

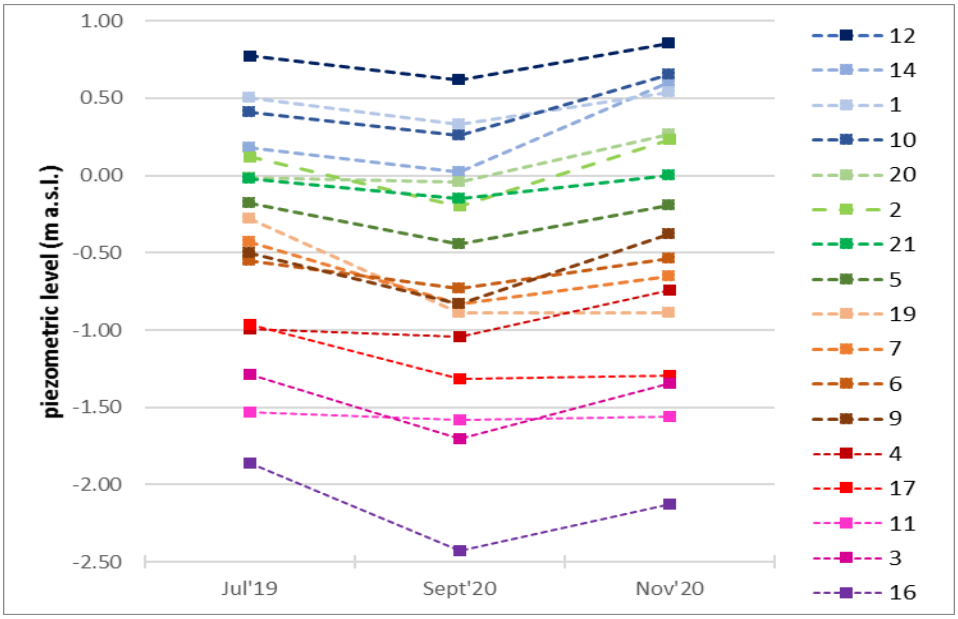

Fig. 3.6 Comparison of water levels recorded at different piezometers during the three periods of field activity carried out in the whole network.

At each site a vertical gradient of EC was observed in almost all periods, thus suggesting a constant coexistence of salt and fresh-water and the consequent mixing processes. However, in December 2019, after a significant rainfall period (Fig. 3.3), at some sites (e.g. #14 and #19) the local and inland water recharge was able to replace most of the saltwater with freshwater into the aquifer. This process generated vertical profiles with constantly low EC values. Among the investigated waters, those intercepted by the piezometers close to the shoreline (20, 21) were characterized by high EC values, testifying that the direct seawater intrusion mechanism dominated at least in this part of the study area. Nevertheless, the highest EC values were recorded at #5, in the southern transect (Fig. 3.7). This site was characterized by EC values even higher (about 65 mS/cm) than that of typical seawater (about 50 mS/cm), and this feature was persisting after prolonged period of purging. Since the lagoon, extending to the east from #5 (Fig. 3.2), effectively contains freshwater (some measurements were performed to verify such an observation) that arrives from the Cerba canal (#18, southern transect), a possible influence of seawater affected by

continuative evaporation is to be excluded. Other possible causes can thus be invoked such as the presence of i) an ancient or a fossil seawater characterized by EC higher than that of present seawater, and/or ii) dissolution of evaporitic minerals, possibly related to transitional deposits.

Generally speaking, when compared to the Cerba canal, the Lamone river showed higher EC values, which here denoted the presence of seawater ingression along the riverbed and up to almost 4 km inland from the shoreline (e.g. #23, northern transect). This canal also showed seasonal dynamics: in December 2019, at #23 only freshwater was recognized, whereas during other periods, freshwater was flowing above a saltwater wedge and mixed with it. The presence of brackish waters into the canal for several kilometers inland might represent an additional cause of seawater intrusion in the shallow aquifer. Actually, the EC pattern of vertical profiles recorded in the waters from the piezometer close to the canal is congruent with such a mechanism. It is matter of fact that, especially at #10, a TDS increase up to 5 m depth and a sort of salinity decrease at increasing depths were shown. This is likely when saltwater would be infiltrating from the surface, and specifically from the near

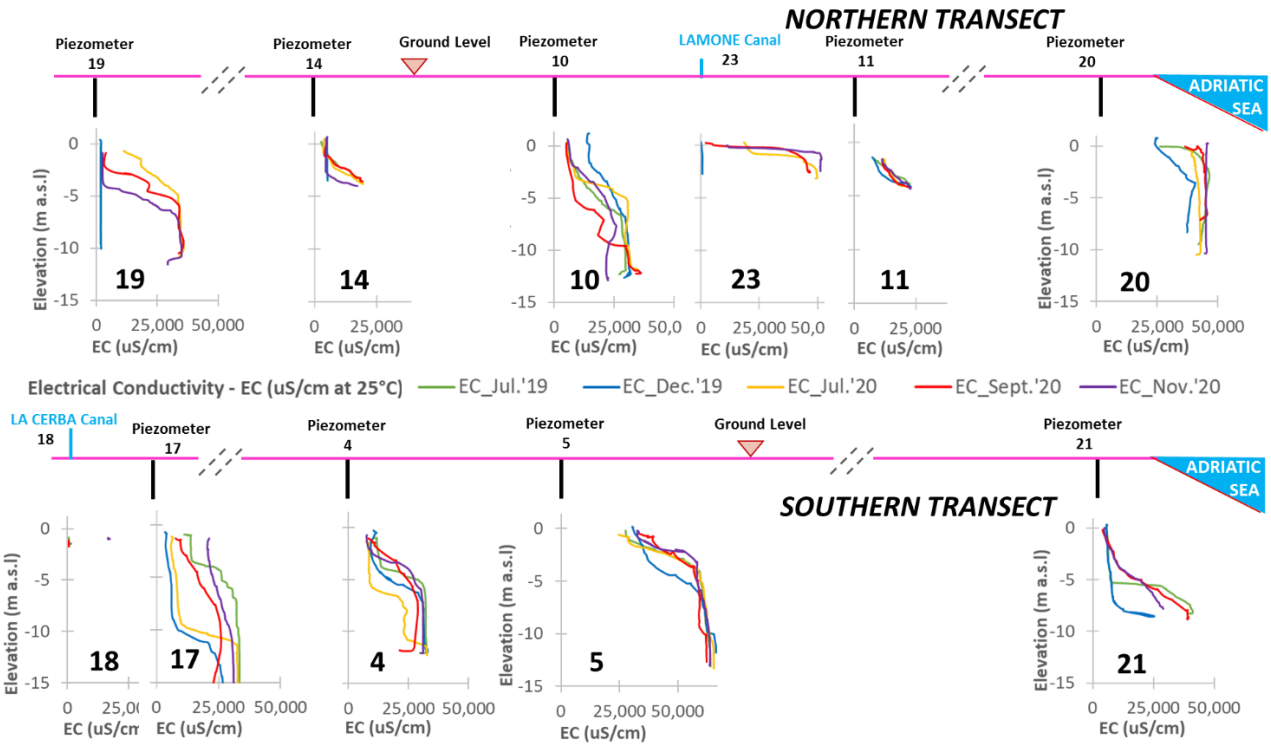

Lamone river. In any case, for confirming this hypothesis further geochemical markers are to be evaluated as reported in the following paragraphs.

Fig. 3.7 Electrical conductivity (EC) logs along the northern (above) and southern (below) transects in the five periods of survey.

3.3.2 Water physicochemical parameters and chemical and isotopic composition

Tables 3.2, 3.6 and 3.8 are listing temperature (°C) and pH values, the concentrations of major anions (HCO_3^-, Cl^-, F^-, Br^-, NO_3^-, NO_2^- and SO_4^{2-}) and cations (Ca^{2+}, Mg^{2+}, Na^+, K^+ and NH_4) and the total dissolved solids (TDS) in mg/L, and the oxygen and hydrogen isotopic signature (expressed as $\delta^{18}O$ ‰ vs. V-SMOW and δD ‰ vs. V-SMOW) for the July 2019, September 2020 and November 2020 surveys, respectively. Tables 3.3 and 3.7 also report the concentrations of selected trace elements (Al, Sb, As, Ba, B, Li, Rb, V and Sr in µg/L, SiO_2 in mg/L). Tables 3.4 and 3.5 list the temperature (°C) and pH values and the range of measured electrical conductivity (E.C., in mS/cm) for the December 2019 and July 2020 surveys, respectively, in those selected sites arranged along the two main transects orthogonal to the coastline. In case of sampling at two different depths, “top” and “bot” (the latter stands for bottom) are added to the site number.

Code	T	pH	HCO_3	F	Cl	Br	NO_3	NO_2	SO_4	Ca	Mg	Na	K	NH_4	TDS	$\delta^{18}O$	δD
July 2019	°C		mg/L	mg/L	mg/L	mg/L	mg/L	mg/L	mg/L	mg/L	mg/L	mg/L	mg/L	mg/L	mg/L	‰ vs. V-SMOW	‰ vs. V-SMOW
1	18.6	7.76	538	0.48	652	2.7	16	0.030	104	44	64	530	34	4.2	1990	-6.94	-48.3
2	18	7.18	1016	19	11636	57	17	0.030	1757	145	877	7447	192	35	23198	-2.52	-17.3
3	16	6.86	285	7.4	9915	58	15	0.082	3500	347	915	6274	283	55	21655	-2.58	-20.4
4 top	17	7.35	777	3.6	3811	16	15	0.007	931	340	280	2421	35	3.3	8634	-5.01	-36.9
4 bot	15.9	7.12	633	8.0	9262	31	6.6	0.033	2569	615	966	5210	106	24	19431	-3.16	-24.3
5 top	18.7	6.94	515	25	10496	43	11	0.705	4009	836	897	5856	75	2.5	22766	-3.60	-24.3
5 bot	16.2	7.26	656	11	20378	78	15	0.157	5922	428	2178	12815	371	23	42875	-0.20	-7.2
6	19.7	6.86	459	0.7	116	0.4	1.2	0.030	101	67	41	150	19	0.26	955	-7.36	-48.5
7	18.8	6.86	270	1.7	1852	6.3	30	0.426	297	440	181	732	32	5.6	3847	-6.87	-45.5
8	15.6	7.1	459	6.0	11473	53	3	0.010	3198	548	904	6643	237	4.4	23528	-2.31	-18.8
9 top	16	7.75	1074	0.59	2176	6.1	19	0.026	117	117	176	1282	32	5.4	5004	-6.75	-43.8
9 bot	14.8	7.67	1177	1.2	5644	23	5.5	0.043	881	150	452	3854	111	22	12320	-5.24	-36.5
10	16.7	8.46	1194	1.8	4552	19	2.5	0.007	425	202	360	2614	65	7.5	9443	-5.37	-36.3
11	16.6	7.16	967	2.3	4629	18	1.4	0.046	478	299	435	2402	38	3.5	9274	-4.57	-31.5
12	17.5	7.24	438	1.4	2072	7.7	2.9	0.010	322	141	140	1113	72	0.71	4311	-6.79	-47.1
13	31.3	8.15	187	21	16809	71	2.9	0.010	5853	428	1304	10285	378	0.45	35339	0.04	-0.5
14	20.5	7.2	833	0.59	525	3.2	35	0.033	54	122	79	339	42	7.0	2040	-6.66	-45.9
15	31	8.68	181	0.2	41	0.2	3.8	0.525	58	46	19	37	9.2	0.10	395	-8.41	-56.1
16 top	19.8	7.46	993	5.4	4409	19	26	0.039	361	427	382	2246	46	1.1	8915	-7.29	-47.0
16 bot	17.1		1003	11	9483	55	29	0.033	1731	237	773	5626	142	28	19117	-4.60	-32.4
17	16.5	7.17	1100	1.9	6617	20	6.3	0.023	340	246	495	3292	98	13	12230	-5.87	-41.1
18	29.7	8.21	193	0.31	42	0.18	2.4	0.026	62	49	19	34	8.1	0.13	409	-8.33	-57.2
19	20.8	7.24	682	0.33	265	1.7	1.4	0.030	105	134	61	201	4.5	0.39	1457	-7.71	-50.5
20	18.2	7.3	495	15	13980	63	5.5	0.016	5071	437	1147	8891	210	11	30326	-1.55	-11.8
21	19.1	7.63	299	1.6	1630	5.9	4.8	0.025	310	170	180	661	61	0.45	3323	-6.89	-45.3

Table 3.2 Physicochemical parameters, chemical and isotopic data of the water samples of the July 2019 survey

Code	Al	Sb	As	Ba	B	Li	Rb	V	SiO_2	Sr
July 2019	µg/L	µg/L	µg/L	µg/L	µg/L	µg/L	µg/L	µg/L	mg/L	µg/L
1	< 5	< 0.1	2.1	17	462	17	10	0.2	5.5	406
2	7.0	0.1	7.4	1196	2966	21	30	1.9	18	4530
3	< 5	0.1	4.8	51	2499	36	35	0.1	4.2	2190
4 top	< 5	0.2	79	98	300	17	15	0.4	14	2780
4 bot	< 5	0.1	110	382	364	24	32	0.8	12	6800
5 top	< 5	0.1	7.2	69	124	35	17	0.4	14	5650
5 bot	< 5	0.1	54	148	3393	21	69	0.8	9.0	8600
6	< 5	0.1	0.7	8.2	239	5.1	< 1	0.4	14	255
7	< 5	0.1	0.5	126	73	14	11	0.2	17	1630
8	255	0.1	3.6	75	2162	41	30	0.8	8.0	4490
9 top	5.0	0.1	39	157	716	6.9	6.8	1.5	16	950
9 bot	7.0	0.2	21	336	1804	9.9	14	2.9	17	2050
10	16	< 0.1	11	441	538	14	11	1.3	15	2420
11	< 5	< 0.1	146	1155	611	19	11	0.3	14	2860
12	< 5	< 0.1	1.2	77	594	9.5	6.4	0.3	11	960
13	< 5	0.3	4.1	21	3675	64	104	1.7	1.0	6900
14	6.0	0.1	2.5	84.9	282	22	3.9	2.0	23	1150
15	6.0	0.3	1.9	30	53	5.4	5.0	1.5	3.9	411
16 top	8.0	0.1	2.2	427	499	14	10	0.9	10	3120
16 bot	< 5	< 0.1	5.0	737	1948	16	26	1.5	13	4940
17	10	0.1	13	392	1023	24	14	1.3	14	3040
18	9.0	0.3	2.2	39.3	59	5.8	3.4	1.1	3.5	423
19	< 5	0.1	7.9	138	260	16	< 1	0.3	14	1250
20	< 5	0.1	2.9	297	2430	20	21	1.4	9.3	5390
21	5.0	0.2	11	123	590	34	14	0.3	11	1530

Table 3.3 Trace elements contents of the water samples of the July 2019 survey

Code December 2019	Temperature °C	pH	E.C. (range) mS/cm
4	13.1	7.39	10.32 ÷ 33.13
5	13.2	7.16	34.82 ÷ 66.41
10	12.8	7.66	14.46 ÷ 29.03
11	14.4	7.36	7.34 ÷ 23.04
14	16.2	7.19	4.95 ÷ 5.24
17	14.2	7.48	3.32 ÷ 30.17
18	9.0	7.53	1.5
19	17.4	7.12	1.55 ÷ 1.88
20	15.0	7.28	25.23 ÷ 37.33
21	15.4	7.33	6.18 ÷ 21.2
23	9.3	8.67	0.57

Table 3.4 Physicochemical parameters of the December 2019 survey. Temperature and pH data refer to water at the end of purging and EC range derives from vertical log, with the exception of the surface water bodies (#18 and #23).

Code July 2020	Temperature °C	pH	E.C. (range) mS/cm
4	13	7.04	17.09 ÷ 25.4
5	14.5	7.04	56.2 ÷ 58
10	13	7.4	14.02 ÷ 16.51
11	13.5	6.06	11.95 ÷ 12.39
14	17	6.95	1.16 ÷ 1.22
17	14	6.8	15.2 ÷ 25.3
18	26.7		0.56
19	17	6.8	6.72 ÷ 7.05
20	15	6.85	38.5 ÷ 39.3
23	27.3		18.32 ÷ 40.38

Table 3.5 Physicochemical parameters of the July 2020 survey. Temperature and pH data refer to water at the end of purging and EC range derives from vertical log, with the exception of the surface water bodies (#18 and #23).

Code	T	pH	HCO_3	F	Cl	Br	NO_3	NO_2	SO_4	Ca	Mg	Na	K	NH_4	TDS	$\delta^{18}O$	δD
September 2020	°C		mg/L	mg/L	mg/L	mg/L	mg/L	mg/L	mg/L	mg/L	mg/L	mg/L	mg/L	mg/L	mg/L	‰ vs. V-SMOW	‰ vs. V-SMOW
1	16.76	7.92	516	0.9	793	2.0	19	0.016	136	69	75	534	34	5.5	2184	-7.49	-53.19
2 top	16.45	7.08	863	1.6	5390	18	3.3	0.046	1599	336	287	3825	63	1.0	12387	-5.34	-36.04
2 bot	14.02	7.28	576	0.68	18367	52	0.97	0.062	5233	422	1447	10269	231	31	36629	-0.68	-7.06
3 top	16.14	8.06	971	0.73	5300	19	15	0.026	1763	85	312	4054	124	5.2	12648	-3.79	-28.99
3 bot	14.71	7.39	432	1.2	14536	34	0.78	0.026	4032	357	1053	8434	256	7.1	29143	-1.82	-12.14
4	14.22	7.17	632	0.7	9229	21	16	0.020	1748	470	792	4920	73	14	17914	-3.44	-26.50
5	16.6	6.81	567	1.0	16011	42	13	0.036	5088	782	1343	9744	187	7.7	33786	-1.33	-7.15
5*	14.74	7.12	604	1.8	21145	57	0.1	0.033	8690	596	1628	12906	309	19	45957	-0.40	-10.43
6	16.38	8.02	447	0.83	122	0.18	2.2	0.115	112	39	31	199	21	0.77	975	-7.34	-52.87
7	16.44	6.99	416	0.9	2645	8.4	12	0.016	507	587	262	1041	57	6.7	5543	-6.41	-45.00
9	15.34	7.5	926	0.38	1129	2.7	1.6	0.020	172	214	115	763	23	3.0	3350	-6.70	-46.57
10 top	16.72	7.42	1116	0.78	1420	3.9	1.7	0.026	513	190	126	1161	27	3.2	4563	-5.73	-41.79
10 bot	14.46	7.45	1337	0.71	8035	16	5.3	0.043	1400	310	625	4350	103	19	16201	-4.50	-31.41
11	15.62	7.19	1081	0.44	5563	14	0.51	0.030	873	319	503	2996	52	9.0	11411	-4.15	-33.38
12	15.9	7.17	653	0.71	2849	9.8	1.95	0.023	775	216	262	1879	82	0.58	6729	-6.50	-49.56

14	20.3	7.14	915	0.9	1509	4.3	34	0.026	89	151	148	867	62	9.0	3789	-6.72	-49.73
16	19.4	7.38	1091	1.2	13013	30	1.6	0.026	92.1	239	844	6572	154	25	22062	-4.10	-26.16
17 top	15.11	6.98	1196	0.66	3625	9.8	30	0.039	1291	296	384	2407	98	8.7	9346	-6.31	-45.00
17 bot	14.63	7.21	1143	1.4	9136	31	0.41	0.039	1835	252	778	5847	144	18	19185	-4.66	-35.01
18	26.07	8.68	154	0.23	34	0.05	3.9	0.046	52	46	14	25	7.1	0.45	336	-8.12	-60.19
19	17.27	6.83	1086	0.6	5752	16	5.5	0.046	1040	284	494	3594	78	7.4	12357	-5.13	-37.59
20	16.17	7.33	451	1.9	14225	42	0.31	0.043	4825	487	1246	9830	224	10	31342	-1.48	-12.04
21	16.82	7.59	301	1.7	1923	5.1	0.27	0.020	502	131	200	999	74	0.65	4138	-6.95	-50.48
23	25	7.99	173	0.9	1390	3.9	13	0.030	309	82	102	744	34	0.45	2852	-8.10	-56.17
23 top	22.8	8.02	174	1.4	3395	9.7	9.5	0.082	489	119	234	1785	66	0.38	6283	-7.45	-50.74
23 bot	23.3	8.2	180	1.4	5503	17	5.7	0.066	1581	195	447	3373	126	0.45	11430	-6.24	-44.41
24	23.2	8.47	194	0.23	45	0.08	8.4	0.043	63	64	15	36	12	0.12	436	-8.82	-61.04
25	23.4	8.2	183	0.72	8107	19	2.5	0.053	1959	235	576	4413	206	0.45	15702	-5.03	-37.42

Table 3.6 Physicochemical parameters, chemical and isotopic data of the water samples of the September 2020 survey

Code September 2020	Al µg/L	Sb µg/L	As µg/L	Ba µg/L	B µg/L	Li µg/L	Rb µg/L	V µg/L	SiO_2 mg/L	Sr µg/L
1	< 5	< 0.1	46	38	429	16	12	0.2	10	620
2 top	< 5	0.2	78	63	1426	27	9.8	0.5	16	2435
2 bot	< 5	< 0.1	43	203	1091	31	50	1.1	12	7185
3 top	< 5	0.1	4.2	38	2949	20	21	0.6	12	1078
3 bot	< 5	< 0.1	43	102	2630	27	49	0.3	13	4291

4	< 5	0.1	135	320	394	18	28	0.7	15	5452
5	< 5	0.2	36	129	571	28	42	0.3	16	7329
5*	< 5	0.1	112	167	1070	19	57	0.6	13	8131
6	6	0.2	2.5	6.3	351	3.5	0.67	0.6	19	206
7	< 5	0.1	1.8	210	61	12	18	0.4	25	2597
9	< 5	0.1	51	104	571	5.1	5.0	0.9	18	1023
10 top	< 5	0.1	23	149	352	11	6.3	0.5	20	1183
10 bot	< 5	< 0.1	6.9	712	693	14	17	1.5	19	3707
11	< 5	< 0.1	169	1362	610	17	13	0.2	18	3244
12	< 5	< 0.1	1.2	184	589	9.7	9.7	0.2	14	1692
14	< 5	< 0.1	0.8	107	382	25	5.5	2.7	24	1182
16	< 5	0.2	11	842	2117	13	25	1.3	16	5341
17 top	< 5	0.2	49	372	747	26	12	1.2	17	3429
17 bot	96	0.1	14	760	1050	18	22	1.4	20	4727
18	< 5	0.4	1.3	32	26	1.6	3.2	1.1	4.9	312
19	< 5	0.1	13	569	602	14	6.9	0.4	17	3704
20	< 5	0.1	8.2	282	996	12	18	0.9	11	6016
21	< 5	0.1	16	118	665	22	17	0.1	14	1436
23	< 5	0.4	1.9	37	211	6.9	9.7	1.4	6.2	787
23 top	17	0.5	1.9	37	409	14	20	1.3	5.8	1295
24	7	0.3	1.6	39	34	2.5	7.9	1.2	6.7	352
25	9	0.3	2	33	848	28	44	1.3	5.1	2768

Table 3.7 Trace elements contents of the water samples of the September 2020 survey

Code November 2020	T °C	pH	HCO_3 mg/L	F mg/L	Cl mg/L	Br mg/L	NO_3 mg/L	NO_2 mg/L	SO_4 mg/L	Ca mg/L	Mg mg/L	Na mg/L	K mg/L	NH_4 mg/L	TDS mg/L	$\delta^{18}O$ ‰ vs. V-SMOW	δD ‰ vs. V-SMOW
1	16.1	8.1	516	1.5	775	2.6	0.13	0.020	59	37	49	541	33	3.8	2017	-7.40	-51.9
2 top	14.4	7.2	769	4.7	7015	24	23	0.033	727	319	326	4177	83	2.0	13469	-4.88	-34.4
2 bot	13.5	7.3	544	5.0	18026	62	3.7	0.039	1769	402	1246	9581	218	27	31884	-0.72	-8.3
3 top	14.5	7.9	836	4.8	8123	35	3.8	0.026	1396	153	488	5095	165	5.0	16304	-3.49	-26.1
3 bot	14.2	7.3	333	4.8	15582	56	5.2	0.016	2046	418	1086	9195	260	15	29001	-1.90	-14.2
4	13.8	7.2	644	4.9	12125	38	3.0	0.043	845	582	888	5343	95	15	20584	-3.21	-24.9
5 top	14.6	6.8	556	4.7	17548	66	0.7	0.059	1978	920	1164	8090	106	7.0	30441	-2.37	-20.9
5 bot	13.5	7.3	601	5.2	24960	134	2.8	0.039	2580	522	1862	13640	370	21	44698	-0.28	-8.3
6	14.7	8.3	467	0.5	118	0.3	1.8	0.030	92	21	20	223	17	0.5	961	-7.40	-49.4
7	14.9	7.18	417	0.14	2262	7.1	36	0.062	197	476	205	895	51	5.5	4552	-6.65	-43.1
9	13	7.76	936	0.95	1605	4.5	2.9	0.030	107	225	153	980	23	3.5	4041	-6.68	-45.3
10 top	13.6	7.29	1193	1.1	5914	19	36	0.026	614	339	498	3572	99	7.7	12292	-4.84	-32.2
10 bot	13.2	7.38	1342	1.9	9464	31	11	0.026	799	345	810	5750	102	17	18673	-4.07	-29.3
11	14.3	7.13	1030	0.46	5955	21	4.2	0.046	188	248	558	3420	52	0.8	11477	-3.89	-29.2
12	14.9	7.16	523	0.12	2785	8.6	0.43	0.020	336	170	218	1720	75	0.2	5837	-6.55	-46.5
14	16.1	7.19	1005	0.87	879	3.3	27	0.049	36	170	124	615	40	6.5	2907	-5.88	-43.9
16	13.9	7.41	1076	4.7	15370	44	6.8	0.036	1045	587	1398	7233	248	20	27032	-4.18	-28.5
17 top	14.5	7.16	1011	2.5	9050	32	9.4	0.039	263	256	586	4453	165	12	15840	-5.61	-38.7
17 bot	14.2	7.41	931	4.9	12195	44	4.6	0.033	1027	171	828	6801	154	21	22182	-4.59	-33.7
18	6.9	7.97	949	0.74	5413	20	3.7	0.194	237	175	416	3183	105	11	10513	-4.64	-35.4
19	17.6	6.9	1146	0.4	7108	18	2.7	0.033	291	302	548	3833	113	6.6	13368	-5.18	-35.8
20	15	7.16	415	0.5	17210	53	12	0.059	1574	476	1196	9464	177	11	30588	-1.62	-12.3
21 top	14.5	7.58	309	4.5	2177	10	1.2	0.062	335	123	208	1169	82	0.2	4419	-6.71	-46.6
21 bot	14.5	7.66	322	2.6	5552	21	1.4	0.164	505	170	403	3089	167	3.5	10237	-5.62	-38.6
23 top	9	8.15	264	5.0	4068	15	6.7	0.026	492	147	279	2138	88	0.3	7503	-6.17	-37.1
23 bot	13	8.19	181	4.8	19531	66	2.5	0.020	2369	422	1486	10964	367	1.2	35394	-0.65	-5.7
24	6.4	8.4	289	0.11	42	0.17	2.9	0.095	57	77	22	40	15	0.3	545	-7.52	-48.7
25 top	9.3	8.18	268	0.4	4495	15	2.8	0.390	622	161	327	2553	120	0.2	8565	-5.84	-36.1
25 bot	11.4	8.2	284	4.6	20746	75	11	0.033	2137	430	1453	10553	347	0.5	36041	-0.91	-7.0

Table 3.8 Physicochemical parameters, chemical and isotopic data of the water samples of the November 2020 survey

Water temperatures ranged from 14.8 °C (#9 bot) to 31.3 °C (#13), from 14 °C (#2 bot) to 26.1 °C (#18) and from 6.4 °C (#24) to 17.6 °C (#19) for the July 2019, September 2020 and November 2020 surveys, respectively. The temperature was varying from 9 °C (#18) to 17.4 °C (#19) and from 13 °C (#4 and #10) to 27.3 °C (#23) for the December 2019 and July 2020 transect surveys, respectively.

The pH showed a high variability, being comprised between 6.86 (#3, #6 and #7) and 8.68 (#15), from 6.81 (#5) to 8.68 (#18) and from 6.8 (#5 top) to 8.4 (#24) for the July 2019, September 2020 and November 2020 surveys, respectively. The pH values were between 7.12 (#19) and 8.67 (#23) and between 6.06 (#11) and 7.4 (#10) in December 2019 and July 2020, respectively.

The measured electrical conductivity (EC), which is directly related to the ion concentration, varied in transect surveys, from 0.57 to 66.41 mS/cm and from 0.56 to 58 mS/cm for the December 2019 and July 2020, respectively. The TDS values were from 395 mg/L (#15) to 42.9 g/L (#5 bot), from 336 mg/L (#18) to 46 mg/L (#5*) and from 545 mg/L (#24) to 44.7 g/L (#5 bot) for the July 2019, September 2020 and November 2020 surveys, respectively.

Among major anions, chloride (Cl^-) was the most abundant species in each sample (Tables 3.2, 3.6 and 3.8), reaching the highest concentration (up to 25 g/L in November 2020) at #5 in all the sampling campaigns, with the exception of #6, #14, #15, #18 and #19 in July 2019, #6, #18 and #24 in September 2020 and #6, #18 and #24 in November 2020, since they had bicarbonate (HCO_3^-) as the most abundant anion (up to 1005 mg/L at #14 in November 2020). The sulfate (SO_4^{2-}) abundance was characterized by a relatively high variability: from 54 (#14), 52 (#18) and 36 (#14) mg/L in the July 2019, September 2020 and November 2020 surveys, respectively, up to 8690 mg/L at #5 in all the sampling campaigns. Among minor anions, nitrate (NO_3^-) and nitrite (NO_2^-) presented an extremely large variability, from 0.1 (#5* in September 2020) to 36 (#10 top in November 2020) mg/L and from 0.007 (#4 top and #10 in July 2019) to 0.71 (#5 top in July 2019) mg/L, respectively. Bromide (Br^-) ranged from 0.05 (#18 in September 2020) to 134 (#5 bot in November 2020) mg/L, whilst fluoride (F^-) varied between 0.11 (#24 in November 2020) and 25 (#5 top in July 2019) mg/L.

Among major cations, sodium (Na^+) was the most abundant species in all the water samples, reaching the highest concentrations (up to 13.6 g/L in November 2020) at #5

independently by the sampling campaign, with the exception of those presenting calcium (Ca^{2+}) as the dominant cation, i.e. #15, and #18 in July 2019, #18 and #24 in September 2020 and #24 in November 2020 (Tables 3.2, 3.6 and 3.8). Ca^{2+} reached the highest concentration (920 mg/L) at #5 top in November 2020. The content of magnesium (Mg^{2+}) was varying from 14 mg/L (#18 in September 2020) up to 2178 mg/L (#5 bot in July 2019), whilst that of potassium (K^{+}) was from 4.5 (#19 in July 2019) to 378 mg/L (#13 in July 2019). Eventually, ammonium (NH_4^{+}) showed a large variability, ranging between 0.1 (#15 in July 2019) to 55 mg/L (#3 in July 2019).

Among trace elements (Tables 3.3 and 3.7), aluminum (Al) concentrations were below or slightly above the detection limit (5 µg/L), except for samples #8 in July 2017 (255 µg/L) and #17 bot in September 2020 (96 µg/L). Arsenic (As), barium (Ba), boron (B) and strontium (Sr) contents ranged between 0.5 (#7 in July 2019) and 169 (#11 in September 2020) µg/L, between 6.3 (#6 in September 2020) and 1362 (#11 in September 2020) µg/L, between 26 (#18 in September 2020) and 3675 (#13 in July 2019) µg/L and between 206 (#6 in September 2020) and 8600 (#5 bot in July 2019) µg/L, respectively. Lithium (Li), rubidium (Rb), vanadium (V) and silica (SiO_2) concentrations were up to 64 (#13 in July 2019), 104 (#13 in July 2019), 2.9 (#9 bot in July 2019) and 25 (#7 in September 2020) µg/L, respectively. Antimony (Sb) contents were below or slightly above the detection limit (0.1 µg/L).

The $\delta^{18}O$ and $\delta^{2}H$ values (Tables 3.2, 3.6 and 3.8) ranged between -8.41 (#15) and 0.04 ‰ V-SMOW (#13) and -57.2 (#18) and -0.5 ‰ V-SMOW (#13) in July 2019, respectively; -8.82 (#24) and -0.40 ‰ V-SMOW (#5*) and -61.04 (#24) and -7.06 ‰ V-SMOW (#2 bot), in September 2020, respectively. Finally, in November 2020 they were varied between -7.52 (#24) and -0.28 ‰ V-SMOW (#5 bot) and -51.9 (#1) and -5.7 ‰ V-SMOW (#23 bot), respectively.

The waters were classified by the Langelier-Ludwig (L-L) diagram (Fig. 3.8), also named as “Square Diagram” (Langelier & Ludwig, 1942), which is divided into four quadrants, allowing to define the water dominant composition, from bottom right and anticlockwise: i) bicarbonate-alkaline earth (Ca^{2+}-Mg^{2+}-HCO_3^{-}), ii) bicarbonate alkaline (Na^{+}-HCO_3^{-}), iii) sulfate-chloride alkaline (Na^{+}-Cl^{-}-SO_4^{2-}) and iv) sulfate-chloride alkaline earth (Ca^{2+}-Mg^{2+}-Cl^{-}-SO_4^{2-}). This classification method was based on the proportion, recalculated to 50, of the following ion pairs (in meq/L): Na^{+}+K^{+}, Ca^{2+}+Mg^{2+},

$Cl^-+SO_4^{2-}$ and $HCO_3^-+CO_3^{2-}$. The Cl^--HCO_3^--SO_4^{2-} and $(Na^+ + K^+)$-Ca^{2+}-Mg^{2+} ternary diagrams (Figs. 3.4 and 3.5, respectively), are coupled with the square diagram to determine the major anionic and cationic components of each water sample.

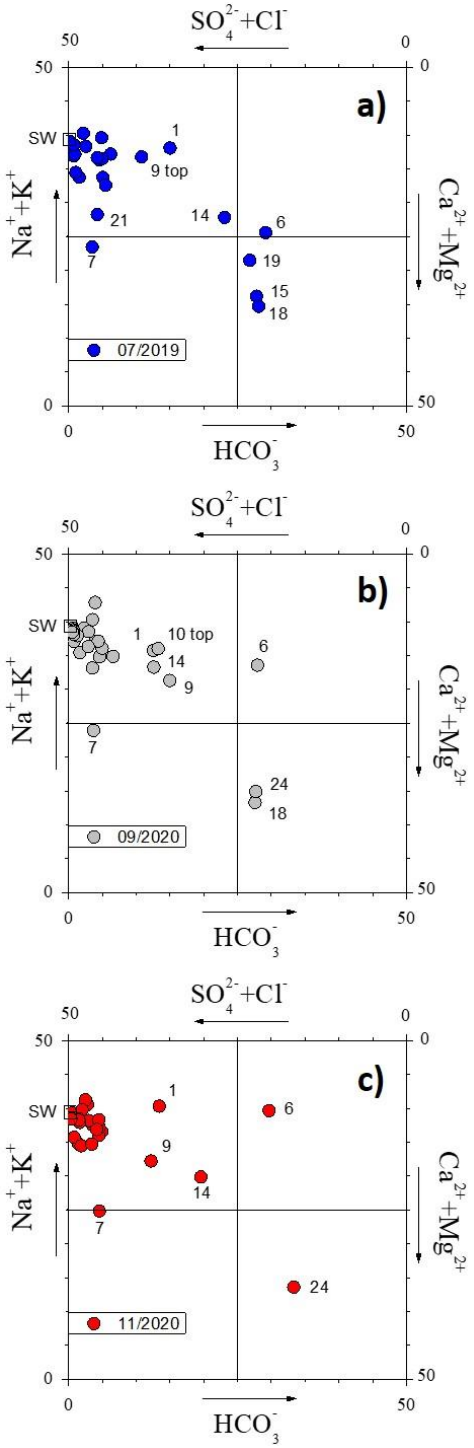

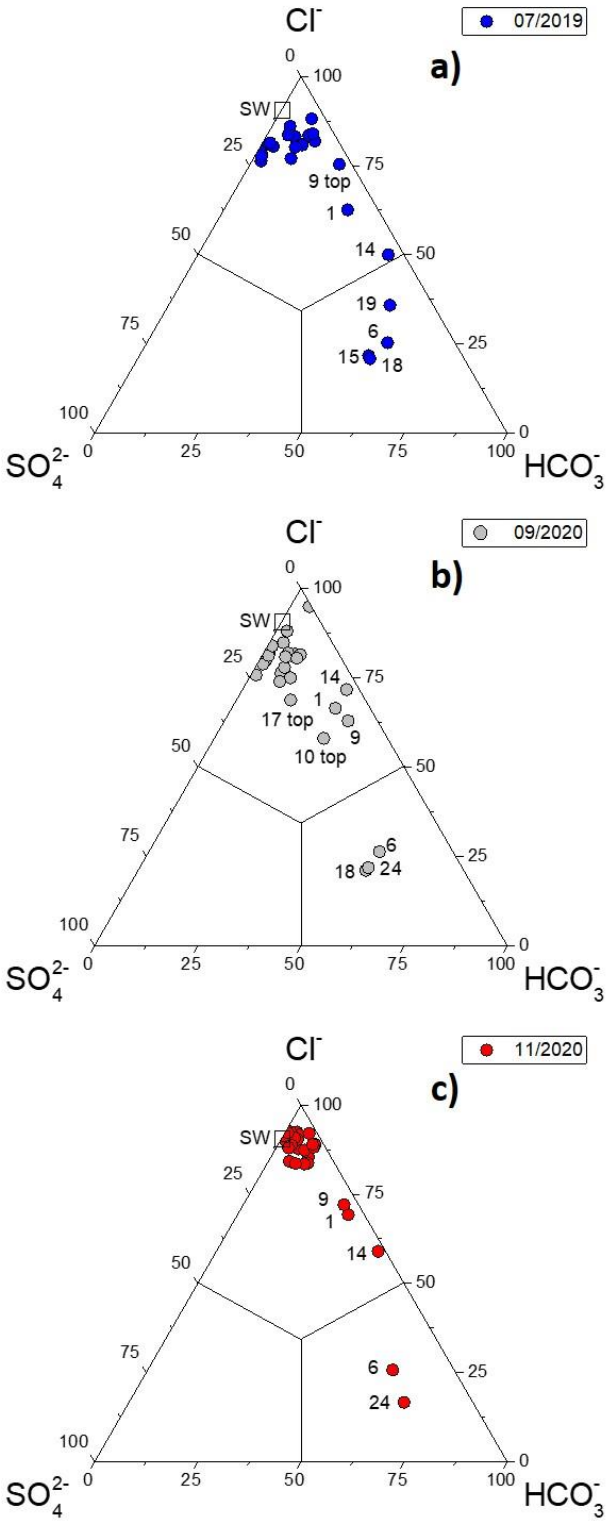

Fig. 3.8 L-L diagrams for the investigated samples in a) July 2019, b) September 2020 and c) November 2020. SW indicates the average composition of seawater. See the text for further details.

Fig. 3.9 Cl^--HCO_3^--SO_4^{2-} ternary diagram for the investigated samples in a) July 2019, b) September 2020 and c) November 2020. SW indicates the average composition of seawater. See the text for further details.

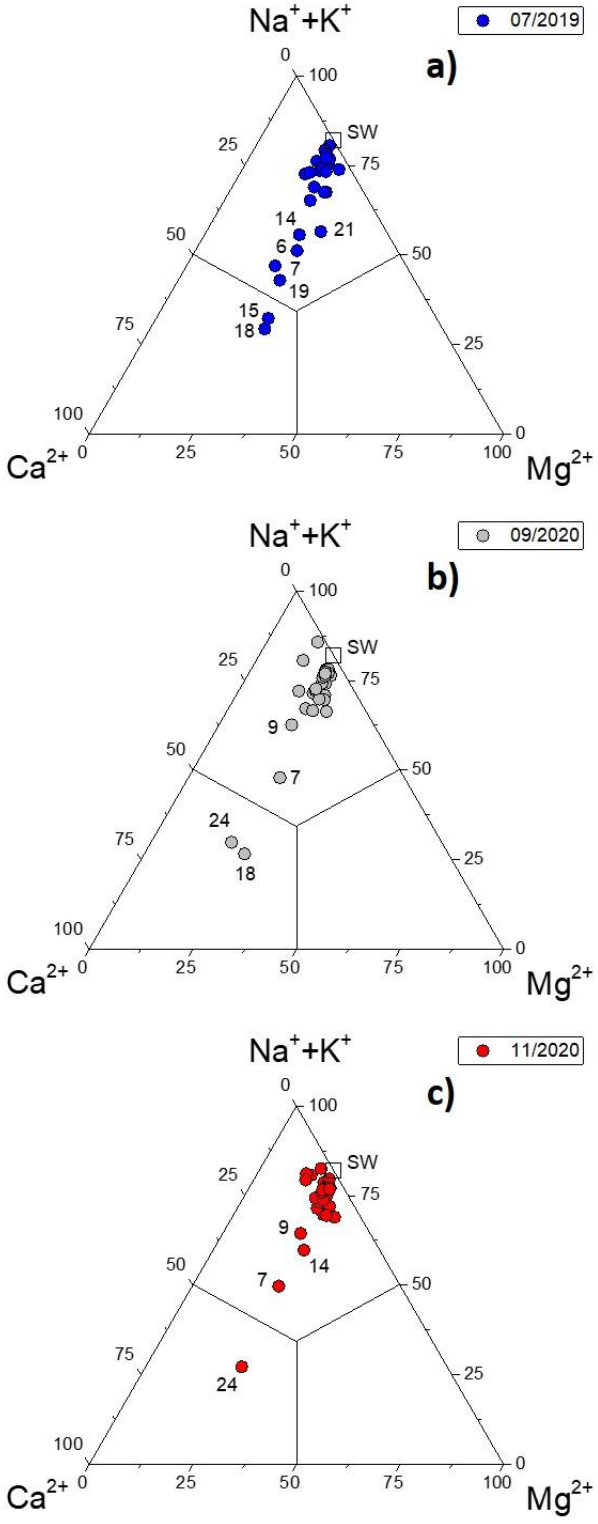

Fig. 3.10 ($Na^+ + K^+$)-Ca^{2+}-Mg^{2+} ternary diagram for the investigated samples in a) July 2019, b) September 2020 and c) November 2020. SW indicates the average composition of seawater. See the text for further details.

Most samples are characterized by a Na^+-Cl^- composition, being closer to the average composition of seawater (SW). This composition is also confirmed by the high concentrations of Br and B (Tables 3.2, 3.6 and 3.8 and Tables 3.3 and 3.7). Nevertheless, some samples are distributed in other fields of the classification diagrams. For example, #7 was characterized in all the sampling campaigns by an enrichment in Ca^{2+} and Mg^{2+} (Fig. 3.10). Consequently, it stands at the limit between the Na^+-Cl^--SO_4^{2-} and Ca^{2+}-Mg^{2+}-Cl^--SO_4^{2-} quadrants in the L-L diagram (Fig. 3.8), whilst #1, #9 and #14 showed an enrichment in HCO_3^- (Fig. 3.9), with #14 also presenting an evident enrichment in Ca^{2+} and Mg^{2+} in July 2019 and November 2020 (Figs. 3.3 and 3.5), respectively. On the contrary, the sample #6 has a Na^+-HCO_3^- composition in all the campaigns. Some samples also fall in the Ca^{2+}-Mg^{2+}-HCO_3^- quadrant of the L-L diagram (Fig. 3.8), i.e. #15 and #19 in July 2019, #18 in July 2019 and September 2020 and #24 in September and November 2020, thus showing the expected composition typical of surface and shallow ground waters. It is also worth noting that some samples show a considerable variation in composition between one campaign and another, e.g. #18 shifted to a Na^+-Cl^- composition in November 2020, as well as #19 in the surveys of September and November 2020 (Figs. 3.3, 3.4 and 3.5).

3.4 Discussion

3.4.1 Water origin and physical-chemical processes in the shallow aquifer of Ravenna

The geochemical results confirmed that the Ravenna shallow aquifer is significantly affected by salinization process, as already previously documented (Giambastiani et al., 2007; Antonellini et al., 2008; Antonellini and Mollema, 2010; Laghi et al., 2010; Mollema et al., 2013, 2015; Greggio et al., 2020). The great majority of waters were indeed characterized by both Na^+-Cl^- compositions and high TDS values (Tables 3.2, 3.6 and 3.8). Importantly, in those sites where water samples were collected at two different depths, the shallower layer was always characterized by a lower TDS when

compared with that collected at the well bottom, thus confirming a phreatic character of the system favorable to freshwater infiltration. The latter process and its variability over seasons are well evident from vertical logs (Fig. 3.7), which remark the sensitivity of the system to the hydrological regime. As previously evidenced, a few samples show a relatively distinct geochemical composition such as (Na^++K^+)-

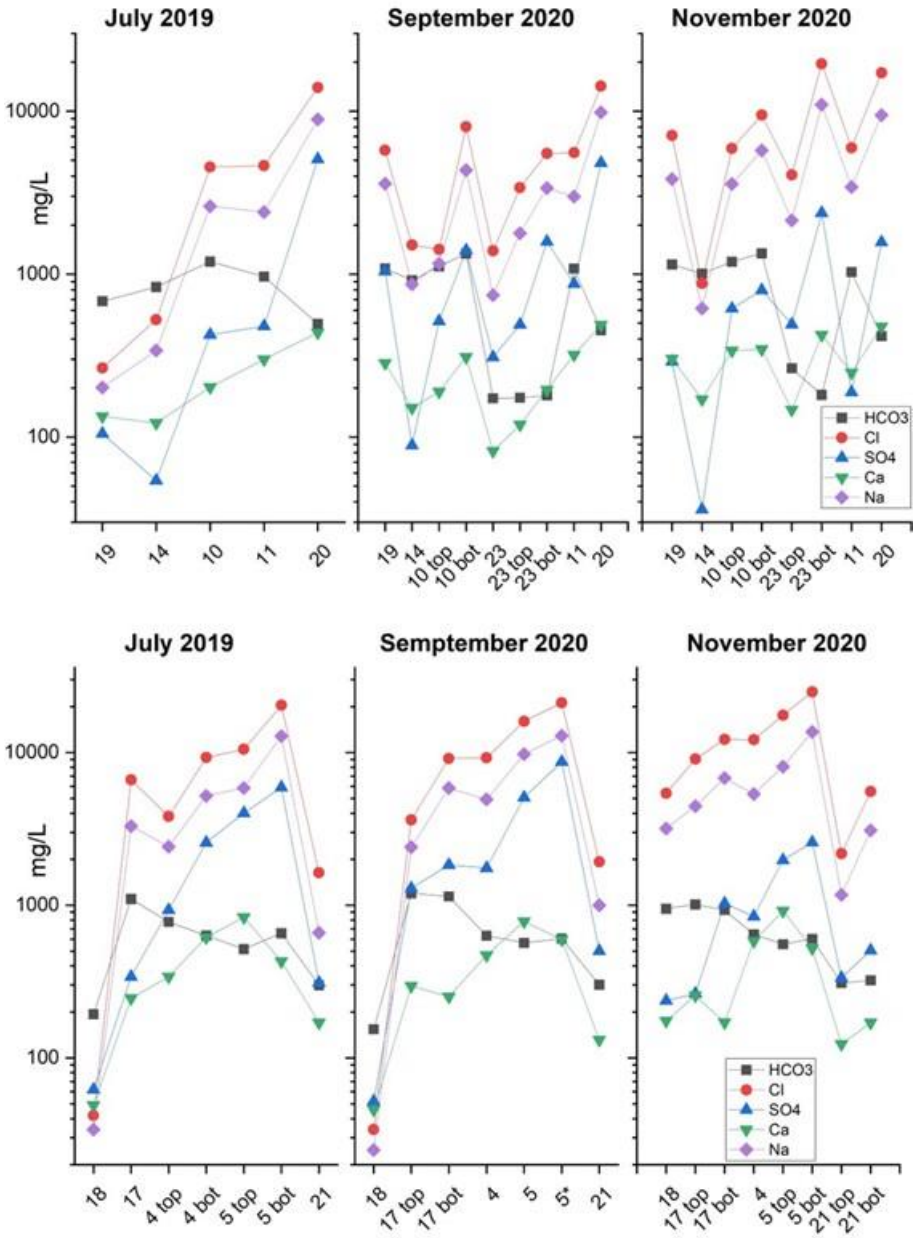

Fig. 3.11 Spatial trends of HCO_3^-, Cl^-, SO_4^{2-}, Ca^{2+} and Na^+ contents in the two transects orthogonal to the coastline for the July 2019, September 2020 and November 2020 sampling campaigns

HCO_3^- (#6), (Ca^{2+}+Mg^{2+})-HCO_3^- (#15 and #19 in July 2019, #18 in July 2019 and September 2020, #24 in September and November 2020) and (Ca^{2+}+Na^+)-Cl^- (#7) geochemical facies. When focusing on the two main transects orthogonal to the coastline (#20, #11, #23, #10, #14, #19 and #21, #5, #4, #17, #18, respectively) in the July 2019, September 2020 and November 2020 sampling campaigns, although with some exceptions, a clear increase towards the sea of the solutes intimately associated with a marine intrusion (i.e. Na^+, Cl^- and SO_4^{2-}) was observed (Fig. 3.11).

In agreement with the vertical logs, these data confirm the active process of underground seawater intrusion from the shoreline. It is to underline the partial inconsistency between the chemical concentration and the EC values of vertical log, as in the case of the piezometer #21, which in the southern transect is close to the shoreline. Despite #21, logs are confirming the general trend of increasing salinity as moving towards the shoreline (Fig. 3.7), the concentration of typical seawater components in the #21 water resulted lower than those of most samples collected from other piezometers along the same transect (Fig. 3.11). This apparent contradiction is very likely attributable to a different hydraulic transmissivity of different layers through which the all-screened piezometers develop. In particular, the lower layer of the piezometer stratigraphic sequence seems to have a lower transmissivity with respect to the upper layer. Under this condition, when the water column is static and the logs are performed, the vertical salinity is mainly affected by both the real geometry of the saltwater wedge and the density relationship between fresh, in the upper part, and seawater in the lower part. On the contrary, when the sampling pump is working (during sampling), a major inflow of freshwater in the piezometer is promoted by the higher transmissivity of the upper layer, thus creating a dilution within the piezometric pipe.

The diagram proposed by Alcalá and Custodio (2008) also supports the general presence of seawater intrusion in the system (Cl^-/Br^- molar ratio vs. Cl^-; Fig. 3.12). Most samples fall close to the Cl^-/Br^- seawater value and the seawater intrusion field, with just a few points close to those fields representative of coastal or inland areas (e.g. #6, #15, #18, #24). The graphs of Fig. 3.13, representing Cl^- vs. Na^+ (a) and vs. Mg^{2+} (b), respectively, in which conservative mixing lines (dashed) are also displayed, show that the water samples are arranged along a freshwater-seawater trend. The mixing was modeled starting from #18 (September 2020), as representative of

freshwater, at which seawater fractions were gradually added: from 1% up 100% (pure seawater). The sample that clearly deviates from the main trend is #6 in the Cl^- vs. Na^+ diagram, due to its Na^+-HCO_3^- composition.

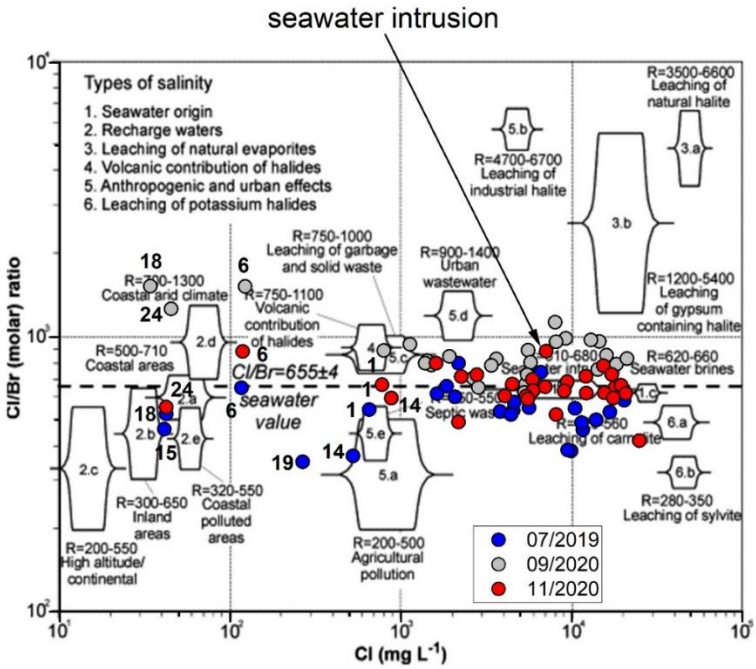

Figure 3.12 Diagram Cl^-/Br^- molar ratio vs. Cl^- (mg/L) for all the samples. Modified from Alcalá and Custodio (2008). See the text for further details.

Similar and more detailed information is achieved when the isotopic ratios of oxygen ($\delta^{18}O$) and hydrogen ($\delta^{2}H$) are taken into account, since they enable pointing out specific processes (e.g. evaporation, presence of different water components also in case of similar chemistry, etc.) in addition to the seawater intrusion. The $\delta^{2}H$ vs. $\delta^{18}O$ values of the analyzed waters (Tables 3.2, 3.6 and 3.8) are reported Fig. 3.14a, b and c for the July 2019, September 2020 and November 2020 campaigns, respectively. The diagrams also include the Global Meteoric Water Line (GMWL) (Craig, 1961), the V-SMOW (Standard Mean Ocean Water) and the Po river (Mollema et al., 2013) composition as well as the Northern Italy Meteoric Water Line (NIMWL: Longinelli & Selmo, 2003). The sample indicated with “Po” refers to the isotopic composition of the

Emilia-Romagna Channel that brings the Po river waters to the coastal farmland for irrigation.

The water samples tend to be distributed parallel to the GMWL and NIMWL and slightly shifted to the right, depicting a straight line with the SMOW. The clear increasing trend of the isotopic values suggests an increasing interaction and mixing between freshwater and seawater. Many samples are indeed arranged along the line that represents the binary mixing between SMOW and Po river waters. It is also worth noting that the isotopic values tend to be heavier for the "bot" than those of "top" samples in several sites where shallow and deep waters were collected. The former group has an isotopic composition that approaches that of Po, although in November 2020, especially with respect to that of September 2020, a clear shift along the mixing line, which is particularly evident for the Cerba canal (#18), is highlighted. For this surficial water, such increase in the isotope signature is congruent with the significant high EC value and chemical solute concentrations observed in November 2020, indicating a possible intrusion of seawater along the canal. In the other cases, the higher isotopic values with respect to the previous sampling periods is likely tied to the isotopic signal of local rainfall that occurred between September 2020 and November 2020 (Fig. 3.3). This hypothesis would confirm the significant infiltration rate that characterizes the phreatic sandy aquifer, which is also consistent with the general increase of the piezometric levels observed in November 2020 with respect to those of September 2020 (Fig. 3.6), as well as with the variability of the EC logs over seasons (Fig. 3.7).

A general arrangement of the samples along a mixing trend is also observed in the $\delta^{18}O$ vs. Cl^- diagram (Fig. 3.15), where the light blue box is representative of the seawater (SW) composition.

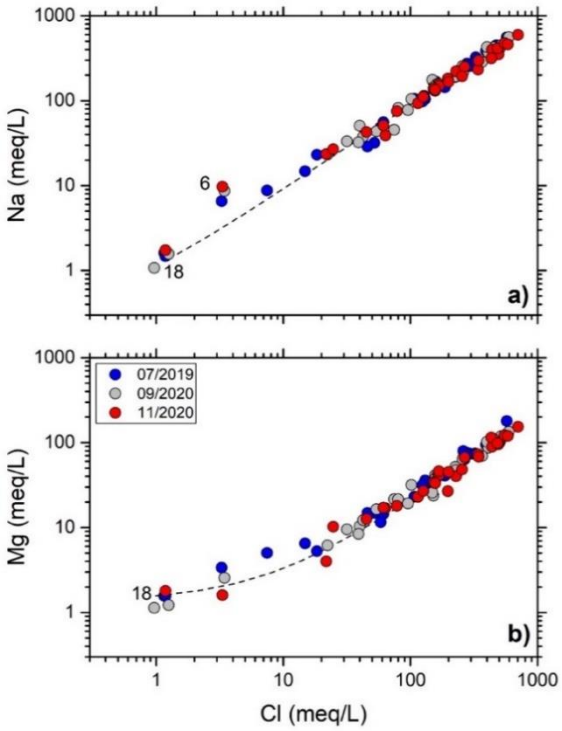

Fig. 3.13 Cl^- vs. Na^+ (a) and vs. Mg^{2+} diagrams. The dashed lines represent the geochemical modeling related to the mixing with seawater. See the text for further details.

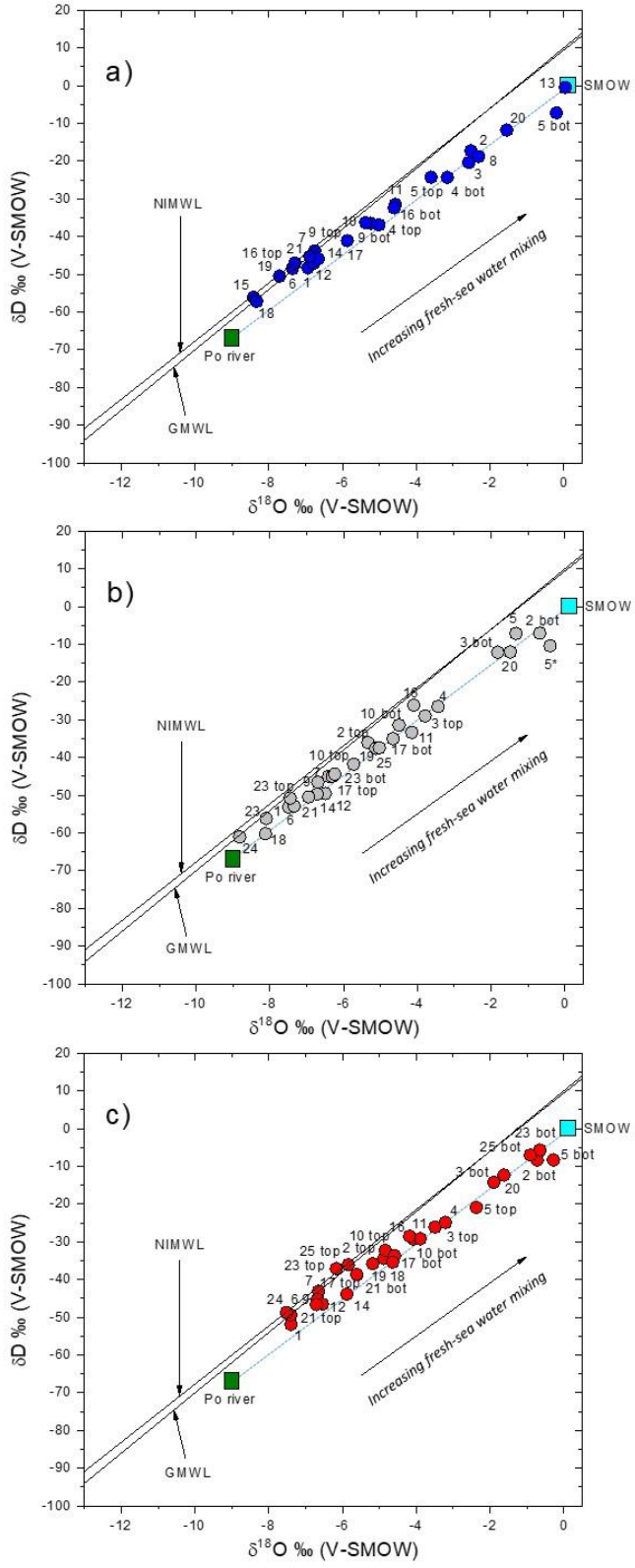

Fig. 3.14 $\delta^{18}O$ vs. $\delta^{2}H$ diagram for the investigated samples in a) July 2019, b) September 2020 and c) November 2020. See the text for further details.

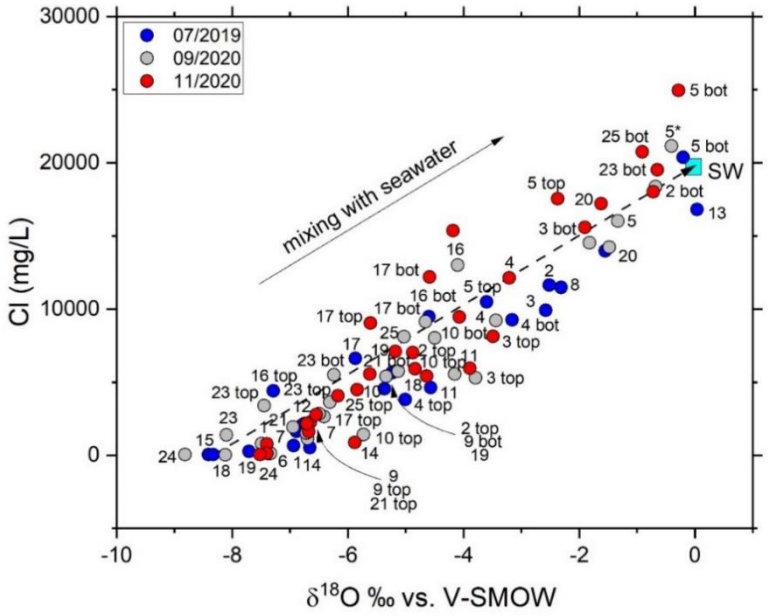

Fig. 3.15 $\delta^{18}O$ vs. Cl^- binary diagram. The light blue box represents the seawater (SW) composition. See the text for further details.

However, the conservative mixing freshwater-seawater is not the only process that occurs in the shallow aquifer of the Ravenna coastal area. If we again dwell on the L-L classification diagram (Fig. 3.16), the water samples seem indeed to define different trends starting from the Na^+-Cl^- field, i.e.: 1) along a hypothetical seawater/Ca^{2+}-HCO_3^- (freshwater) mixing line, as evidenced by the previous graphs, 2) to the Na^+-HCO_3^- and 3) the Ca^{2+}-Cl^- fields. This distinction, which has also been observed in other coastal areas affected by marine ingression (e.g. Capaccioni et al., 2005; Cerrina Feroni et al., 2010), should not be interpreted as the result of a simplistic mixing process involving generic fresh and seawater end-members, but also as a likely occurrence of cation-exchange reactions. Therefore, in order to evaluate the Mg^{2+}- and Ca^{2+}-excess and the Na^+- and K^+-deficiency (and vice versa) compared to the concentrations expected for a sea and ground water mixing process, the fraction of seawater from each sample was first calculated by a mass balance of chloride, since it is not involved in any ion exchange process. The considered chloride concentration as representative of freshwater was that of #18 (September 2020). Subsequently, the differences of the aforementioned cations (Δ) with respect to the concentrations expected from mixing

between seawater and groundwater were calculated, as suggested by Cerrina Feroni et al. (2010). In Fig. 3.17, the semi-logarithmic correlation diagrams between chloride and ΔCa^{2+}, ΔMg^{2+}, ΔNa^{+} and ΔK^{+} for the sampled waters are reported. Ion exchange processes are evident in terms of both Ca^{2+} and Mg^{2+} enrichment and Na^{+} and K^{+} depletion for those samples belonging to the Na^{+}-Cl^{-} geochemical facies. Among the most affected samples, #5 stands out, even if its composition, which had TDS values even higher than those of seawater, could also indicate the local presence of hypersaline fluids at depth, as it is apparently not influenced by the nearby lagoon that receives a freshwater input from the Cerba canal. An enrichment of Ca^{2+} seems to determine the compositional shift of sample #7 towards Ca^{2+}-Cl^{-} waters, as also highlighted in the L-L classification diagram (Fig. 3.16) and probably resulting of seawater ingression into an originally freshwater aquifer (Capaccioni et al., 2005). These evidences also result from an examination of the Cl^{-} vs. Ca^{2+} graph (Fig. 3.18), constructed similar to the diagrams of Fig. 3.13, in which the conservative seawater-freshwater mixing line (dashed) is also displayed. In particular, the arrangement of the points related to #1 and, in particular, #6 suggests a possible refreshening process of an originally saline aquifer, mainly determined by a depletion of Ca^{2+} (Capaccioni et al., 2005). This is again confirmed by the shift towards the Na^{+}-HCO_3^{-} field in the L-L diagram (Fig. 3.16), suggesting an underground transfer of freshwater by canals in the southern part of the area, with particular regard to the Cerba canal that flows in the proximity of the piezometer #6.

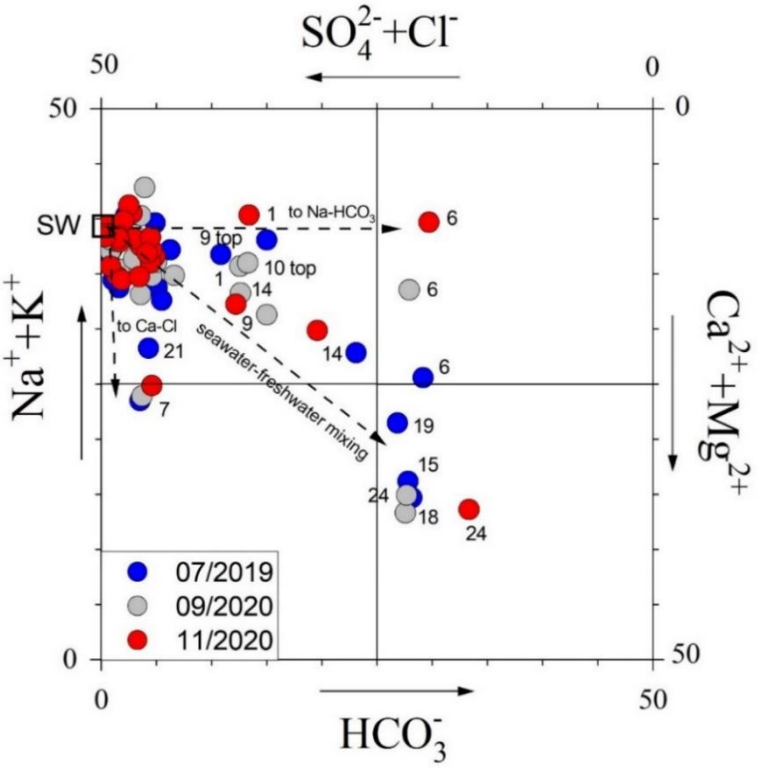

Fig. 3.16 L-L diagrams for all the investigated samples. SW indicates the average composition of seawater. See the text for further details.

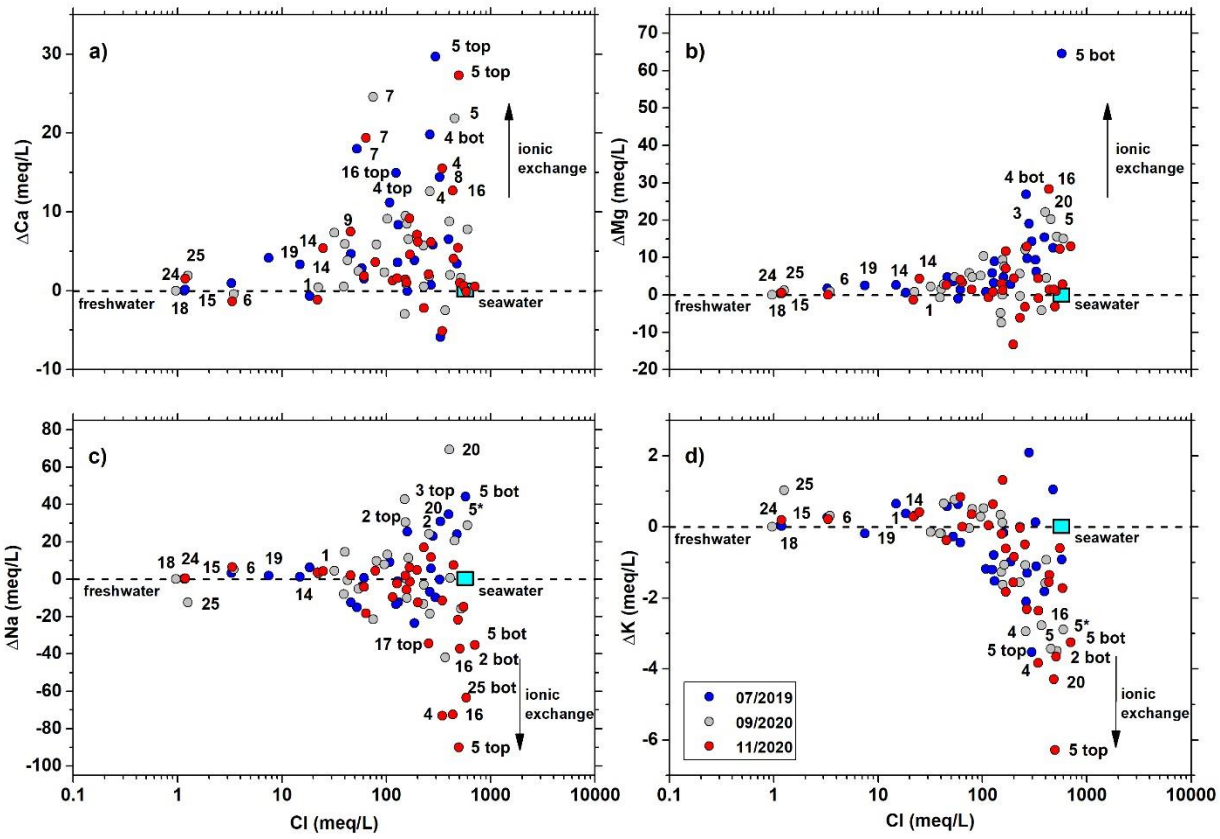

Fig. 3.17 Semi-logarithmic correlation diagrams between chloride and ΔCa (a), ΔMg (b), ΔNa (c) and (d) ΔK for the sampled waters. The light blue box represents the seawater (SW) composition

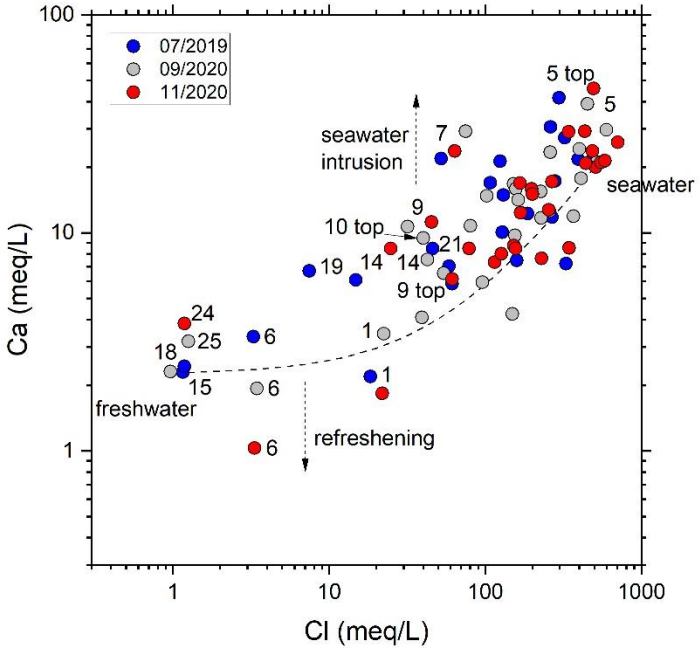

Fig. 3.18 Cl^- vs. Ca^{2+} binary diagram. The dashed lines represent the geochemical modeling related to the mixing with seawater. See the text for further details.

On the contrary, the Lamone river seems to act as a possible carrier of saline water into the aquifer, as shown in the $\delta^{18}O$ vs Cl^- diagram (Fig. 3.19), where the light blue box is representative of the seawater (SW) composition. The graph plots the sampled points of the Lamone river and the compositions of #10, located near the river, and reports two hypothetical mixing trends related to the “Lamone-seawater“ and “local infiltration water-seawater”, respectively. The black arrow (Fig. 3.19) identifies the compositional variation that affects #10, differentiating between superficial (top) and deep (bot) water, confirming the salinization effect induced by the Lamone river to the shallow aquifer.

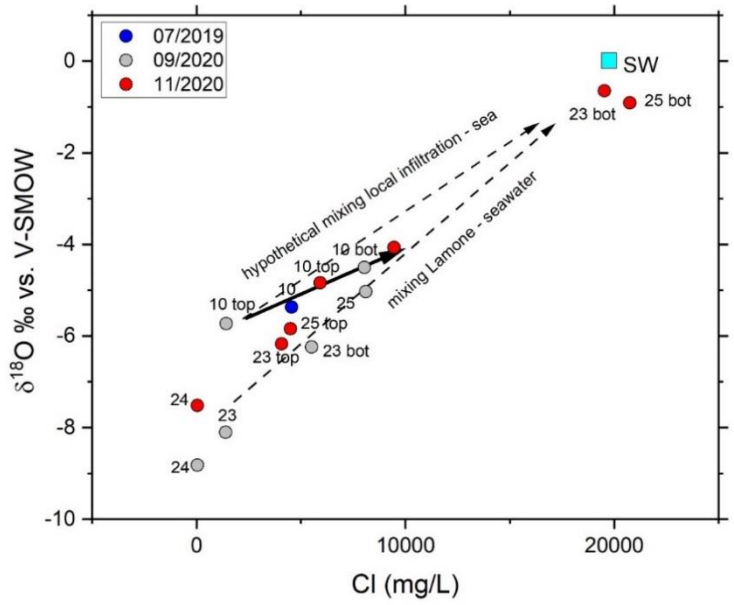

Fig. 3.19 $\delta^{18}O$ vs Cl^- diagram, plotting the sampled points of the Lamone river and the sample #10. The light blue box is the seawater (SW) composition. See the text for further details

Actually, by using the $\delta^{18}O$ vs Cl^- conservative diagram for all those waters close to the northern and southern transects (Fig. 3.11), it is possible to better define the role of the Lamone river and Cerba canal with respect to the aquifer system and recognize the main components and mixing processes in the groundwater system, as follows:

- In the northern transect (Fig. 3.11a), the points representative of freshwater (low Cl^-) are in the $\delta^{18}O$ range of -6 ÷ -9 ‰, in which the lower isotopic signatures concern the inland samples from the Lamone river (#23, #24), whereas the heavier signatures regard the shallow piezometer #14 (total depth 6 m). Taking into account all these information, but also in agreement with the isotopic data by Longinelli and Selmo (2003) and Tazioli et al. (2019), we can consider the above-mentioned Lamone river samples as representative of the rainfall occurring in the hill-mountain catchment of this watercourse. On the other hand, the #14 waters represent the locally infiltrated rainwater. The placement of all the other samples in the diagram is the result of mixing between these two main components (inland Lamone river, LR, and local infiltration

water, LIW) and the seawater (SW). In particular, at #20 (on July 2019 and September 2020) and #11 it is well recognizable the seawater intrusion that directly occurs in the aquifer from the shoreline and mixes with the locally infiltrating rainfall (points lying on the LIW-SW mixing line). Most of the remaining groundwater samples interested by medium-high to very high Cl^- concentration (in any case higher than 1500-2000 mg/L) indicates the prevalence of an indirect mechanism of saltwater intrusion, which occurs by a transfer to the aquifer of the Lamone waters mixed with the seawater rising along the same river. As already discussed, this mechanism is particularly evident for #10 (see also Fig. 3.19 and relative discussion). However, it also appears dominant in other cases, as the Cl^- concentration increases and tend to approach the LR-SW mixing line for the waters samples from the same piezometer (e.g. #12 or #9, but also #20 of November 2020 with respect to the others from the July 2019 and September 2020 surveys). The input from the Lamone river seems also evident in the inland part of the studied area, i.e. in correspondence of #19, whose groundwater present absolute values and variations of Cl^- concentrations and $\delta^{18}O$ values consistent with the range of the Lamone samples at #24 and #23. It should be noted that in July 2019 #19 shows the lowest isotopic signature observed in all the groundwater samples analyzed in this study. The relative value of $\delta^{18}O$ is incompatible with rainfall occurring at the local altitudes, but it is consistent with the rainfall occurring in the hill-mountain zones and brought to the coastal plain by the Lamone river (see as the sample #19 almost overlaps the samples collected in the river at the nearby #24 site).

- In some piezometers from, or close to, the southern transect (Fig. 3.11b) is also evident the direct mixing process between the seawater wedge developed from the shoreline and groundwater generated by local rainfall infiltration (all the samples from #3 and most from #4, lying over the LIW-SW mixing line). Furthermore, the role of stream waters seems also to be important in terms of groundwater feeding and its effects on the groundwater quality in this sector. The waters from the Cerba canal (#18), entering the aquifer and affecting the isotope signatures of local groundwater, are representative of this condition, as in most sampling periods they are characterized by low Cl^- concentrations (and EC values; see also logs data in Fig. 3.7) and $\delta^{18}O$ values lower than -8 (testifying a drainage from hill zones). As already mentioned, this is particular evident at the shallow piezometer #6 (total depth 4 m), which is close to

the canal and hosts waters with intermediate characteristics between the freshwater of the Cerba canal (#18) and locally infiltrated rainfall. Starting from this term of mixing, represented by #6 in Fig. 3.11b, a distribution of groundwater samples (all the #21 samples, the #17top sample in September 2020, the #5 sample in July 2019 and the #4 sample in November 2020) along a line towards the point representative of the seawater (SW) is observed. Such an alignment is suggesting a mixing process between the seawater wedge from the shoreline and groundwater generated by the combination of locally infiltrated rainfall and freshwater from the Cerba canal. Most samples collected at #17, the latter being very close to the Cerba canal (CC), lie directly on the CC-SW line, which is representative of a theoretical mixing between the freshwater of the same canal (#18, in most cases) and seawater. Contrarily to the Lamone river, no several sampling points distributed within the Cerba canal from the inland part of the studied area down to the sea are available. Consequently, it was not possible to experimentally verify whether a significant mixing seawater-freshwater was really occurring within the canal. However, if we consider the "#6-SW" alignment and the location on the territory of those piezometers belonging to it, as well as the low EC values measured in the lagoon close to #5 where the Cerba canal flows before reaching the sea, a significant and persistent process of mixing freshwater-seawater within the canal is unlikely. This appears at least confirmed at the sole monitoring point of the Cerba canal (#18), where the EC values and chemical-isotopic features congruent with the presence of seawater were only recognized in one survey (November 2020). Moreover, when the $\delta^{18}O$-$\delta^{2}H$ pair a significant evaporation process can be excluded, since the brackish water at #18 in November 2020 falls on the LIW-SW line and not on the CC-SW line (Fig. 3.11b), suggesting a possible input in the canal of the local groundwater mixed with SW. Therefore, a mixing within the Cerba canal between its typical freshwater and SW would seem unlikely also in that period. On the contrary, the possible drainage within the canal of a local groundwater mixed with the seawater wedge would have been favored by the very low hydrometric level (-1.46 a.s.l.) measured in that period at #18 (Table 3.1). Given the absence of a freshwater-seawater mixing within the canal, we can conclude that the #17 samples lying on, or close to, the CC-SW line (Fig. 3.11b) are likely the results of a local mixing process between freshwater infiltrated from the same canal and the SW presents at

depth in the aquifer (the piezometer develops down to a depth of 19 m; the bottom is at about -17 m a.s.l.).

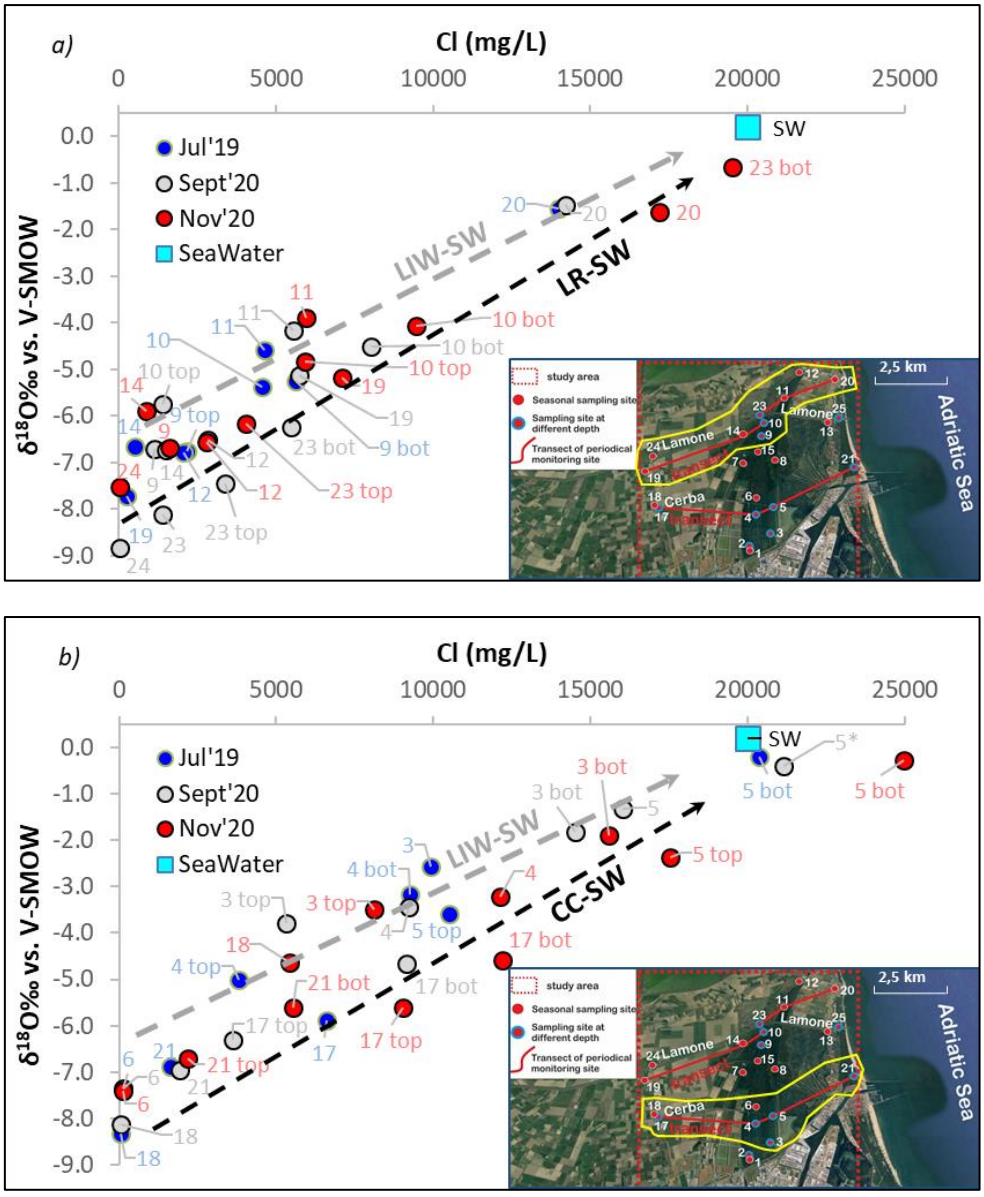

Fig. 3.11 $\delta^{18}O$ vs Cl^- diagram, plotting the points sampled along, or close to, the northern (a) and southern (b) transects. LIW-SW is the theoretical line of mixing between local infiltration water and seawater; LR-SW and CC-SW are respectively the theoretical lines of mixing Lamone river-seawater and Cerba canal-seawater. The yellow polygons in the maps encompass the points considered in the respective diagrams

As for the sulfate, the TDS vs. SO_4^{2-} (in mg/L) binary diagram of Fig. 3.11 shows that with respect to the line representing a hypothetical mixing trend between freshwater

and seawater, a significant number of water samples is enriched in SO_4^{2-} while others show a SO_4^{2-} depletion.

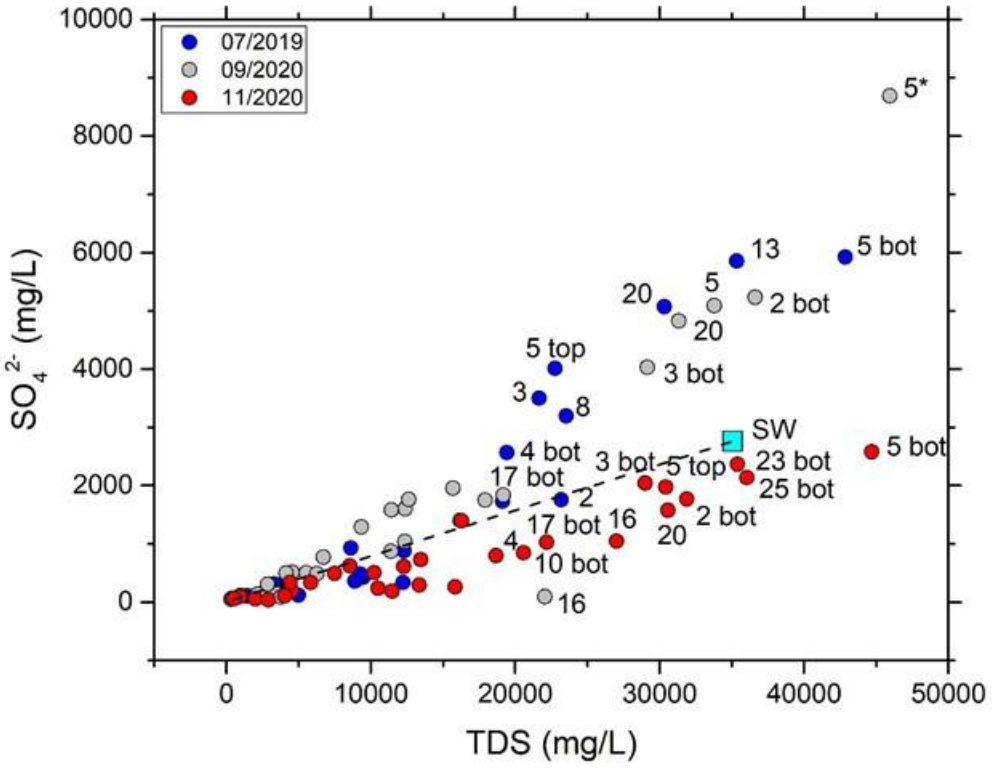

Fig. 3.12 TDS vs. SO_4^{2-} diagram. The light blue box represents the seawater (SW) composition. See the text for further details.

Greggio et al. (2020) suggested that the sulfate depletion may be due to organic matter degradation in anoxic conditions, producing H_2S and favoring the precipitation of sulfides (e.g. pyrite) by microbial activity and fed by the constant SO_4^{2-} input from seawater (Mollema et al., 2013 and references therein). Contrarily, SO_4^{2-} enrichments can likely be related to an opposite process, i.e. pyrite oxidation favored by an increase in dissolved oxygen (Greggio et al., 2020 and references therein).

3.4.2 Trace elements

The selected trace elements from the shallow aquifer of Ravenna are referred to June 2019 and September 2020 sampling campaigns. It should be noted that siderophile elements (Fe, Mn, Co and so forth) were not analyzed, being basic components of the metallic material that makes up most of the sampled piezometers. The used regulatory reference is the following: Legislative Decree 152/2006 Annex 5, Part IV, Table 2 - Groundwater Limits (Contamination Threshold Concentration).

Al was below the required threshold (200 µg/L) in all the samples, except for sample #8 in July 2019, probably depending also in this case on material the piezometer was built. Sb was always well below the permissible concentration (5 µg/L). As reported in Tables 3.3 and 3.7, many samples had As concentration above the regulatory limit (10 µg/L) and in the same range previously highlighted by Dinelli et al. (2010), Mollema et al. (2013, 2015) and Greggio et al. (2020). A possible As source may be related to pyrite oxidation, this mineral being formed by SO_4^{2-} reduction during decomposition processes of organic material hosted within the alluvial sediments (Dinelli et al., 2010; Mollema et al., 2013, 2015; Greggio et al., 2020). According to Greggio et al. (2020), the high concentrations of Ba (up to 1.36 mg/L) and SiO_2 (up to 25 mg/L) are attributable to the alteration of silicate minerals during prolonged water–sediment interaction processes. The relatively high concentrations of B, with many samples exceeding the regulatory limit (1 mg/L; Tables 3.3 and 3.7), are intimately associated with the intrusion of seawater (Greggio et al., 2020), whose average content is 4.6 mg/L. On the contrary, the low Li concentrations (up to 64 µg/L) probably indicate depletion due to sorption processes by phyllosilicates during the seawater intrusion (Greggio et al., 2020 and references therein). Rb (up to 104 µg/L) and Sr (up to 8.6 mg/L) concentrations are in the range of those reported by Greggio et al. (2020), suggesting a conservative mixing in the aquifer for these elements (Mollema et al., 2015). V (up to 2.9 µg/L) concentrations did not show any specific criticality.

3.5 Conceptual model and conclusions

The hydrogeological, physical-chemical and geochemical-isotopic data, as well as their mutual comparison, allowed to recognize the main water components involved in the studied coastal system, and define the principal physical and chemical processes presently occurring. In most cases, the mechanisms that regulate these processes were recognized and new insights into the processes of seawater intrusion and aquifer

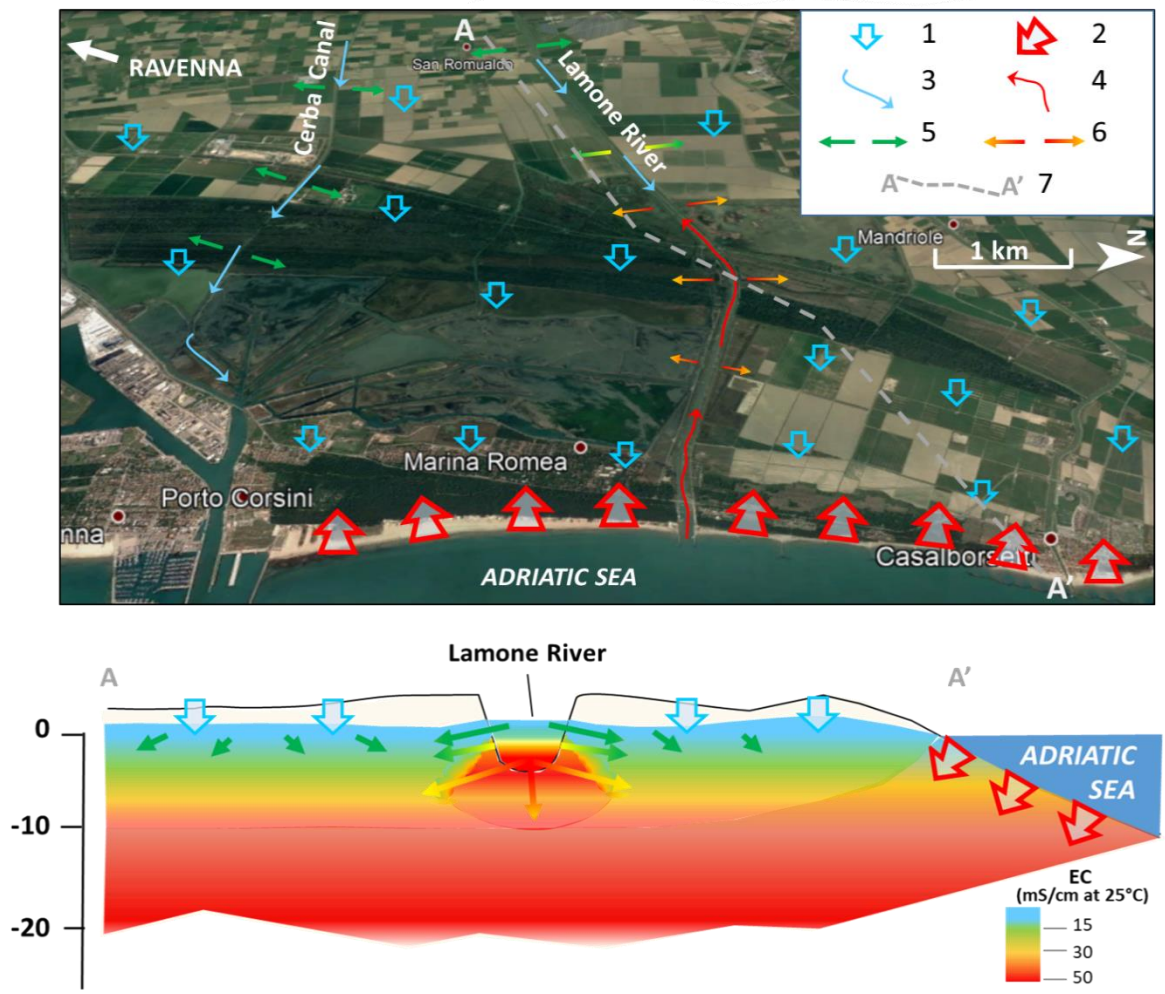

recharge with respect to the previous studies were provided.

In other words, at the end of the experimental activities a semi-quantitative conceptual model of the coastal shallow aquifer that extends in the northern part of the Ravenna municipality can be proposed. A description of the conceptual model is below provided and synthetically graphitized in Fig. 3.12.

Fig. 3.13 Schematic conceptual model of the shallow coastal aquifer of Ravenna: 1) local rainfall infiltration; 2) seawater intrusion from the shoreline; 3) freshwater flow in superficial water courses; 4) seawater intrusion along river beds; 5) transfer of freshwater from superficial water courses to groundwater; 6) transfer of saline and brackish water from the superficial water courses to groundwater; 7) trace of the section A-A'. EC= Electrical conductivity

The main aspects describing the conceptual model of the sandy phreatic aquifer under study can be summarized, as follows:

- The aquifer receives three main water inputs, which consist of diffuse recharge by local rainfall, concentrated infiltration by superficial watercourses and saline wedge from the shoreline.
- The combination of these components is quite evident all over the system, which therefore can be regarded as highly dynamic. The hydrological regime indeed seasonally affects the mixing among the different inputs, thus highlighting how the aquifer system is strongly sensitive to the hydrologic regime and consequently to the climate conditions. At the same time, such a behavior furthermore points out that the aquifer can generally be characterized by a good permeability.
- Within the aquifer, saline and brackish waters prevail although, at several sites, down to depth of 5 m, freshwater or relatively low EC (< 5 mS/cm) waters are present, especially during the wet season. The surface watercourses significantly contribute to supply freshwater to the shallow aquifer, with particular reference to the Cerba canal. Nevertheless, in the inland sector of the coastal area the Lamone river also seems to provide freshwater able to feed the aquifer. The two main river courses are indeed characterized in the inland parts by an isotopic signature typical of the mountain-hill areas, which enable tracing the water transfer towards the aquifer.
- The seawater intrusion occurs into the aquifer by two main mechanisms: i) the typical underground intrusion of the saline wedge from the shoreline, and ii) the feeding from watercourses into which seawater is entering the riverbed from their mouth. In this second case, the Lamone river plays a key role, because it is affected by seawater intrusion along the riverbed up to some kilometers inland (at least 5 km) and it transfers seawater and/or a mix of seawater and freshwater into the aquifer. On the other hand, the Cerba canal does not appear to be significantly interested by seawater. It is

essentially transferring its freshwater to the aquifer, thus contributing together with the local rainfall infiltration to mitigate the underground salt wedge effects.

- The freshwater-seawater mixing, occurring in the aquifer, is not everywhere chemically conservative. In some sectors of the groundwater system, ion exchange processes were recognized, indicating dynamics of the freshwater-seawater transition zones or even complete replacements of one water type by the other. In particular, seawater is intruding zones previously dominated by freshwater in the sector close to the Lamone river, but also near the shoreline. On the contrary, in the sector where the freshening processes mediated by the Cerba canal are active, freshwater invade zones of the aquifer previously interested by seawater. Other physical-chemical processes, such as phenomena of SO_4^{2-} reduction during the decomposition of organic material, or mineral oxidation (e.g. pyrite), seem to be alternating in various zones according to the oxidant-reductive conditions. Furthermore, such alternating phases could be at the origin of storage in solid phase and successive re-mobilization in water solution of trace elements, with contents higher that the Contamination Threshold Concentrations defined by environmental legislations (e.g. As resulted to be over 10 µg/L in many samples).

As a general outcome, this study has remarked the high vulnerability of the shallow aquifer to seawater intrusion and the significant sensitivity of the system to meteo-climate conditions since it suffers the effects tied to the intrusion processes. These features are particularly exposing this aquifer system, given the general trend of climate evolution and the related sea level rise phenomena. Accordingly, the threats for the studied shallow aquifer can result to be enhanced by the fact that the system can also receive seawater by the surface watercourses. Owing to the effects of sea level rise and climate conditions, which are increasingly characterized by extreme regimes with long dry periods, the superficial watercourses can facilitate the inland transfer of seawater up to several kilometers, within their riverbeds and then towards the groundwater system. The management of the territory is expected to take into account such specific aspects, in order to plan appropriate actions for mitigating the effects of sea level rise and climate evolution and guarantee the survival of peculiar ecosystems such as those of the Ravenna coastal system.

3.6 References

Alcalá, F. J., & Custodio, E. (2008). Using the Cl/Br ratio as a tracer to identify the origin of salinity in aquifers in Spain and Portugal. Journal of Hydrology, 359(1-2), 189-207.

Amorosi, A., Colalongo, M.L., Pasini, G., Preti, D., 1999. Sedimentary response to late squaternary sea-level changes in the Romagna Coastal Plain (Northern Italy). Sedimentology 46, 99– 121.

Antonellini, M., Mollema, P., Giambastiani, B. et al. (2008). Salt water intrusion in the coastal aquifer of the southern Po Plain, Italy. Hydrogeol J 16, 1541. https://doi.org/10.1007/s10040-008-0319-9.

Antonellini, M., Mollema, P. (2010). Impact of groundwater salinity on vegetation species richness in the coastal Pine forests and wetlands of Ravenna, Italy. Ecol. Eng. 236, 1201–1211.

Amorosi A, Centineo MC, Dinelli E, Lucchini F, Tateo F (2002) Geochemical and mineralogical variations as indicators of provenance changes in Late Quaternary deposits of SE Po Plain. Sedimentology 151:273–292

Bondesan M, Favero V, Vignals MJ (1995). New evidence on the evolution of the Po-delta coastal plain during the Holocene. Quat Int 29/30:105–110.

Campo, B., Amorosi, A., Vaiani, S. C. (2017). Sequence stratigraphy and late Quaternary paleoenvironmental evolution of the Northern Adriatic coastal plain (Italy). Palaeogeography, Palaeoclimatology, Palaeoecology 466: 265–278.

Capaccioni, B., Didero, M., Paletta, C., & Didero, L. (2005). Saline intrusion and refreshening in a multilayer coastal aquifer in the Catania Plain (Sicily, Southern Italy): dynamics of degradation processes according to the hydrochemical characteristics of groundwaters. Journal of Hydrology, 307(1-4), 1-16.

Capo D. (2011) Studio dell'intrusione salina all'interno di un acquifero freatico costiero (Ravenna; Italia), PhD Thesis, Dottorato di Ricerca in Scienze della Terra- XXIV° CICLO, Università di Bologna, 212 pp.

Cerrina Feroni, A., Da Prato, S., Doveri, M., Ellero, A., Lelli, M., Marini, L., Masetti G., Nisi, B., Raco, B. (2010). Caratterizzazione Geologica, idrogeologica e Geochimica dei Corpi Idrici Sotterranei Significativi della Regione Toscana (CISS): 32CT010 "Acquifero costiero tra Fiume Cecina e San Vincenzo", 32CT030 "Acquifero costiero tra Fiume Fine e Fiume Cecina", 32CT050 "Acquifero Cecina". Mem. Descr. Carta Geol. d'It. LXXXIX, pp. 5–80.

Craig, H. (1961). Isotopic variations in meteoric waters. Science, 133(3465), 1702-1703.

C.S.I.-Ra Project 2009. Coastal Salt Intrusion (Ravenna Area) – Rapporto Finale. Convenzione ENI-FAM 1/2009. 8 Volumi.

Dinelli, E., Kralj, M., Schwarz, S., Antonellini, M., Gabbianelli, G., & Hamer, K. (2010). Groundwater chemistry and arsenic occurrence in the phreatic aquifer system of the San Vitale pine forest. SWIM21 - 21st Salt Water Intrusion Meeting, 16-19.

Giambastiani B.M. (2007) Evoluzione idrologica ed idrogeologica della Pineta di San Vitale. Phd Thesis, Dottorato di Ricerca in Scienze Ambientali: Tutela e Gestione delle Risorse Naturali, XXII Ciclo, Alma Mater Studiorum - Università di Bologna, 200 pp.

Giambastiani, B. M., Antonellini, M., Essink, G. H. O., & Stuurman, R. J. (2007). Saltwater intrusion in the unconfined coastal aquifer of Ravenna (Italy): a numerical model. Journal of Hydrology, 340(1-2), 91-104.

Greggio, N., Giambastiani, B., Mollema, P., Laghi, M., Capo, D., Gabbianelli, G., ... & Dinelli, E. (2020). Assessment of the Main Geochemical Processes Affecting Surface Water and Groundwater in a Low-Lying Coastal Area: Implications for Water Management. Water, 12(6), 1720.

Laghi, M. (2010). L'interazione tra acque fluviali superficiali e acque sotterranee in zona costiera: il sistema dell'estuario del Fiume Lamone, PhD Thesis, Dottorato di Ricerca in Scienze Ambientali: Tutela e Gestione delle Risorse Naturali, XXII Ciclo, Alma Mater Studiorum - Università di Bologna, 214 pp.

Laghi, M., Mollema, P., Antonellini, M. (2010). The influence of river bottom topography on salt water encroachment along the Lamone River (Ravenna, Italy), and implications

for the salinization of the adjacent coastal aquifer. In: World Environmental and Water Conf., Providence, USA.

Langelier, W. F., & Ludwig, H. F. (1942). Graphical methods for indicating the mineral character of natural waters. Journal-American Water Works Association, 34(3), 335-352.

Longinelli, A., & Selmo, E. (2003). Isotopic composition of precipitation in Italy: a first overall map. Journal of Hydrology, 270, 75–88.

Mollema, P. N., Antonellini, M., Dinelli, E., Gabbianelli, G., Greggio, N., & Stuyfzand, P. J. (2013). Hydrochemical and physical processes influencing salinization and freshening in Mediterranean low-lying coastal environments. Applied Geochemistry, 34, 207-221.

Mollema, P. N., Antonellini, M., Dinelli, E., Greggio, N., & Stuyfzand, P. J. (2015). The influence of flow-through saline gravel pit lakes on the hydrologic budget and hydrochemistry of a Mediterranean drainage basin. Limnology and oceanography, 60(6), 2009-2025.

Rizzini, A. (1974). Holocene sedimentary cycle and heavy mineral distribution, Romagna-Marche Coastal Plain, Italy. Sedimentary Geology 11, 17–37.

Tazioli, A., Cervi, F., Doveri, M., Mussi, M., Deiana, M., Ronchetti, F. (2019). Estimating the isotopic altitude gradient for hydrogeological studies in mountainous areas: Are the low-yield springs suitable? Insights from the northern Apennines of Italy. Water (Switzerland) 11, 1–17. https://doi.org/10.3390/w11091764.

Vandenbohede, A., Mollema, P.N., Greggio, N., Antonellini, M. (2014) Seasonal dynamic of a shallow freshwater lens due to irrigation in the coastal plain of Ravenna, Italy. Hydrogeology Journal, 22 (4), pp. 893-909.

3.7 Appendix

3.7.1 Characteristics and coordinates for each site

Characteristics and coordinates of the points belonging to the network of survey.

Code	Type	Depth (m)	Est (GaussBoaga_Roma40)	Nord (GaussBoaga_Roma40)	Reference altitude by GPS (m a.s.l.)	GPS altitude error (m)
1	**piezometer**	6	2299247.58	4926985.29	2.03	1.53
2	**piezometer**	14	2299230.49	4927177.43	1.50	0.91
3	**piezometer**	6	2300012.50	4927728.65	0.20	0.86
4	**piezometer**	13	2299509.21	4928614.70	0.91	< 0.05
5	**piezometer**	14	2300187.55	4928919.24	1.06	< 0.05
6	**piezometer**	4	2299512.19	4929408.71	1.25	< 0.05
7	**piezometer**	4	2299657.85	4931360.55	1.89	0.98
8	**piezometer**	6	2300422.58	4931370.98	1.54	< 0.05
9	**piezometer**	17	2299863.93	4932843.53	1.62	< 0.05
10	**piezometer**	16	2300041.04	4933634.69	2.61	1.28
11	**piezometer**	6	2301095.45	4935391.44	1.52	< 0.05
12	**piezometer**	6	2301964.81	4937354.00	3.38	1.30
14	**piezometer**	6	2299142.38	4932951.26	1.75	< 0.05
15	**canal**	-	2299700.63	4931862.11	0.37	< 0.05
16	**piezometer**	20	2296993.40	4925241.20	0.17	< 0.05
17	**piezometer**	19	2295680.94	4929027.20	1.48	< 0.05
18	**canal**	-	2295593.55	4929103.65	3.29	< 0.05
19	**piezometer**	10	2294918.87	4930946.83	1.51	< 0.05
20	**piezometer**	12	2303734.57	4936732.80	1.86	1.03
21	**piezometer**	12	2303767.97	4930923.00	1.50	1.71
23	**canal**	-	2299830.63	4934270.68	6.57	< 0.05
24	**canal**	-	2295168.36	4931825.65	9.36	< 0.05
25	**canal**	-	2303540.26	4934013.27	4.76	< 0.05

3.7.2 Sampling form for each site

4. PILOT AREA: NERETVA DELTA

4.1 Study area

The Neretva River flows only 22 km of its 225 km course through Croatia. In its upper reaches the Neretva is a torrential mountain river, but in the last 30 km its flow calms down in a wide alluvial valley with several river courses forming a delta over an area of about 12,000 hectares before it flows into the Adriatic Sea. The soils in the Neretva Delta were formed by the deposition of alluvial and soil material washed out of the hilly karst area within the basin. Attempts to cultivate the wetland through melioration and hydraulic engineering measures have reduced the delta over time from a former 12 runs to only 3 runs, leaving parts of a Mediterranean wetland as one of the last and most valuable remaining wetlands in Europe. These parts are now protected as ornithological and ichthyological reserves and as a natural landscape. The river valleys of the Croatian karst region, including the Neretva delta, are particularly fragile and vulnerable ecosystems and therefore a valuable subject for professional and scientific studies.

In this region, between the main course of the Neretva, the side channel and the Adriatic Sea, there are about 5,000 hectares of irrigated agricultural land, which today is mainly used by family farms. Agriculture is now the most important economic activity in the area, providing a livelihood for more than 30,000 people.

Both natural values and habitat diversity and agricultural use depend primarily on the water balance of the area, which is under the influence of the Neretva River. Numerous karst watercourses within the basin bring large amounts of fresh water into the valley, especially in winter, replenishing the aquifer. In addition, the delta is under considerable maritime influence. Due to its specific hydrogeological characteristics, seawater infiltrates the surface and groundwater streams, especially Neretva River. Salt enters the small watercourses from saline springs located at the edge of the valley - from an aquifer where the water is saline, especially in deeper layers. The changes in hydrological conditions are significantly influenced by numerous hydraulic

engineering projects and facilities in the catchment area of the Neretva in its headwaters (Bosnia and Herzegovina) - hydropower plants and reservoirs - which contribute to increasingly intensive seawater intrusion and cause groundwater salinization.

Irrigation is a compulsory agricultural practise in this region. However, it is the withdrawal of water for irrigation that can increase seawater intrusion and increase the salinity of springs. The use of saline water for irrigation causes what is known as "secondary salinization" - a degradation of soil quality that is harmful from both an environmental and economic perspective. Extensive research has been carried out in recent years to undertake an agricultural and environmental assessment of the region, including detailed soil mapping, monitoring of water and soil salinity, identification of soil contaminants and recent deposits of heavy metals. It was found that soil salinization in the Lower Neretva region occurs in three ways: Formation of production areas by digging deep saline sediments to the surface; capillary rise of saline water in the soil profile; and irrigation with saline water. The Neretva Delta is located on the southern Adriatic coast of Croatia (43°00 N, 17°30 E) (Fig. 1). It is an intensively managed riparian delta, the extent of which has been limited to 12 thousand hectares thanks to the activities of numerous land reclamation projects. (Fig. 1). A detailed description of the geomorphology, soil characteristics and land use of the floodplain can be found in Romić et al. (2012). The most specific feature of the site is the lower-lying parcels with predominantly polder-like soils, which were formed in the past by intensive land reclamation and hydromelioration. The functionality of the polder system is maintained by a network of pumping stations that protect the area from flooding.

The hydraulic transport system of the polder compartments is generally based on the drainage system, which consists of a network of drainage canals, pumping stations and gates complexes to release water into canals that discharge the water into the sea. The excess water that needs to be discharged from the polder is mainly generated by precipitation and can be reduced by evapotranspiration or infiltration. The amount and distribution of precipitation over time are important not only to quantify the amount of water to be discharged, but also because they strongly influence water quality.

The lower Neretva River Valley was formed on two very different groups of sediments: (1) Mesozoic and Paleogene carbonate rocks with some Paleogene fl ysch; and (2) Quaternary sediments and weakly lithi fied deposits. Carbonate rocks form the bedrock of the valley, its flanks, and smaller isolated hills within the valley. These rocks are highly fractured and deeply karstified. Numerous faults, fissures, joints, and sinkholes make the carbonate rocks highly permeable to water and allow for the accumulation and circulation of groundwater. However, the permeability of these rocks can vary greatly depending on the degree of faulting and karstification. One of the main characteristics of these rocks is that all direct precipitation immediately percolates into the subsurface, with the exception of large and prolonged precipitation events that may result in brief surface runoff. Such runoff also often discharges into percolating streams or may flood the valley surface. The flysch deposits present along the northwestern and southeastern valley margins are of limited thickness and lateral extent. These deposits are largely impermeable, but are cut by faults and provide a partial barrier to groundwater flow. Surficial Quaternary Sediments consists mainly of peat and clay (organic marsh deposits) underlain by clayey sands, sands of variable grain size, sandy clay, gravelly sands, sandy gravels and Holocene gravels (alluvial sediments) and Pleistocene conglomerates. Within these sediments there are three main aquifers: (1) in Holocene sands; (2) in Middle Pleistocene gravels; and (3) in Lower Pleistocene conglomerates and gravels. Above sea level, fresh water with a free water table from the surrounding karst massif directly feeds the valley, while at elevations below sea level, the water is saline and enters the valley under pressure. In winter, the lower Neretva area needs to be protected from flooding and the water level in the drainage channels needs to be regulated, while in the dry growing season it needs to be irrigated and protected from seawater intrusion. Runoff from the Neretva River varies greatly, with minimum amounts occurring in summer and autumn and maximum amounts in winter and spring (Romić and Vranjes 2010). Due to the many underground karst streams in the basin, there are many springs that carry large amounts of water, especially in winter. Groundwater coming from this surrounding karst area supplies numerous streams, lakes and cavities. This great variability in the geology and

morphology of the karst bedrock favours water flow and mixing of seawater with freshwater. Seawater infiltrates surface waters, especially Neretva River. Salinization of smaller streams is caused by mixing with water from brackish karst springs at the limestone margins of the valley (Bonacci and Roje-Bonacci 1997) and from the aquifer with highly saline groundwater in the deeper layers. Numerical modelling has shown significantly different characteristics of the shallow and deep aquifers in the lower Neretva River (Gotovac 2005). The deep aquifer has been shown to be connected to the sea, so salinity does not change significantly in either regime, dry or rainy. Since there is a constant hydraulic gradient in the vertical direction, the model shows that 10 million cubic metres of highly saline brackish water flow through the confining clay layer into the shallow aquifer annually (Gotovac 2005).

The dynamics of the Neretva Delta are determined by the tidal fluctuations of the Adriatic Sea and upstream tributaries, which depend on the operational aspects and management of the hydropower system of the reservoirs and dams built in its middle reaches in BiH. Neretva River has a distinct seasonal character, typical of the Mediterranean climate, with a well-defined high water period from October to April and a low water period from May to September.

This report covers the implementation of activity 4.1. „Case studies: physical investigation“ with following:

1. spatial, temporal and methodological characterisation of surface water, groundwater and soil monitoring on agricultural land in the Neretva river vally (2009 – 2018);
2. development and interpretation of soil map in GIS, with the norms according to World Reference Base for Soil Resources (WRB) for initial analysis and risk assessment of salt ingression and soil salinization for the Neretva river vally;
3. development and interpretation of land use map GIS for the Neretva river vally;
4. spatial and temporal statistical analysis of the quality (indicators indicating the penetration of salt water) of surface and shallow groundwater and physical and chemical properties of soil. This is followed by the seasonal monitoring established within the ASTERIS project.

4.2 Materials and methods

4.2.1 Climatic conditions

The area is semi-arid with a Mediterranean climate characterised by hot, dry summers and wet winters. Most precipitation occurs from October to April, with an annual average (1988-2017) of 1230 mm. The mean annual air temperature is 15.7°C, with the highest mean monthly air temperature (25.2°C) in July. Annual Penman-Monteith Reference evapotranspiration is 1196 mm, with the highest mean monthly value of 191 mm occurring in July. Climatic conditions are favourable for fruit growing and field crop production throughout the year is possible only with regular irrigation during dry season.

4.2.2 Spatial, temporal and methodological characterisation of surface water, groundwater and soil monitoring on agricultural land in the Neretva Delta (2009 – 2018)

Project „Monitoring of water and soil salinization in the Neretva River valley“ is set as a complete programme for monitoring the area of Neretva River valley which aims to:

1. monitor spatial changes and seasonal stratification of soil salinization
2. monitor seasonal changes and spatial trend of surface water salinization
3. monitor seasonal changes and spatial trend of groundwater salinization

The five-year monitoring cycle includes six monitoring subregions in the Lower Neretva Valley which have been classified, based on previous research, as areas with highest risk of salinization.

The monitoring plan includes sampling and testing of surface and groundwater for parameters that are indicative for assessment of water chemical status. Monitoring of surface water in Neretva River valley is organized at 15 sampling stations on a monthly basis (table 4.1.). Monitoring of groundwater is also organized on a monthly basis, but from 7 sampling stations – shallow piezometers (Pz – 1 to Pz – 7) that are positioned at the depth of 4 m. Shallow piezometers are installed in close proximity of soil

sampling station. Coordinates of surface and groundwater sampling stations are determinated by GPS and are shown in tables (table 4.1. and 4.3.). Surface water samples are collected by directly filling a hand-held bottle sampler. Groundwater samples are collected using a submersible water pump. Sampling and handling of surface and groundwater samples is done in accordance with HRN EN 5667-6, 2016, HRN ISO 5667-11, 2011. Samples are transported to the laboratory in refrigerated tanks meeting the temperature requirements, and mechanical protection and protection against contamination requirements. All analyses are done in the Analytical laboratory of the Department of Soil Amelioration (University of Zagreb Faculty of Agriculture).

Table 4.1. Surface water monitoring station locations

Location	Y	X
Neretva vodozahvat	6472978	4767278
CS Luke	6464398	4765730
Luke kanal	6464458	4764854
CS Koševo Vrbovci	6471281	4762839
Vrbovci lateralni kanal	6471488	4764174
Vrbovci kanal	6471234	4764040
CS Vidrice	6461332	4761937
Vidrice lateralni kanal	6461714	4759775
Vidrice kanal	6461941	4760304
CS Opuzen Ušće	6457304	4762910
Opuzen Ušće kanal	6459136	4763595
Jasenska kanal	6460837	4765921
Mala Neretva	6463745	4762840
Komin kanal	6463667	4765451
Banja kanal	6460506	4766954

Physiochemical water quality properties

Physiochemical water quality parameters are determinated in surface and groundwater (table 4.2) in accordance with Regulation on water quality standards (NN 56/2013).

Table 4.2. Chemical and physical parameters analyzed in surface and groundwater samples in the laboratory

Parameter	Method
Total suspended solids	Determination of total suspended solids with membrane filter
pH	ISO 10523:2008 Water quality — Determination of pH
electrical conductivity (EC_w)	HRN EN 27888, 2008. Water Quality - Determination of Electrical Conductivity. International Organisation for Standardisation. Croatian Standard Institute
NO_3-N, NO_2-N, NH_4-N	HRN EN ISO 11732, 2008. Water Quality - Determination of Ammonium Nitrogen -Method by Flow Analysis (CFA and FIA) and Spectrometric Detection. International Organisation for Standardisation. Croatian Standard Institute HRN EN ISO 13395, 1998. Water Quality - Determination of Nitrite Nitrogen and Nitrate Nitrogen and the Sum of both by Flow Analysis (CFA and FIA) and Spectrometric Method. International Organisation for Standardisation. Croatian Standard Institute.
dissolved phosphorus	HRN EN ISO 15681-2, 2008.Water Quality - Determination of Orthophosphate and Total Phosphorus Contents by Flow Analysis (FIA and CFA) - Part 2:Method by Continuous Flow Analysis (CFA). International Organisation for Standardisation. Croatian Standard Institute.
K	Water quality — Determination of sodium and potassium — Part 3: Determination of sodium and potassium by flame emission spectrometry
HCO_3^-	Determination of bicarbonate by acid-base titration with H_2SO_4
Ca, Mg	ISO 11885:2009 Water quality — Determination of selected elements by inductively coupled plasma optical emission spectrometry (ICP-OES)
Cl and SO_4	ISO 15682:2000: Water quality — Determination of chloride by flow analysis (CFA and FIA) and photometric or potentiometric detection Water quality — Determination of sulphate by flow analysis (CFA)
Na	Water quality — Determination of sodium and potassium — Part 3: Determination of sodium and potassium by flame emission spectrometry
TOC	ISO 20236:2018 Water quality — Determination of total organic carbon (TOC), dissolved organic carbon (DOC), total bound nitrogen (TNb) and dissolved bound nitrogen (DNb) after high temperature catalytic oxidative combustion

Methodology of soil monitoring

Monitoring of agricultural soil in the Neretva River valley is organized at 7 sampling stations (P1, P2, P3, P4, P5, P6 and P7). On each soil monitoring station soil samples

were collected and analyzed twice a year, at the end of the winter/wet season, and at the end of the summer/dry season. In both seasons, soil sampling is done with a probe from 4 soil depths: 0-25 cm, 25-50 cm, 50-75 cm and 75-100 cm. Individual soil samples for every depth are then put in a bag with tag containing monitoring station, depth and sampling date.

Table 4.3. Soil monitoring stations and shallow piezometers locations

Location	Identification of soil monitoring station (P)/piezometer (Pz)	Y	X
Vrbovci	P5/Pz5	6471263	4763979
Luke	P1/Pz1	6464437	4764868
Vidrice	P3/Pz3	6461886	4760416
Opuzen ušće – Glog	P2/Pz2	6460829	4765863
Opuzen ušće – Jasenska	P4/Pz4	6459102	4763532
Komin	P6/Pz6	6463667	4765453
Banja	P7/Pz7	6460513	4766955

Preparation of soil samples for analyses: Preparation is done in accordance with standardized procedure of soil preparation for physical and chemical analyses (HRN ISO 11464:2004). Air dried samples are crushed and sieved through sieves with a density of 2000 µm, and one part of them is sieved through sieves with a density of 250 µm.

Soil samples archiving: All 2000 µm fraction soil samples are archived in plastic containers with a volume up to 0,5 L and are kept for minimum of 10 years (recommended by „Croatian Soil Monitoring Programme“) in laboratory archive.

Chemical and physical parameters that are analyzed in soil samples:

- pH of saturated soil paste;
- Electrical conductivity of saturated soil paste (EC_e);
- K concentration of saturated soil paste;
- NO_3-N concentration of saturated soil paste
- NO_2-N concentration of saturated soil paste
- NH_4-N concentration of saturated soil paste
- PO_4-P concentration of saturated soil paste

- HCO_3 concentration of saturated soil paste
- Ca concentration of saturated soil paste
- Cl concentration of saturated soil paste
- Mg concentration of saturated soil paste
- Na concentration of saturated soil paste
- SO_4 concentration of saturated soil paste

Soil salinity assessment

Soil salinity expressed as EC_e is linearly related to the yield of cultivated crops. That is why, most commonly used criteria for evaluating soil salinity, are those which validate the effect on yield of different crops. General criteria for soil salinity classification should be adjusted depending on specific agroecological conditions of the given area. Because of this, when assessing soil salinity for the area of the Neretva River valley, criteria for soil classification are: EC_e<2 dS m^{-1} – non-saline soil; EC_e 2 - 8 dS m^{-1} – salt-affected soil; EC_e >8 dS m^{-1} – saline soil (Husnjak, 2014).

Laboratory quality assurance

Evaluation of quality control procedure in the Analytical laboratory of the Department of Soil Amelioration is carried out at the internal and external level. Internal quality control is done by using reference materials from interlaboratory comparison testing in each analysis for physical and chemical parameters. In addition to reference samples, blanks and repeated measurements are included in each series of unknown soil samples.

External quality control is done by the participation of the Laboratory in interlaboratory comparison testing. The Analytical laboratory of the Department of Soil Amelioration has been participating in the international comparison procedures for soil and sediment analyses WEPAL-ISE (Wageningen University, Netherlands) continuously since 2002, four times a year. The reference materials used in the daily analysis control of the Laboratory are from the above mentioned comparison procedure, and are selected

based on the greatest possible similarity between the matrix of the reference sample and the analyzed soil samples. In 2018, the Analytical Laboratory of the Department of Soil Amelioration participated in interlaboratory comparison testing in the field of water analysis for macronutrient, in collaboration with the University of Natural Resources and Applied Life Sciences, Department of Agrobiotechnology, IFA - Tullin, Center for Analytical Chemistry from Vienna (Austria).

4.3 Results and discussion

4.3.1 Soil map of the Neretva river valley

In order for Work package 4 (WP4) „Identyfing needs and barriers in coastal aquifer management“ to be realized as part of ASTERIS Project, soil map of the Neretva river vally has been developed. This map will be used as one of the crucial basis for initial risk assessment of soil and water salinization of the observed area and for developing a model of the risk based on future scenarios.

The main source for making a soil map was „Soil suitability map of Croatia“ scale 1:50 000, and also existing data from other, more detailed soil maps. Water surfaces and bigger settlements are separately singled out. The map shows 27 soil mapping units, water surfaces and settlements, figure 4.1.

Soil map legend is shown in table 4.4. Names of each soil mapping units are shown both in Croatian and English, and also in accordance to World Reference Base for Soil Resources (WRB) clasification. Soil map was developed in a digital form as a shp file with attributing data of soil mapping units in Croatian, English and according to WRB classification system.

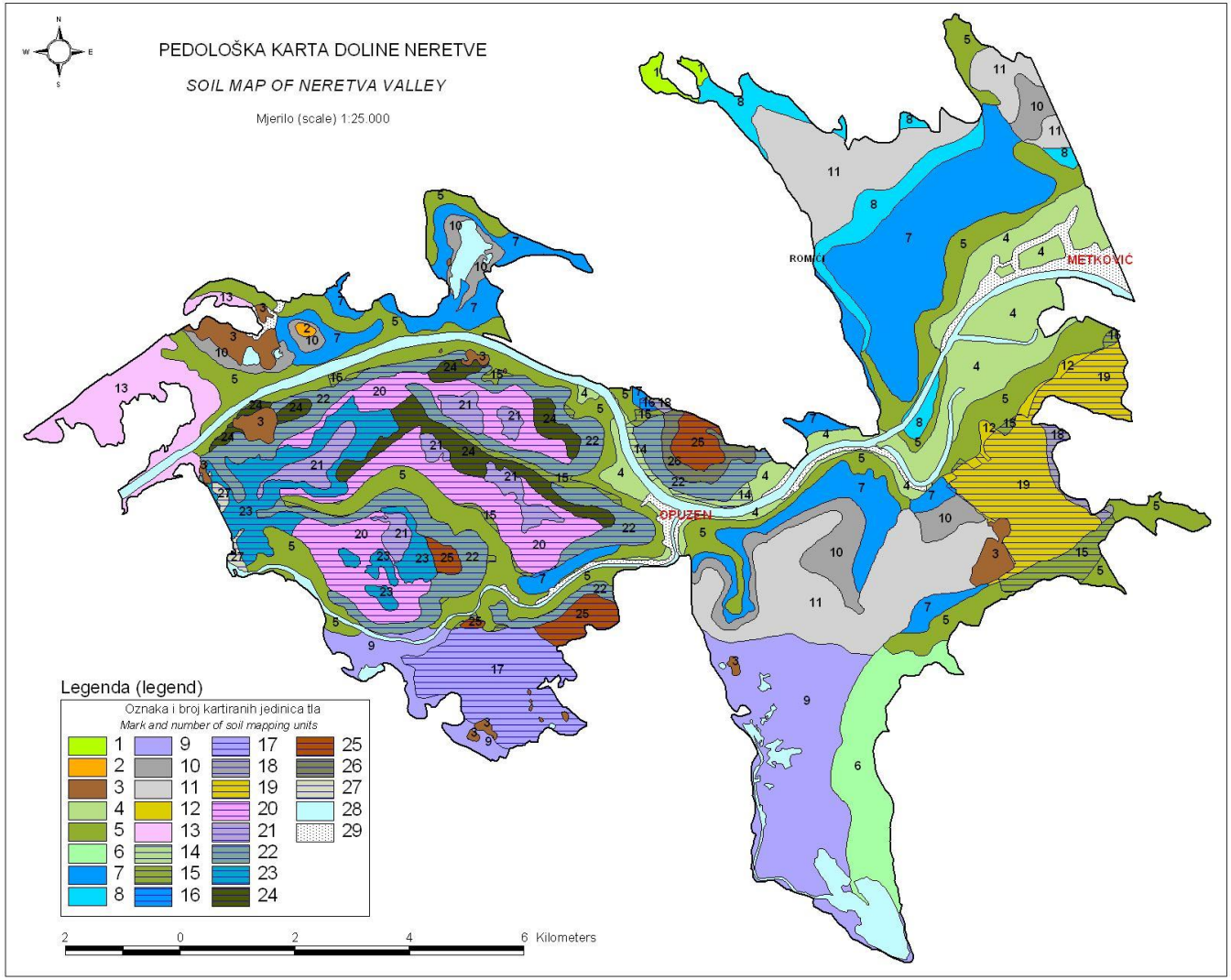

Fig. 4.1 Soil map of the Neretva river valle

Table 4.4. Legend of the soil map of the Neretva river valley according to the Croatian soil classification in English and Croatian and according to the WRB classification (WRB, 2014)

Kartirana jedinica tla (soil mapping units)				Zastuplje-nost (share) %	Površina (area) ha
Prema klasifikaciji tla Hrvatske ***According to the Croatian soil classification in Croatian***		Prema klasifikaciji tla Hrvatske na engleskom *According to the Croatian soil classification in English*	Prema WRB klasifikaciji *According to the WRB classification*		
Broj ***(number)***	Sastav i struktura *Composition and structure*	Sastav i struktura *Composition and structure*	Sastav i struktura* *Composition and structure**		
1	Koluvij aluvijalno-koluvijalni, karbonatni, ilovasti, neoglejeni	Colluvium alluvial-colluvial, calcareous, loamy, nongleyic	Colluvic REGOSOL calcareous fluvic loamic	100	38,4
2	Smeđe tlo na vapnencu tipično, plitko do srednje duboko Crvenica tipična, srednje duboka do duboka Crnica ocrveničena na vapnencima	Calcocambisol, typical, shallow to medium deep Terra rossa, typical, medium deep to deep Calcomelanosol, rhodochromic	Leptic chromic CAMBISOL clayic to loamic Rhodic CAMBISOL clayic to loamic Lithic mollic cambic LEPTOSOL humic	70 20 10	6,5
3	Smeđe tlo na vapnencu tipično, plitko do vrlo plitko Crvenica tipična, plitka Crnica posmeđena na vapnencu	Calcocambisol, typical, shallow to very shallow Terra rossa, typical, shallow Calcomelanosol, cambic	Leptic chromic CAMBISOL clayic to loamic Leptic rhodic CAMBISOL clayic to loamic Lithic mollic cambic LEPTOSOL humic	50 30 20	180,0
4	Aluvijalno karbonatno neoglejeno tlo, vrlo duboko, djelomično meliorirano (mjestimično kolmirano)	Alluvial soil, calcareous, nongleyic, very deep, partly hidroameliorated (sporadically with filling up)	Nongleyic calcaric FLUVISOL loamic to clayic (partly hidroameliorated, sporadically with filling up)	100	695,9
5	Aluvijalno karbonatno oglejeno tlo, vrlo duboko, djelomično meliorirano (mjestimično kolmirano)	Alluvial soil, calcareous, gleyic, very deep, partly hidroameliorated (sporadically with filling up)	Gleyic calcaric FLUVISOL loamic to clayic (partly hidroameliorated, sporadically with filling up)	100	1634,4
6	Aluvijalno oglejeno tlo, nekarbonatno (mjestimično kolmirano)	Alluvial soil, gleyic, noncalcareous (sporadically with filling up)	Gleyic FLUVISOL loamic to clayic (sporadically with filling up)	100	344,8

7	Močvarno glejno amfiglejno, humusno, karbonatno	Eugley, amphigleyic, humic, calcareous	Reductigleyic fluvic calcaric GLEYSOL clayic humic	100	1311,5
8	Močvarno glejno amfiglejno, mineralno, karbonatno	Eugley, amphigleyic, mineral, calcareous	Reductigleyic fluvic calcaric GLEYSOL clayic	100	290,6
9	Močvarno glejno amfiglejno, mineralno, nekarbonatno,	Eugley, amphigleyic, mineral, noncalcareous	Reductigleyic fluvic GLEYSOL clayic	100	889,5
10	Močvarno glejno tresetno, srednje humificirano	Eugley histosol, medium humified	Histic fluvic GLEYSOL humic hemic	100	394,4
11	Niski treset duboki, slabo do jako humificirani	Histosol of level terrain, deep, poorly to very humified	Fibric to sapric HISTOSOL fluvic	100	1110,0
12	Rigolana tla vitisola i hortisola Rigolana tresetna tla, srednje duboka te srednje do jako humificirana	Rigosol from vitisol and hortisol Rigosol from histosol, medium deep, medium to very humified	Hortic ANTHROSOL fluvic loamic to clayic Hortic histic ANTHROSOL fluvic hemic to sapric	90 10	35,7
13	Solončak kloridni, duboko zaslanjeni	Solonchak, chlorid, deeply salinated	Subaquatic fluvic SOLONCHAK chloridic	100	291,8
Hidromeliorirna tla kanalima, pretežno kolmirana ***Hidromeliorated soils with canals (largely with filling up)***					
14	Aluvijalno karbonatno neoglejeno tlo, vrlo duboko, hidromeliorirano kanalima, pretežno kolmirano	Alluvial soil, calcareous, nongleyic, very deep, hidroameliorated with canals, largely with filling up	Nongleyic calcaric FLUVISOL loamic to clayic (hidroameliorated with canals, largely with filling up)	100	32,2
15	Aluvijalno karbonatno oglejeno tlo, vrlo duboko, hidromeliorirano kanalima, pretežno kolmirano	Alluvial soil, calcareous, gleyic, very deep, hidroameliorated with canals, largely with filling up	Gleyic FLUVISOL loamic to clayic (hidroameliorated with canals, largely with filling up)	100	171,4
16	Močvarno glejno amfiglejno, humusno, karbonatno, hidromeliorirano kanalima, pretežno kolmirano	Eugley, amphigleyic, humic, calcareous, hidroameliorated with canals, largely with filling up	Reductigleyic fluvic calcaric GLEYSOL clayic humic (hidroameliorated with canals, largely with filling up)	100	7,1
17	Močvarno glejno amfiglejno, mineralno, nekarbonatno, hidromeliorirano kanalima, pretežno kolmirano	Eugley, amphigleyic, mineral, noncalcareous, hidroameliorated with canals, largely with filling up	Reductigleyic fluvic GLEYSOL clayic (hidroameliorated with canals, largely with filling up)	100	396,6
18	Močvarno glejno tresetno, srednje humificirano, hidromeliorirano kanalima, pretežno kolmirano	Eugley histosol, medium humified, hidroameliorated with canals, largely with filling up	Histic fluvic GLEYSOL humic hemic	100	34,9

			(hidroameliorated with canals, largely with filling up)		
19	Rigolana tla vitisola i hortisola, hidromeliorirana kanalima, pretežno kolmirana Rigolana tresetna tla, srednje duboka te srednje do jako humificirana, hidromeliorirana kanalima, pretežno kolmirana	Rigosol from vitisol and hortisol, hidroameliorated with canals, largely with filling up Rigosol from histosol, medium deep, medium to very humified, hidroameliorated with canals, largely with filling up	Hortic ANTHROSOL fluvic loamic to clayic (hidroameliorated with canals, largely with filling up) Hortic histic ANTHROSOL fluvic hemic to sapric (hidroameliorated with canals, largely with filling up)	90 10	466,5
20	Hidromeliorirano tlo kanalima, srednje duboko zaslanjeno, iz maritimnog humoznog karbonatnog tla, pretežno kolmirano	Hidroameliorated soil with canals, medium deep, salinated, from maritime humic and calcareous soil, largely with filling up	Hortic ANTHROSOL fluvic gleyic salic (hidroameliorated with canals, largely with filling up)	100	673,9
21	Hidromeliorirano tlo kanalima, jako zaslanjeno, iz maritimnog mineralnog karbonatnog tla, pretežno kolmirano	Hidroameliorated soil with canals, very salinated, from maritime mineral and calcareous soil, largely with filling up	Hortic ANTHROSOL fluvic gleyic hypersalic (hidroameliorated with canals, largely with filling up)	100	213,0
22	Močvarno glejno amfiglejno humozno, karbonatno i nekarbonatno, zaslanjeno, hidromeliorirano kanalima, pretežno kolmirano tlo	Eugley, amphigleyic, humic, calcareous and noncalcareous, salinated, hidroameliorated with canals, largely with filling up	Reductigleyic fluvic calcaric GLEYSOL clayic humic salic (hidroameliorated with canals, largely with filling up)	100	748,1
23	Hidromeliorirano tlo kanalima, iz maritimnog mineralnog karbonatnog tla, pretežno kolmirano	Hidroameliorated soil with canals, from maritime mineral and calcareous soil, largely with filling up	Hortic ANTHROSOL fluvic gleyic (hidroameliorated with canals, largely with filling up)	100	351,4
24	Hidromeliorirano tlo kanalima, iz tresetnog plitkog, jako humificiranog tla, pretežno kolmirano	Hidroameliorated soil with canals, from shallow, very humic histosol, largely with filling up	Hortic histic ANTHROSOL fluvic gleyic (hidroameliorated with canals, largely with filling up)	100	248,0
25	Rigolano tlo iz dubokog glinastog tresetnog tla, hidromeliorirano kanalima, pretežno kolmirano Rigolano tlo iz dubokog tresetnog tla, hidromeliorirano kanalima, pretežno kolmirano	Rigosol from deep histosol, clayic, hidroameliorated with canals, largely with filling up Rigosol from deep histosol, hidroameliorated with canals, largely with filling up	Hortic histic ANTHROSOL fluvic clayic (hidroameliorated with canals, largely with filling up) Hortic histic ANTHROSOL fluvic (hidroameliorated with canals, largely with filling up)	85 15	163,9

26	Rigolano tlo iz močvarno glejnog trestnog tla, hidromeliorirano kanalima, pretežno kolmirano	Rigosol from eugley histosol, hidroameliorated with canals, largely with filling up	Hortic histic ANTHROSOL fluvic (hidroameliorated with canals, largely with filling up)	100	65,6
27	Submarinsko nerazvijeno tlo (protopedon), hidromeliorirano kanalima, mjestimično kolmirano	Protpedon, hidroameliorated with canals, largely with filling up	Subaquatic fluvic GLEYSOL (hidroameliorated with canals, sporadically with filling up)	100	19,0
UKUPNO za kartirane jedinice tla (TOTAL FOR SOIL MAPPING UNITS)					**10.814,8**
28	Rijeke i jezera (WATER BODIES)				639,7
29	Veća naselja s okućnicama (SETTLEMENTS)				205,5
SVE UKUPNO (TOTAL)					**11.660,0**

* U zagradama su navedene značajke koje potpunije obilježavaju referentnu grupu tala
* (*in the brackets are list of properties which more fully characterize the soil reference group*)

4.3.2 Agricultural land use map of the Neretva river vally

The main source for developing Agricultural land use map of the Neretva river vally was „ Map of agricultural land use in Croatia (Ondrašek et al., 2019)“. For detection of agricultural land use/management in 2017 the principal national database ARKOD was used. ARKOD is geometric database which serve as e-systems for identification and description of land parcels, i.e. records of agricultural land use/management and farm register to the Agency for Payments in Agriculture, Fisheries and Rural Development to award agricultural subsidies. However, for the land parcels that were not registered 2017 in ARKOD/AGRONET, a classification of land use was done using GIS tools and additional datasets like visual interpretation of satellite images from Sentinel 2, Google Earth, digital orthophoto map and CORINE Land Cover 2018 for Croatia. This was used to single out polygons which are characterized as “complex cultivation patterns” and represent areas (land) that are not registered in ARKOD system, but are singled out, with above mentioned methodology, as agricultural land parcels.

Total mapped area for the Neretva river valley is 11.661,5 ha (figure 4.2). The map highlights 10 categories of agricultural land use (registered in ARKOD 2017 system). In addition, areas (P) were calculated for each category within the mapped area for the Neretva river valley (table 4.5.). Areas that are not in the ARKOD system (complex cultivation patterns) occupied 3957,4 ha.

Table 4.5. Agricultural land use (ARKOD 2017) of the mapped area for the Neretva river valley

Land use	P (ha)
Arable land	640.9
Greenhouse	45.2
Meadows	39.3
Karst pastures	7.29
Vineyards (including extirpated vineyards)	47.26
Olive groves	73.2
Orchards	2141
Mixed permanent crops (including other permanent crops)	73.2
Other land use	2.35
Total	**3069.7**

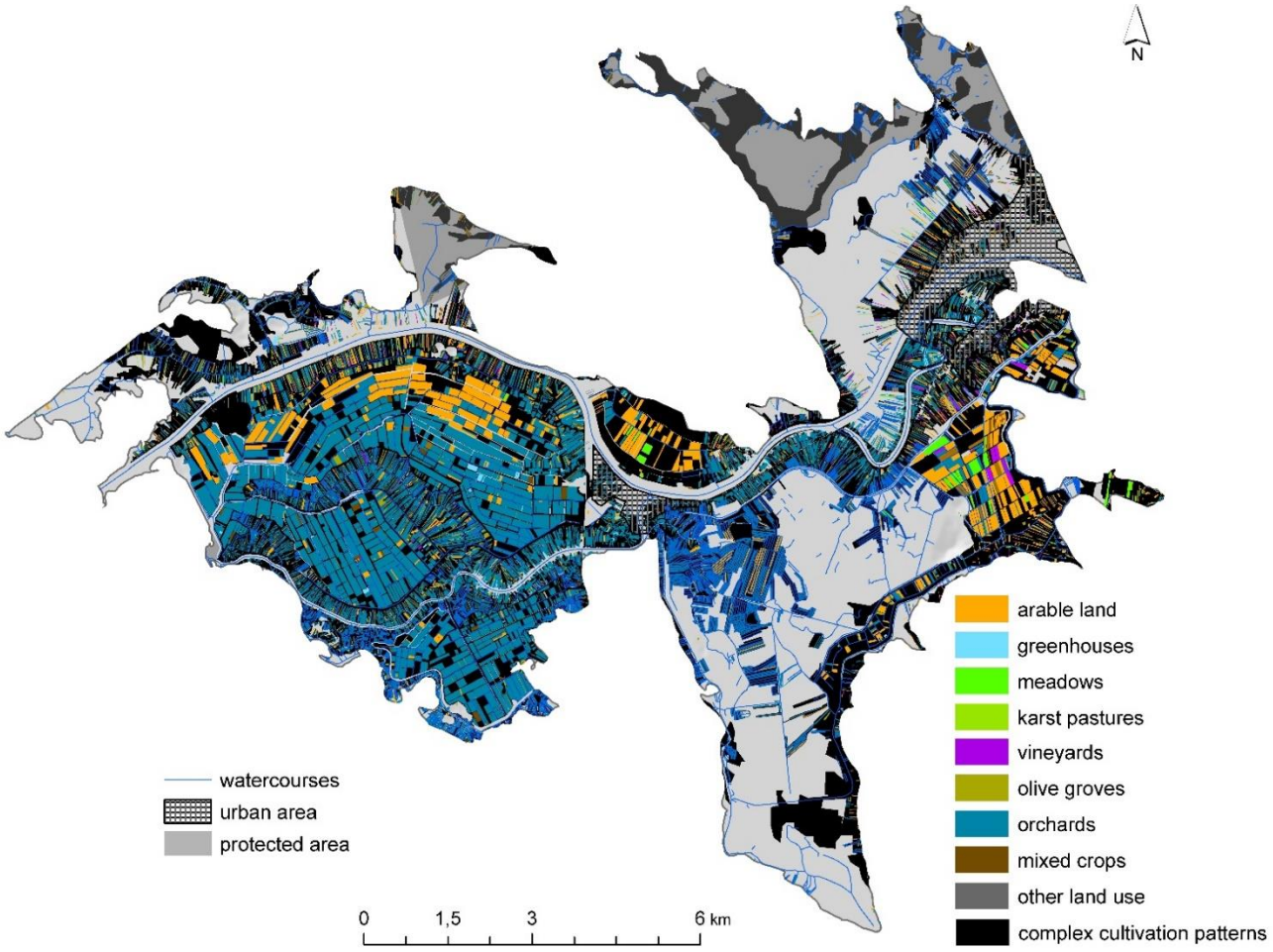

Fig. 4.2 Agricultural land use map of the Neretva river vally

4.3.3 Spatial and temporal statistical analysis of the quality (indicators indicating the ingresion of salt water) of surface and groundwater and physical and chemical properties of the soil

Position of water monitoring stations is shown in Figure 4.3. Surface and groundwater monitoring stations were grouped into 4 groups (table 4.6), with and natural watercourses are joined in one group due to similar position and function within monitoring area.

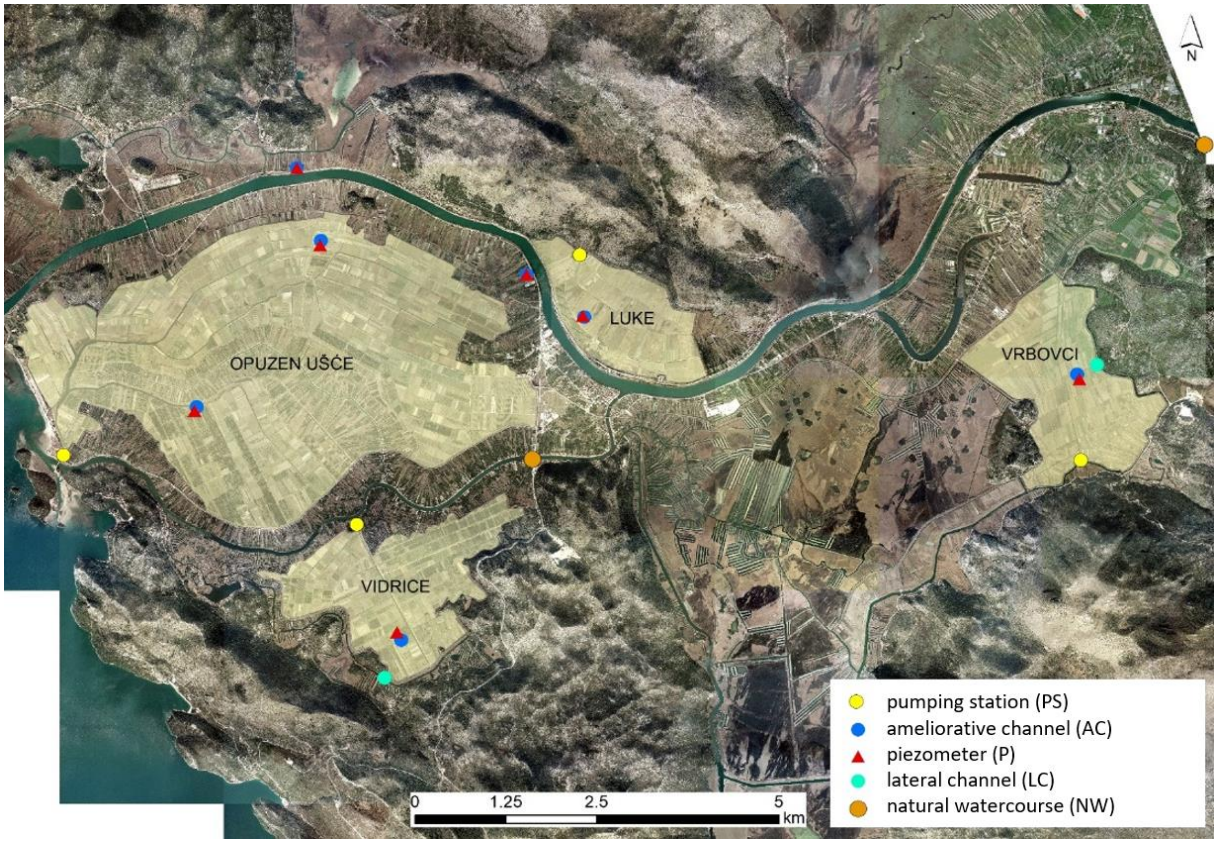

Fig. 4.3 Scheme of the stations for monitoring of the salinity status in surface and groundwater (from shallow piezometers)

Table 4.6. Groups of surface and groundwater monitoring stations according to the type of water body

Group of monitoring stations	Type of water body and location
Group 1	Natural watercourses (NW): Neretva, Mala Neretva, channel Vrbovci, channel Vidrice
Group 2	Pumping stations (PS): Luke; Vrbovci; Vidrice; Opuzen ušće
Group 3	Ameliorative channels (AC): Luke, Vidrice, Vrbovci, Opuzen ušće-Jasenska, Opuzen ušće
Group 4	Piezometers (P): Luke; Vidrice; Opuzen ušće-Jasenska, Opuzen ušće; Vrbovci

According to statistical indicators from Table 4.7. it is evident that in the period from 2009-2018 minimum value of electrical conductivity (EC_w) of 0,19 dS m^{-1} is determined in the monitoring group 3 (surface water monitoring stations established on ameliorative channels), and maximum value of 38,9 dS m^{-1} in the group 4 (groundwater monitoring stations from shallow piezometers), which also has the highest arithmetic mean of 9,7 dS m^{-1}. The coefficient of variation, as a complete measure of relative dispersion, higher than 70% indicates a very strong variability of the observed set, so from the obtained results it can be concluded that the EC_w values were extremely variable in groundwater (coefficient of variation = 109%). The results of the statistical analysis suggest that groundwater in the Neretva Valley belongs to the class of moderately saline waters (arithmetic mean EC_w in the range of 2-10 dS m^{-1}) to very heavily saline waters (maximum value of EC_w in the range of 25-45 dS m^{-1}). The highest arithmetic mean EC_w in the surface waters was determined in the group 2 (surface water monitoring stations established at the pumping stations), which also classifies them in the class of moderately saline waters. It is evident that the operation of the pumping station affects the inflow of salt from groundwater when it is mineralized, but also of unsalted water depending on the location. Namely, the operation of the pumping station lowers the water level and increases the pressure gradient in the vertical direction. Although the range of EC_w values in the group 2 ranged from 0,71 dS m^{-1} to 9,23 dS m^{-1}, the small coefficient of variation (37%) indicates lower variability in the degree of salinity or smaller deviations of the measured EC_w values from the determined arithmetic mean which is also associated with the operation of pumping stations, or their collection channels. It is important to

note that the highest value of EC_w in surface waters in the Neretva Valley was recorded in the group 3 of ameliorative channels (21 dS m^{-1}). Unlike other groups of surface water monitoring stations, the value of EC_w varies relatively the most in natural watercourses, which is expressed through a coefficient of variation of 71%. However, according to the determined value of the arithmetic mean of 1,06 dS m^{-1}, natural watercourses can be classified in the class of slightly saline waters (EC_w 0,7 - 2 dS m^{-1}).

Table 4.7. Summary statistics of electrical conductivity, ECw (dS m^{-1}) in groups of stations within monitoring area for time period 2009-2018

Parameter: EC_w (dS m^{-1})	*Group 1* Natural watercourses	*Group 2* Pumping stations	*Group 3* Ameliorative channels	*Group 4* Piezometers
n – number of samples	468	468	585	585
Arithmetic mean	1,06	4,02	3,63	9,7
Median	0,76	3,72	3,0	5,50
Standard deviation	0,75	1,47	2,5	10,6
Minimum	0,26	0,71	0,19	0,29
Maximum	4,83	9,23	20,9	38,9
Coefficient of variation	71	37	69	109

Figure 4.4. shows Sen's slope estimator for A) amelioration channel Luke from the group 3 in which the absolute maximum EC_w in surface waters was determined and B) Opuzen ušće piezometer from the group 4 with the highest arithmetic mean and absolute maximum of EC_w. A statistically significant positive trend of EC_w values at the significance level of 0.1% was determined at the monitoring station Opuzen ušće piezometer and at the significance level 1% at the monitoring station ameliorative channel Luke.

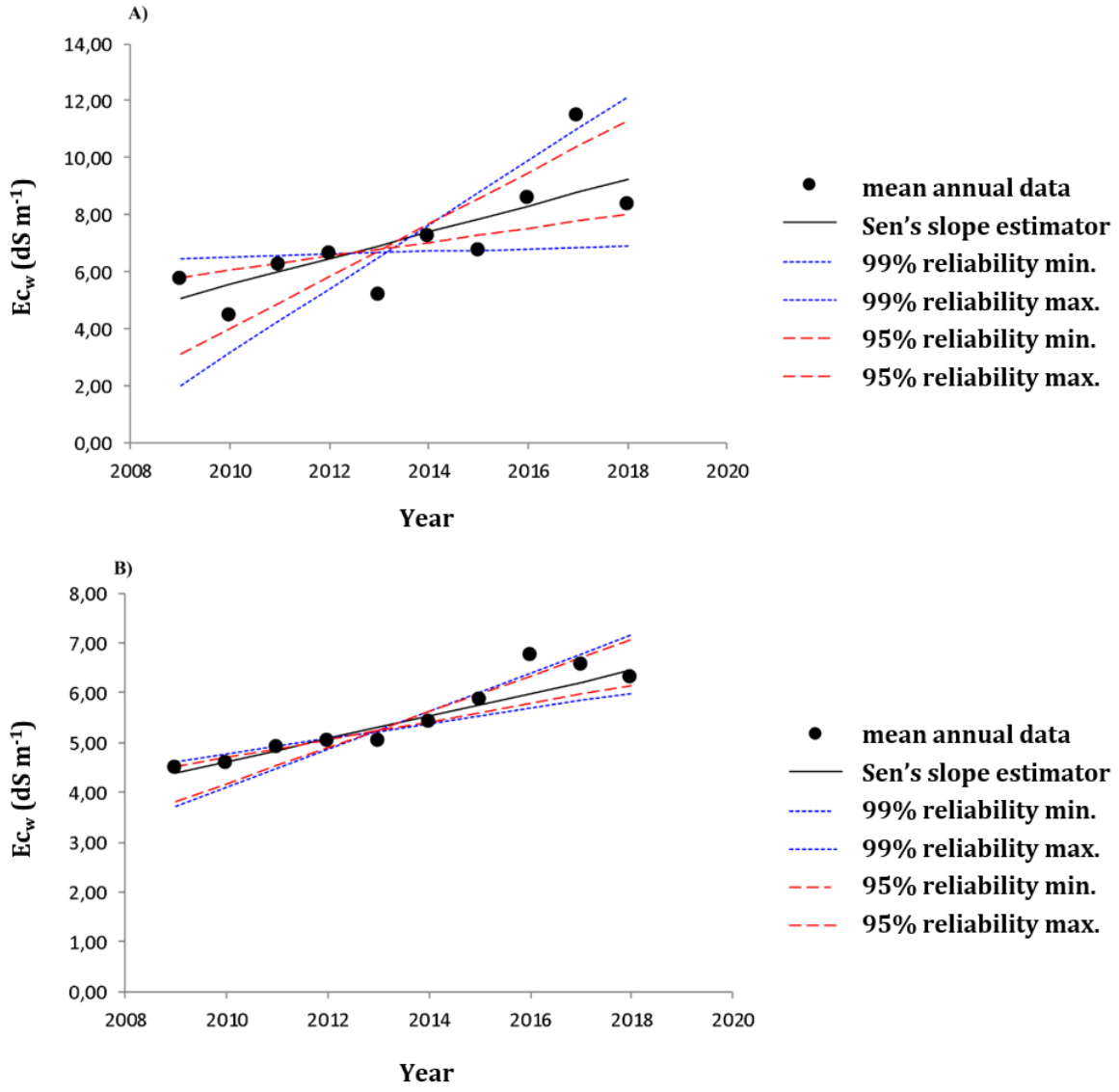

Fig. 4.4 Mean values of ECw and Sen's slope estimator for stations A) ameliorative channel Luke and B) Opuzen ušće piezometer with two levels (95% and 99%) of reliability of estimated slope

Correlation among chemical parameters indicating salinity processes was done for each monitoring station in time period 2009-2018 and it is presented in tables 4.8.-4.11. One station is selected from each water body group. It is evident and expected that there is high statistically significat positive correlation between EC_w and Na^+ and Cl^-.

Table 4.8. Correlation matrix for chemical parameters for time period 2009-2018 at station river Neretva (group 1)

	EC_w	K	P	pH	HCO_3^-	Cl^-	SO_4^{2-}	Ca^{2+}	Mg^{2+}	Na^+
EC_w	**1,00**									
K	**0,34**	**1,00**								
P	-0,15	**0,23**	**1,00**							
pH	0,08	0,00	**-0,41**	**1,00**						
HCO_3^-	**-0,17**	0,13	**0,40**	**-0,28**	**1,00**					
Cl^-	**0,98**	**0,42**	-0,09	0,04	**-0,18**	**1,00**				
SO_4^{2-}	**0,74**	**0,30**	0,01	0,10	-0,04	**0,74**	**1,00**			
Ca^{2+}	0,13	0,17	**0,29**	-0,12	**0,62**	0,12	**0,29**	**1,00**		
Mg^{2+}	**0,58**	**0,35**	-0,05	0,03	0,03	**0,64**	**0,47**	0,10	**1,00**	
Na^+	**0,99**	**0,39**	-0,13	0,05	**-0,21**	**1,00**	**0,73**	0,10	**0,62**	**1,00**

Values in bold are different from 0 with a significance level alpha=0,05

Table 4.9. Correlation matrix for chemical parameters for time period 2009-2018 at station PS Vidrice (group 2)

	EC_w	K	P	pH	HCO_3^-	Cl^-	SO_4^{2-}	Ca^{2+}	Mg^{2+}	Na^+
EC_w	**1,00**									
K	**0,92**	**1,00**								
P	0,04	**0,20**	**1,00**							
pH	**-0,35**	**-0,37**	**-0,24**	**1,00**						
HCO_3^-	**0,49**	**0,58**	**0,33**	**-0,25**	**1,00**					
Cl^-	**0,67**	**0,67**	0,06	**-0,23**	**0,31**	**1,00**				
SO_4^{2-}	**0,51**	**0,61**	**0,27**	**-0,26**	**0,67**	**0,32**	**1,00**			
Ca^{2+}	**0,42**	**0,56**	**0,30**	**-0,23**	**0,73**	**0,28**	**0,72**	**1,00**		
Mg^{2+}	**0,65**	**0,73**	**0,23**	**-0,22**	**0,50**	**0,44**	**0,49**	**0,75**	**1,00**	
Na^+	**0,93**	**0,90**	0,03	**-0,35**	**0,37**	**0,65**	**0,42**	**0,33**	**0,61**	**1,00**

Values in bold are different from 0 with a significance level alpha=0,05

Table 4.10. Correlation matrix for chemical parameters for time period 2009-2018 at station DC Luke (group 3)

	EC_w	K	P	pH	HCO_3^-	Cl^-	SO_4^{2-}	Ca^{2+}	Mg^{2+}	Na^+
EC_w	**1,00**									
K	**0,93**	**1,00**								
P	-0,17	-0,10	**1,00**							
pH	**-0,57**	**-0,46**	0,03	**1,00**						
HCO_3^-	**0,34**	**0,39**	0,11	**-0,38**	**1,00**					
Cl^-	**0,97**	**0,92**	-0,13	**-0,53**	**0,31**	**1,00**				
SO_4^{2-}	**0,78**	**0,76**	-0,06	**-0,59**	**0,58**	**0,75**	**1,00**			
Ca^{2+}	**0,78**	**0,67**	-0,08	**-0,67**	**0,62**	**0,73**	**0,91**	**1,00**		
Mg^{2+}	**0,98**	**0,92**	-0,14	**-0,56**	**0,39**	**0,96**	**0,82**	**0,80**	**1,00**	
Na^+	**0,99**	**0,92**	-0,14	**-0,55**	**0,31**	**0,98**	**0,75**	**0,74**	**0,97**	**1,00**

Values in bold are different from 0 with a significance level alpha=0,05

Table 4.11. Correlation matrix for chemical parameters for time period 2009-2018 at station piezometer Opuzen ušće (group 4)

	EC_w	K	P	pH	HCO_3^-	Cl^-	SO_4^{2-}	Ca^{2+}	Mg^{2+}	Na^+
EC_w	**1,00**									
K	**0,59**	**1,00**								
P	**0,31**	**0,37**	**1,00**							
pH	-0,08	-0,05	0,14	**1,00**						
HCO_3^-	**0,60**	**0,81**	**0,42**	-0,01	**1,00**					
Cl^-	**0,44**	**0,70**	0,09	-0,12	**0,77**	**1,00**				
SO_4^{2-}	0,07	-0,10	**-0,58**	**-0,38**	**-0,20**	0,01	**1,00**			
Ca^{2+}	-0,04	0,04	**-0,59**	**-0,39**	-0,02	**0,33**	**0,60**	**1,00**		
Mg^{2+}	**0,42**	**0,73**	**0,33**	-0,06	**0,79**	**0,66**	-0,17	0,00	**1,00**	
Na^+	**0,66**	**0,89**	**0,37**	-0,08	**0,86**	**0,76**	-0,14	0,01	**0,76**	**1,00**

Values in bold are different from 0 with a significance level alpha=0,05

Monitoring of soil salinization in the Neretva River valley is carried out at 7 monitoring stations (P) distributed within melioration units. By determining the degree of soil salinization in the period March/April, the ability of the soil to maintain the equilibrium state of salt in the soil profile is assessed. This gives an insight to whether the precipitation during the autumn-winter period was sufficient for a significant salt leaching from soil profile. In addition, this period coincides with the beginning of sowing/planting the most important crops in the delta area. Knowing the degree of soil

salinization in the germination and early growth stages is of crucial importance because plants at these stages are highly sensitive to increased salt concentrations. The second sampling was carried out after 6 months, in the September/October period. This is a period preceded by high air temperature, significant soil water losses due to evapotranspiration, low precipitation and applying irrigation. All of the above poses a great risk for salt accumulation in soil. Out of all soil monitoring stations, highest average EC_e value of 3,75 dS m^{-1} was at Vidrice melioration area, both in summer and winter sampling period (table 4.12). Soil salinity was highest in the winter sampling period in Vidrice melioration area. In the summer period, maximum value of EC_e was at monitoring station P-5 of the Vrbovci melioration area where the lowest average value of EC_e in winter sampling period was determinated. Such high variability of EC_e at P-5 monitoring station is confirmed by the coefficient of variation of 95 % during summer sampling period. From the obtained results, it can be concluded that the EC_e values were least variable at the soil monitoring stations with the highest determined means of salinization, and that was station P-3 of the Vidrice melioration area. Considering the criteria that salt affected soils (depth up to 1 m) have an average value ranging from 2 to 8 dS m^{-1} (Husnjak, 2014), soil at monitoring stations of Vidrice area, Opuzen ušće-Glog and Banja can be classified as salt affected during winter/wet sampling period. In the summer sampling period, in addition to the previously mentioned stations, the soil was salt affected at stations Opuzen Ušće-Jasenska and Komin.

Table 4.12. Summary statistics for EC_e (dS m^{-1}) on soil monitoring stations (depth up to 1 m) in Neretva River valley for period 2009.-2018.

EC_e (dS m^{-1})		P-1 Luke	P-2 Jasenska	P-3 Vidrice	P-4 Glog	P-5 Vrbovci	P-6* Komin	P-7* Banja
Average	Winter	1,09	1,68	3,25	2,06	0,67	1,06	2,27
	Summer	1,3	2,94	3,75	2,14	1,14	2,43	2,79
Stdev.	Winter	0,86	0,99	1,13	0,93	0,25	0,59	0,9
	Summer	0,9	1,67	0,73	0,99	1,08	1,38	0,66
Minimum	Winter	0,38	0,41	0,97	0,53	0,4	0,31	0,89
	Summer	0,5	0,64	2,21	0,81	0,43	1,03	1,59
Maximum	Winter	4,79	4,7	4,95	3,74	1,41	2,29	4,18
	Summer	3,6	6,02	5,41	4,12	6,06	5,79	4,43
V (%)	Winter	78,8	58,9	34,68	45,1	37,37	55,58	39,91
	Summer	63,8	56,8	19,57	46,2	95,45	56,81	23,7

*time series of measurements for period 2014.-2018.

4.3.4 Spatial, temporal and methodological characterization of drinking water sources in the pilot area of the Neretva Delta

The area included in the monitoring is defined as the area of the Neretva Groundwater Body (GWB) (area of 2 035 km^2), which is a transboundary water body, the largest part of which is located in neighboring Bosnia and Herzegovina. From the hydrological aspect, the Neretva GWB on Croatian territory can be divided into:

- Area of water sources along the right bank of the Neretva River,
- Area of water sources along the left bank of the Neretva River and the coast of Dubrovnik,
- Neretva river delta with thick deposits of alluvial and marine sediments
- Pelješac peninsula (Biondić et al., 2016.).

The spatial distribution of all water monitoring stations for which data were submitted (12 stations in total) is shown in Figure 4.5 The northernmost monitoring station is the Opačac karst spring, located in Imotsko polje, followed by the Banja spring monitoring station in Rastočko polje and the Butina spring in Vrgoračko polje. In the valley Neretva River there are three measuring stations, Klokun, Modro Oko and Prud springs. In neighboring Bosnia there are two monitoring stations, Station Doljani and Žitomislići, which are very important for the Neretva River valley (Figure 4.6). The Doljani monitoring station is located upstream of the town of Metković, right on the state border. The Žitomislići monitoring station represents the relevant profile for the inflow coming into the valley from the upper part of the Neretva River basin. South of the Neretva River valley there are several other water quality monitoring stations, Nereze in Slano, on the coast of Dubrovnik there are Ombla and Duboka Ljuta, and the southernmost measuring station Ljuta is located in the Konavle area.

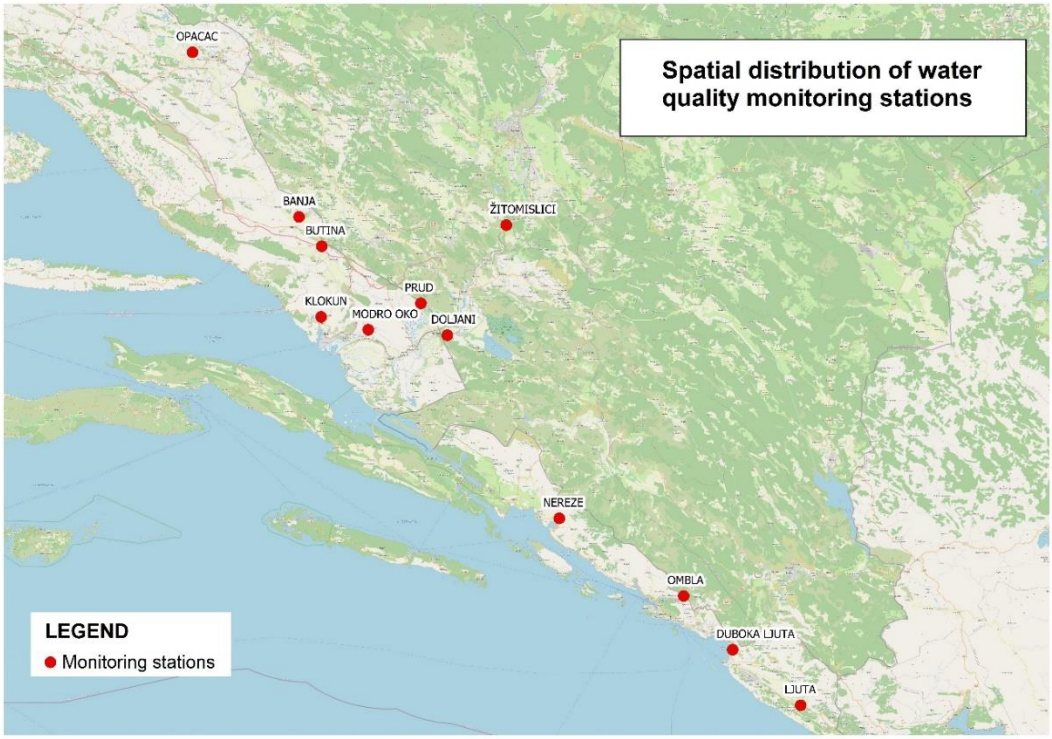

Fig. 4.5 Spatial distribution of water quality monitoring stations

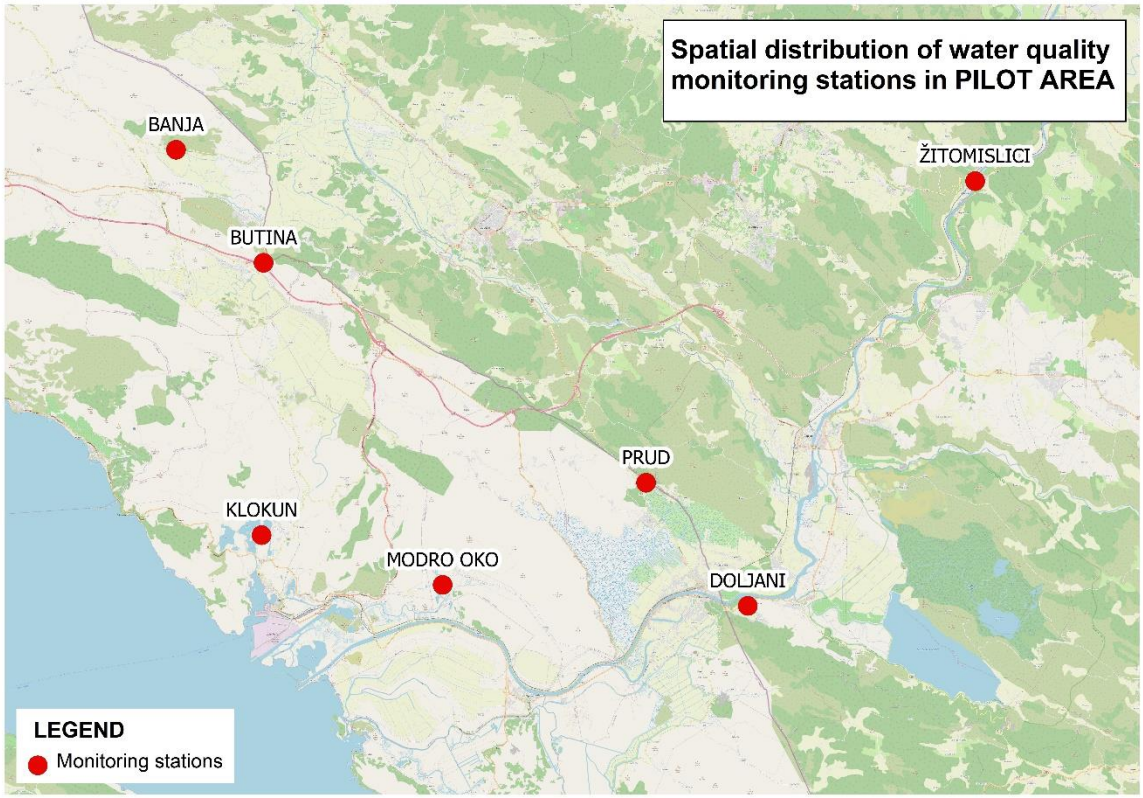

Fig. 4.6 Spatial distribution of water quality monitoring stations in PILOT AREA

As an upstream boundary condition of the water quality of Neretva River, the data from the Žitomislići station were used. This monitoring station is under the direct influence of the operation of the Mostar hydropower plant. Data on water quality at this station are publicly available on the website of the Agency for the Adriatic Sea Basin from Mostar and cover the period from 2009 to 2019. In addition to the Žitomislići station, the monitoring station that represents the entry point into the Republic of Croatia is the Doljani station on the border between Croatia and Bosnia, for which data for the period 2010 to 2019 were available. Additionally, data from over 20 water quality monitoring stations for the wider Neretva River area were submitted. However, the sampling frequency varies significantly from station to station, from once a year to once a month. Also, data availability period varies from on station to the other. For most stations, data are available from 2010 to 2019, while for five of them they are available only for period 2015-2019. Table 1.1 shows all stations for which the data were provided, time period of data availability, frequency of sampling and water quality parameters that were analyzed.

Table 4.13. Water quality monitoring stations in the Dubrovnik Neretva County and their characterization

Monitoring station	Period	Sampling frequency	Type of water	Water quality parameters	Data source
Žitomislići	2009-2020	monthly	Surface water	Temperature, pH, BPK5, Dissolved oxygen, EC, Suspended particles, $KMnO_4$, Oxygen saturation, Total P, Total N, NH_4, NO_3, PO_4	Agency for the Adriatic Sea Basin
Doljani	2010-2019	weekly		pH, EC, Cl, $KMnO_4$	Institute of public health Dubrovnik Neretva County
Prud	2010-2019	several times a year		pH, EC, Cl, SO_4^{2-}, $KMnO_4$	Institute of public health Dubrovnik Neretva County
Spring Opačac	2009-2019	monthly/ quarterly	Surface water	EC, Cl, SO_4^{2-}	Croatian Waters
Butina, spring	2009-2019	monthly/ quarterly	Surface water	EC, Cl, SO_4^{2-}	Croatian Waters
Spring Norin, Prud	2009-2019	monthly/ quarterly	Surface water	EC, Cl, SO_4^{2-}	Croatian Waters
Ombla, spring	2009-2019	monthly/ quarterly	Surface water	EC, Cl, SO_4^{2-}	Croatian Waters
Ljuta, spring Konavle	2009-2019	monthly/ quarterly	Surface water	EC, Cl, SO_4^{2-}	Croatian Waters
Banja	2015-2019	quarterly	Groundwater	Temperature, EC, Cl, SO_4^{2-}	Croatian Waters
Duboka Ljuta	2015-2019	quarterly	Groundwater	Temperature, EC, Cl, SO_4^{2-}	Croatian Waters
Nereze, Slano	2015-2019	quarterly	Groundwater	Temperature, EC, Cl, SO_4^{2-}	Croatian Waters
Klokun	2015-2019	quarterly	Groundwater	Temperature, EC, Cl, SO_4^{2-}	Croatian Waters
Modro Oko	2015-2019	quarterly	Groundwater	Temperature, EC, Cl, SO_4^{2-}	Croatian Waters

Water quality parameters analyzed at individual stations also differ from each other. Parameters that would indicate problems of seawater intrusion into coastal aquifers include pH, electrical conductivity (EC), chloride concentration and sulphate concentration (Table 4.14).

Table 4.14. Water quality parameters on each station

Station/parameter	pH	EC	Cl-	SO_4^{2-}
Žitomislići	●	●		
Doljani	●	●	●	
Prud	●	●	●	●
Opačac		●	●	●
Butina		●	●	●
Norin (Prud)		●	●	●
Ombla		●	●	●
Ljuta		●	●	●
Banja		●	●	●
Duboka Ljuta		●	●	●
Nereze		●	●	●
Klokun		●	●	●
Modro Oko		●	●	●

The available data used in the analysis include 12 water quality monitoring stations. For the north most monitoring station Opačac, data for electrical conductivity (EC), chloride concentration (Cl^-) and sulphate concentration (SO_4^{2-}) for the period 2009-2019 were analyzed. Table 4.15 presents overview of the results of statistical analysis of these data.

Table 4.15. Results of statistical analysis for Opačac monitoring station

	EC µS/cm	Cl^- mg/l	SO_4^{2-}
N	76	75	75
Average	398	5.4	11
Minimum	344	2.6	2.4
Maximum	575	12	50
Standard deviation	33	1.7	6.9
Variability coefficient (%)	8.3	32	61

The analysis of available data (n=76) showed that in the period 2009-2019 electrical conductivity ranged between 344 µS/cm and 575 µS/cm, and the average was 398 µS/cm (Figure 4.7). Concentration of Cl^- in water ranged from a minimum of 2.6 mg/l to a maximum of 12 mg/l, with an average of 5.4 mg/l (Figure 4.8). Concentration of

SO_4^{2-} in water ranged from a minimum of 2.4 mg/l to a maximum of 50 mg/l, with an average of 11 mg/l (Figure 4.9).

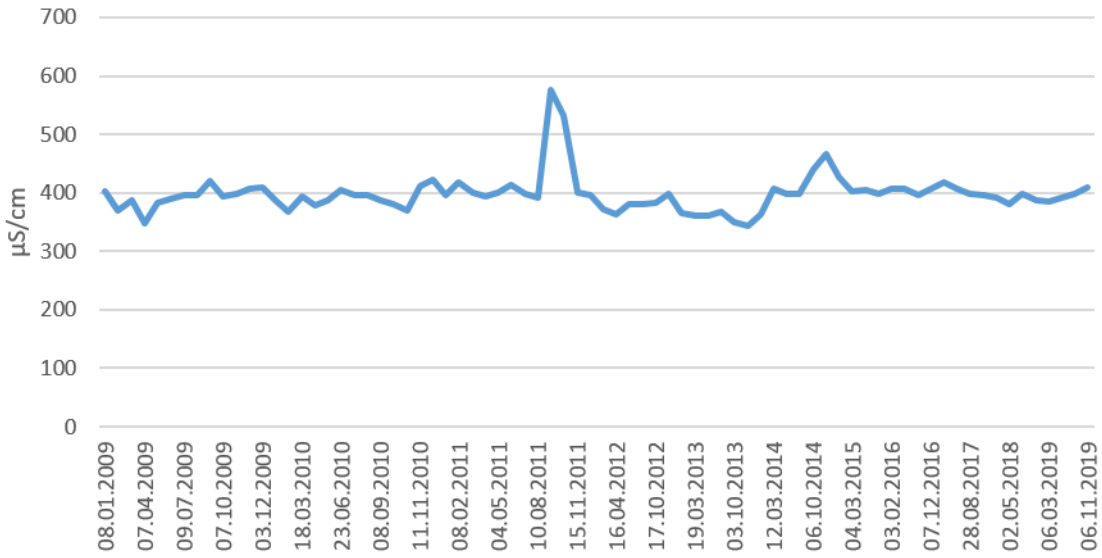

Fig. 4.7 Electrical conductivity values for monitoring station Opačac (2009.-2019.)

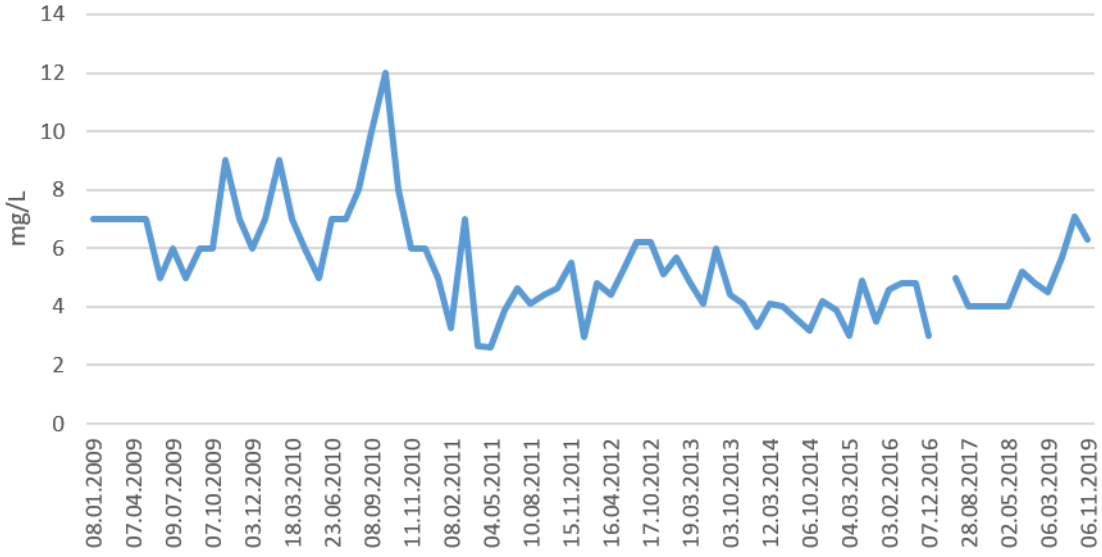

Fig. 4.8 Chloride concentration values for monitoring station Opačac (2009.-2019.)

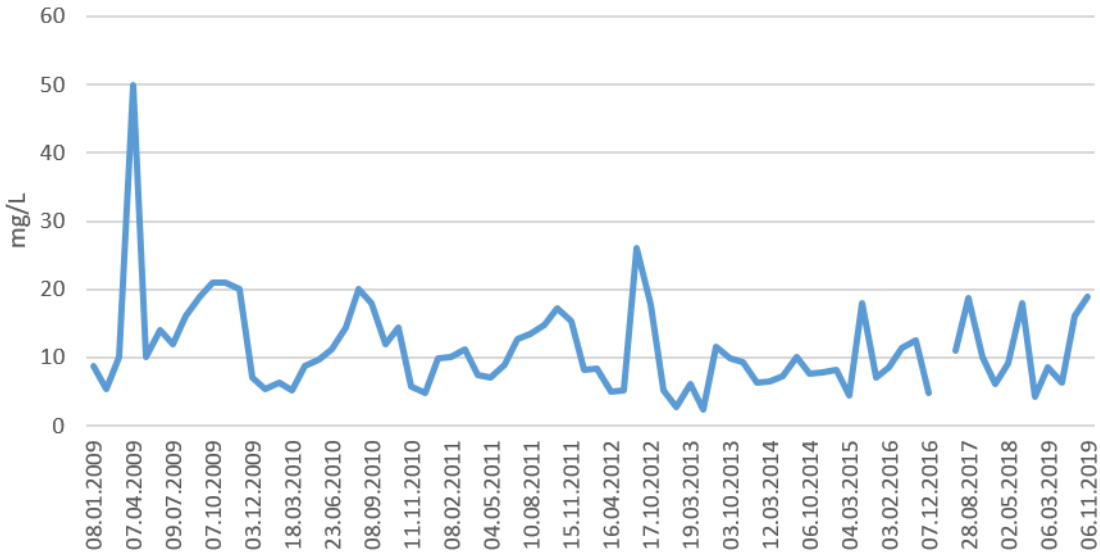

Fig. 4.9 Sulphate concentration values for monitoring station Opačac (2009.-2019.)

For monitoring station Banja, data for electrical conductivity (EC), chloride concentration (Cl^-) and sulphate concentration (SO_4^{2-}) for the period 2009-2019 were analyzed. Table 4.16 presents the overview of the results of statistical analysis.

Table 4.16. Results of statistical analysis for Banja monitoring station

	EC µS/cm	Cl^- mg/l	SO_4^{2-}
N	20	20	20
Average	487	3.8	75
Minimum	303	2.8	3.2
Maximum	850	5.5	270
Standard deviation	179	0.6	90
Variability coefficient (%)	37	17	121

The analysis of available data shows that in the period 2015-2019 sampling was performed only 21 times. The value of electrical conductivity ranged from 303 µS/cm to 850 µS/cm, with an average of 487 µS/cm (Figure 4.10). Chloride concentration ranged from 2.8 mg/l to maximum of 5.5 mg/l with an average of 3.8 mg/l (Figure 4.11). The variability of SO_4^{2-} was high (variability coefficient > 100%) ranging from minimum of 3.2 mg/l to maximum of 270 mg/l with an average of 75 mg/l (Figure 4.12).

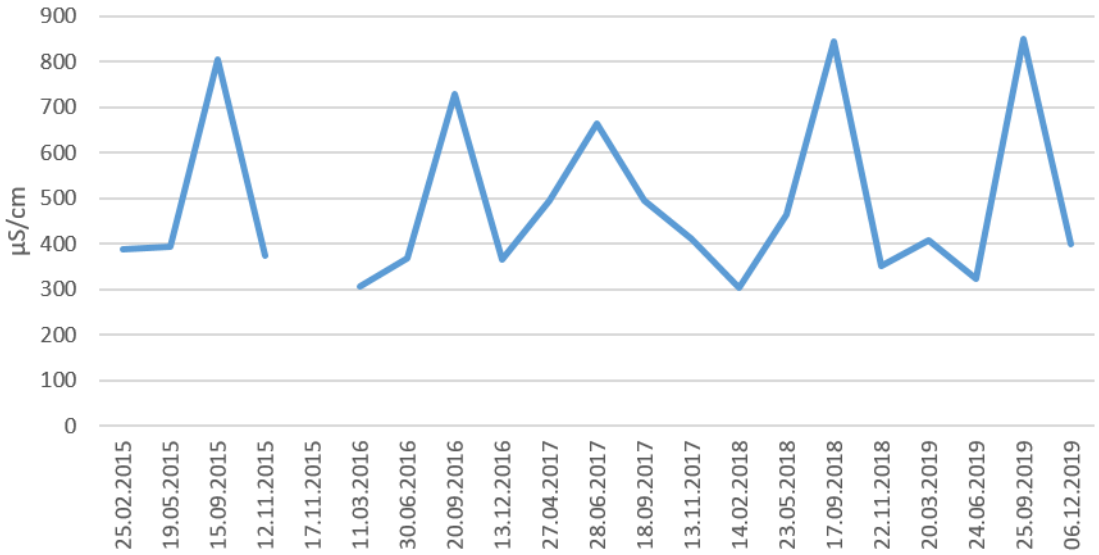

Fig. 4.10 Electrical conductivity values for monitoring station Banja (2015.-2019.)

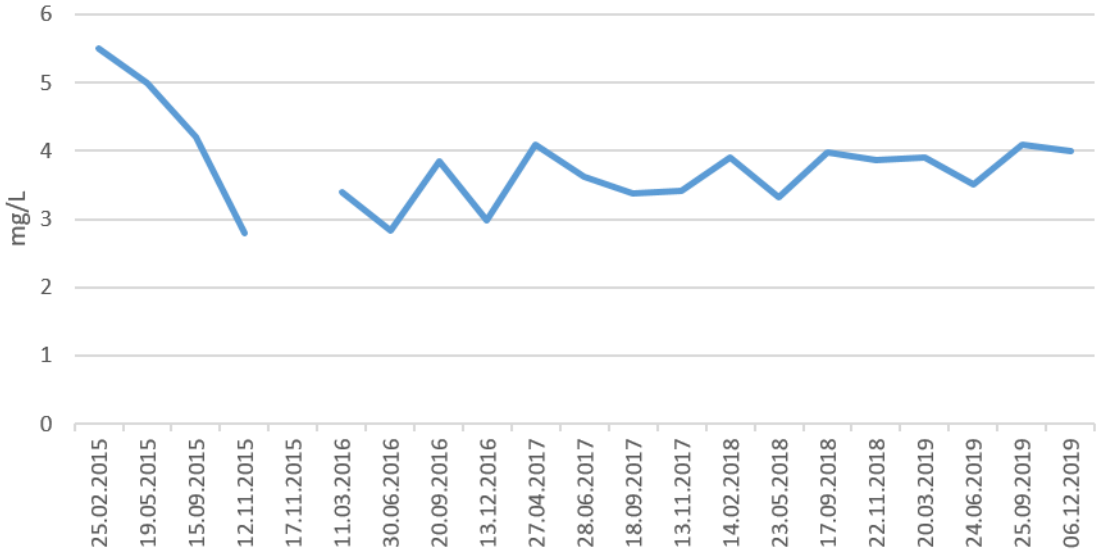

Fig. 4.11 Chloride concentration values for monitoring station Banja (2015.-2019.)

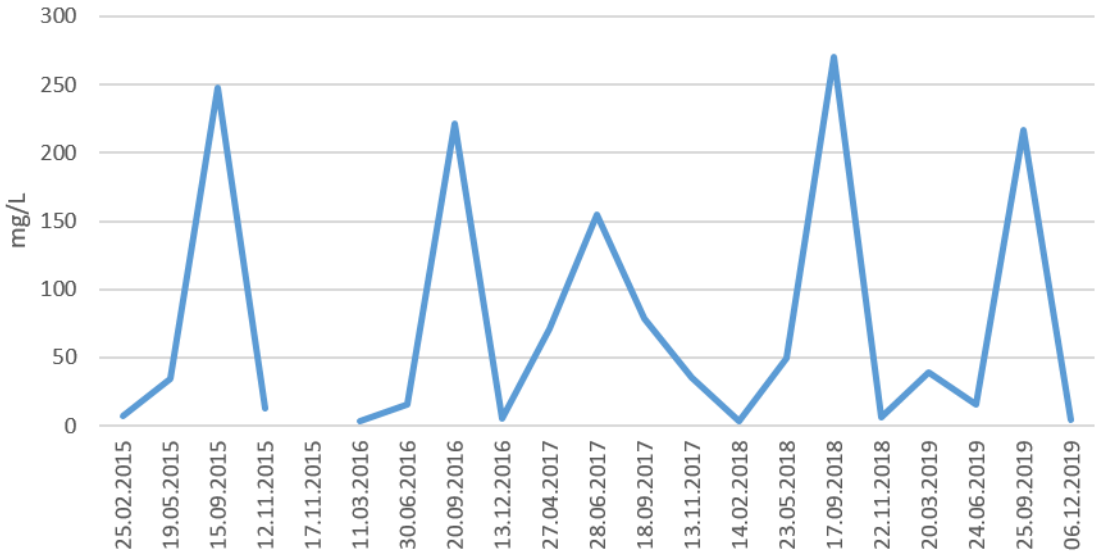

Fig. 4.12 Sulphate concentration values for monitoring station Banja (2015.-2019.)

For monitoring station Butina, data for electrical conductivity (EC), chloride concentration (Cl^-) and sulphate concentration (SO_4^{2-}) for the period 2009-2019 were analyzed. Table 4.17 presents the overview of the results of statistical analysis.

Table 4.17. Results of statistical analysis for Butina monitoring station

	EC µS/cm	Cl^- mg/l	SO_4^{2-}
N	70	70	70
Average	581	6.0	136
Minimum	287	3.3	11
Maximum	1036	18	400
Standard deviation	205.5	2.1	124
Variability coefficient (%)	35	35	91

The analysis of available data shows that in the period 2009-2019 sampling was performed 70 times. The value of electrical conductivity ranged from 287 µS/cm to 1036 µS/cm, with an average of 581 µS/cm (Figure 4.13). Chloride concentration ranged from minimum of 3.3 mg/l to maximum of 17.9 mg/l with an average of 6.0 mg/l (Figure 4.14). Sulphate concentration ranged from minimum of 11.2 mg/l to maximum of 400 mg/l with an average of 136.0 mg/l (Figure 4.15).

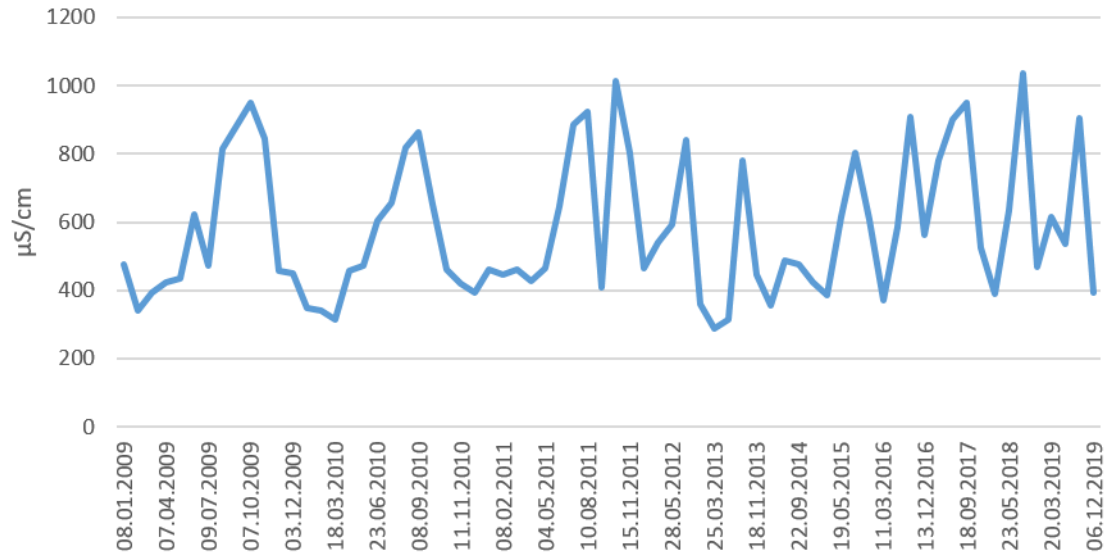

Fig. 4.13 Electrical conductivity values for monitoring station Butina (2009.-2019.)

Fig. 4.14 Chloride concentration values for monitoring station Butina (2009.-2019.)

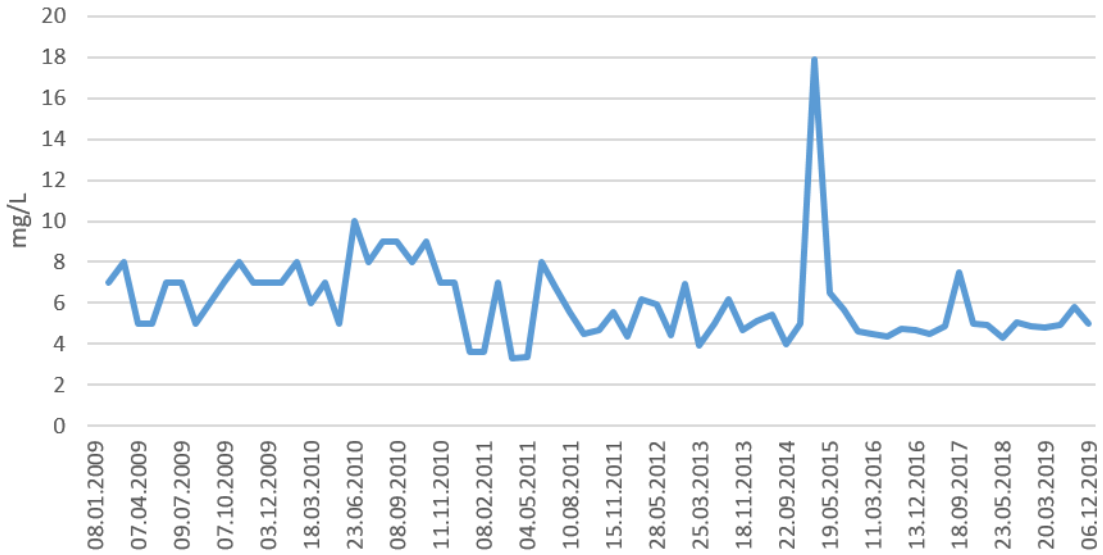

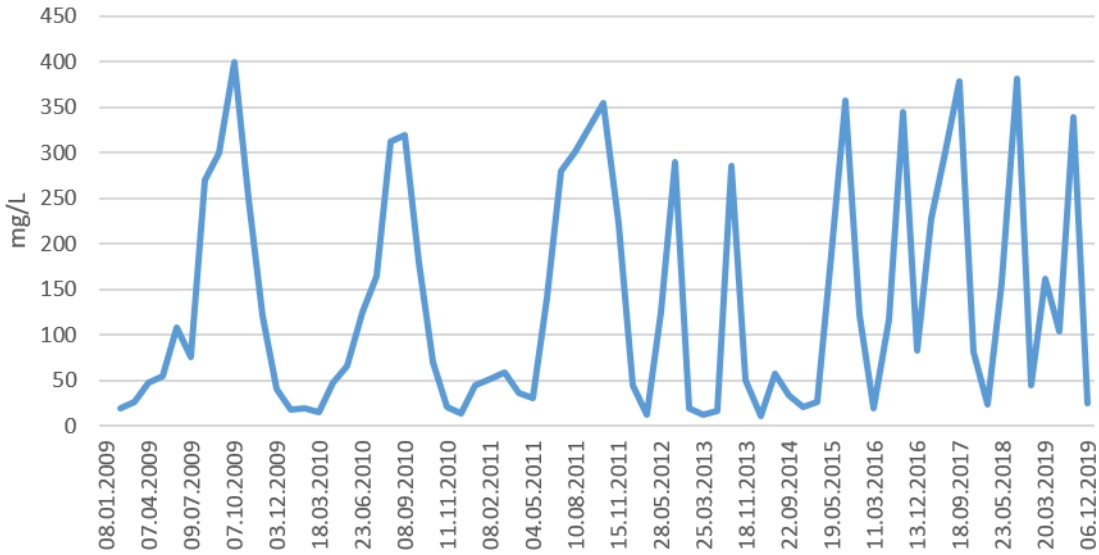

Fig. 4.15 Sulphate concentration values for monitoring station Butina (2009.-2019.)

For monitoring station Klokun, data for electrical conductivity (EC), chloride concentration (Cl^-) and sulphate concentration (SO_4^{2-}) for the period 2015-2019 were analyzed. Table 4.18 presents the overview of the results of statistical analysis.

Table 4.18. Results of statistical analysis for Klokun monitoring station

	EC µS/cm	Cl^- mg/l	SO_4^{2-}
N	20	20	20
Average	550	5.2	104
Minimum	387	4.1	19
Maximum	900	8.1	346
Standard deviation	143	1.0	90
Variability coefficient (%)	26	20	87

The analysis of available data shows that in the period 2015-2019 sampling was performed only 21 times. The value of electrical conductivity ranged from 387 µS/cm to 900 µS/cm, with an average of 550 µS/cm (Figure 4.16). Chloride concentration ranged from minimum of 4.1 mg/l to maximum of 8.1 mg/l with an average of 5.2 mg/l (Figure 4.17). Sulphate concentration ranged from minimum of 18.7 mg/l to maximum of 346.4 mg/l with an average of 103.5 mg/l (Figure 4.18).

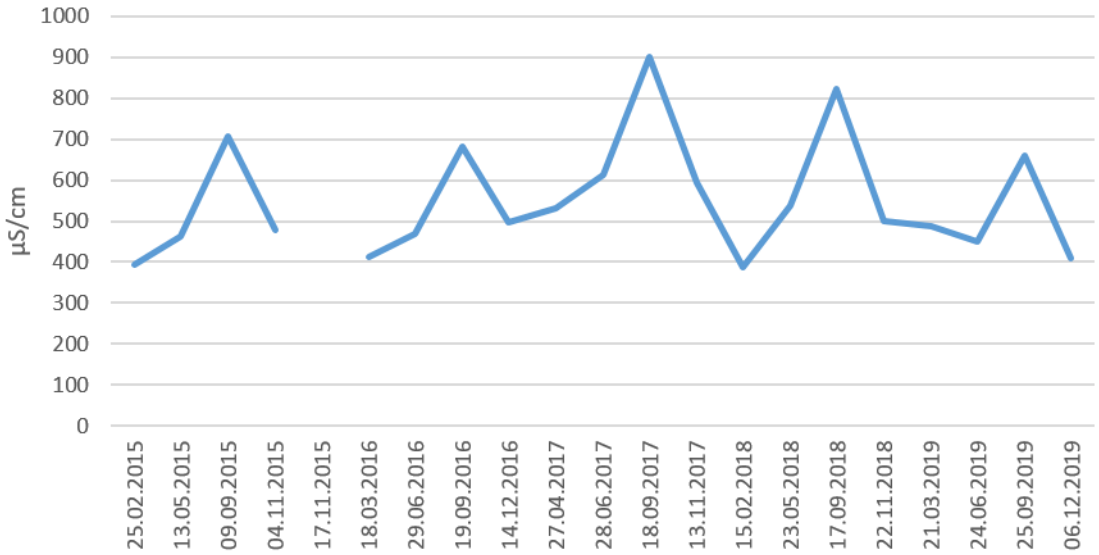

Fig. 4.16 Electrical conductivity values for monitoring station Klokun (2015.-2019.)

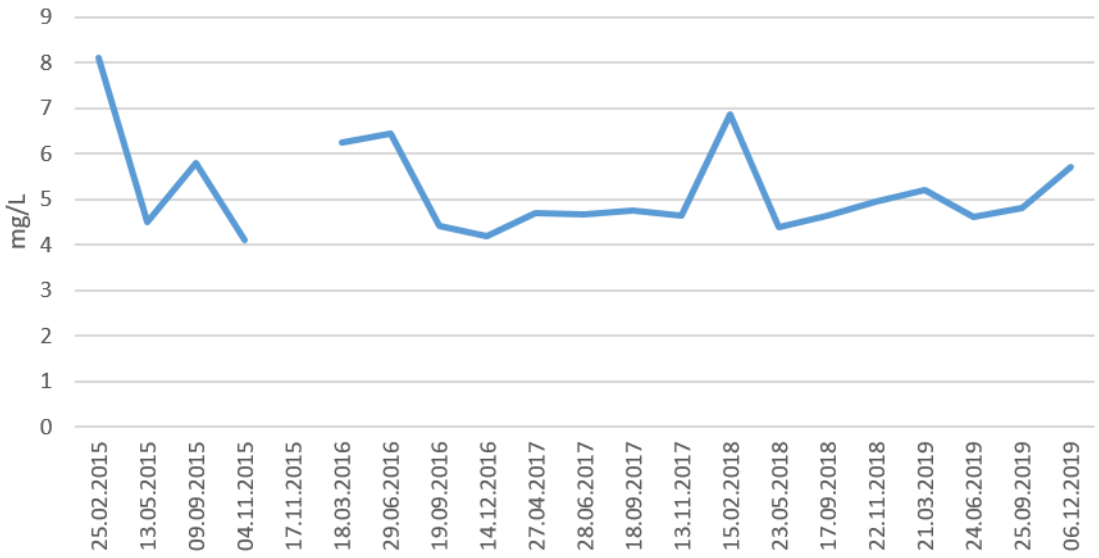

Fig. 4.17 Chloride concentration values for monitoring station Klokun (2015.-2019.)

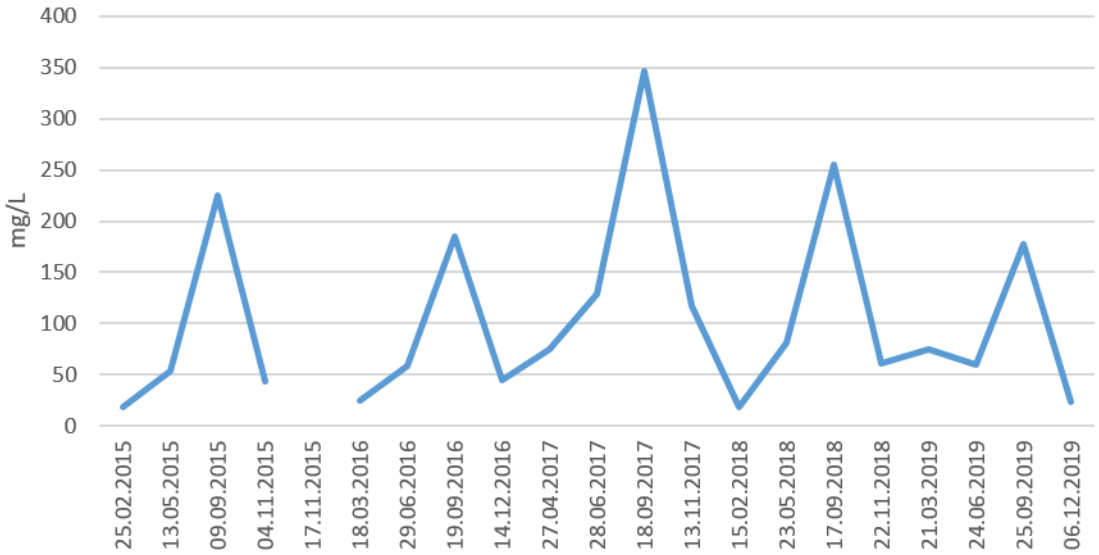

Fig. 4.18 Sulphate concentration values for monitoring station Klokun (2015.-2019.)

For monitoring station Modro Oko, data for electrical conductivity (EC), chloride concentration (Cl^-) and sulphate concentration (SO_4^{2-}) for the period 2015-2019 were analyzed. Table 4.19 presents the overview of the results of statistical analysis.

Table 4.19. Results of statistical analysis for Modro Oko monitoring station

	EC µS/cm	Cl^- mg/l	SO_4^{2-}
N	20	20	20
Average	631	10.7	147
Minimum	378	5	18
Maximum	1039	40	384
Standard deviation	222	10	128
Variability coefficient (%)	35	95	87

The analysis of available data shows that in the period 2015-2019 sampling was performed only 21 times. The value of electrical conductivity ranged from 387 µS/cm to 1039 µS/cm, with an average of 631 µS/cm (Figure 4.19). Chloride concentration ranged from minimum of 5.0 mg/l to maximum of 40.0 mg/l with an average of 10.7 mg/l (Figure 4.20). Sulphate concentration ranged from minimum of 18.1 mg/l to maximum of 383.6 mg/l with an average of 147.4 mg/l (Figure 4.21).

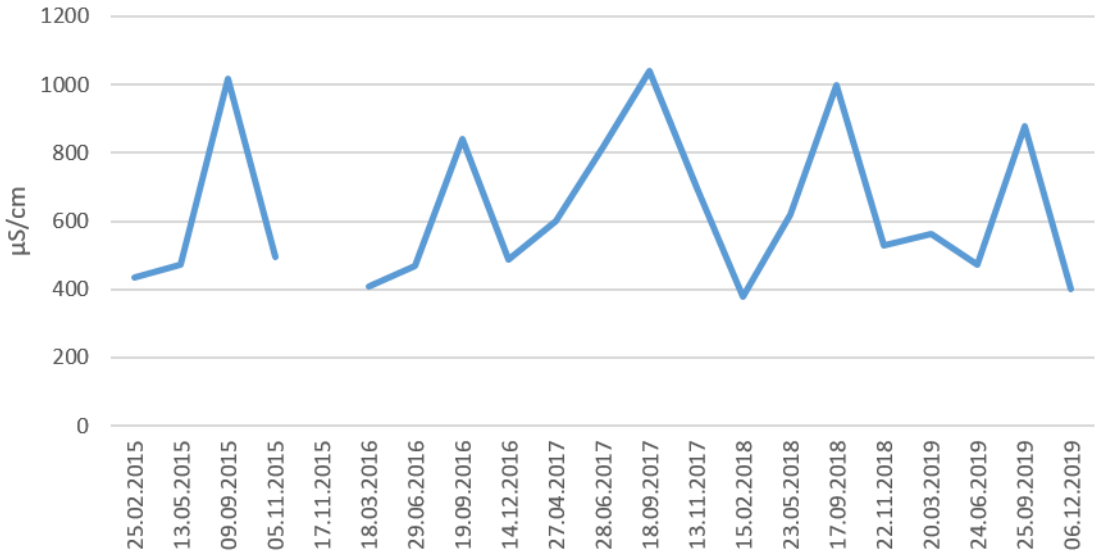

Fig. 4.19 Electrical conductivity values for monitoring station Modro Oko (2015.-2019.)

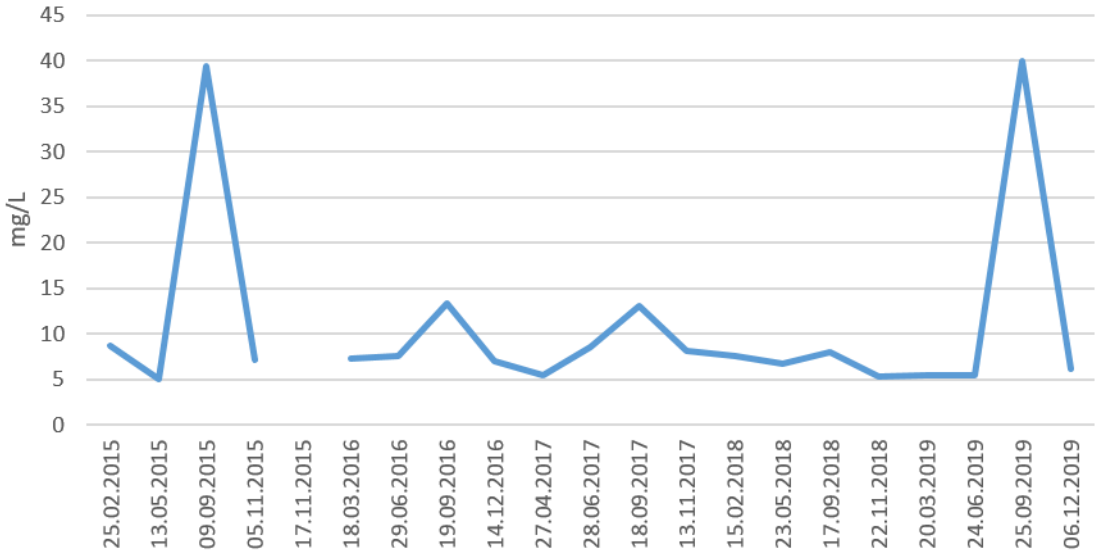

Fig. 4.20 Chloride concentration values for monitoring station Modro Oko (2015.-2019.)

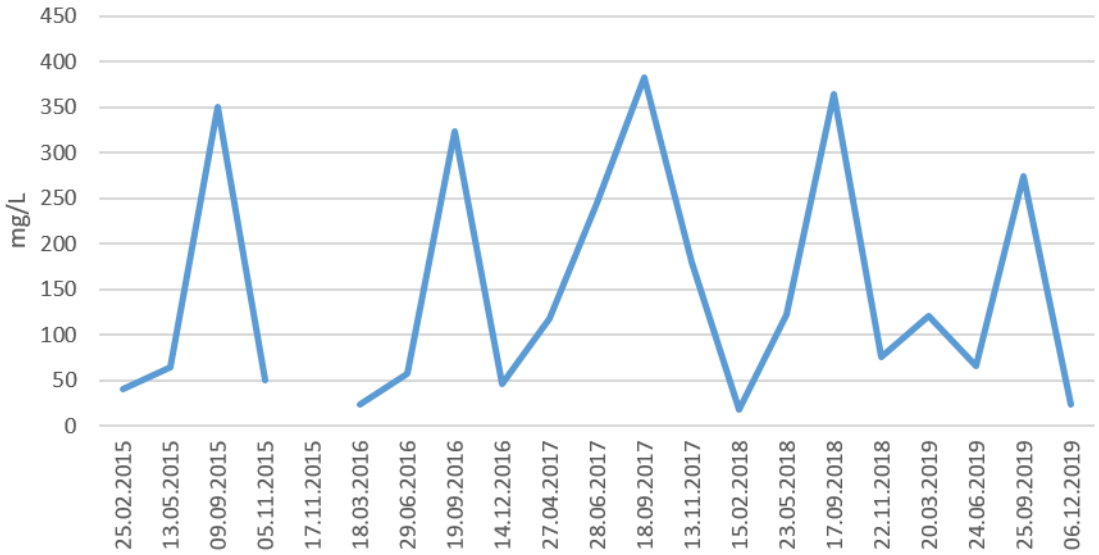

Fig. 4.21 Sulphate concentration values for monitoring station Modro Oko (2015.-2019.)

For monitoring station Prud, data for electrical conductivity (EC), pH, chloride concentration (Cl^-) and sulphate concentration (SO_4^{2-}) for the period 2010-2019 were analyzed. Table 4.20 presents the overview of the results of statistical analysis.

Table 4.20. Results of statistical analysis for Prud monitoring station

	pH	EC µS/cm	Cl^- mg/l	SO_4^{2-}
N	88	88	88	87
Average	7.3	655	22	124
Minimum	7	478	4.3	3,9
Maximum	7.6	1023	41	285
Standard deviation	0.1	119	5.7	77
Variability coefficient (%)	1.4	18	26	62

The analysis of available data shows that in the period 2010-2019 sampling was performed 88 times. pH value ranged from 7.0 to 7.6 with an average of 7.3 (Figure 4.22). The value of electrical conductivity ranged from 478 µS/cm to 1023 µS/cm, with an average of 655 µS/cm (Figure 4.23). Chloride concentration ranged from minimum of 4.3 mg/l to maximum of 41.4 mg/l with an average of 5.2 mg/l (Figure 4.24). Sulphate concentration ranged from minimum of 3.9 mg/l to maximum of 285 mg/l with an average of 124 mg/l (Figure 4.25).

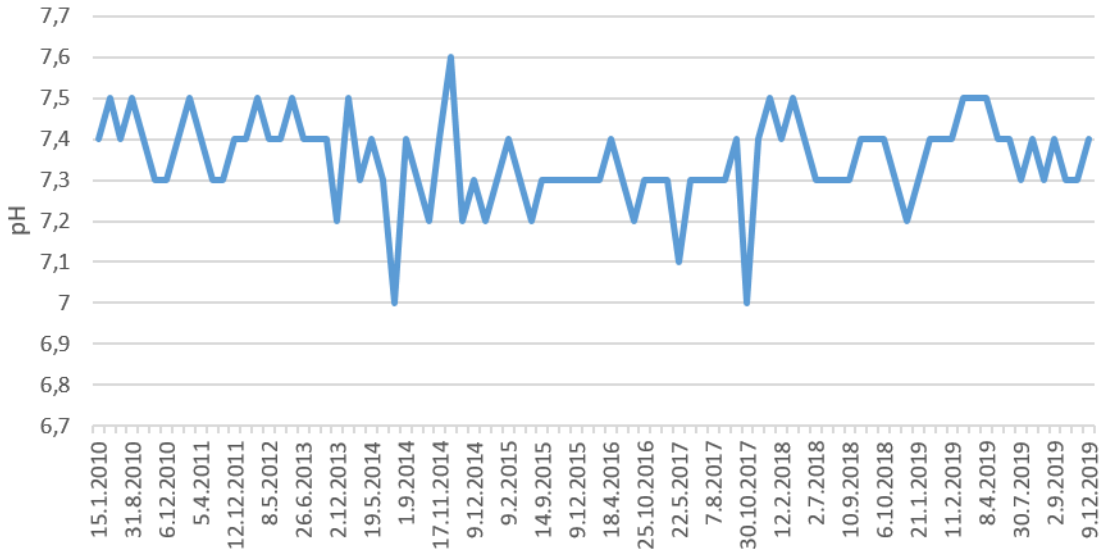

Fig. 4.22 pH values for monitoring station Prud (2010.-2019.)

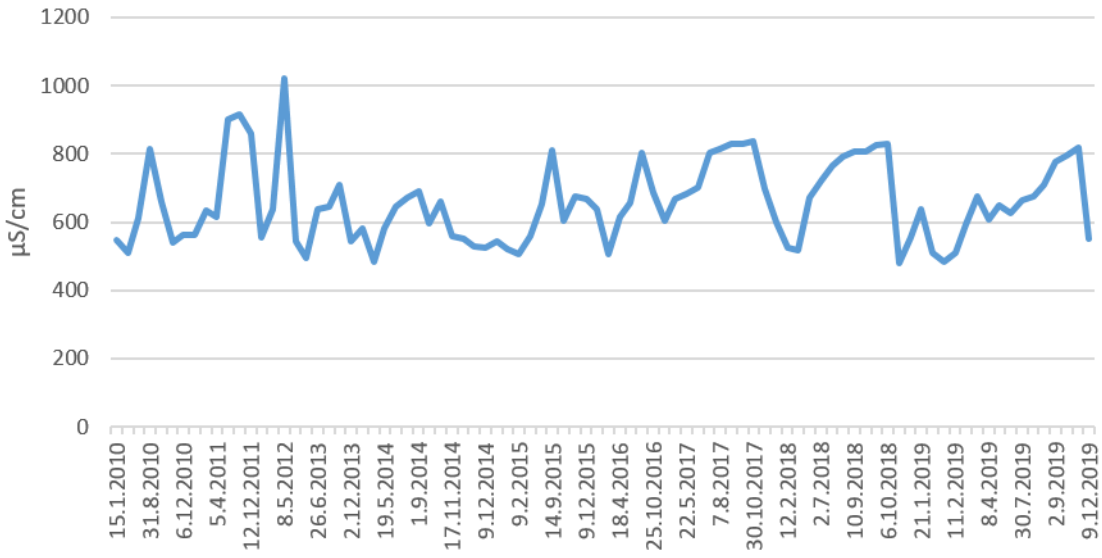

Fig. 4.23 Electrical conductivity values for monitoring station Prud (2010.-2019.)

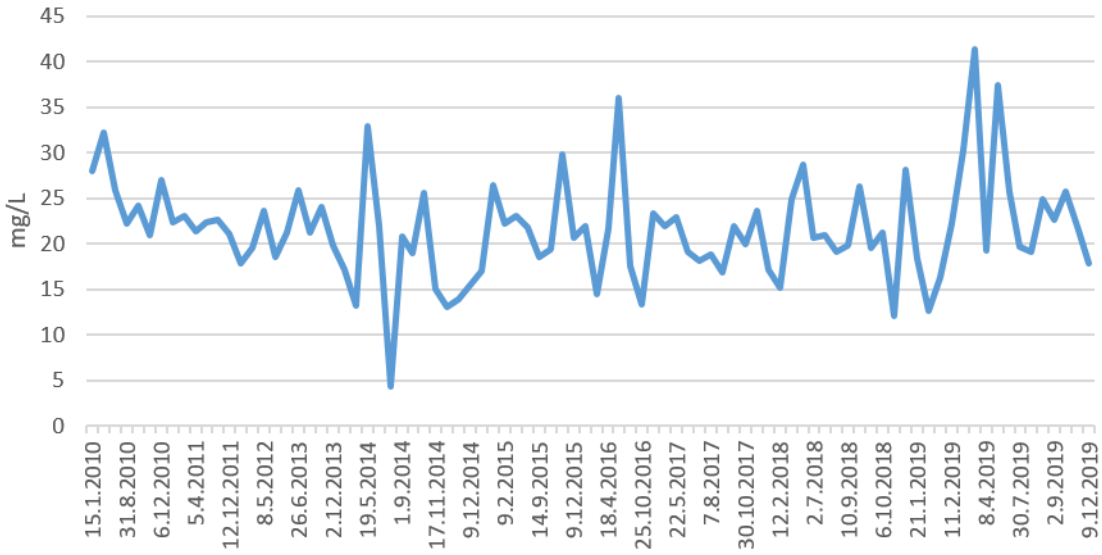

Fig. 4.24 Chloride concentration values for monitoring station Prud (2010.-2019.)

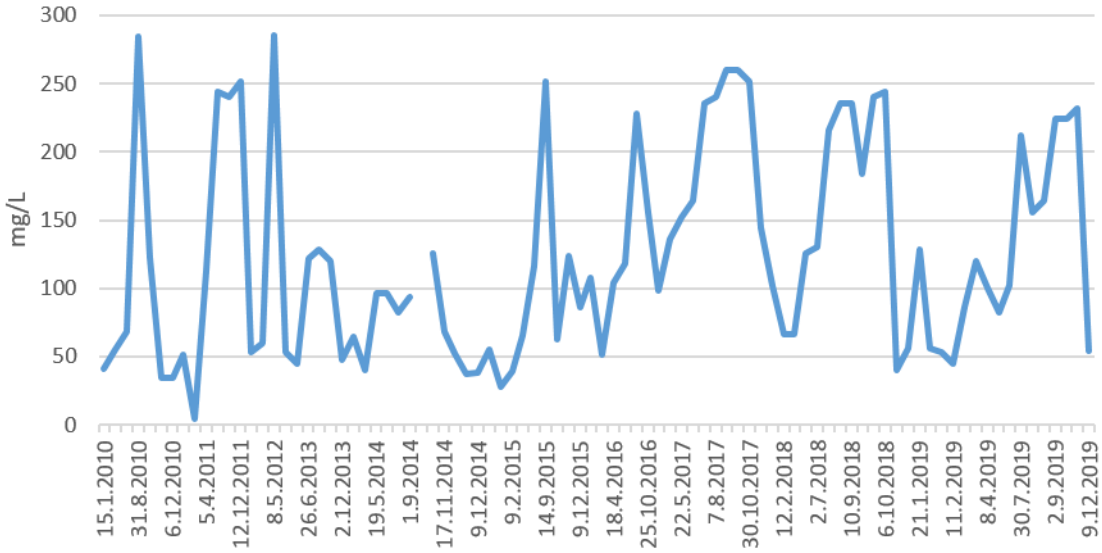

Fig. 4.25 Sulphate concentration values for monitoring station Prud (2010.-2019.)

For monitoring station Doljani, which represents the entry station into Republic of Croatia, data for electrical conductivity (EC), pH and chloride concentration (Cl^-) and sulphate concentration (SO_4^{2-}) for the period 2010-2019 were analyzed. Table 4.21 presents the overview of the results of statistical analysis.

Table 4.21 Results of statistical analysis for Doljani monitoring station

	pH	EC µS/cm	Cl^- mg/l
N	543	551	549
Average	7.4	847	152
Minimum	6.9	297	3.9
Maximum	8.2	4880	1358
Standard deviation	0.1	477	155
Variability coefficient (%)	1.8	56	102

The analysis of available data shows that in the period 2010-2019 sampling was performed 551 times. pH value ranged from 6.9 to 8.2 with an average of 7.4 (Figure 4.26). The value of electrical conductivity ranged from 291 µS/cm to 4880 µS/cm, with an average of 847 µS/cm (Figure 4.27). Chloride concentration ranged from minimum of 3.9 mg/l to maximum of 41.4 mg/l with an average of 1358 mg/l (Figure 4.28).

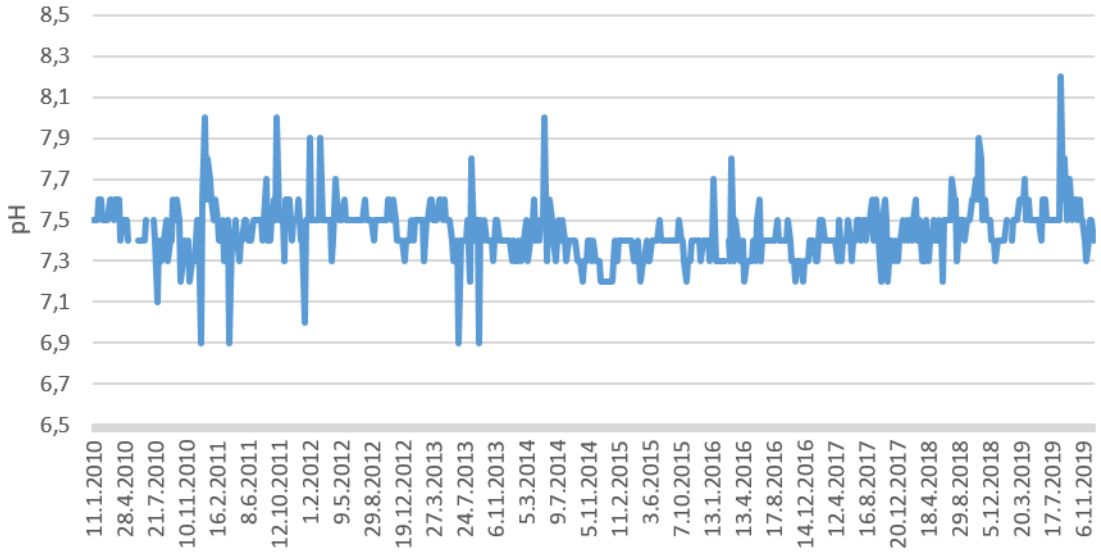

Fig. 4.26 pH values for monitoring station Doljani (2010.-2019.)

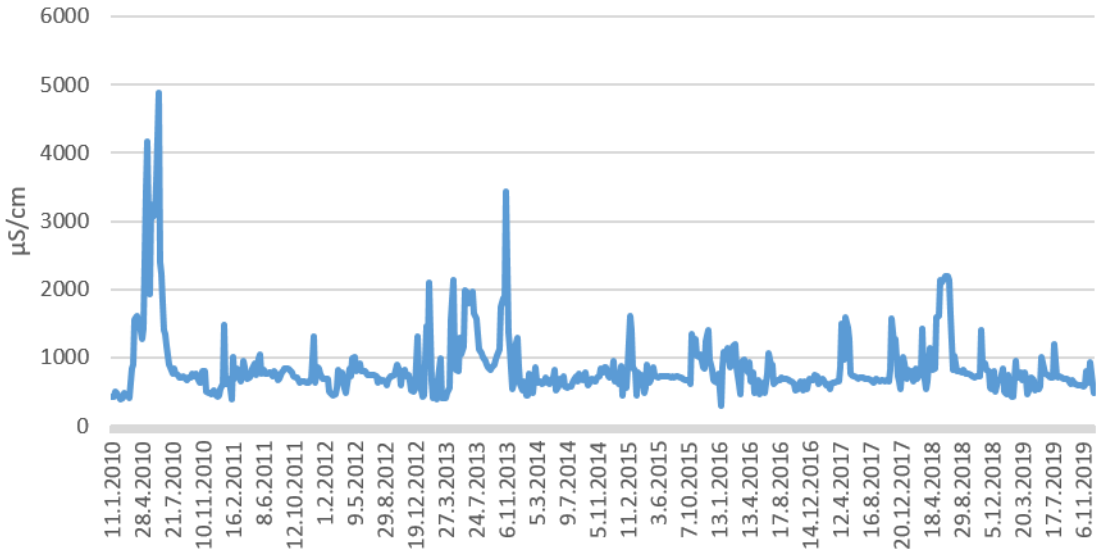

Fig. 4.27 Electrical conductivity values for monitoring station Doljani (2010.-2019.)

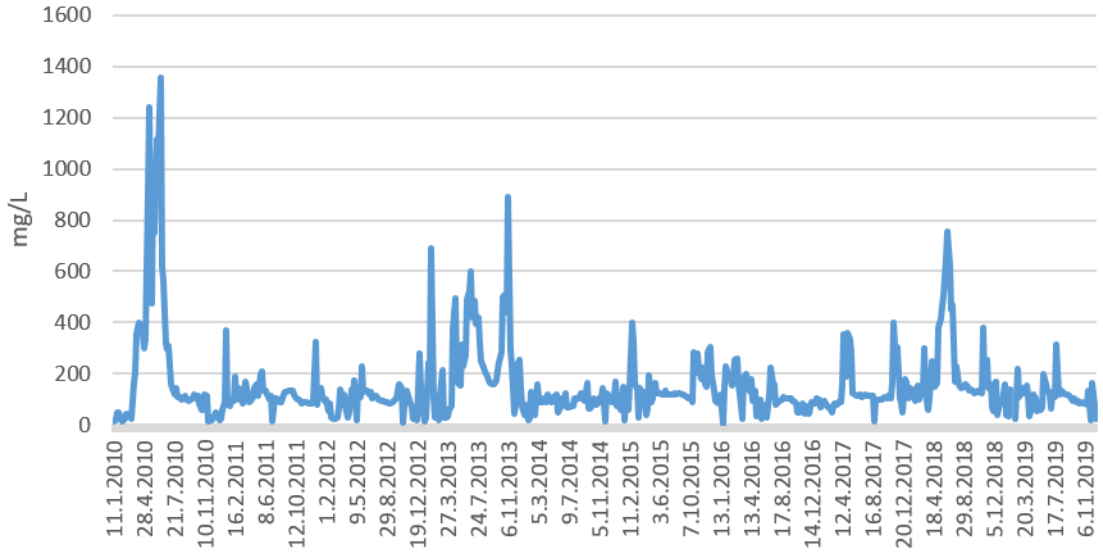

Fig. 4.28 Chloride concentration values for monitoring station Doljani (2010.-2019.)

For monitoring station Žitomislići, data for electrical conductivity (EC) and pH for the period 2009-2019 were analyzed. Table 4.22 presents the overview of the results of statistical analysis.

Table 4.22. Results of statistical analysis for Žitomislići monitoring station

	pH	EC µS/cm
N	131	131
Average	8,07	323
Minimum	7.6	263
Maximum	8.4	410
Standard deviation	0.1	22
Variability coefficient (%)	1.6	6.8

The analysis of available data shows that in the period 2009-2019 sampling was performed 131 times. pH value ranged from 7.6 to 8.4 with an average of 8.1 (Figure 4.29). The value of electrical conductivity ranged from 263 µS/cm to 410 µS/cm, with an average of 323 µS/cm (Figure 4.30).

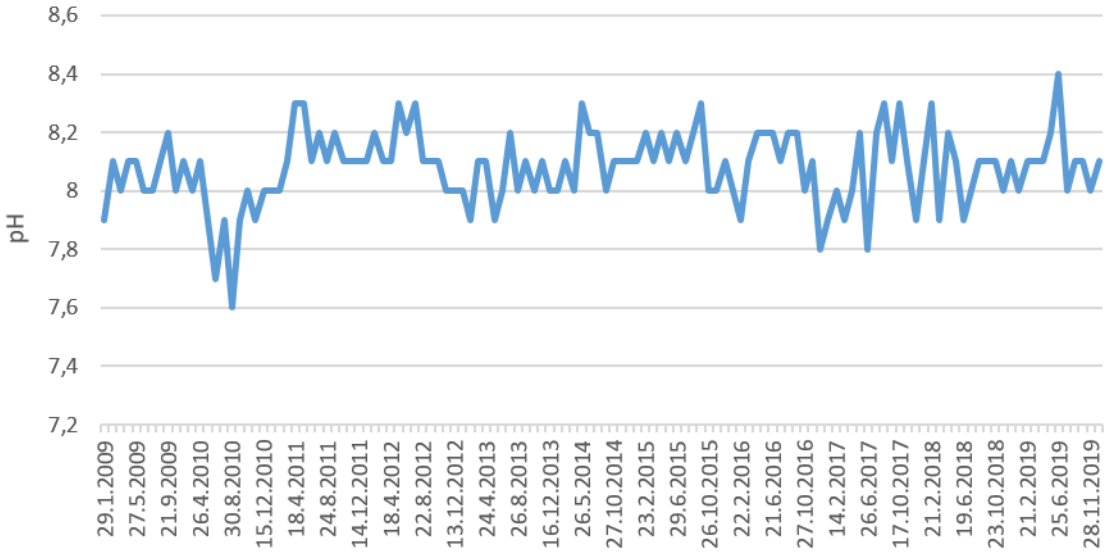

Fig. 4.29 pH values for monitoring station Žitomislići (2009.-2020.)

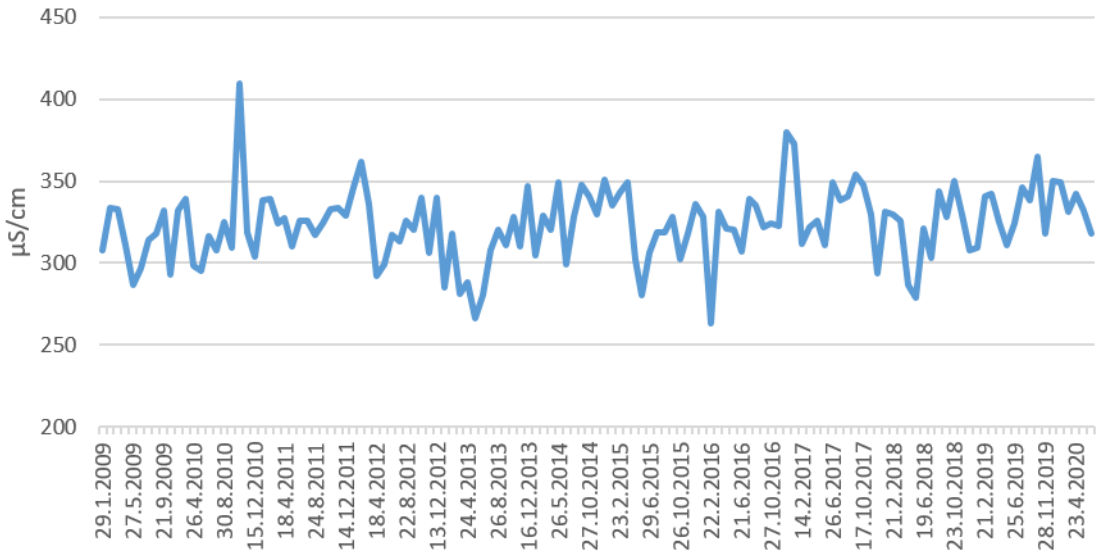

Fig. 4.30 Electrical conductivity values for monitoring station Žitomislići (2009.-2020.)

For monitoring station Nereze, data for electrical conductivity (EC), chloride concentration (Cl^-) and sulphate concentration (SO_4^{2-}) for the period 2015-2019 were analyzed. Table 4.23 presents the overview of the results of statistical analysis.

Table 4.23. Results of statistical analysis for Nereze monitoring station

	EC	Cl^-	SO_4^{2-}
	µS/cm	mg/l	
N	20	20	20
Average	667	104	17
Minimum	362	22	5.5
Maximum	1148	231	34.3
Standard deviation	221	67	8.7
Variability coefficient (%)	33	64	50

The analysis of available data shows that in the period 2015-2019 sampling was performed only 21 times. The value of electrical conductivity ranged from 362 µS/cm to 1148 µS/cm, with an average of 667 µS/cm (Figure 4.31). Chloride concentration ranged from minimum of 21.8 mg/l to maximum of 231 mg/l with an average of 104.1 mg/l (Figure 4.32). Sulphate concentration ranged from minimum of 5.5 mg/l to maximum of 34.3 mg/l with an average of 17.3 mg/l (Figure 4.33).

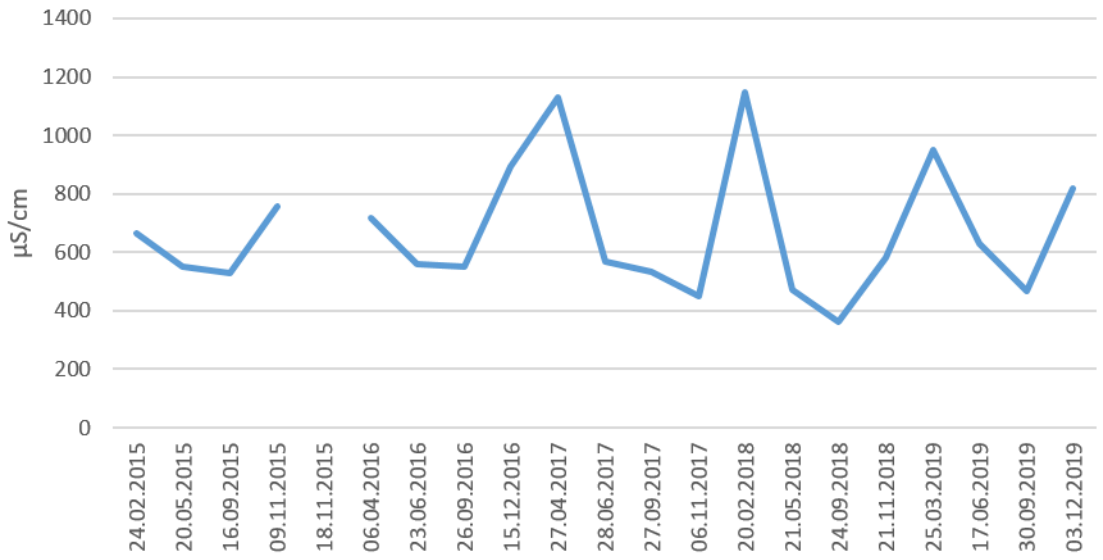

Fig. 4.31 Electrical conductivity values for monitoring station Nereze (2015.-2019.)

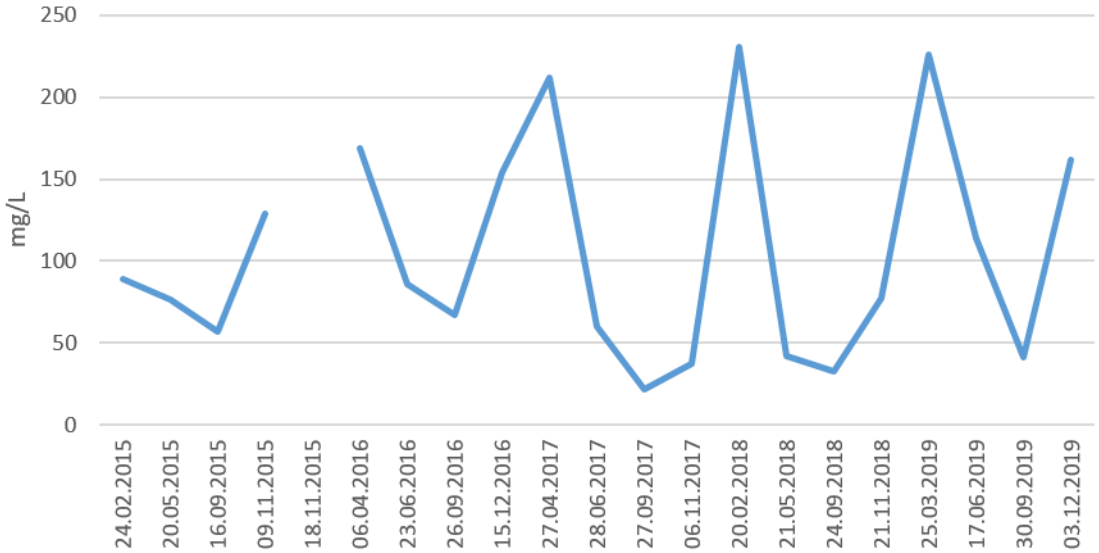

Fig. 4.32 Chloride concentration values for monitoring station Nereze (2015.-2019.)

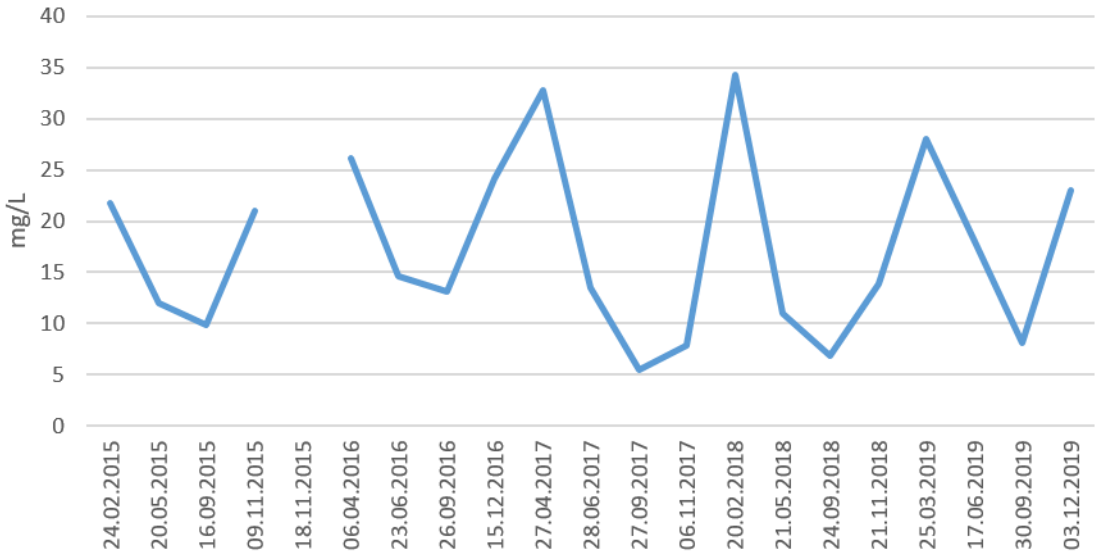

Fig. 4.33 Sulphate concentration values for monitoring station Nereze (2015.-2019.)

For monitoring station Ombla, data for electrical conductivity (EC), chloride concentration (Cl^-) and sulphate concentration (SO_4^{2-}) for the period 2009-2019 were analyzed. Table 4.24 presents the overview of the results of statistical analysis.

Table 4.24. Results of statistical analysis for Ombla monitoring station

	EC	Cl^-	SO_4^{2-}
	µS/cm	mg/l	
N	63	63	63
Average	352	5.3	4.3
Minimum	263	2.7	1.9
Maximum	471	9.0	8.0
Standard deviation	29	1.7	1.3
Variability coefficient (%)	8.3	32	31

The analysis of available data shows that in the period 2009-2019 sampling was performed 71 times, but data only 63 measurements were used for analysis. The value of electrical conductivity ranged from 263 µS/cm to 471 µS/cm, with an average of 352 µS/cm (Figure 4.34). Chloride concentration ranged from minimum of 2.7 mg/l to maximum of 9.0 mg/l with an average of 5.3 mg/l (Figure 4.35). Sulphate concentration ranged from minimum of 1.9 mg/l to maximum of 8.0 mg/l with an average of 4.3 mg/l (Figure 4.36).

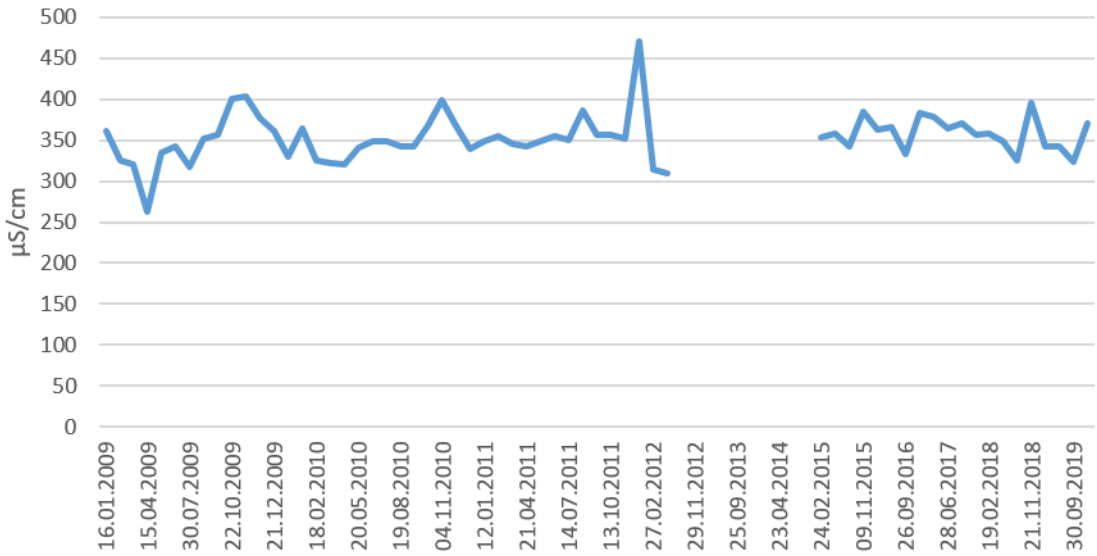

Fig. 4.34 Electrical conductivity values for monitoring station Ombla (2009.-2019.)

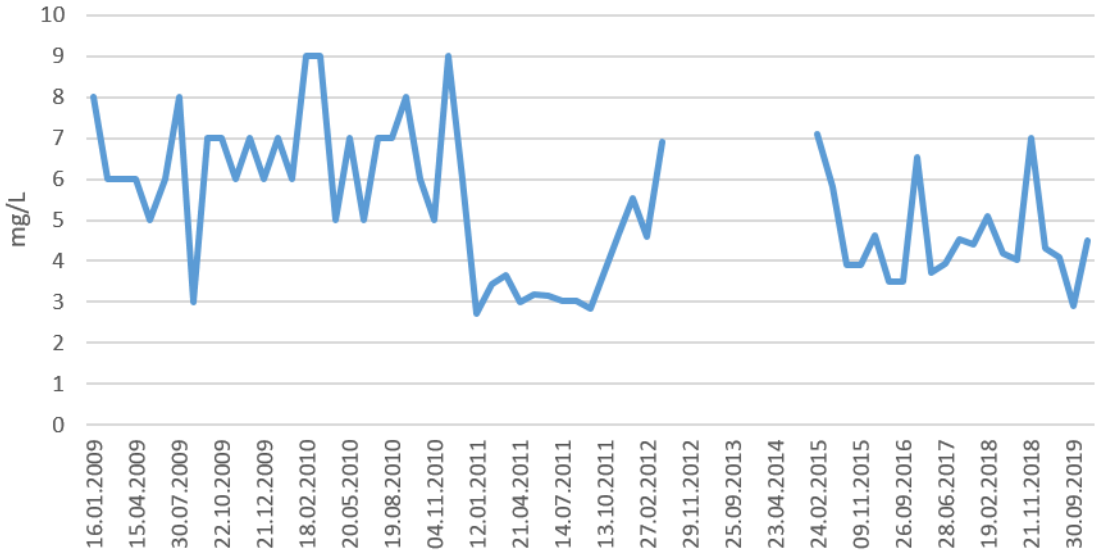

Fig. 4.35 Chloride concentration values for monitoring station Ombla (2009.-2019.)

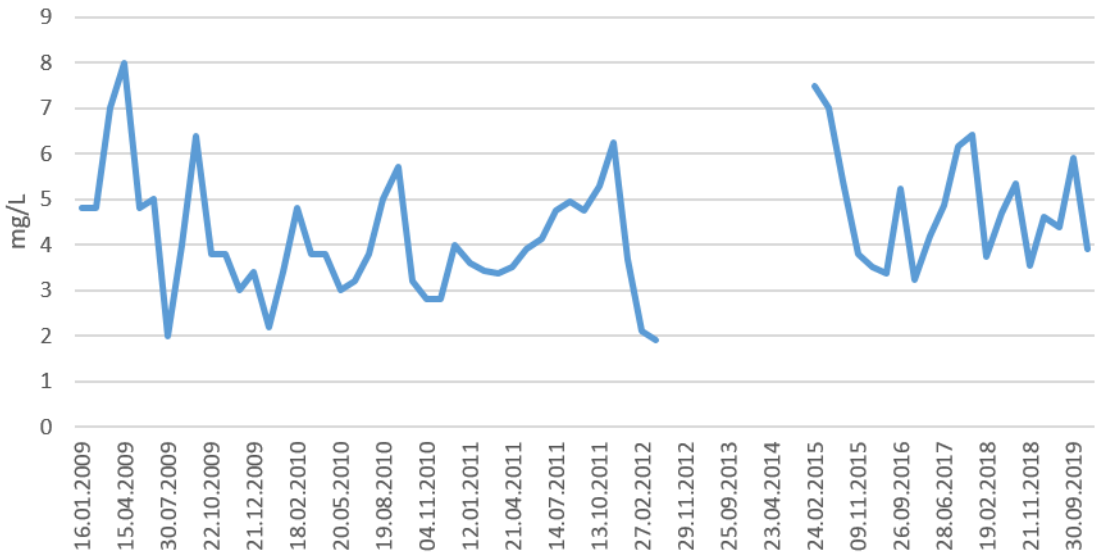

Fig. 4.36 Sulphate concentration values for monitoring station Ombla (2009.-2019.)

For monitoring station Duboka Ljuta, data for electrical conductivity (EC), chloride concentration (Cl^-) and sulphate concentration (SO_4^{2-}) for the period 2015-2019 were analyzed. Table 4.25 presents the overview of the results of statistical analysis.

Table 4.25. Results of statistical analysis for Duboka Ljuta monitoring station

	EC µS/cm	Cl^- mg/l	SO_4^{2-}
N	20	20	20
Average	336	5.4	3.5
Minimum	304	3.3	2.3
Maximum	462	8.3	5.2
Standard deviation	35	1.3	0.6
Variability coefficient (%)	10	23	18

The analysis of available data shows that in the period 2015-2019 sampling was performed only 21 times. The value of electrical conductivity ranged from 304 µS/cm to 462 µS/cm, with an average of 336 µS/cm (Figure 4.37). Chloride concentration ranged from minimum of 3.3 mg/l to maximum of 8.3 mg/l with an average of 5.4 mg/l (Figure 4.38). Sulphate concentration ranged from minimum of 2.3 mg/l to maximum of5.2 mg/l with an average of 3.5 mg/l (Figure 4.39).

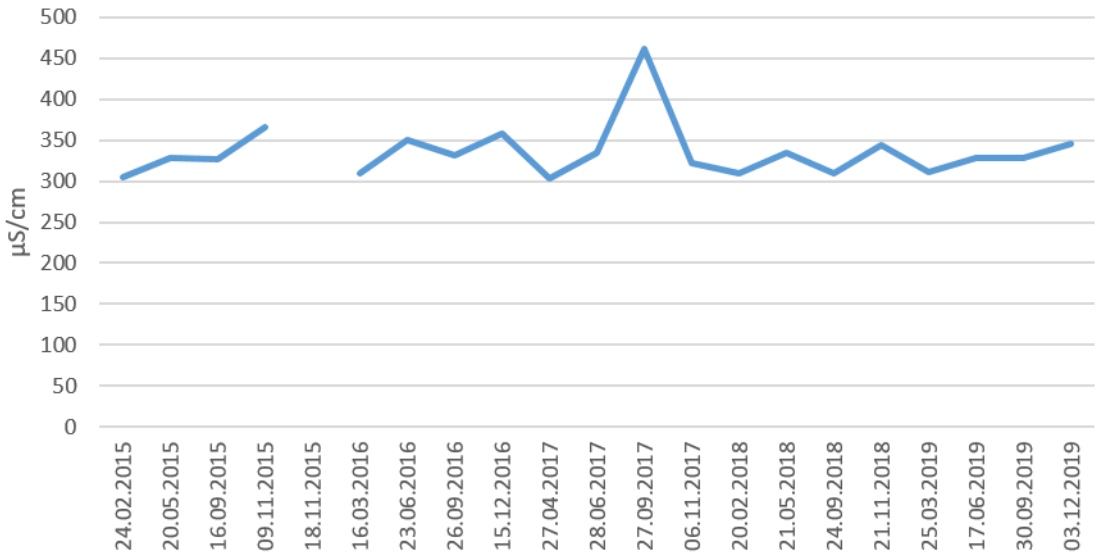

Fig. 4.37 Electrical conductivity values for monitoring station Duboka Ljuta (2015.-2019.)

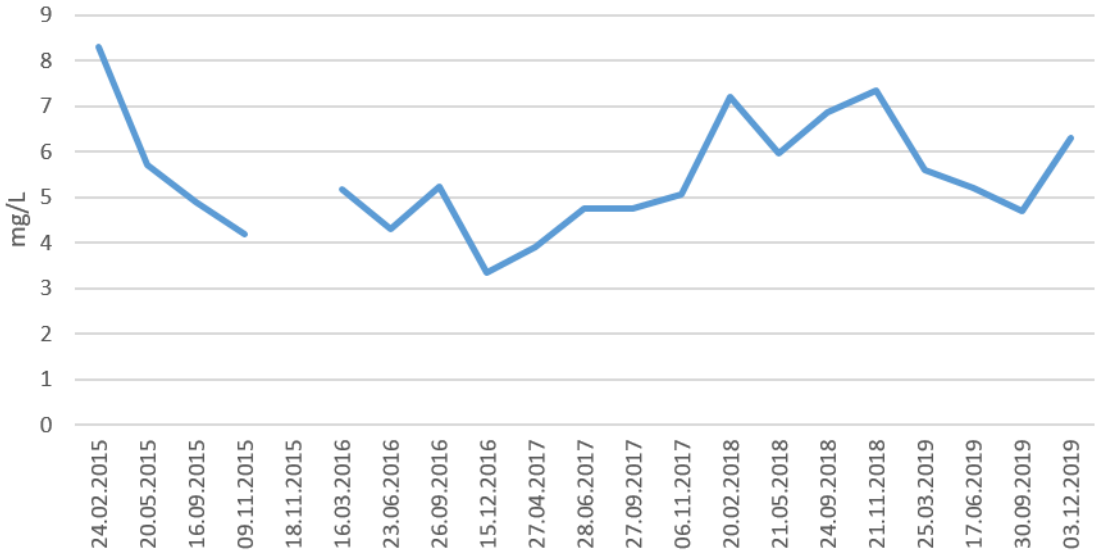

Fig. 4.38 Chloride concentration values for monitoring station Duboka Ljuta (2015.-2019.)

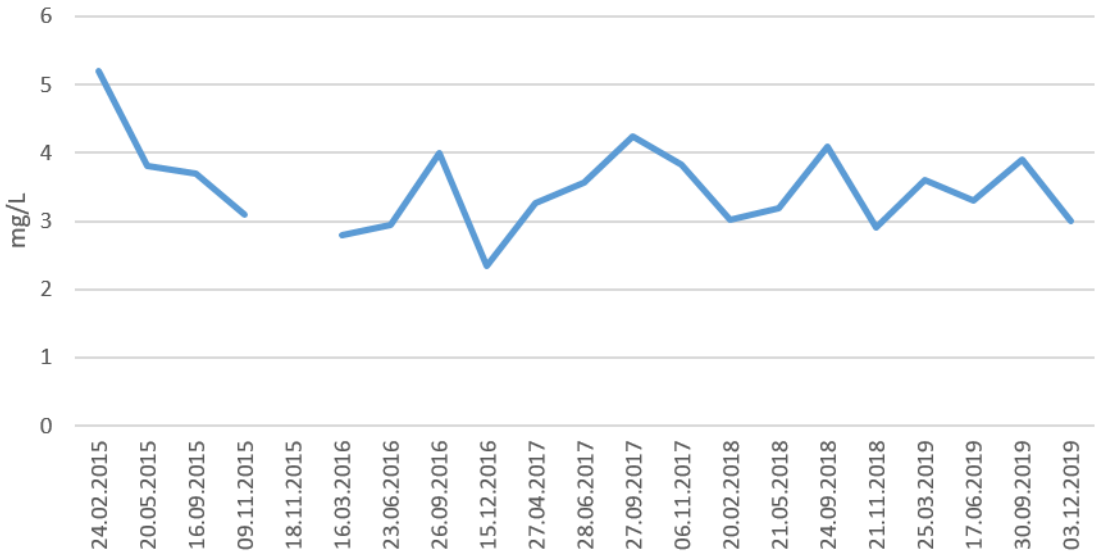

Fig. 4.39 Sulphate concentration values for monitoring station Duboka Ljuta (2015.-2019.)

For the south most monitoring station Ljuta, data for electrical conductivity (EC), chloride concentration (Cl^-) and sulphate concentration (SO_4^{2-}) for the period 2009-2019 were analyzed. Table 4.26 presents the overview of the results of statistical analysis.

Table 4.26. Results of statistical analysis for Ljuta monitoring station

	EC µS/cm	Cl^- mg/l	SO_4^{2-}
N	71	71	71
Average	294	5.3	3.0
Minimum	246	2.7	0.6
Maximum	464	13	28
Standard deviation	32	2.2	3.1
Variability coefficient (%)	11	41	106

The analysis of available data shows that in the period 2010-2019 sampling was performed 71 times. The value of electrical conductivity ranged from 246 µS/cm to 464 µS/cm, with an average of 294 µS/cm (Figure 4.40). Chloride concentration ranged from minimum of 2.7 mg/l to maximum of 13.0 mg/l with an average of 5.3 mg/l (Figure 4.41). Sulphate concentration ranged from minimum of 0.6 mg/l to maximum of 28 mg/l with an average of 3.0 mg/l (Figure 4.42).

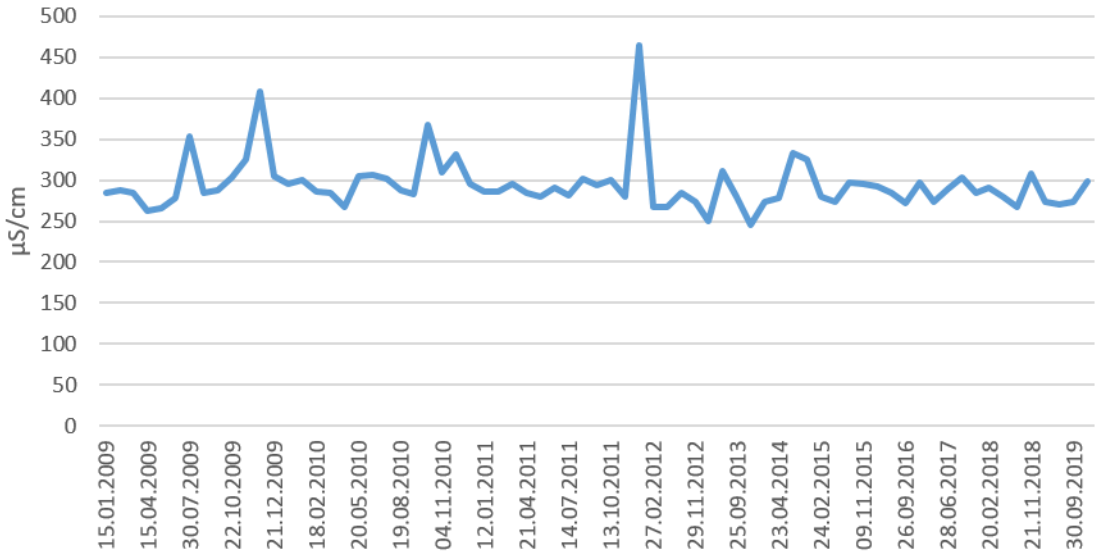

Fig. 4.40 Electrical conductivity values for monitoring station Ljuta (2009.-2019.)

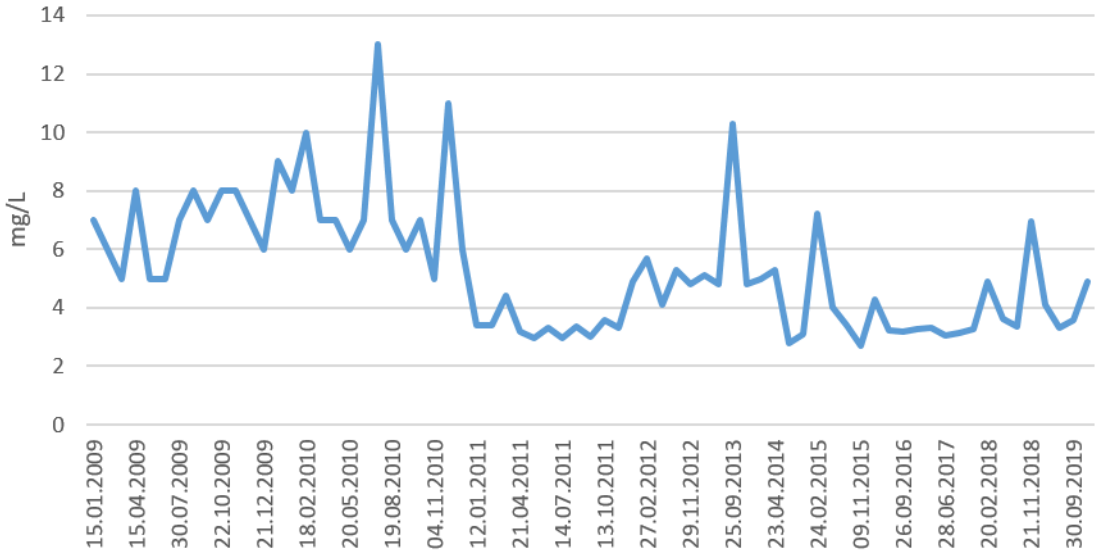

Fig. 4.41 Chloride concentration values for monitoring station Ljuta (2009.-2019.)

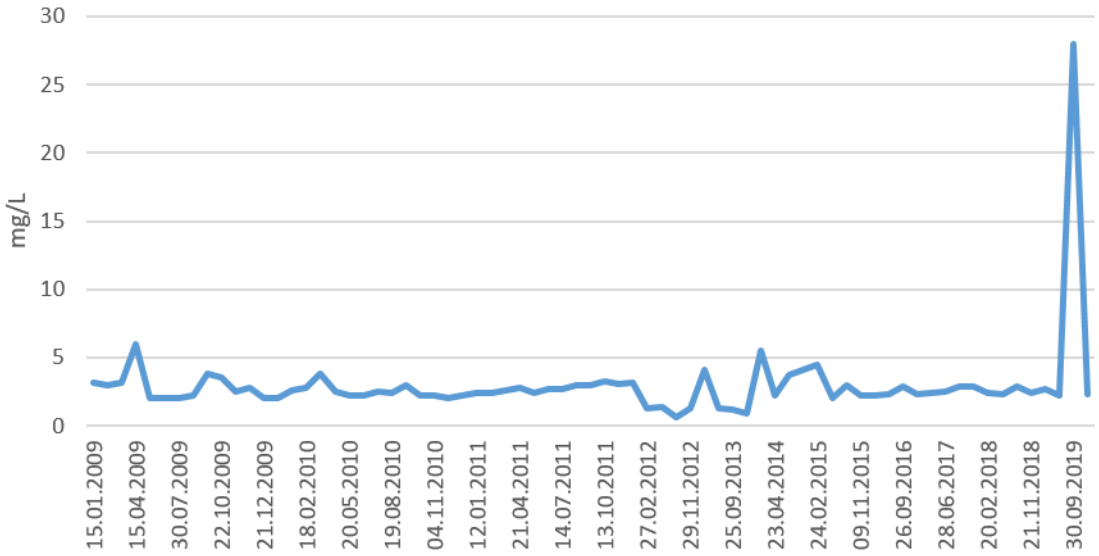

Fig. 4.42 Sulphate concentration values for monitoring station Ljuta (2009.-2019.)

4.3.5 Spatial, temporal and methodological characterization of monitoring network established in the framework of the Asteris project in the pilot area of the Neretva Delta

Sampling sites were selected based on a monitoring network used in a previous work (see Section 4.3.3). A total of 11 sampling sites were selected for seasonal monitoring, of which the surface water monitoring sites were River Neretva (Metković), River Mala Neretva and Vrbovi lateral canal. Groundwater was monitored in two different types of piezometers:

(i): deep piezometers: D1, D2, D3 and D4 with the following caharachistics (Srzic et al., 2020):

Piezometer	overall depth (m)	perforation height (m)	aquifer
D1	37.50 m	1.20	confined
D2	34.39	3	gravelly media
D4	25.24	2	confined

and shallow piezometers (ii): Jasenska, Luke, Vidrice and Vrbovci piezometers made of 110 mm diameter plastic tube, with a porous section between 3 to 4 meters depth (Romić et al., 2020).

Water samples were collected at the end of the dry season (Figure 4.44) and at the end of the wet season. Surface water samples were collected by directly filling a hand-held bottle sampler. Groundwater samples were collected using piezometer tube samplers that were purpose-built for water sampling. Water samples were tightly sealed and transported to the laboratory protected from light and excessive heat. Surface and groundwater samples were collected according to standardized procedures (HRN EN 5667-6, 2016; HRN ISO 5667-11, 2011). Samples used for the determination of orthophosphate (o-PO4) were filtered through a membrane filter (0.45-µm mesh) immediately after sampling. Samples used for the determination of ammonium nitrogen (NH4-N) were preserved by adding sulfuric acid to adjust the sample to a pH of approximately 2. The following chemical and physical parameters are analyzed in water samples in the Analytical laboratory of the Department of Amelioration (MELILAB) - accredited laboratory in the field of water sampling and analyses according to the HRN EN ISO/IEC 17025:2007 normative document.

Parameter	Method
pH	ISO 10523:2008 Water quality — Determination of pH
electrical conductivity (EC_w)	HRN EN 27888, 2008. Water Quality - Determination of Electrical Conductivity. International Organisation for Standardisation. Croatian Standard Institute
NO_3-N, NO_2-N, NH_4-N	HRN EN ISO 11732, 2008. Water Quality - Determination of Ammonium Nitrogen - Method by Flow Analysis (CFA and FIA) and Spectrometric Detection. International Organisation for Standardisation. Croatian Standard Institute HRN EN ISO 13395, 1998. Water Quality - Determination of Nitrite Nitrogen and Nitrate Nitrogen and the Sum of both by Flow Analysis (CFA and FIA) and Spectrometric Method. International Organisation for Standardisation. Croatian Standard Institute.
orthophosphate (o-PO4)	HRN EN ISO 15681-2, 2008.Water Quality - Determination of Orthophosphate and Total Phosphorus Contents by Flow Analysis (FIA and CFA) - Part 2:Method by Continuous Flow Analysis (CFA). International Organisation for Standardisation. Croatian Standard Institute.
K	Water quality — Determination of sodium and potassium — Part 3: Determination of sodium and potassium by flame emission spectrometry
HCO_3^-	Determination of bicarbonate by acid-base titration with H_2SO_4
Ca, Mg	ISO 11885:2009 Water quality — Determination of selected elements by inductively coupled plasma optical emission spectrometry (ICP-OES)
Cl and SO_4	ISO 15682:2000: Water quality — Determination of chloride by flow analysis (CFA and FIA) and photometric or potentiometric detection Water quality — Determination of sulphate by flow analysis (CFA)
Na	Water quality — Determination of sodium and potassium — Part 3: Determination of sodium and potassium by flame emission spectrometry

Data quality control assurance for water analysis was performed by the quality management system according to HRN EN ISO /IEC 17025(2007) standard, by

participation in the interlaboratory comparison program and by analysis of available reference materials with known concentration values.

Aliquots of 100 ml unfiltered water were collected at each site for isotopic analyses. Oxygen and hydrogen isotopes (expressed as δ18O ‰ vs. V-SMOW and δD ‰ vs. V-SMOW, respectively) were determined by IRMS (Isotope Mass Ratio Spectrometry) at the CNR-IGG of Pisa and the University of Parma (Italy) using an automated preparation line coupled to a Finnigan MAT Delta Plus dual collector mass spectrometer.

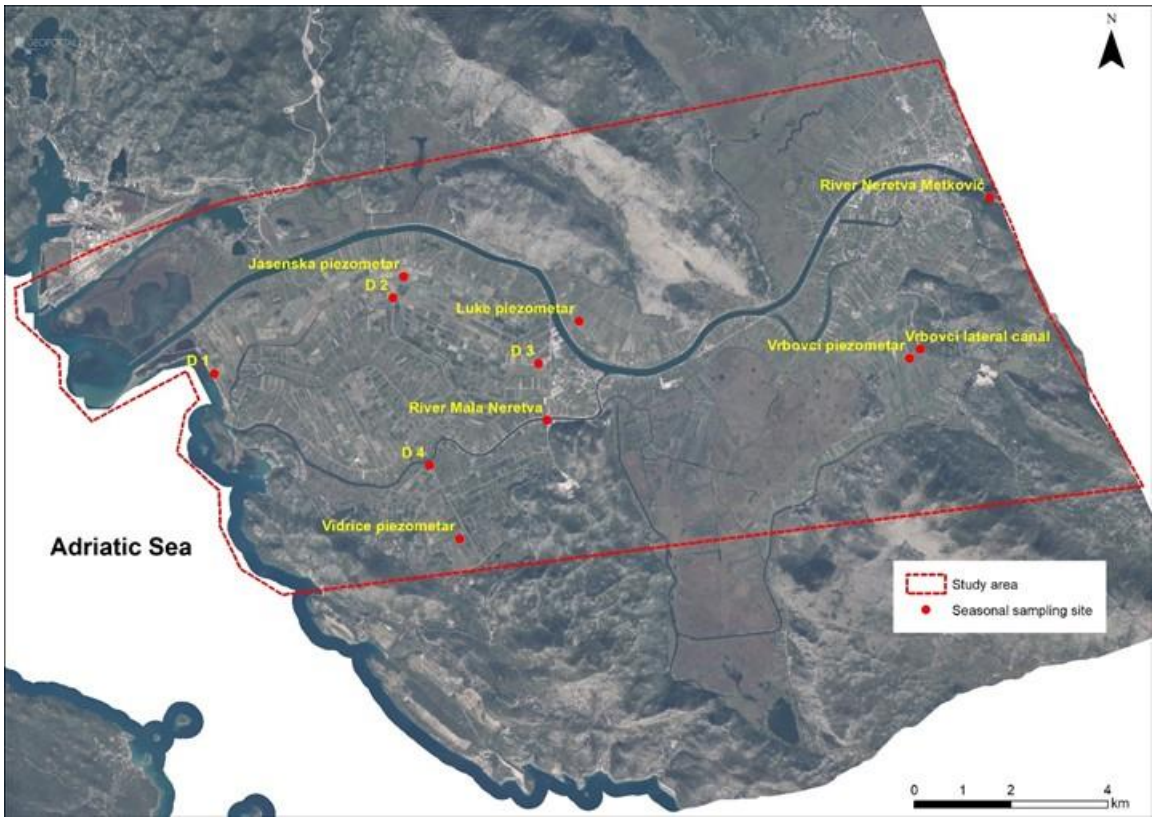

Fig. 4.43 Study area and monitoring network for the Neretva Delta

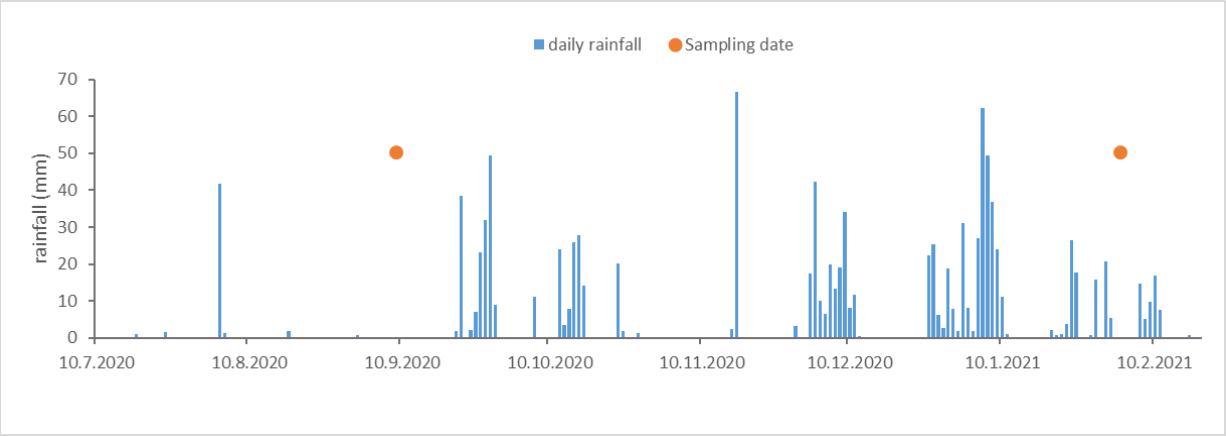

Fig. 4.44 Daily rainfall and periods of water sampling activities in the Neretva Delta (data provided by automated weather station at the pilot site, Pinova Meteo Weather Station http://pinova-meteo.com/hr_HR/)

Tables 4.27, and 4.28 show electrical conductivity in mS/m (EC_w) and pH values, concentrations of major anions (HCO_3^-, Cl^-, NO_3^-, NO_2^-, SO_4^{2-} and PO_4) and cations (Ca^{2+}, Mg^{2+}, Na^+, K^+, and NH_4), and oxygen and hydrogen isotope signatures (expressed as δ18O ‰ vs. V-SMOW and δD ‰ vs. V-SMOW) for the September 2020 and Februry 2021 measurements, respectively.

Table 4.27 Physico-chemical parameters, chemical and isotopic data of the water samples from the September 2020 sampling campaign

Sampling date:	9-Sep-20														
Code	pH	EC_w 25°C	HCO_3^-	NH_4 - N	NO_3 - N	NO_2 - N	PO_4-P	Cl^-	SO_4^{2-}	Ca^{2+}	K^+	Mg^{2+}	Na^+	$\delta^{18}O$	δD
	25°C	mS / m						mg/L						‰ vs. V-SMOW	‰ vs. V-SMOW
River Mala Neretva	8.0	92.60	195	0.86	0.16	<0,01	<0,01	181	56	56	4.1	21	96	-7.18	-46.4
River Neretva Metković	7.9	80.60	204	0.89	0.31	<0,01	<0,01	137	55	55	3	18	72	-8.41	-54.8
Vrbovci lateral canal	7.5	50.10	244	0.67	<0,08	<0,01	<0,01	45	10.0	10	<1,0	6.8	21	-6.70	-41.9
Luke piezometar	7.0	688	424	2.10	<0,08	<0,01	<0,01	1689	1175	1175	32	146	845	-5.69	-36.6
Vrbovci piezometar	7.0	123.6	464	1.50	<0,08	<0,01	0.021	117	182	182	9.7	18	41	-6.04	-38.8
Vidrice piezometar	7.1	912	763	30	4.30	0.120	0.1	2573	738	738	96	162	1436	-4.98	-28.8
D 1	7.5	5280	92	2.5	0.16	0.26	0.010	20630	2773	871	378	1160	11240	0.89	5.4
D 2	7.8	3180	226	28	<0,08	0.14	0.047	12192	478	201	282	351	6720	-2.04	-9.8
D 3	7.7	3910	59	11	<0,08	0.92	<0,01	14360	1749	574	312	654	7910	-1.50	-8.6
D 4	7.6	2090	1052	47	<0,08	0.017	0.20	7278	379	102	199	381	4050	-4.13	-24.9

Table 4.28 Physico-chemical parameters, chemical and isotopic data of the water samples from the February 2021 sampling campaign

Sampling date:	3-Feb-21														
Code	pH	EC_w 25°C	HCO_3^-	NH_4 - N	NO_3 - N	NO_2 - N	PO_4-P	Cl^-	SO_4^{2-}	Ca^{2+}	K^+	Mg^{2+}	Na^+	$\delta^{18}O$	δD
	25°C	mS / m	mg/L											‰ vs. V-SMOW	‰ vs. V-SMOW
River Mala Neretva	7.5	63.4	268	0.76	0.17	<0,01	<0,01	79	18	79	1.7	8.8	36	-7.53	-44.25
River Neretva Metković	7.9	39.4	217	0.83	0.34	<0,01	0.018	16	17	66	<1,0	5.8	5.5	-8.27	-50.10
Vrbovci lateral canal	7.5	78.1	281	0.83	0.28	<0,01	<0,01	118	20	87	2.6	11	59	-7.81	-46.28
Luke piezometar	7.1	266	403	0.89	49	0.014	<0,01	435	298	312	6.6	29	214	-6.07	-36.89
Vrbovci piezometar	7.1	130.3	390	0.79	38	<0,01	<0,01	101	89	196	<1,0	16	60	-6.32	-36.69
Vidrice piezometar	7.3	1081	1342	32	<0,08	0.015	2.7	2514	1973	365	103	412	1520	-4.77	-29.11
Jasenska piezometar	7.3	2370	2562	90	<0,08	0.023	7.2	7346	717	199	203	576	4290	-4.38	-27.16
D 1	7.4	5440	110	2.4	0.14	0.065	0.012	20445	2745	801	408	1148	11200	0.77	5.27
D 2	7.9	3240	275	28	<0,08	0.37	0.046	11943	377	191	302	363	6550	-2.10	-12.09
D 3	8.4	4050	38	17	<0,08	0.42	<0,01	14580	1713	669	328	591	7850	-1.50	-8.66
D 4	7.7	2120	1098	45	<0,08	0.12	0.22	6700	317	89	206	387	4040	-4.12	-24.70

The pH values ranged from 7.0 (Luke and Vidrice piezometar) to 8.0 (River Mala Neretva) and from 7.1 (Luke and Vidrice piezometar) to 8.4 (D3) in September 2020 and February 2021, respectively.

Electrical conductivity (EC_w), which is directly related to ion concentration, varied across the transects from 50.1 (Vrbovci lateral canal) to 5280 mS/m (D1) and from 39.4 (River Neretva-Metković) to 5440 mS/m (D1) in September 2020 and February 2021. Among the major anions, chloride (Cl^-) was the most abundant species in majority of the samples and reached the highest concentration up to 20630 mg/L in September 2021 at deep piezometer D1. The only exceptions to this are the water samples from the river mala Neretva, River Neretva Metković, Vrbovci side channel and Vrbovci piezometar in both sampling campaigns, because they had bicarbonate (HCO_3^-) as the most abundant anion. Sulfate (SO_4^{2-}) abundance was characterized by relatively high variability, ranging from 10 mg/L (Vrbovci lateral canal), and up to 2773 mg/L at D1 in the September 2020. Among the minor anions, nitrate (NO_3^-) showed extremely high variability in sampling campain at the end of the wet season ranging from 0.08 to 49 (Luke piezometar) mg/L. Among the major cations, sodium (Na^+) was the most abundant species in all water samples and reached the highest concentrations (up to 11240 mg/L in September 2020) at D1, regardless of the sampling campaign, except for those that had calcium (Ca^{2+}) as the dominant cation, i.e. Luke and Vrbovci Piezometer in September 2020, and River Mala Neretva, River Neretva Metković, Vrbovci side channel and Luke and Vidrice piezometer in February 2021. Ca^{2+} reached the highest concentration (1175 mg/L) at Luke piezometer in September 2020. Magnesium (Mg^{2+}) concentration varied from 5.8 mg/L (River Neretva Metković in February 2021) to 1160 mg/L (D1 in September 2020), while potassium (K^+) concentration ranged from 1.0 (Vrbovci side channel in both sampling campaign and at River Neretva Metković in February 2021) to 408 mg/L (D1 in February 2021). Finally, ammonium (NH_4^+) showed great variability and ranged from 0.76 (River Mala Neretva) to 90 mg/L (Jasenska Piezometer) in February 2021. Maximum values of δ18O and δ2H 0.89 ‰ V-SMOW and 5.4 ‰ V-SMOW, respectively, were recorded in both sampling camapines and in the deep piezometer D1 and minimum values in River Neretva Metković.

The Neretva River is characterized by typical interseasonal discharge fluctuations. The analysis of collected surface and groundwater samples from the Neretva Delta can show a large spatial and seasonal variability in relation to the geochemical character of the water. The ternary diagrams (Na+K)- Mg-Ca and Cl-SO4-HCO3 for cationic and for anionic species are shown in Figs. 4.45-4.48, starting from the concentrations expressed in meq/L and calculated to 100%. The main anion triangular diagram shows that the water samples in September 2020 belong to the Cl range (Fig. 4.45). The chloride character of the samples is particularly pronounced in deep piezometers due to the direct connection of the aquifer with the sea. HCO3- is always present in relatively lower concentrations, with the exception of samples from the Vrbovci piezometer and the Vrbovci lateral canal, taken in September 2020 and February 2021, respectively (Fig. 4.45 and Fig. 4.46), and River Neretva Metković and River Mala Neretva. The plots of Figs. 4.47-4.48 show a clear dominance of Na+K among cations for the majority of the collected samples in September 2020, with the exception of two shallow piezometers Luke and Vrbovci. In the February 2021 sampling campaign, both the surface water samples and the groundwater samples at the Luke and Vrbovci piezometers are dominated by Ca2+.

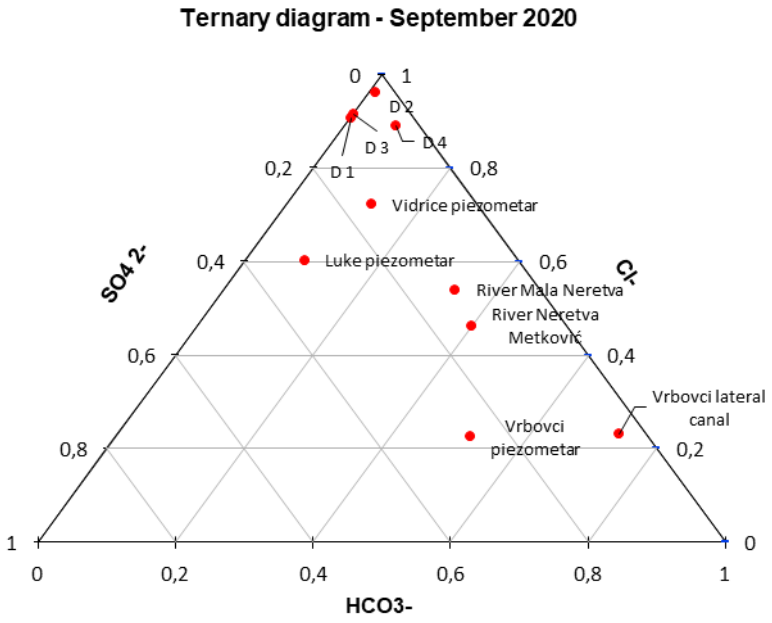

Fig. 4.45 Cl-HCO_3-SO_4 ternary diagram for the investigated samples in September 2020

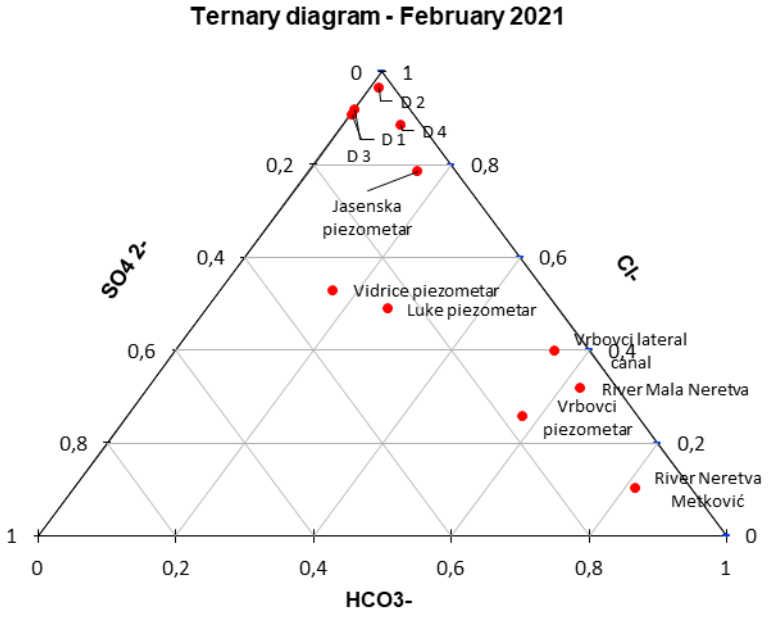

Fig. 4.46 Cl-HCO_3-SO_4 ternary diagram for the investigated samples in February 2021

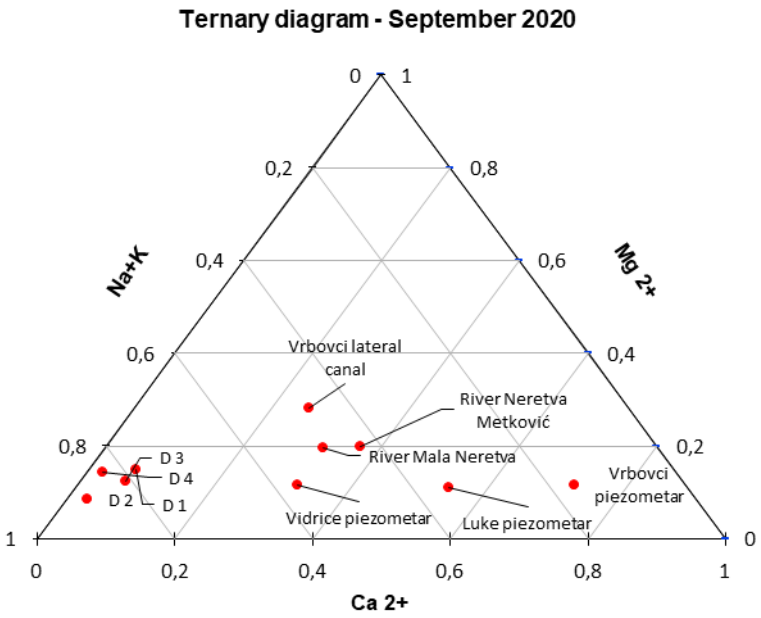

Fig. 4.47 (Na + K)-Ca-Mg ternary diagram for the investigated samples in September 2020

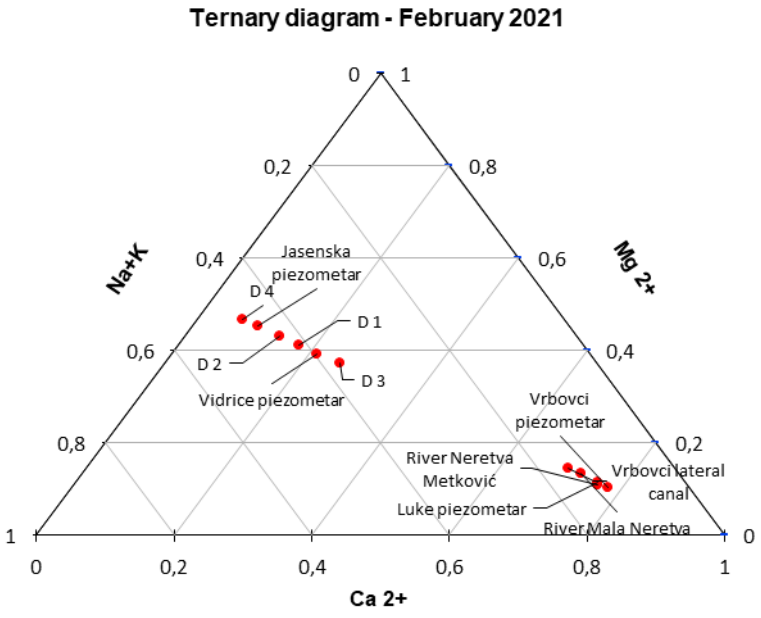

Fig. 4.48 (Na + K)-Ca-Mg ternary diagram for the investigated samples in February 2021

4.4 Conclusions

Of all the stations studied in three groups (pumping stations, melioration canals and piezometers), the mean value of EC_w ranged from 2 to 10 dS m^{-1} and was classified as moderately saline water (primary drainage water and groundwater). The mean value of ECw of natural streams ranged from 0.7 - 2 dS m^{-1} and was classified as slightly saline water. High coefficients of variation, high maximum values and statistically significant positive trends of ECw may indicate a possible increase in EC_w in both surface and groundwater in the valley Neretva River. In this sense, the most critical stations in terms of water salinity are the monitoring stations in the melioration channels and groundwater. Of the 7 soil monitoring stations, the soil was salinized at 5 of them. The greatest risk due to soil salinization and the associated consequences for agricultural production was observed in the Vidrice melioration area. It is a cautionary fact that soil was slightly to moderately salinated in all monitoring stations during the period 2009 to 2018, with observed maximum values of ECe higher than 2 dS m^{-1}.

The results of surface and groundwater quality monitoring in the Neretva Delta, carried out within the Asteris project during two seasons, showed the sensitivity of groundwater and surface water to salinization. The dominance of Cl anions and the sum of Na and K cations indicate salinization processes. This process is particularly pronounced during the dry season.

4.5 References

***IUSS WORKING GROUP WRB (2014): World reference base for soil resources 2014. World Soil Resources Reports. FAO, Rome, No. 106, 181 p.

Biondić, R., Rubinić, J., Biondić, B., Meaški, H., Radišić, M. (2016): Definiranje trendova i ocjena stanja podzemnih voda na području krša u Hrvatskoj, Sveučilište u Zagrebu Geotehnički fakultet, Sveučilište u Rijeci Građevinski fakultet, 14-011/15.

Bogunović, M., Vidaček, Ž., Racz, Z., Husnjak, S., Sraka, M. (1996): Namjenska pedološka karte RH mjerila 1:300.000. Sveučilište u Zagrebu Agronomski fakultet, Zavod za pedologiju

Husnjak, S. (2014): Sistematika tala Hrvatske. Sveučilišni udžbenik. Hrvatska sveučilišna naklada, Zagreb, 368 pp.

Ljubenkov, I., Vranješ, M. (2012): Numerički model uslojenog tečenja – primjer zaslanjivanja korita rijeke Neretve (2004), Građevinar 64 (2012) 2, str. 101-112.

Ondrašek G., Romić D., Bakić Begić H., Bubalo Kovačić M., Husnjak S., Mesić M., Šestak I., Salajpal K., Barić K., Bažok R., Pintar A., Romić M., Krevh V., Konjačić M., Vnučec I., Zovko M., Brkić Ž., Žiža I., Kušan V. (2019). Određivanje prioritetnih područja motrenja podzemnih voda unutar intenzivnog poljoprivrednog prostora (SAGRA 2). Sveučilište u Zagrebu Agronomski fakultet, Zagreb, 335 pp.

Romić, D., Castrignanò, A., Romić, M., Buttafuoco, G., Bubalo Kovačić, M., Ondrašek, G., Zovko, M. 2020. Modelling spatial and temporal variability of water quality from different monitoring stations using mixed effects model theory // Science of The Total Environment, 704 (2020), 1-10 doi:10.1016/j.scitotenv.2019.135875

Romić, D., Romić M., Zovko, M., Bubalo, M., Ondrašek, G., Husnjak, S., Sričević, I., Maurović, N., Bakić, H., Matijević, L., Vranješ, M (2014): Petogodišnje izvješće (2009-2013) monitoringa zaslanjivanja tla i vode u dolini Neretve

Romić, D., Zovko, M., Romić, M., Bubalo Kovačić, M., Ondrašek, G (2019): Petogodišnje izvješće (2014-2018) Monitoring zaslanjenja voda i poljoprivrednih tala na području doline Neretve